UNIVERSITÀ
DEGLI STUDI
FIRENZE

DIEF
DIPARTIMENTO
DI INGEGNERIA
INDUSTRIALE

Micro turbo expander design for small scale ORC: Tesla turbine

A dissertation submitted in partial fulfilment of the requirements for the degree of

Doctor of Philosophy in Industrial Engineering

Curricula: Energy and Innovative Industrial and Environmental Technologies

Scientific Area: ING–IND/09

Ph.D. Candidate:	Ing. Lorenzo Talluri
Tutor:	Prof. Giampaolo Manfrida
Co-Tutor:	Prof. Daniele Fiaschi
Co-Tutor:	Prof. Vincent Lemort
Ph.D. School Coordinator:	Prof. Maurizio De Lucia

Ph.D. School Cycle: XXXI (2015–2018)

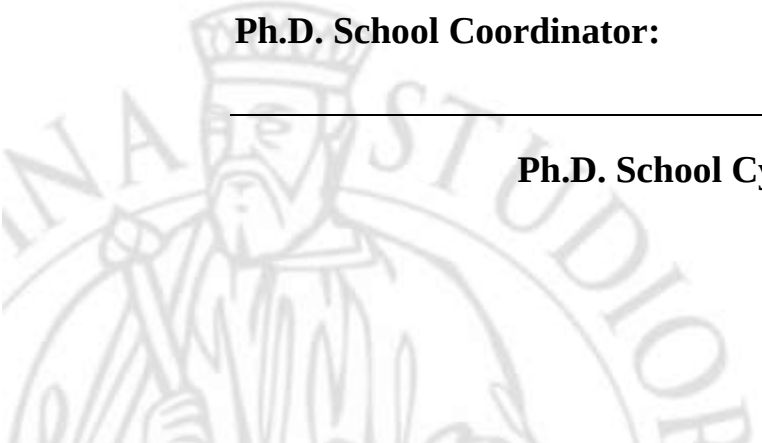

Abstract

Over the last years, the increase in energy consumption coupled with ever more stringent regulations on pollutants emissions and the massive advent of renewables in the energy market, have promoted the development of distributed energy systems and thus of an increasing interest towards small and micro power generation systems. In this context, the ORC progressively became the leading technology in the field of low size energy conversion systems (<100 kW) and low temperature applications (<150°C). Nonetheless, this technology still deserves further developments, especially regarding the design of specific components, which should grant features of reliability, acceptable performance level and, often even more important, affordable price in order to ensure the attractiveness of the whole energy system. It is the case of the small and micro expanders (tens to few kW scale). A possible solution for micro–size expanders is the Tesla expander, which is a viscous bladeless turbine that holds the desired characteristics of low cost and reliability. This expander was first developed by N. Tesla at the beginning of the 20th century, but it did not stir up much attention due to the strong drive towards large centralized power plants, where this technology becomes no longer competitive against those belonging to bladed expanders. In the recent years, due to the increasing appeal towards micro power generation and energy recovery from wasted flows, this cost effective expander technology rose a renovated interest.

In the present study, a 2D numerical model is realized and a design procedure of a Tesla turbine for ORC applications is proposed. A throughout optimization method is developed by evaluating the losses of each component and by introducing an innovative rotor model. The main optimizing parameters of the turbine, such as the rotor inlet/outlet diameter ratio, channel width–rotor diameter ratio and tangential velocity–rotational speed ratio at rotor inlet are highlighted and assessed.

The 2D model results are further exploited through the development of 3D computational investigation, which allows an accurate comprehension of the flow characteristics, which are difficult to depict with a 2D code.

Finally, two prototypes are designed, realized and tested. The former one is designed to work with air as working fluid, with the stator made in ABS with additive manufacturing technique, in order to show a possible cost effective way of realization. The obtained experimental results of this prototype well match the numerical predictions. A 94 W net power output with 11.2% efficiency are measured.

The second prototype is designed to work with organic fluids (specifically with R404A), and it is ultimately tested with R1233zd(E). A standard metal manufacturing is followed for this prototype. The achieved experimental results confirmed the validity and the large potential applicative chances of this emerging technology, especially in the field of micro

sizes, low inlet temperature and low expansion ratios. 371 W net power output at 10% shaft efficiency are obtained.

The experimental results allowed the validation of numerical models, which was among the main objectives of this work. In this way, the numerical procedure may be reliably employed as the tool for the accurate and optimised design of Tesla turbines for organic Rankine cycles but also for applications with gas like air.

As a final remark, it can be affirmed that the operability of the Tesla expander was demonstrated in this work. Thus, it may be considered as a suitable and realizable solution to tackle one of the present issues related to micro expanders, namely high costs and low reliability, which, moreover, suffers off design conditions only to a limited extent.

The realization of a reliable design tool is another fundamental outcome of the present work.

Acknowledgments

Coming towards the end of such a full, absorbing and gratifying journey, I feel that there are a lot of people, whom I should thank; as without their help I could not have reached such a coveted destination.

First and foremost, I wish to express my deepest gratitude to professor Manfrida and professor Fiaschi, for giving me the opportunity to join their research group. This opportunity, coupled to the constant trust, the precious advices received, as well as the patience that they had towards me throughout these years made me grow, both from a professional and human perspective. For this, I am heartily grateful.

I wish to demonstrate my sincere thankfulness to professor Lemort, who allowed me to spend an unforgettable and valuable experience in the Thermodynamics Laboratory of Université de Liège. I really wish to thank him and his entire research group, who contributed to my professional growth and, who patiently gave me lots of advices, which I have treasured. A very special thanks goes to Dr. Dumont and Mr. Labenda, whom above all others invested lots of their time for assisting me in this project. I also wish to especially thank Ir. Dickes and Ir. Parthoens.

My deepest gratitude goes also to Professor Ferrara and his entire research group, thanks to whom I was able to carry out a fundamental part of this project. I wish to thank above all Dr. Galoppi and Dott. Figini, for their support, their patience and their constructive advices during my stay at Linea Lab.

I am also particularly grateful to Dott. Tempesti and Dr. Secchi, my very first colleagues, who helped me overcome difficulties, as well as providing me with very precious advices and being in reality, more than colleagues, tutors and friends. I wish to express my thanks to all my past and present colleagues, with a very special acknowledgment to Dott. Ciappi and Dott. Pacini, for the time they took in aiding me, but above all for their patience, which was seriously put to test. Thanks to Stefano, for all of his blessings.

My thoughts also go to the people, outside the academic world, who influenced my life. I really wish to express my upmost thanks to my family, without whom I would not be the man I am today. Thank you for the constant support that you provided throughout the years. Last, but not the least, I wish to thank Gaia. I am really indebted to you. I really thank you from the bottom of my heart, as you have always supported me, and you have always pushed me to go after my dreams, enjoying the trip together with me.

Table of Contents

List of Figures

List of Tables

Nomenclature

$\dot{m}$	Mass flow rate [kg/s]
$\dot{W}$	Power [W]
A	Area [m^2]
a	Coefficient [–]
b	Channel height [m]
CF	Compactness factor [W/cm^3]
CFD	Computational Fluid Dynamics
CHP	Cogeneration of Heat and Power
D	Diameter [m]
D_h	Hydraulic diameter [m]
d_s	Specific diameter [–]
E	Kinetic energy [J/kg]
EES	Engineering Equation Solver
EoS	Equations of State
ex	exponent
f	Body force per unit mass [m/s^2]
F	Force [N]
$\mathcal{G}$	Gap [m]
h	Specific enthalpy [J/kg]
h	Heat transfer coefficient [W/m^2K]
H	Height [m]
H_s	Stator height [m]
I	Specific rothalpy [J/kg]
k	Thermal conductivity [W/mK]
L	Length [m]
L_t	Length of thermal entry region [m]
m	camber line length [m]
M	Moment [Nm]
Ma	Mach number [–]
n	Turbulent coefficient [–]
n_{ch}	Number of Rotor channels per Stator
NR	Total number of discretization step
n_s	Specific Speed [–]
Nu	Nusselt number [–]
ORC	Organic Rankine Cycle
P	Power [W]
p	Pressure [Pa]
Pr	Prandtl number [–]
Q	Heat [W]
r	Radius [m]
R	Rotor Inlet/Outlet diameter ratio [–]
Re	Reynolds number [–]
rpm	Revolution per minute
s	Disks thickness [m]
s	Infinitesimal trajectory length [m]
S_e	Length of viscous entry region [m]
SH	Super heating level [°C]

t	Thickness [m]
t	Time [s]
T	Temperature [°C]
TRL	Technology Readiness Level
TW	Throat width [m]
TWR	Throat width ratio [–]
u	Peripheral velocity [m/s]
v	Absolute velocity [m/s]
V	Volume [m^3]
w	Relative velocity [m/s]
w	Width of plenum chamber [m]
W	Specific work [J/kg]
WHR	Waste Heat Recovery
x	Non–dimensional radius [–]
X, Y	Cartesian coordinates
Z	Number of nozzles [–]

Greek symbols

α	Absolute flow angle [°]
α	Camber line angle [°]
β	Expansion ratio [–]
β	Relative flow angle [°]
β	Stagger angle [°]
γ	Relative flow angle [°]
ε	Partialization degree [–]
ζ	Loss coefficient [–]
ζ	Friction factor [–]
η	Efficiency [–]
θ	Absolute flow angle [°]
θ	Wrap angle [°]
λ	Thermal expansion coefficient [1/°C]
μ	Dynamic viscosity [kg/ms]
ν	Kinematic viscosity [m^2/s]
ξ	Non–dimensionalized kinetic energy [–]
ρ	Density [kg/m^3]
σ	Material Stress [Pa]
σ	Tangential velocity ratio at rotor inlet [–]
τ	Wall shear stress [Pa]
Φ	Flow coefficient [–]
Φ	Velocity ratio [–]
Ψ	Load coefficient [–]
ω/Ω	Rotational speed [rad/s]

Subscripts and superscripts

0x	Total condition at section x
0	Stator inlet value
1	Stator outlet value
2	Rotor inlet value
3	Rotor outlet value
4	Diffuser inlet value

5	Diffuser outlet value
all	Allowable
ch	Channel
cl	Camber line
con	Contraction
diff	Diffuser
down	Lower bound
e	Fluid element
en	Enlargement
h	Hydraulic
i	Discretization step
in	Inlet
kin	Kinetic
N	Nozzle
n	Power law exponent
out	Outlet
PS	Pressure Side
r	Radial direction
r	Relative
r	Rotor
R	Rodger
SS	Suction side
st	Stator
swirl	Swirled
t	Tangential
t	Throat
t	Time
tot	Total
tt	Total to total
up	Upper bound
w	Wetted
z	Axial direction
θ	Tangential direction

1 Introduction

The world scenario recently experienced a strong increase in energy consumption demand, associated with a series of issues related to the exhaustion, environmental impact and cost of the resources, especially for fossil fuels. This framework encourages the search of alternative energy solutions for power generation, as well as the improvement of already existing conversion systems.

Over the last years, research on energy systems has focused on small, distributed systems for cogeneration, which cover the requirements of heat and power generation both in domestic buildings and industrial facilities, with an emphasis on smart grid solutions which can effectively deal with problems of load/generation mismatch and integration of energy storage.

When applied to intermediate and low–temperature resources, a modern popular technology is the Organic Rankine Cycle, whose applications are being extended to small size (5–50 kW_e). This technology substitutes water with organic–based compounds as working fluid. The main advantage of these fluids is that they are suitable for low temperature applications, as they allow moderate saturation temperatures and pressures and high molecular mass. Indeed, several studies were performed on ORCs applied to low–medium temperature thermal resources. Such applications range from recovery of heat from gas turbine discharge, internal combustion engines or industrial waste heat, energy conversion from biomass, solar or geothermal resources represent another common field of application.

Nonetheless, when micro applications are taken into account, one of the main issues with Organic Rankine Cycles is linked to the expander, as this component often involves high manufacturing costs and offers low reliability. The Tesla turbine, with its relatively simple structure, appears to be a potentially reliable and low–cost expander, which could find its market in the low–power range.

1.1 Motivation

The application of Tesla turbines to small and mini ORC cycles could allow the opening–up of this new niche market, where ORCs have been hindered mainly by the high initial investment cost, by delivering an affordable expander technology with minimal maintenance requirements. The application to low enthalpy systems will allow the spread of ORC cycles at capillary level, similarly to smart grids, with an EU application potential of thousands of units. Therefore, it is of great interest to conduct a research analysis on such an innovative component, which could potentially become a breakthrough technology for energy harvesting from industrial wastes of heat and low pressure flows, due to its low cost and reliability characteristics.

1.2 Objectives and structure

1.2.1 Objectives

This research project aims to the thermo–fluid dynamic assessment of an innovative boundary layer bladeless expander (Tesla type turbine) for mini and micro energy conversion systems, which could become a strong competitor of the actual employed micro expanders thanks to its very attractive compromise between efficiency and costs.

The main objectives of the present research can be resumed in the following:

1) Development of a numerical 2D model which allows the prediction of the performance of a Tesla turbine for different working fluids, applying real gas assumption and introducing sudden expansion and contraction pressure losses;

2) Definition of a comprehensive scheme for thermo–fluid dynamic and mechanical design and optimization of the expander;

3) Development of computational fluid dynamics analysis to depict the flow behaviour inside a Tesla turbine;

4) Validation of 2D built numerical model with experimental campaign both on air and organic working fluids.

1.2.2 Structure

The thesis is comprised of five chapters, including the initial introduction chapter.

Chapter 2 is dedicated to the literature review, where the “state of the art” of the Tesla turbine researches is assessed. Furthermore, a brief introduction on ORC technologies is presented, with a particular focus on micro expanders. At the end of the chapter a statistic summary of the available literature on Tesla turbines is reported.

Chapter 3 is dedicated to the methodology and models utilized in this thesis. Particularly the 2D in house EES code is accurately described, presenting each component model. The prototypes design procedure is assessed and the mechanical verification scheme and the computational analysis settings are presented.

Chapter 4 is dedicated to the analysis of results. The obtained results are divided in three main Sections. The first Section dealing with 2D in house code simulation, second Section depicting CFD analysis results and last Section displaying the achieved experimental data.

Chapter 5 is dedicated to the conclusions of this research and recommendations for future work.

2 Literature Review

2.1 Word Energy Scenario

In 2017, the net electricity production grew by 0.8% compared to 2016. A significant increase of the power production share (16.7%) was given by renewable energies, with a consequent reduction (even if small) of fossil fuels share (by 1%).

In OECD countries power production by renewable energies accounted for 23.7% of the global generation; fossil fuels contribution was of 58.7% and the remaining part was filled by nuclear power (17.6%), as displayed in Fig. 2.1 [1].

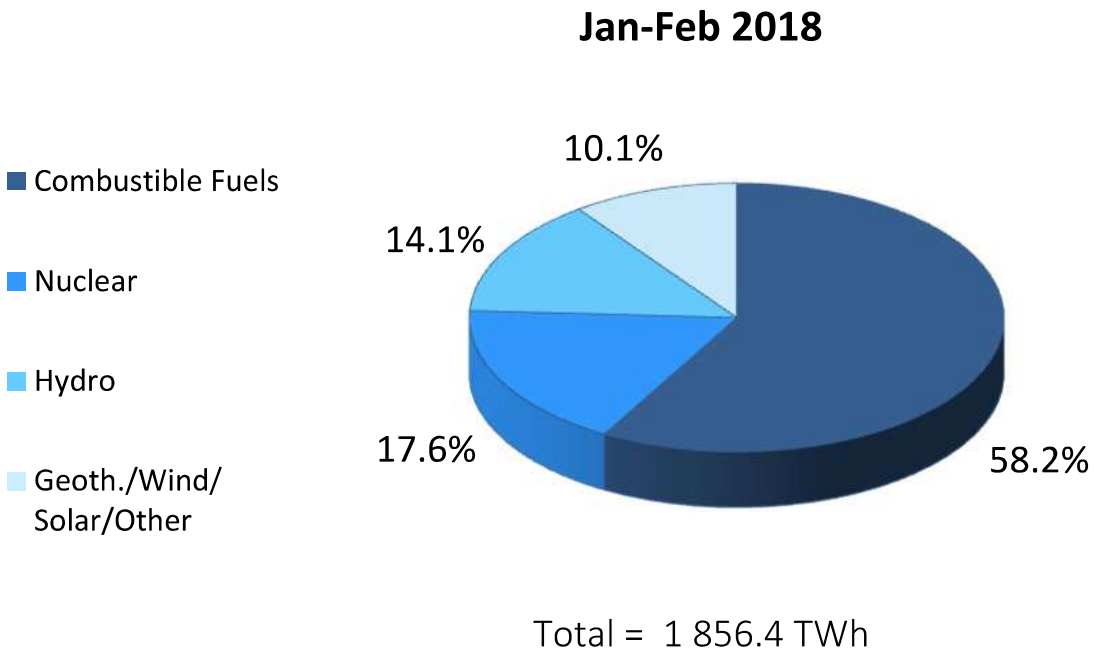

Fig. 2.1 OECD Electricity Production by Fuel Type [1]

The increase in renewable energy share is certainly due by the strong concern given by climate change. Particular attention is given to the energy use and greenhouse gases production. Indeed, among human activities that produce greenhouse gases, the energy sector is by far the main contributor (68% share [2]).

The European Union is strongly committed to tackle climate change and it has set a comprehensive package of policy measures to reduce greenhouse gas emissions. Particularly, H2020 directives on climate change targets the 20–20–20 policy that is of a reduction in 20% of greenhouse emissions (from 1990 levels), a total share of energy production by renewable energy of 20% and a 20% improvement in energy efficiency. In compliance to these strongholds, the EU policy pushes towards a transition to decentralised energy system production, that is through the employment of distributed

power generation and storage devices in households, as well as to the maximisation of energy recovery from industrial process, which actually waste precious resources, such as heat/cold and pneumatic energy [3].

This framework encourages the search of alternative energy solutions for power generation, as well as the improvement of already existing conversion systems, particularly in the field of small and medium power range, which is also the basis to move towards the direction of distributed energy systems. Particularly, in recent years, energy research focused on small, distributed systems for cogeneration, which cover the requirements of heat and power generation both in domestic buildings and industrial facilities. Specifically, the affected market ranges from big industrial energy sectors, such as textile, food, steel, glass industries to small domestic cogeneration of heat and power unites or to inverse cycles (like domestic compression chillers or heat pumps).

In order to efficiently exploit the waste heat from industrial processes, as well as to develop small efficient cogeneration systems, which could also be connected to renewable technologies, conventional power generation systems (open cycle gas turbine and steam cycle) do not seem the most appropriate. Indeed, in the last few decades a new technology, based on organic fluids compounds, which are characterized by lower saturation temperature and pressure and higher molecular mass when compared to steam, has taken lead for a wide range of applications where heat and/or temperature from the energy sources are limited, such as waste heat recovery applications (WHR) or power generation from renewable energies (Fig. 2.2). This technology is known as ORC (Organic Rankine Cycle).

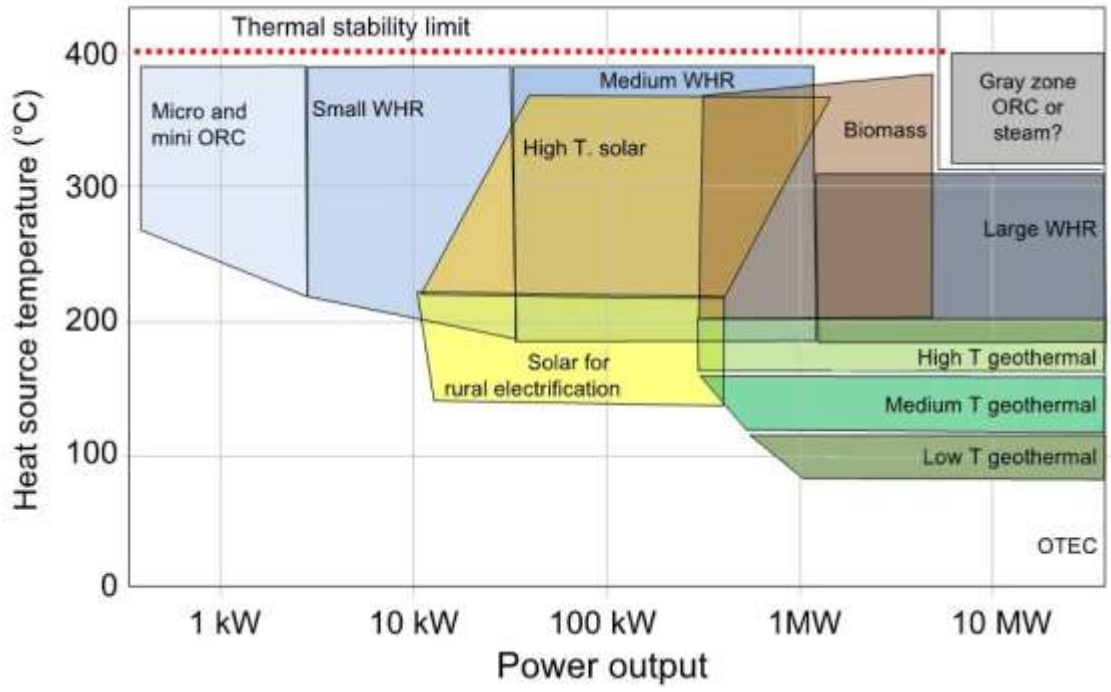

Fig. 2.2 Organic Rankine cycle fields of applications [4]

2.2 Overview of Organic Rankine Cycle

In order to have of a clear understanding of the reasons of the rising of interest of the ORC technology, a comparison with traditional power generation systems both from a thermodynamic and a Turbomachinery points of views needs to be carried out.

First of all, a distinction of power production technologies is given by the architecture of the cycle, "open" or "closed". In open cycles the working fluid experiences material exchanges with the environment, both at inlet and outlet of the cycle; an example is the gas turbine cycle, utilizing air as working fluid. Closed cycles, on the other hand, are characterised by a working fluid that consecutively operates a cyclic series of thermodynamic transformations; an example is the Rankine (or the Hirn) cycle, which uses water (steam) as working fluid. Another important aspect to remark is the possible transformations that can take place in a power generation system with external heat sources (excluding therefore internal combustion engines), which are: nearly adiabatic transformation (typically, in pumps, compressors and turbines/expanders) and nearly isobaric transformations (typically, in heat exchangers).

Cherishing the above–mentioned difference in cycle architectures and the possible thermodynamic transformations, the open–air cycle will be first analysed through second law efficiency assessment. Assuming a fixed constant temperature for the heat source and a fixed ambient temperature of a simple open cycle, the cycle efficiency can be expressed as shown in Eq. (2.1).

$$\eta = \left(1 - \frac{T_0}{T_{max}}\right) - \left(T_0 \sum_i^N \frac{\Delta S_i}{Q_{in}}\right) \tag{2.1}$$

Where:

- $1 - \frac{T_0}{T_{max}}$ is known as the "Carnot" efficiency, which is the upper limit that any traditional thermodynamic cycle can achieve;
- $T_0 \sum_i^N \frac{\Delta S_i}{Q_{in}}$ is the sum of the losses related to each cause of irreversibility.

Particularly, the second term of Eq. (2.1) can be decomposed in 8 main losses, as suggested in [4] and shown in Fig. 2.3 (corresponding colour in bracket near losses bullet point):

- pressure losses (red);
- fluid–dynamic losses in compressor (green);
- heat transfer losses in the heat introduction process (purple);
- fluid–dynamic losses in expansion process (azure);
- losses due to mixing of hot air to atmosphere (orange);

- heat losses to the environment (royal blue);
- mechanical/electrical losses (light red);
- heat transfer losses in the recuperator (if present, light green).

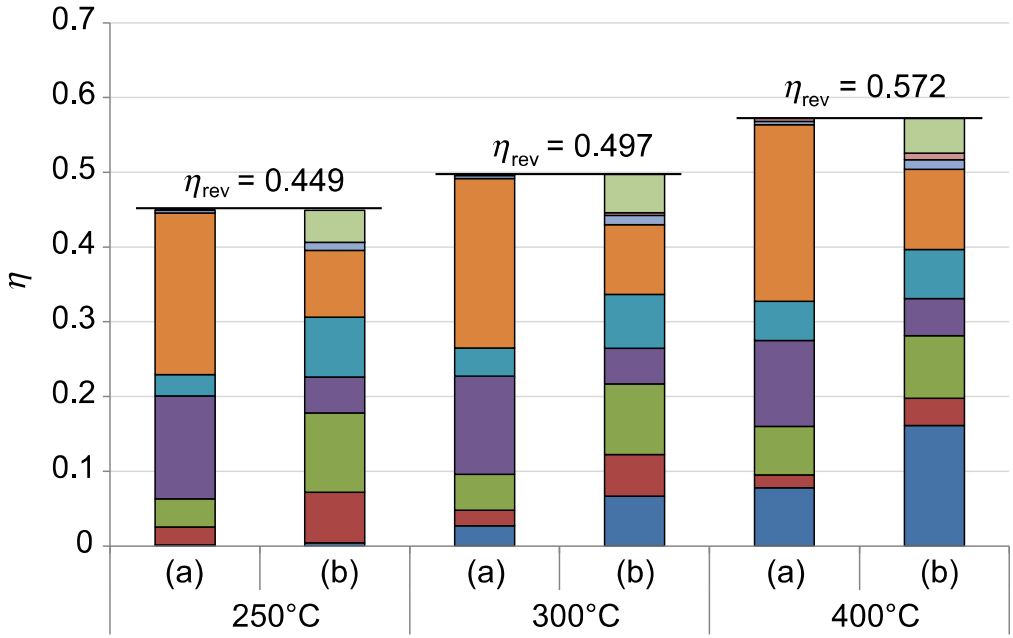

Fig. 2.3 Second Law efficiency (dark blue) and efficiency losses at various heat source temperature. $\boldsymbol{\eta_{rev}}$ is Carnot efficiency, (a) consider simple cycle and (b) recuperative cycle. Optimal cycle pressure ratio at each temperature is considered [4]

As can be noted from Fig. 2.3, the second law efficiency for open cycle architecture decrease drastically for lower temperatures, due to the increasing of the various losses.

Comparing gas cycles to closed–loop Organic Rankine cycles for temperature values below 400°C, the advantages of the ORC solution are quite relevant. First, a better coupling of both high and low temperature heat transfer processes can be realized more easily; in subcritical Rankine cycle, evaporation and condensation processes take place, allowing for large parts of transformations a constant temperature heat exchange. This feature is particularly appreciated for heat transfer with the environment, which often requires a relevant heat capacity, and it ensures a major lowering of the irreversibility in the process of heat transfer. Furthermore, pressurization of the cycle can be obtained using pumps (liquid conditions) instead of compressors (gas conditions), reducing greatly the amount of work required (and the irreversibility in the process).

Taking as reference the analysis conducted in [4], where three different fluids (water, benzene and MDM) were utilized in order to estimate the efficiency of a Rankine cycle with an upper resource temperature of 240°C, it can be claimed that Rankine cycles can reach efficiency which are closer to the upper Carnot limit when compared to gas cycles. Particularly, as shown in Fig 2.4, the reachable efficiencies by a Rankine cycle are in the

range of 70–85% of the maximum achievable efficiency (compared to the 30% in the case of the gas cycle). Particularly, it is seen, that even if the three fluids have very different molecular structures, the achievable cycle efficiency (when recuperated architecture is utilized) is very close between one and another. The assumed conditions for the analysis conducted in [4] are resumed in Tab. 2.1.

Table 2.1 Assumed variables of analysis conducted in [4] for comparison of gas cycles and Rankine cycles

Variable	Assumed value
Ambient Temperature	15°C
Condensation Temperature	30°C
Evaporation Temperature	240°C
Pump efficiency	0.85
Turbine efficiency	0.85
Pressure losses	10% of evaporation pressure
Thermal losses	1% of heat input
Mechanical/electrical efficiency	95%

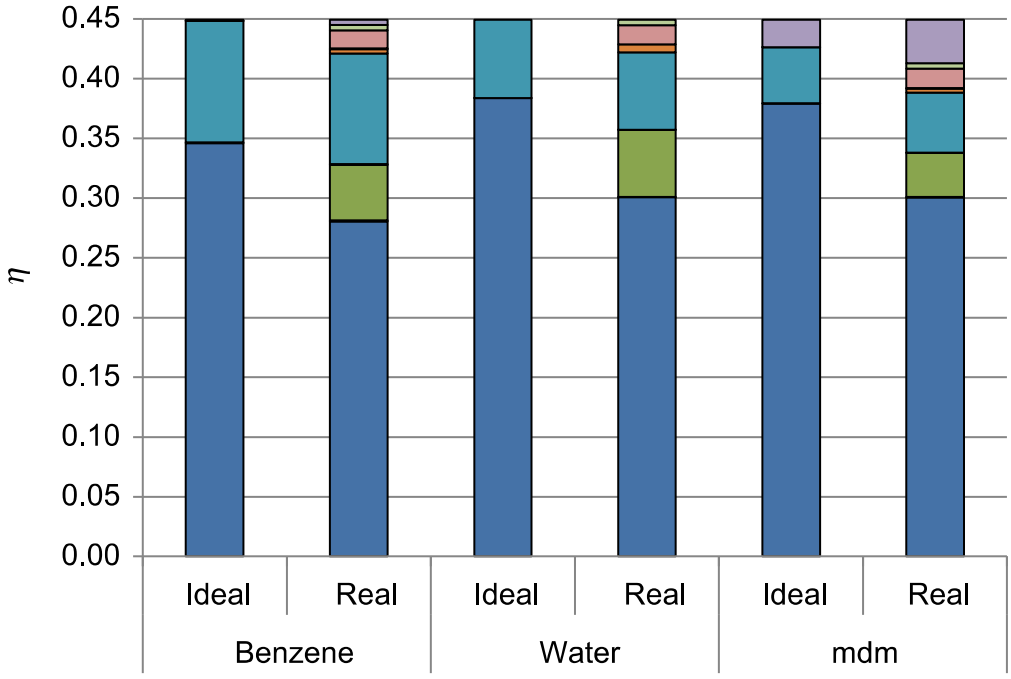

Fig. 2.4 Second law efficiency (dark blue) for three different saturated Rankine (ideal and real) cycles with assumed condition resumed in Tab. 2.1 The cycle losses represented consider: fluid–dynamic losses in pump (red), fluid–dynamic losses in turbine (green), pressure losses (purple), heat transfer losses in the liquid preheating (azure), heat transfer losses in the evaporation process (orange), heat transfer losses in the heat rejection to environment (royal blue), mechanical/electrical losses (light red), heat losses to the environment (light green), heat transfer losses in the recuperator (light purple) [4]

After the comparison between gas cycles and Rankine cycle for low temperature heat sources, the reasons why organic fluids are preferable to water for low–temperature energy resources are highlighted. The first issue when dealing with the steam Rankine cycle for low temperature application is the wet expansion process. Indeed, as displayed in Fig. 2.5, the expansion of a saturated cycle is within the liquid–vapour dome, on the other hand, for organic compounds, with higher molecular complexity (increasing molecular complexity modify the inclination of the vapour curve, known also as backward vapour line) the expansion can be dry, which will guarantee that no blade erosion issue will present. Furthermore, in the steam Rankine cycle, in order to have high turbine performances, the expander design is very costly, as a correct design will involve multi–stage turbine, with variable speed shafts. Indeed, for low power ranges the construction of an efficient steam expander becomes very difficult, as the steam flow rate would be drastically small with conversely relatively a high expansion ratio. Also the development of steam volumetric expanders is subject to many negative issues, especially regarding the complexity of the expander (appropriate lubrication system, high friction losses, difficulty to realize an adiabatic expander).

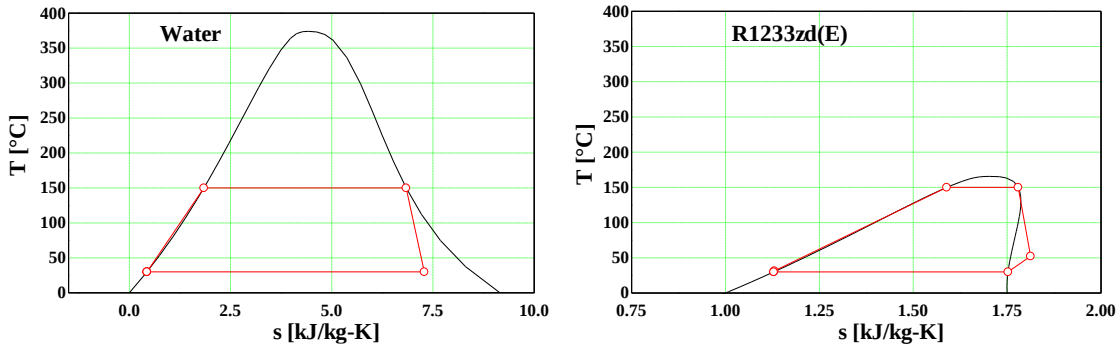

Fig. 2.5 Temperature – Entropy diagrams of saturated Rankine cycles for Water and R1233zd(E); Evaporator temperature of 150°C, Condensing temperature of 30°C

Once the thermodynamic (when compared to gas cycle) and turbomachinery (when compared to steam Rankine cycle) advantages of ORC for low temperature heat resources have been assessed, a comprehensive review on the applications, working fluid selection and expanders utilized is required in order to fully grasp the strong and weak points of this technology, as well as its maturity level.

2.3 ORC State of the art

2.3.1 Overview of ORC market

The first concept of the ORC technology was developed by T. Howard in 1826 [5], developing a system to produce 18 kW of energy with ether as working fluid. After the first spark, ORC technology started being extensively investigated, but at first it was confined to niche markets, as the safety conditions of the power plants were not adequate. Therefore, it took a whole century before the first example of "modern" ORC was realized by D'Amelio at University of Naples [6], [7]. Specifically, the developed ORC utilized solar energy as heat source for single stage turbine running with ethyl chloride as working fluid. Finally, it is in the 1960s that ORC finally bloomed thanks to the research work of Tabor and Bronicki (founder of Ormat technologies) at the National Physic Laboratory in Israel and of Angelino, Macchi and Gaia (this last founder of Turboden Ltd.) at Politecnico di Milano.

ORMAT was founded in 1964 and Turboden in 1970. These two companies are still today the biggest players in the ORC market. In more recent years, many new companies have been established; a list of the major manufacturers, as well as the total number of installed units and capacities is shown in Tab. 2.2.

Table 2.2 List of manufacturers, data updated at 31st December 2016 [6]

Manufacturer	ORC units	Total [MW]	Manufacturer	ORC units	Total [MW]
ABB	2	3.8	gt – Energy Tech	2	0.7
Adoratec	23	16.4	Johnson Control	1	1.8
BEP – E–rational	20	3.6	Kaishan	40	27.2
Canetix /CETY	50	6.3	Opcon	3	2.0
DurrCyplan	6	1.2	Orcan	16	0.3
Electratherm	55	3.14	**ORMAT**	**1102**	**1701**
Enerbasque	3	0.13	Rank	5	0.07
Enertime	2	1.6	TAS	17	143
Enex	1	9.3	TMEIC	1	1
Enogia	11	0.26	Triogen	37	5.2
Exergy	**34**	**300**	**Turboden**	**267**	**363**
General Electric	6	101	UTC Powr	10	2.8
GMK	18	5.3	Zuccato	21	1.7

In [6] an interesting study on the current ORC market was developed, assessing the total installed capacity (updated at 31st December 2016) at around 2701 MW for a total of 1754

ORC units. The many fields of applications were also considered and resumed as shown in Fig 2.6. One of the main and unparalleled advantages of ORC technology is that it is adaptable to any heat resource, allowing its application in many fields: from heat recovery applications at gas turbine discharge [8]–[10], or in internal combustion engines [11] or industrial waste heat [12], [13], to energy conversion from renewables such as biomass [14], solar [15], [16], geothermal resources [17], [18], as well as to micro–scale CHP units [19]–[22]. Furthermore, the ORC technology allows also the harnessing of ocean thermal power gradient (OTEC) [23].

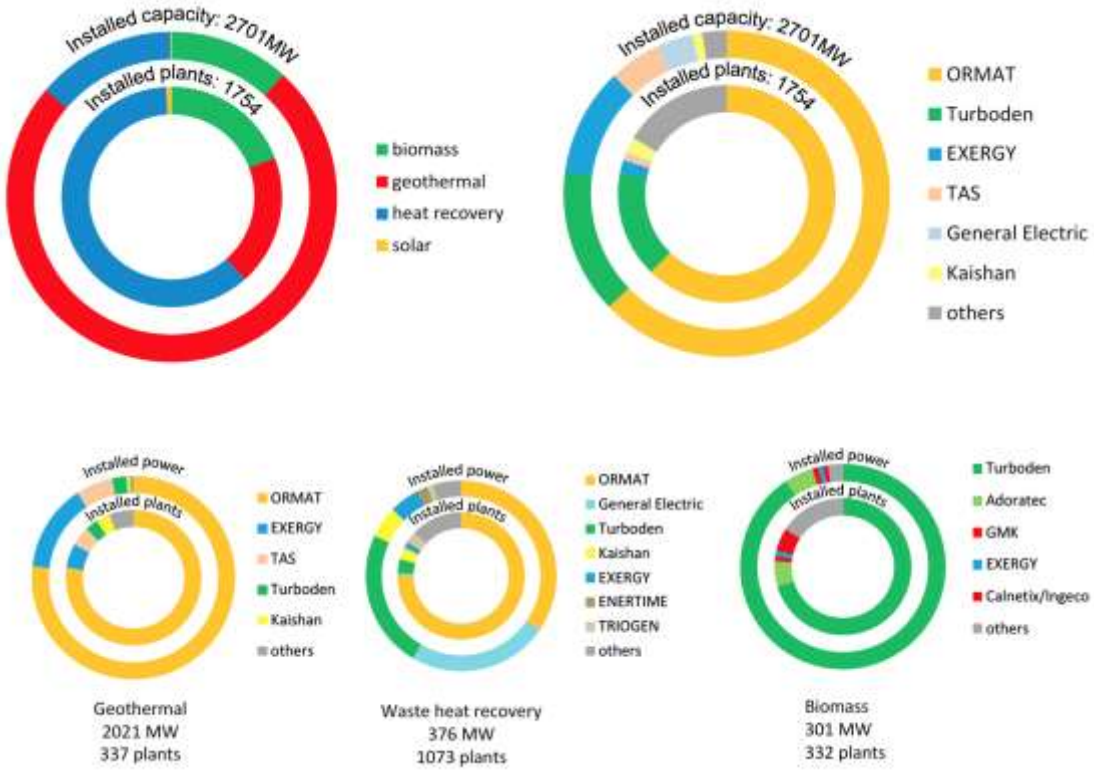

Fig. 2.6 Market share per application and per manufacturer [6]

As can be noted from Fig 2.6, Ormat is the leader in ORC technologies and the principal application to which this technology is associated is energy conversion in geothermal power plants (especially in the USA where the total installed capacity of geothermal ORC plants is about 750 MW). Nonetheless, another application, which is emerging in the last few years, is related to industrial waste heat recovery. In this field, ORMAT is still the principal manufacturer, but the supremacy is not defined, as both General Electric and Turboden owns a considerable share of installed power. Actually, the main application in the heat recovery field is recuperation from Diesel engines or gas turbines exhaust gases, as shown in Fig. 2.7. It is to be remarked that there is still plenty of room for expansion in this sector, as witnessed by the low share in energy intensive industries such as metal, cement and glass sectors. Finally, the evolution of the total installed ORC capacity is being displayed in Fig 2.8. Particularly, it is interesting to note how the global energy

prices, represented by the crude oil prices directly influences the ORC market. Before XXI century, ORC technology was basically only applied to geothermal application, but as the crude oil prices started rising and environmental issues emerged, these new technologies started expanding in the other sectors, especially in the biomass heat recovery applications.

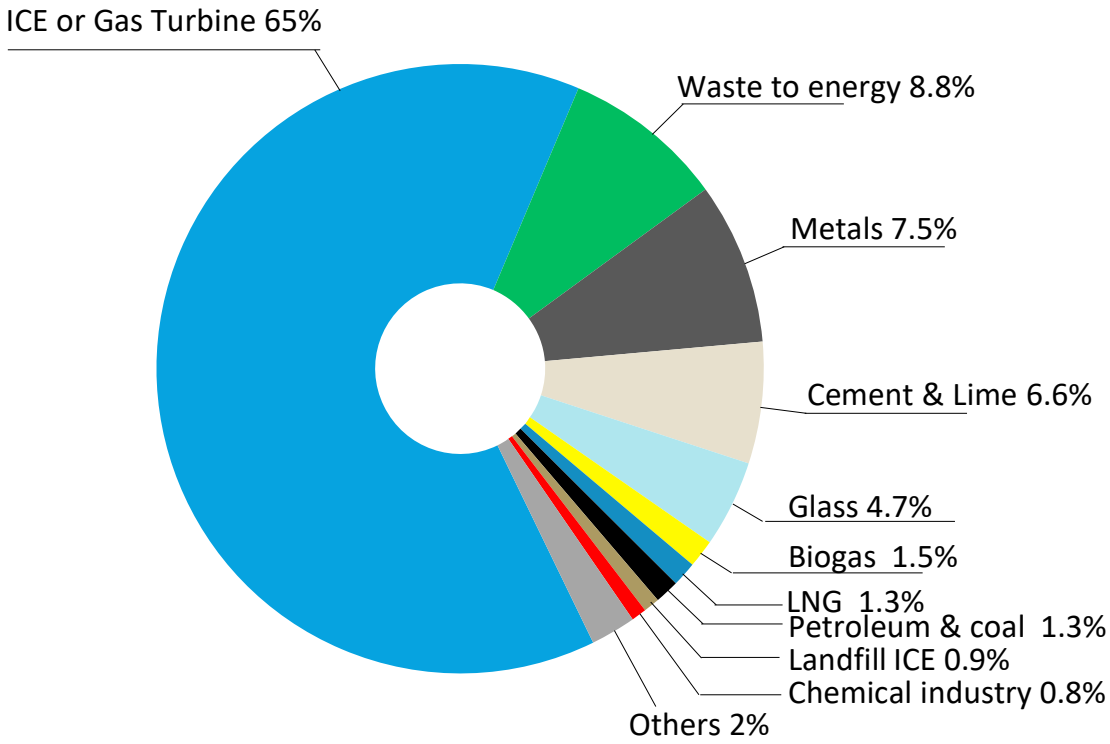

Fig. 2.7 Installed capacity share in heat recovery application [6]

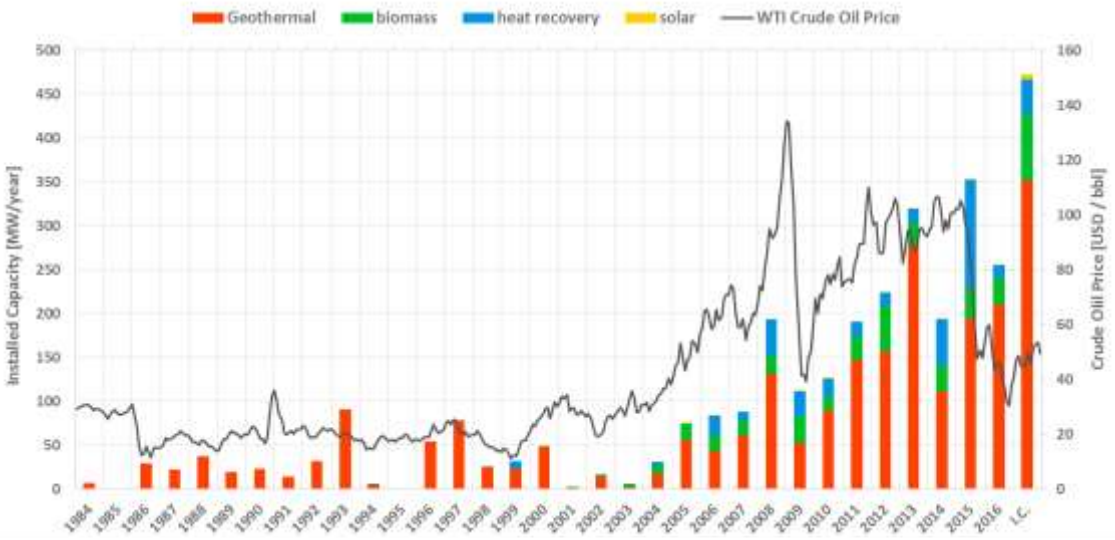

Fig. 2.8 Installed ORC capacity from 1984 up to 2017, with different application highlighted [6]

2.3.2 ORC architectures

ORC technology presents several degree of optimization in the design process. The main ones can be resumed to 5: operating parameter selection (mainly pressure), working fluid selection, component selection, cycle architecture and control strategy. Differently from steam Rankine cycle, ORC can easily incorporate components such as re–heaters or recuperators, as well as to develop supercritical cycle at relatively low heat sources temperature. These features allow a possible enhancement in cycle efficiency, as well as the feasibility of cost–effective solutions.

The simplest structure of an ORC is often called basic ORC and is composed of 4 main components: two heat exchangers (an evaporator and a condenser), a pump and an expander, as shown in Fig. 2.9a. In order to increase the thermal efficiency of the simple basic cycle, various modifications have been proposed, from the simplest with a recuperator (Fig 2.9b), to multi pressure configuration (Fig 2.9c), flash (Fig 2.9d) and ejector layout (Fig. 2.9e).

The ORC with recuperator enhances thermal efficiency though the utilization of a recuperative heat exchanger at turbine exit. The exhaust gases at the turbine pre heat the fluid at evaporator inlet, allowing thus a reduction of the heat input to the ORC, while maintaining the same level of power output [24].

The multi pressure level configuration has been introduced in order to decrease the irreversibility in the heat transfer process at the evaporator. The match between the higher–pressure level and the heat source is improved and this allows an increase in thermal efficiency. It is to be remarked that an accurate optimization of the two–pressure level is fundamental in order to obtain the lowest level of irreversibility. The drawback of this configuration, which enables the global thermal efficiency of the power plant, is the increase in the complexity of the layout, and consequently of power plant costs [25], [26].

The ORC flash cycle is used when zeotropic mixtures are employed as working fluid. The advantage of zeotropic mixtures is that evaporation does not occur at fixed temperature, allowing hence a better heat transfer process. Nonetheless, as for the multi–pressure solution, even if there is an increase in thermal efficiency, there is also an increase in power plant complexity and costs [27].

Ejector type ORCs have been investigated with the aim of increasing the expansion ratio of the turbine, allowing therefore a higher power production. The simplest configuration is obtained introducing an ejector at turbine exhaust and a second stage evaporator. The second stage evaporator allows the vaporization of the primary fluid of the ejector, which consents the reduction of the pressure of the turbine discharge stream [28]. Other ejector ORC configurations have been assessed; introducing the ejector in parallel to the turbine,

using a bleed of the turbine as the hot primary stream, or utilizing the hot stream at turbine exit as the primary flow of the ejector in order to develop a combined ORC–refrigeration cycle. The disadvantages of the ejector ORC configuration are the presently low ejector efficiencies and the increase of complexity of the cycle when compared to simple and recuperative arrangements [29]–[31].

Not only ORC layout can be listed as possible architecture modification, but also advanced thermodynamic cycles need to be taken into account. Indeed, several solutions, which utilize basically the same components configuration, can take place, such as trilateral cycles, super critical cycles or trans–critical cycles. Trilateral cycles, or often–called triangular cycle, employ the same components of a basic ORC, with the exception of the expander, which is specially designed to work in two–phase conditions. The main advantage of a triangular cycle would be the possibility of optimal matching of evaporator temperature profiles. Nonetheless, actually, there are not efficient expanders which work in two–phase region [32].

Both trans–critical (TC) and super–critical (SC) cycles bypass the two–phase region when heated, allowing a good thermal match between working fluid and heat source. The difference between TC and SC cycles is that in the former one, condensation still takes place in the two–phase region. These two cycles configurations allow an increase in power production; however, the thermal efficiency is usually comparable or even a bit lower than other cycle configurations, due to the increase of heat demand [33].

Finally, Tab. 2.3 resumes the possible cycle architecture, as well as the challenges related to each configuration. It seems clear that, as it often occurs in engineering design, there is not an optimal solution, but each configuration has advantages and disadvantages which should be carefully weighted and assessed depending on the specific application.

Table 2.3 Possible ORC architecture [24]

Cycle	Modifications	Challenges
Recuperative	Extra heat exchanger	Only beneficial if lower cooling limit of flue gasses
Flash	Added Separator, throttling valve, mixer, extra heat exchanger	Performance comparable to basic ORC; many extra components
Multi pressure	Multiple pumps and heat exchangers	Many extra components needed
Trilateral	Two phase expander	Availability of high efficiency two–phase expanders
Trans/Super critical	Super critical fluids	High pressure; working fluid stability
Ejector	Added evaporator, ejector	Ejector efficiency

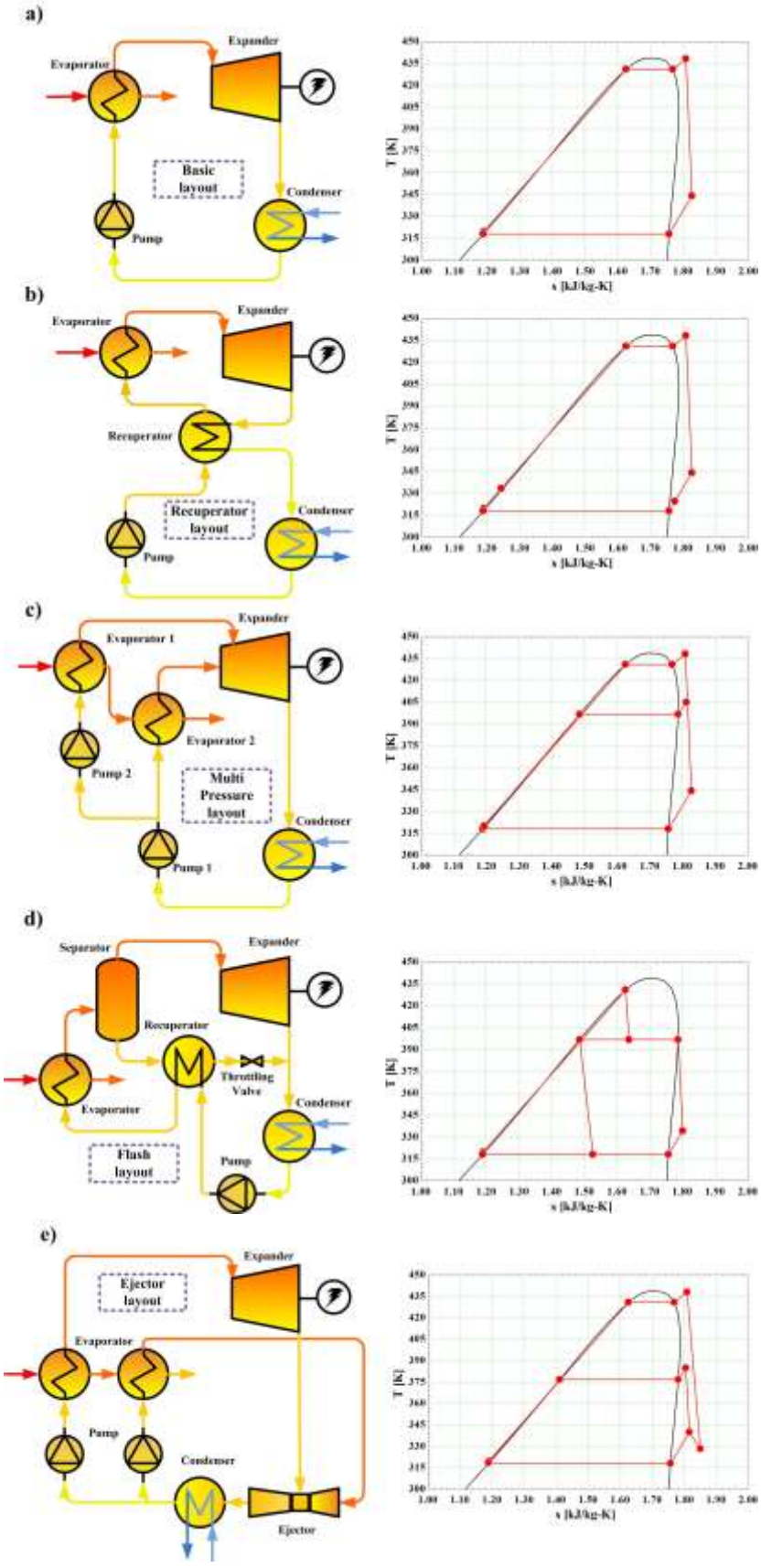

Fig. 2.9 ORC layout. a) basic, b) recuperative, c) multi pressure, d) flash, e) ejector

2.3.3 Working fluid selection

As previously stated, the thermodynamic cycle of an organic Rankine cycle exploits the same concept of a steam Rankine cycle, nonetheless, the utilization of organic fluids adds a further degree of freedom for the system design. Indeed, lifting the limitation of water or air as working fluids, it is possible to select the most appropriate fluid, which guarantees the optimal compromise between thermodynamic efficiency and technical system configuration, as well as plant costs. An example of the increased flexibility given by the fluid selection is given by the possibility of exploiting supercritical cycle configuration at low temperature of the heat source. Furthermore, there is an increased level of versatility in the selection of pressure and density levels within the system, which are almost independent from the upper cycle temperature.

Organic fluids have a lower boiling point than water and higher molecular complexity, which are properties that make ORCs suitable for small–medium size power plants (1–5000 kW) and for heat recovery applications. Nevertheless, organic fluids need to comply with many constraints, which may be very tight depending of the field of operation. Indeed, optimal organic fluids should be [35]:

- Non–toxic, inflammable, non–corrosive, cost–effective;
- Detain low (or better zero) global warming potential (GWP) and ozone depletion potential (ODP);
- Thermally stable and compatible to sealing material;
- Good lubricant;
- Proper heat transfer properties;

The possibility to choose the most suitable working fluid depending on the application guarantees (i) increased component efficiencies, (ii) usually no vacuum condenser (iii) higher cycle performance compared to gas cycle and steam Rankine cycles. These favourable features gave rise to numerous research studies on the assessment of the optimal working fluid selection [35]–[38].

Organic working fluids can be categorized not only by their molecular structure, but also by the slope of the saturation vapour curve (right side), which is a pivotal feature of these working fluids. There are three types of working fluid: a wet working fluid is called one, which possess a negative slope vapour saturation curve ($\frac{ds}{dT} < 0$); a dry working fluid conversely, is one which is characterised by a positive slope vapour saturation curve ($\frac{ds}{dT} > 0$); finally, an isentropic working fluid is the one which has an almost infinite slope. Fig. 2.10 displays some of the most common organic working fluids saturation curves. Particularly, it is possible to distinguish wet fluid (such as Water, Ammonia or R134a), from dry fluids (such as n–pentane, n–hexane or MM) and isentropic fluids (such as R245fa or R1233zd(E)). From the analysis of Fig. 2.10 it is possible to easily understand

the advantage of dry and isentropic fluids. Particularly, wet fluids require super heating in order to avoid wet expansion, conversely to isentropic and dry fluids, which can therefore be optimized through the utilization of a saturated cycle configuration.

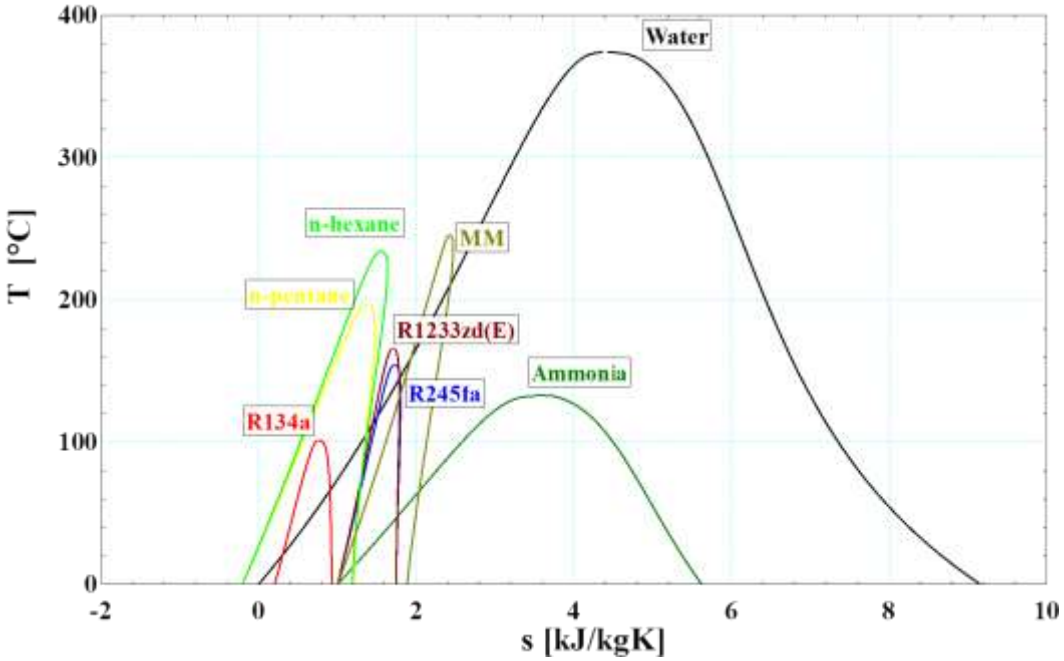

Fig. 2.10 Saturation curves of some common organic working fluid compared to water

The slope of the saturation curve is not the only thermodynamic parameter to be taken into account when selecting the optimal working fluid for an ORC. Tab. 2.4 resumes the principal thermodynamic and physical properties, which need to be considered, while designing an organic Rankine cycle power plant for a specific application.

Another important aspect that needs to be taken into account when selecting the working fluid for a specific application is that it has to be easily obtainable and have reasonable cost. Good availability and low cost fluids are those already used in refrigeration and chemical industries. Keeping in mind that the assessment of the proper working fluid for a specific application needs to be considered in the design process of an ORC, an interesting classification of optimal working fluids to be used as function of the heat resource temperature level has been carried out in [39], and reported in Fig. 2.11.

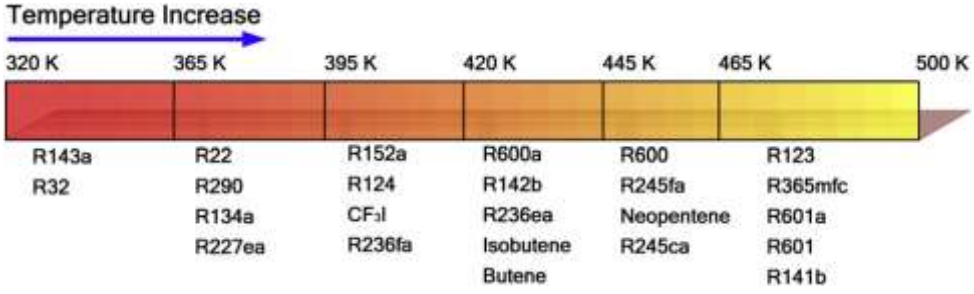

Fig. 2.11 Optimal working fluids as function of heat source temperature [39]

Table 2.4 Principal thermodynamic and physical properties of an organic fluid [36]–[38]

Property	Effect
Vaporization latent heat	At fixed conditions, at a higher latent heat corresponds a higher specific work output; conversely, a lower latent heat allows a better thermal match between working fluid and heat source, as most of the vaporization process occurs at variable temperature.
Density	High vapour density is fundamental if compact, cost effective expander has to be designed. Low vapour density means higher volume flow rate and therefore higher expander dimensions.
Specific heat	Low liquid specific heat allows lower specific work required by the pump.
Critical temperature	High critical temperature allows higher thermal efficiency. The negative side is low pressure at condenser. Furthermore, reduced density, related to working at densities much lower than the critical one, leads to higher expander dimensions.
Boiling Temperature	High boiling temperature leads to higher thermal efficiency, if fluids of the same "family" are compared.
Molecular Mass	High molecular mass allows higher power production at reduced rotational speed, which leads also to a positive effect on turbine efficiency; nonetheless, high molecular mass necessitate of high heat transfer area.
Molecular complexity	Molecular complexity is directly linked to the slope of the vapour saturation curve. Low molecular complexity is linked to wet fluids, while higher molecular complexity is characteristic of dry fluids; high molecular complexity allows higher efficiency at reduced turbine size, moreover it favours the efficiency of the regenerative cycle configuration.
Viscosity	Low viscosity in both liquid and vapour phases allows high heat transfer coefficients and low friction losses in pipes
Thermal conductivity	High thermal conductivity allows better heat transfer
Evaporating pressure	Higher evaporating pressure leads to higher costs and complexity of the layout of the power plant.
Condensing pressure	Condensing pressure should be higher than atmospheric in order to avoid air infiltration into the system.
High temperature stability	Maximum heat source temperature limited by the chemical stability of the working fluid, which tends to deteriorate at high temperatures
High safety level	Low toxicity and flammability required
Environmentally Green	Low ODP and GWP

2.3.4 Expander assessment

The utilization of an ORC is a sound solution when the system is composed by efficient, reliable and low–cost components. A critical component for ORCs is the expander, as it often does not combine low cost and reliability. As the ORC power and hot temperature resources vary strongly depending on the application, the variety of expanders, which can be considered, is also wide. Turbines (axial or radial) as well as volumetric expanders (scroll, screw, vane or piston) are employed depending on hot source and power range.

Axial turbines are often used for plants with power production between 500 kW and few MWs [40], while radial turbines are better suited for the lower power ranges (50–500 kW), due to their low degree of reaction and therefore their capability of dealing with large enthalpy drops at low peripheral speeds, allowing the adoption of a single stage design [41]–[43]. Finally, for very small and micro power range applications (500 W to about 50 kW), volumetric expanders, like scrolls, screws, vane or piston, are usually utilized, although their efficiency is limited by leakages, friction and heat transfer losses [44]–[46]. Several studies have been performed on the assessment of expander selection, depending both on power and volumetric expansion ratio [47] or application [48]. As can be noted both from Figs. 2.12 and 2.13, at higher power ranges the predominant technology is the axial turbine, while for the small–micro power range volumetric expanders dominate. For intermediate power ranges (20–200 kW) the specific application and boundary conditions are the determining factor for expander selection.

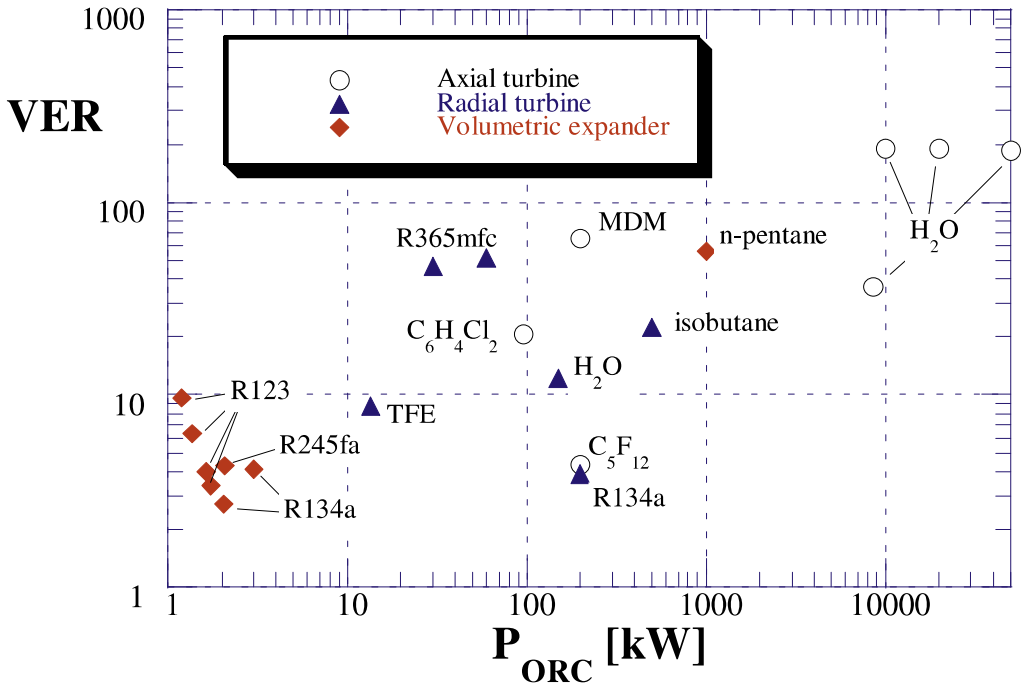

Fig. 2.12 Expander technologies comparison as function of power and volumetric expansion ratio (VER) [47]

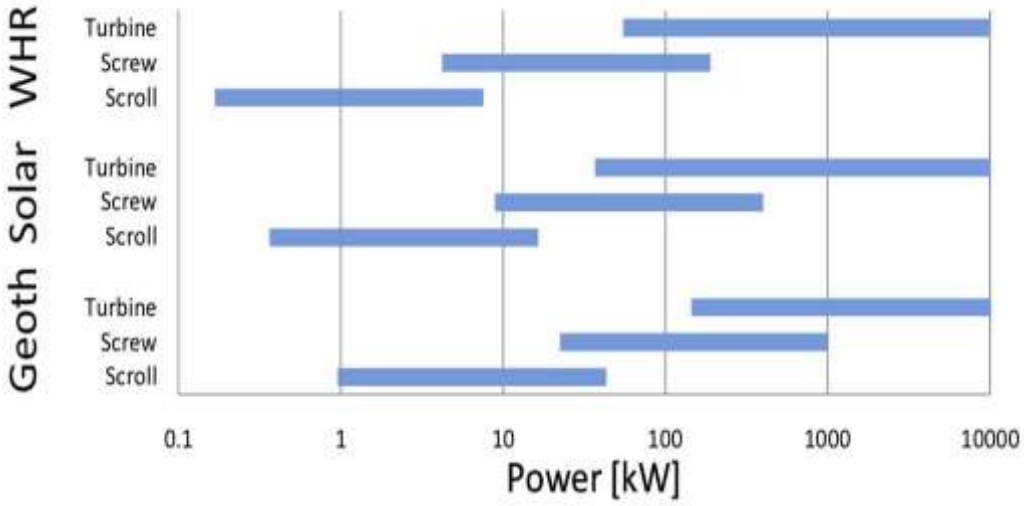

Fig. 2.13 Expander technologies comparison as function of power and application [48]

ORC axial turbines have essentially the same design as steam turbines. Nonetheless, due to the strong difference in thermo physical properties, some peculiar features need to be taken into account:

1. High molar mass implies low sound velocity, which means that when designing the stator, a particular attention has to be taken in order to limit the exit nozzle Mach number to reduce shock losses;
2. Organic fluids realize smaller enthalpy drops then steam, this affects in a different way all kind of turbine losses;
3. High density and small specific volume allow a compact design of the expander;
4. When utilizing organic fluids that are flammable or explosive, special care needs to be taken so that no leakages to air are present.

Considering the above–mentioned features, a one–stage axial turbine is often utilized for high mass flow rate systems, while for lower mass flow rates radial turbines are preferred. The main advantages of radial turbines for low mass flow rate applications can be resumed as follows:

1. High efficiency levels even at off–design conditions (obtained by means of variable–geometry inlet guide vanes);
2. The downscaling of radial turbines is favoured when compared to axial turbines due to the lower sensitivity to geometric inaccuracies of the blade profile;
3. Radial turbines are simpler to manufacture than axial turbines [36];
4. Higher peripheral speeds than axial turbine are possible, which guarantee a higher enthalpy drop per stage;

Axial and radial turbines are actually not appropriate for micro and small power generation units, mainly due to the very high rotational speed, which dramatically increase when the turbine power output is lowered. Therefore, for low power generation positive displacement expanders are predominant. These technologies will be examined in Section 2.3.5, as they can be considered as “direct competitors” of the Tesla turbine.

2.3.5 Micro expanders

As previously stated for small–micro power generation, volumetric expanders are actually the only alternative. The principle of operation of positive displacement expander is the decrease in pressure through an increase in volume. Commonly, the expander is composed by a stator and one or more rotors directly linked to the expander shaft. While the shaft rotates, the geometry of the rotor defines a series of closed working chambers, where the fluid is enclosed. These chambers increase in volume, reducing thus the pressure of the fluid, which transfers energy through shaft momentum exchange (resulting from the pressure developed on moving surfaces). The major difference between volumetric expanders lies fundamentally in the mechanism that determines the variation of the volume of the working chambers, as well as the timing of the thermodynamic processes [49].

The principal positive displacement expanders are: reciprocating piston, screw, scroll and vane. These expanders hold different characteristics, which distinguish one from another. The first feature is the type of motion of the rotor. As shown in Fig. 2.14, three main motion categories exist: reciprocating, orbital and rotary [49]. Each expander belongs to one of these classes. Apart from the Roots expander, all other volumetric expanders possess a built–in volume ratio where the working fluid expands. Another difference between the expanders is represented by the presence (reciprocating piston) or not (scroll, screw, vane, roots) of valves. The absence of valves enhances the reliability of the expander.

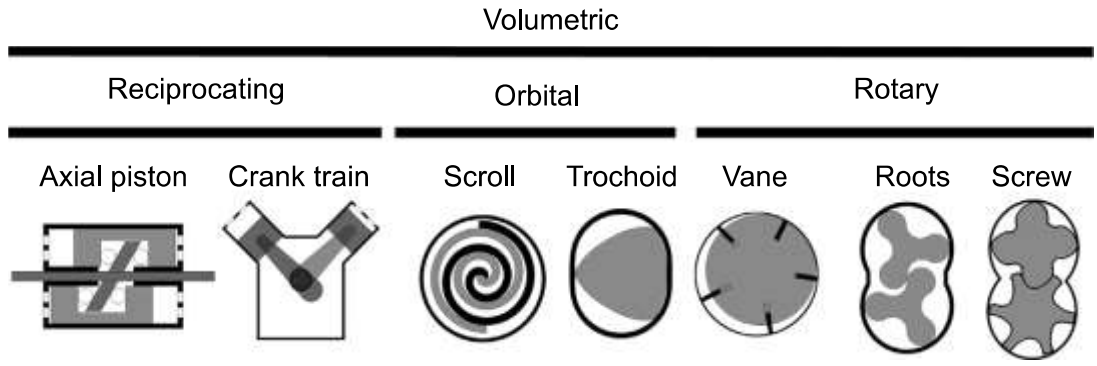

Fig. 2.14 Volumetric expander categories as function of motion type [49]

Scroll expanders are composed by two off–axis spiral–shaped profiles one of them is fixed while the other one is turning, delineating a spiral trajectory. The fluid enters from an opening, which is placed at the centre of the fixed profile, and after expanding through the expansion chambers developed by the rolling of the profile, it exits radially at the discharge chamber. As scroll compressors are very common in refrigeration and air conditioning applications, this expander is often obtained from a compressor just by

reversing the direction of rotation and the inlet and outlet of the fluid. Fig. 2.15 displays the fluid expansion process inside the assessed technology.

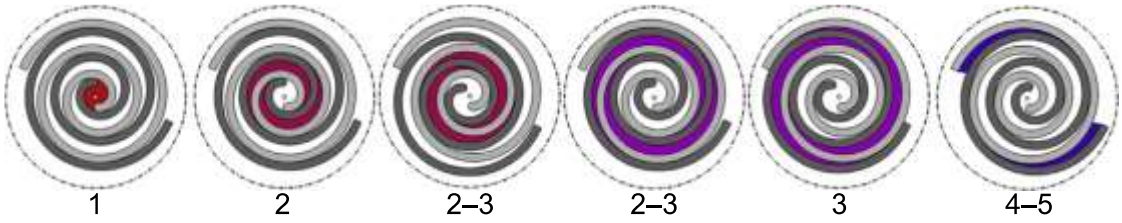

Fig. 2.15 Working fluid evolutions inside a scroll expander [49]

As typical for volumetric expanders, scroll technologies operate on a fixed volumetric ratio, typically between 1.5 and 5 [50]. Moreover, the optimal sizing for an expander is indeed different from that of a compressor, so that using an existing compressor just reversing the direction of shaft rotation results in general in a poor efficiency. Two kinds of losses arise if the operating system volume ratio does not match the expander design volume ratio; which are under–expansion and over–expansion [36]. These losses can hinder the efficiency of the expander, limiting the expansion ratio. Other assessed losses involve friction losses, supply pressure drop, internal leakages and heat transfer [45] [51]. Scroll expanders can be further categorized in two: compliant and cinematically rigid. Compliant scroll tolerates a further movement in a provided direction, which let them be adapt for transient operation or for two–phase flow conditions. A very attractive feature of scroll expanders is that they are very reliable as the total number of moving components is quite low. Furthermore, according to [50], scroll expanders can reach quite high efficiency (>70%), at optimal pressure ratio and rotational speed.

Screw expanders can be categorized in two main types, single screw and twin–screw expanders, as shown in Fig. 2.16. Twin–screw expanders are more common in organic Rankine cycle applications, but the research in single screw is increasing in recent years, due to the favourable feature of having a better balance than twin–screw, which allows achieving an augmented bearing lifespan. The fluid enters from one side of the screw and exit on the opposite side, passing through a sequence of supply, expansion and discharge chambers, which are determined by the turning of the screw(s). The rotational speed that can be achieved with screw expanders is quite high, which implies the necessity of the utilization of gearboxes and control speed equipment. Screw expanders can be lubricated or oil–free. Oil–free expanders have the advantage of being mechanically simple machines and therefore allow simple manufacturing process; conversely, they hold a main disadvantage, that is, higher internal leakage losses. Nonetheless, screw expanders present high efficiency values (up to 80%) with a power range between 1 and 200 kW [52]. A further favourable feature of these expanders is their good ability to tolerate two–phase flows. As scroll expanders, also screw expanders can be easily obtained from a reversed compressor, just changing the direction of rotation. The maximum built in volume ratio of screw expander is about 8.

Fig. 2.16 Single and twin screw expander [52], [53]

The **Roots expander** is similar in principle to a screw expander with a 2D geometry, but it is not as common. Research studies on this kind of expander are quite few. The typical built–in volume ratio is close to one and the power range is typically between 1 and 30 kW. The advantage of this expander is that it can handle easily two–phase flow conditions.

Reciprocating piston expanders for organic Rankine cycles are derived from the well–known design concept developed in various areas, such as automotive, energy or petrochemical industries. The most used design of volumetric expander relies on the crank mechanism, but other mechanism can be utilized, such as free pistons [54] or slash–plate [55]. The main advantage of piston expander is that they are suitable for applications where high temperature and high–pressure ratio are required. The built in volume ratio of a piston expander can be as high as 15. The efficiency value is around 70% and they are suitable for low displacement and low power applications.
The piston expander is the only one between volumetric machines for micro generation in organic Rankine Cycle that requires the utilization of valves. This feature increases the complexity of the machine, lowering its reliability. Furthermore, there are also some other drawbacks, such as lubrication issues and high manufacturing costs.

The **Rotary vane expander** is characterized by a rotary motion of a vaned cylindrical rotor within a housing, which acts as stator. The geometry of the expander is appreciably simple, which guarantees low manufacturing costs. The main advantages of the vane expander are the flat efficiency curve throughout an extended range of operating conditions, the low operating speed, the possibility of accepting two–phase flows and the high expansion ratios achievable (up to 10). Conversely, as most volumetric machine, the vane expander is limited in temperature. Indeed, high inlet expander temperatures are not possible, as they would cause an increase in friction losses in the vanes due to thermal expansion of the rotor, which finally could end up to be locked.

When going through the selection of an expander for micro organic Rankine cycles, many parameters need to be assessed, such as efficiency, pressure ratio, ability to tolerate two phase conditions, rotational speed, reliability and cost. Which is the fundamental feature for expander selection would be determined by the specific application, but some

guidelines can be outlined. Particularly, the comparison between various types of micro expanders for ORC applications is resumed in Tab. 2.5. As previously discussed, in the very small power range, radial turbines are not suitable, and actually volumetric type machines are the only alternative. Among volumetric machines, scroll and rotary vane expanders are more suitable for very small–scale applications, whereas screw and reciprocating piston expanders belong to a higher power output range. Therefore, in this context, the Tesla turbine may represent a direct competitor to scroll and rotary vane expanders, as, if properly designed, it holds the same characteristics of moderate rotational speed (if relatively high rotor diameter is utilized), low manufacturing cost and suitability to very different fluids and applications. Furthermore, conversely to most of volumetric expanders, it does not require lubrication, which may be very important in several applications. Section 2.4 will be centred on the Tesla turbine, from the principle of operation to the actual state of the art.

Table 2.5 Comparison of micro expanders for ORC applications [36][50][53]

Type	Power range [kW]	Rotational speed [rpm]	Cost	Characteristics
Scroll expander	1–10	<10,000	Low	+ High efficiency, low cost – Lubrication requirement
Screw expander	10–200	<10,000	Medium	+Flat efficiency curve at off–design –Difficult to manufacture, lubrication
Reciprocating piston expander	20–100	<12,000	Medium	+Mature technology, high pressure ratio – Heavy weight, complex
Rotary vane expander	1–5	<10,000	Low	+Low cost and low noise –Small power range, lubrication
Radial inflow turbine	50–500	5,000–80,000	High	+Light weight, mature technology –High cost, low efficiency in off–design
Tesla turbine	0.5–10	<10,000	Low	+Low cost, low noise, moderate efficiency, reliable – Few prototype tested (very low TRL)

2.4 The Tesla turbine

2.4.1 Principle of operation

A competitive technology to the actual available micro–expanders is the Tesla turbine, which is a viscous bladeless turbine. This concept was first developed by Nikola Tesla at the beginning of the 20th century, but it went through a long period of indifference due to the run towards large size centralized power plants. Only recently it found a renewed appeal, as its features make it suitable for utilization in small and micro size systems, like ORC applications, where low cost components become very attractive for the exploitation of residual pressure drop. The first description of the turbine (also called friction or disk turbine) was given in the patent submitted by Tesla [56] (Fig. 2.17). This type of radial expander is characterized by the absence of rotor blades, which are replaced by multiple parallel flat disks; a little gap separates the rotor disks from the related stator parts, which consist of one or more tangential nozzles. The working fluid accelerates, expands through the nozzles and enters, almost tangentially, in the gaps between the disks, where it depicts a spiral centripetal path. The working fluid moves from the inlet to the outlet radius due to the difference in pressure determined by friction and by the exchange of momentum, and exits from openings made on the disks at the inner radius. Tesla turbines seem to have several advantages when compared to conventional expanders for low power generation, as their relatively simple structure allows a straight manufacturing process, as well as low cost, reliability, modularity, and versatility. On the other hand, Tesla turbine presents values of efficiency lower than those of conventional turbines. The most critical aspects are the design of the nozzle and of the jet velocity profile.

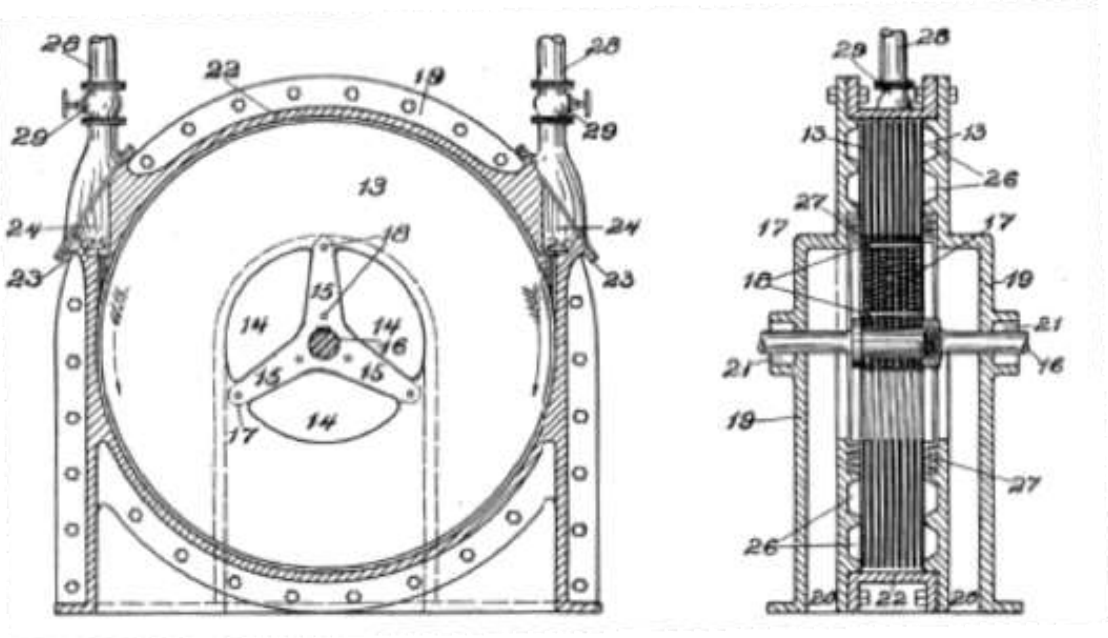

Fig. 2.17 Figs. from Tesla patent, 1913 [56]

2.4.2 Literature review

In this Section the available literature research studies will be briefly assessed. A chronological order will be followed.

1950

After Tesla pioneer work, it was only in the 1950s that the Tesla turbine was further investigated. Particularly, Leaman AB [57] designed and built a prototype of a Tesla turbine utilising air as working fluid. The rotor diameter was of about 0.13 m; the maximum assessed power output was of 87 W and the maximum documented efficiency was 8.6%.

1952

Armstrong JH [58] carried out an accurate study on the design and realization of an experimental test rig to investigate the power and efficiency of the disk turbine. He conducted a test campaign focusing on the identification of the critical issues of the machine, using steam as working fluid; furthermore, different nozzle configurations were analysed. A valuable result was the understanding of one of the causes of inefficiency. Indeed, it was found that the nozzle flow strongly affects the performance of the turbine.

1961

Beans EW [59] performed both a numerical and experimental investigation on the performance of the friction disk turbine. The performance model developed was reliably predicting the performance of the turbine. The performed campaign of investigation allowed assessing a maximum turbine efficiency of over 24% and a power near 1.8 kW.

1965

Rice W [60] realized one of the first analytical/numerical models of the flow inside the Tesla turbine based on simplified Navier–Stokes equations, assuming a steady, incompressible and inviscid flow; moreover, he designed and tested six different disk turbines operating with air. Rice W discovered that the best efficiencies were achieved with small size turbines operating at low flow rates, in contrast with conventional bladed turbines, and suggested the application to small power range, exploiting the qualities of low cost, ease of manufacture, low noise level and reliability.

1966

Beans EW [61] performed a throughout investigation of a 0.15 m scale air Tesla turbine, following the work previously developed in 1961. The performance investigation included the assessment of various channel width (from 0.6 to 12.7 mm), various rotational speeds (from 4000 to 18000 rpm) and various turbine inlet pressure (from 1.7

to 3.75 bar). The assessed efficiencies ranged between 7 and 25%. The maximum obtained power was of 1.8 kW at 3.75 bar of supply pressure and 1.5 mm of channel width.

1967

Matsch L and Rice W [62] developed a mathematical model of the potential flow of an incompressible fluid between two circular disks. The main feature of the analysis was the weighting of the partial admission effects on the flow developing inside the disks. A follow up of the previous work included the effect of rotation of the disks with a flow at low Reynolds number [63].

1968

Boyd KE and Rice W [64] developed a numerical model on the laminar incompressible flow of a Tesla turbine rotor with full peripheral admission. Particularly, various conditions were investigated, changing the three main input parameters: flow rate, Reynolds number and mean tangential velocity component at inlet.

Matsch L and Rice W [65] formulated an asymptotic fully developed flow solution of the flow of an incompressible fluid inside two rotating disks. Particularly, the asymptotic solution is function of two main parameters, Reynolds number and mass flow rate.

1970

Adams R and Rice W [66] performed an experimental investigation of the flow characteristics inside a Tesla turbine rotor. The focus on the analysis was the comparison between experimental measurements of pressure throughout the disks and the numerical model developed in [64]. Experimental results were faithfully predicted by the numerical model.

1971

Boyak BE and Rice W [67] developed an integral solution for the three–dimensional laminar flow inside a Tesla turbine. The developed model was validated against experimental data and the matching with static pressure distribution was found to be very good. The model did not take into account compressibility nor heat transfer, but it was stated that these improvements could be easily achieved.

1972

Lawn MJ [68] exploited the numerical models developed in [67] in order to draw the performance maps of a Tesla disk turbine. The performance maps were realized for various dimensionless tangential velocities at several Reynolds numbers. Efficiency as high as 80% was predicted.

1974

Lawn MJ and Rice W [69] presented the performance maps of Tesla turbines highlighting how efficiency deeply depends on geometry and rotational speed. Particularly, nozzle direction was assessed as a fundamental parameter. It was also claimed that the Tesla turbine could be designed with a high efficiency configuration for any fluid.

Pater et al. [70] performed an experimental campaign in order to investigate the behaviour of the flow inside two corotating disks. Static pressure alongside the disks was measured, as well as flow visualization (through the utilization of a dye) was performed. Previous analytical models developed both for pumps and turbines were thus verified, showing excellent agreement between analytical and experimental results.

1975

Bassett CE [71] developed an integral solution of the compressible flow of Tesla turbines. The developed model was validated against published experimental data, demonstrating a good agreement between numerical and experimental results. The model took into account several parameters, such as inlet Mach number, Reynolds number, rotor diameter, mass flow rates. The maximum efficiency was obtained for the minimum assessed value of flow rate between the disks. It was also found that the optimal rotor radius ratio is between 0.25 and 0.3.

1976

Garrison et al. [72] presented a numerical model for the prediction of laminar compressible flow between Tesla turbines. Particularly, the model efficiency prediction reached values as high as nearly 90%, with low mass flow rates and an optimal rotor inlet/outlet diameter ratio between 0.2 and 0.4.

Steidel R and Weiss H [73] performed an experimental investigation of a Tesla turbine for geothermal applications. The tests were performed in wet conditions, with a vapour fraction between 6 and 15%. The maximum turbine efficiency observed was of a 6.8% at 4000 rpm; the maximum assessed power was of about 2.8 kW at 4000 rpm.

1978

Truman CR et al. [74] developed a numerical model of a laminar flow between two rotating disks of a vapour containing liquid droplets. This type of flow condition is typical of geothermal applications. Vapour–liquid interaction was modelled on the assumption of a drag force coefficient.

1979

Truman CR et al. [75] modified the model developed in [74] in order to simulate flows containing solid particles. The results showed that for very small particle sizes the behaviour of the fluid would not change; but when the particle size increases (>4 μm) the solid particles would not follow the trajectory of the fluid and could also not enter the rotor.

1990

Allen JS [76] exposed a closed–form model for velocity and pressure inside a Tesla turbine rotor, achieved through the assumption of fully developed boundary layer. A closed formulation for evaluation of torque was also formulated. The detailed solution of the Navier Stokes equation reduction was presented.

1991

Rice W [77] presented a state of the art analysis of the Tesla turbine. Particularly, the available models in literature were collected and discussed; an assessment on the possible applications was also carried out. High efficiency, as high as 95%, were claimed for very small mass flow rate, as well as several field of application, from small shaft power application to use of very viscous fluids or geothermal applications.

2001

Sandilya P et al. [78] developed a numerical assessment of the fluid dynamic and mass transfer in a Tesla turbine rotor. The effect of rotation on the shape of velocity was highlighted and compared to the stationary case. Furthermore, the flow pattern, as well as its effect on mass transfer coefficient, was carefully assessed.

2002

Patel N & Schmidt DD. [79] carried out an experimental campaign on a boundary layer turbine using biomass combustion gases as working fluid. The 40 hours campaign was executed in order to verify the effect of deposition, erosion and corrosion of the Tesla turbine due to the substances present in the flue gases. The maximum obtained efficiency was of 11% with 3.2 kW of power output and a rotational speed of 6284 rpm. The same turbine was tested also with steam as working fluid, allowing a power production of 9.3 kW with an efficiency of 13.7% at 6500 rpm.

2003

Lezsovits F [80] investigated the possibility of utilizing a Tesla turbine in a decentralized power generation system based on biomass. The selection of the turbine was justified by

the requirements of reliability, robustness and cost effectiveness; and on the claim that turbine efficiency was not a fundamental parameter for the specific application.

2004

Ladino AFR [81], [82] developed a computational fluid dynamic assessment of a Tesla turbine of a 100 mm rotor outer radius, with air as working fluid. Efficiency of around 20% was obtained for low mass flow rate when both laminar and turbulent model were applied. The visualization of the path lines, as well as the highlighting of pressure losses in the nozzle–rotor interaction was reported.

2006

Couto et al. [83] presented a simple and straightforward model, which allowed assessing the optimal number of channels of a Tesla turbine in order to be applied to a specific application.

2007

Batista M [84] provided an analytical solution of a steady state, incompressible flow of fluid evolving between two rotating disks. The model was obtained through the application of asymptotical evolution of unknown components of velocity and pressure.

Bloudicek P and Palousek D [85] presented a simplified design procedure for the design of a Tesla turbine. The process design, as well as the realization of an experimental campaign with water as working fluid was assessed. The effectiveness (actual machine performance over theoretic machine performance) was evaluated and the maximum reached value was 55% with a 13.63 W power output. The maximum obtained power output was of about 58 W. A significant data, giving evidence to the most attractive feature of the turbine, was the total cost of the prototype, which was of about 124 €.

2008

Deam et al. [86] evaluated the benefits of utilizing Tesla turbines instead of gas turbines for small–scale applications. The development of scaling laws for gas turbine was refined and the results from the model were compared with experimental data on Tesla turbine. The main result was the demonstration that for small–sized turbines, viscous turbines are more efficient than conventional bladed turbines, as the losses are quite high. The assessed experimental turbine efficiency was 23.5%.

Lemma et al. [87] performed a comprehensive experimental and numerical study on a 50 mm rotor Tesla turbine. The assessed performance of the turbine was over 20%, claiming that the main causes of losses were mainly parasitic losses and specifically bearing losses.

If these losses could be avoided, or at least reduced, the turbine efficiency could reach values close to 40%.

Valente A. [88] applied the Tesla turbine concept as an equipment for pressure reduction of Hydrocarbon gases in a near isothermal process. Experimental tests confirmed the wanted characteristic of near isothermal expansion. This allows the expander to be used as a substitute of a Joule–Thomson valve in hydrocarbon pipelines.

2009

Crowell R [89] is the first author to take Tesla turbine as a possible expander candidate for small ORC applications. Particularly, the study assessed an integrated system for residential applications, exploiting solar hot water collectors as heat source with the utilization of a micro ORC in order to produce electricity. The fluid utilized in the simulation was Care30 (a refrigerant blend of Isobutane and Propane with similar characteristics to R134a). The developed model of the turbine was quite simple, as the aim was to assess the power output at the shaft. A turbine efficiency of 30% was assumed, which guaranteed a daily power production of 3.2 kWh.

Hoya GP and Guha A [90] designed and manufactured a flexible test rig for Tesla turbines. They carried out several experimental analyses, comparing various measurement methods and developed a new, simple and cheap approach (angular acceleration method) for measuring torque and power output, which overcame the difficulties associated with the determination of very low torque at very high rotational speed.

Guha A and Smiley B [91] investigated the nozzle, recognizing it as the source of the major irreversibility, according to their test results; they demonstrated that a careful design of the nozzle could reduce the nozzle losses by 40–50%. They showed that utilizing a plenum chamber could result in a total pressure loss of less than 1%; furthermore, it allowed also a considerable enhancement in the uniformity of the jet and an improved overall efficiency of the Tesla turbine.

Lampart P et al. [92] developed a throughout CFD investigation on different Tesla turbine dimensions with Solkatherm SES36 as working fluid. The assessed efficiency of the turbines ranged from 30 to 50% depending on turbine size and rotational velocity. For a 0.32 m shaft diameter the assessed efficiency was around 50% and the power output obtained was between 1.5 and 5 kW.

2010

Carey VP [93] realized a one–dimensional idealized model of momentum transfer in the rotor, and used it to predict the turbine efficiency in a 4 kWe solar Rankine cycle combined heat and power system, using steam as working fluid. His model resulted

similar to the one developed by Rice W [60], using body–forces to represent the wall shear effects, assuming laminar flow: according to it, under optimal design conditions, 75% turbine isentropic efficiency was predicted.

Carey VP [94] exploited the two–dimensional model developed in [93] and compared the possible achievable results that could be obtained with CFD analysis; concluding that 1D/2D model is a useful tool for preliminary design of Tesla turbines.

Emran et al. [95] developed a simple model for estimating the proper sizing of a Tesla turbine dynamometer and generator. Tesla turbine static torque model was assessed, both analytically and experimentally.

Puzyrewski R & Tesch K [96] developed a 1D analytical model of the Tesla rotor calibrating it through 3D CFD analysis. The calibration through 3D CFD allowed to realize very simple and reliable 1D model, which provided the prediction of high efficiency (above 75%) when the gap between the disks is very tight (0.1 mm).

Romanin V et al. [97] investigated the possible power and efficiency enhancement that could be obtained by a commercial Tesla turbine. Particularly, the comparison between experimental data and numerical simulation where performed. The maximum assessed experimental efficiency was 10.1%, while the numerical optimization of the turbine predicted that efficiency higher than 75% could be reached.

2011

Batista M. [98] re–organised the work presented in [84], providing an analytical solution of a steady state, incompressible flow of fluid evolving between two rotating disks.

Choon et al. [99] performed a computational fluid dynamics optimization analysis on a Tesla turbine with water as working fluid with the aim of exploiting the energy hold within the household water supply. The CFD analysis allowed the upgrade of an existing prototype, resulting in an increase in efficiency from 6.8 to 10.7%, with a pressure drop of 0.04 m. The main results were the possibility of applying this technology to such a niche application, as the expander is suited to produce power at very low pressure drops.

Cirincione [100] designed and realized an ORC waste heat recovery system with a Tesla–hybrid turbine, which was claimed to be able to reach isentropic efficiency levels above 70% with steam; the last not reported tests were carried out with R245fa.

Emran TA [101] exploited and further developed the results obtained in [95], improving the torque model of a Tesla turbine, as well as comparing the analytical solution with experimental tests. As a further result, the developed model allowed the design of an improved Tesla turbine with optimal dimensions.

Ho–Yan BP [102] applied the model developed in [60] in order to establish a preliminary design approach for Tesla turbine for Pico Hydro applications. The obtained performance was over 80% for a 300 W power output turbine, working with a pressure head of 20 m and a water flow rate of 2.5 l/s.

Krishnan V et al. [103] realized some micro–turbines (1–2 cm diameter rotors) using commercially available technologies, and tested them with different nozzles and rotors configurations, achieving almost 40% shaft mechanical efficiency.

Lampart P & Jedrzejewski L [104] further developed the analysis presented in [92], considering the Tesla turbine as the expander for a micro–power plant of 20 kW heat capacity. The maximum efficiency obtained from a computational fluid dynamic analysis was 51% with a mass flow rate of Solkatherm SES36 of 0.13 kg/s.

Podergajs M [105] provided a short report on Tesla turbine historical background, flow model and applications. In the report, the author highlighted the range of application where the turbine could be an attractive solution.

Romanin VD and Carey VP [106] developed an integral solution scheme of the fluid dynamics of incompressible, steady flow inside a Tesla turbine rotor. Enhanced drag effect, due to surface micro structuring was also taken into account. The enhancement of efficiency due to surface micro grooving could be effectively relevant, as high as 9% enhancement when compared to smooth surface. The maximum predicted efficiencies of the turbine were over 80%.

2012

Borate HP and Misal ND [107] carried out a performance analysis of the Tesla turbine, with a specific focus on the effect of surface finish and the space between the disks. The assessment was carried out considering water as working fluid. Experimental and theoretical analysis allowed the characterization of the major inefficiency (from the nozzle) and that, if direction grooving on disk surface is applied, an increase in efficiency between 5 to 6% can be achieved.

Peshlakay A [108] performed a numerical and experimental analysis of a Tesla turbine, comparing different nozzles using air, water and steam as working fluids; achieving a rotor efficiency of 95% (± 9.5% uncertainty) and a global turbine efficiency of 31%.

Romanin VD et al. [109] modified the model developed in [106] in order to match the results obtained in [103]. The modified analytical model results were compared with CFD analyses and experimental results. The correlation of the results was fairly good, as, on average, the experimental results efficiency was 45% lower than the expected analytical model results. The discrepancy was mainly due to the not proper modelling of the nozzle.

Romanin VD [110] presented a comprehensive study, which collected analytical perturbation model results, computational fluid dynamic investigation and experimental analysis. The obtained results were presented in [97], [103], [106], [109].

Sengupta S and Guha A [111] presented an analytical model resulting from the reduction of Navier–Stokes equations. They assumed a steady, incompressible and laminar flow, introducing the viscosity of fluid and a velocity gradient near the walls. This mathematical theory represents a simple but effective method of predicting the performance and efficiency of a Tesla turbine.

Van Wageningen T [112] presented a concept review of the Tesla turbine to be utilized as the engine for a flapping wing mechanism. Tesla turbine seemed not to be suitable for this application when compared to two stroke and heat engine.

2013

Bao G et al. [113] defined and validated a numerical model using CFD tools to describe the flow boundary layer; then the model was applied to different organic working fluids to obtain the related performance curves, concluding that best performance can be achieved with thin gap width, turbulent flow and fluids with high kinematic viscosity.

Deng Q et al. [114] proposed and improved the model developed in [91] and compared the analytical formulation with computational fluid dynamic simulations. Various nozzle configurations were taken into account. The highest efficiency (43.6%) of a 0.05 m rotor diameter turbine was reached when the lowest number of nozzle (2) was taken into account, as well as the highest rotational velocity (24,658 rpm) and the largest pressure ratio (0.8).

Guha A and Sengupta S [115] further polished the model presented in [111] and moreover they investigated, for the first time, the roles of each force affecting the power and pressure fields, physically explaining several fluid dynamics behaviours like flow reversal and the shape of complex relative path lines.

Guimaraes LNF et al. [116] considered the Tesla turbine as a possible concept to be applied to an Emergency Core Cooling Systems of a standard power plant. They performed an experimental campaign with air as working fluid, reaching a 55 W power output value.

Gupta HE and Kodali SP [117] presented a state of the art review of the Tesla turbine. The assessed performance, as well as the other main results of investigation of previous research projects were highlighted, taking into account also the patents developed. A special focus has been put on the assessment of possible applications of Tesla turbines.

Khan MUS et al. [118] developed a modified configuration of a Tesla turbine, which merged both the aspect of a bladeless and a bladed turbine. An experimental campaign with water as working fluid was carried out. The average power output of the turbine was of 100 W. This new turbine concept was developed in order to exploit the potential energy of water flows present in canals or rivers. In a successive work, Khan MUS et al. [119] explored the possible applications where the Tesla turbine could be utilized. Particularly, the presented assessment of applications of a Tesla turbine was very wide: from power generation coupled with renewable energy sources, to the utilization in irrigation channels, up to the use in hybrid electric vehicles.

Krishnan VG et al. [120] described a method to scale Tesla turbines to millimetre dimensions, also providing the assessment of loss mechanisms. 40% efficiency was expected even when millimetre scale turbine was considered.

Placco GM et al. [121] considered a modified Tesla turbine as the expander for a passive thermal circuit as a part of an Emergency Core Cooling System of nuclear power plant. An experimental campaign with air as working fluid was conducted, achieving power higher than 100 W with low mass flow rates.

Sengupta S and Guha A [122] investigated the three–dimensional flow field and the flow path lines within a Tesla disk turbine, comparing the results obtained from the analytical theory and the computational fluid dynamics; moreover, they investigated the operating parameters that affect the shape of the path lines within the rotor and the local balance of the various forces.

Yang Z et al. [123] described an innovative method to measure and predict the mechanical power output of a Tesla turbine. The method is based on the rotational inertia of the turbine, as well as on the friction in the bearings. It is called “dynamic dynamometry” and allows the realization of power curves as function of rotational speed.

Zhao D and Khoo J [124] designed and tested a 40 mm bladeless turbine for the harvesting of energy from air and rainwater applications. 0.5 W power output was obtained with air as working fluid at 3300 rpm.

2014

Guha A and Sengupta S [125] developed a similitude study on the flow of the Tesla turbine. The scaling laws were obtained through the Buckingham Pi theorem, which lead to the definition of 7 fundamental non–dimensional numbers (rotor radius ratio, aspect ratio, tangential speed ratio at rotor inlet, flow angle at rotor inlet, dynamic similarity number, power coefficient and pressure drop coefficient). A further study of Guha A and Sengupta S [126] demonstrated that the application of the Euler turbomachinery equation is consistent only if local velocity mass–averaged values are considered.

Hasan A and Benzamia A [127] investigated the effects of temperature and mass flow rate variations on the performance of a Tesla turbine of 100 mm outer rotor diameter, through the means of CFD analysis. The performance of the turbine was found to be dependent on the temperature, as the boundary layer thickness changes due to temperature effects.

Pandey et al. [128] developed a computational analysis of a 1 kW Tesla turbine for pico hydropower applications. A 127 mm rotor outer radius was considered for the calculations, obtaining a total of 777 W for a 9 disks configuration of the turbine, reaching an efficiency of 77.7%.

Schosser et al. [129] carried out an assessment on the design and optimization of a test facility for 3D tomographic PIV measurements of the flow field inside a Tesla turbine rotor. A throughout CFD optimization analysis was carried out on the test rig components and specifically on the Tesla turbine rotor.

Shimeles S [130] performed a design an optimization assessment of a Tesla disk turbine, applying an incompressible steady state computational fluid dynamic analysis. Various rotor configurations were simulated, changing both geometric and fluid dynamic conditions. The maximum predicted rotor efficiency was of about 27%, utilizing air as working fluid. The maximum total power output obtained was of over 6.5 kW at 11500 rpm.

Siddiqui MS et al. [131] presented a computational fluid dynamic assessment of an air Tesla turbine. The turbine dimensions were selected in order to compare the results with experimental data provided in [60]. Different flow configurations were analysed both applying laminar and k–ε turbulence schemes. The maximum efficiency obtained was over 20% with the lowest flow parameter assessed. Efficiencies of numerical and experimental results were comparable.

Singh A [132] derived a closed form expression of the flow field and pressure distribution inside a Tesla turbine rotor by simplifying Navier–Stokes equations. A careful assessment of the flow behaviour as function of the Reynolds number was carried out.

Thawichsri K and Nilnont W [133] performed an experimental investigation on two Tesla turbines, differing in rotor outlet diameter (the first one of 120 mm, the second one of 75 mm). The working fluid expanding through the turbine was Isopentane. Three different hot source temperatures were analysed (70, 80 and 90 °C). For a 0.05 kg/s mass flow rate and a rotational speed of 3000 rpm, the total effectiveness was of 36%, with higher power output given by the bigger turbine.

Zhao D et al. [134] performed an experimental campaign, as well as a computational design assessment, of three Tesla turbines for the harnessing of energy from rainwater. Firstly, an experimental campaign with air as working fluid was conducted; finally, a

rainwater application was assessed. The overall energy conversion assessed was approximately between 2 and 3%.

2015

Baginski P and Jedrzejewski L [135] focused their studies on the assessment of the dynamic analysis of the Tesla turbine. Both strength and modal analysis were carried out through the means of two commercial software (Abaqus and Ansys). The results obtained for the assessed geometry (the same one used in [104], which consisted of a rotor composed by 11 disks, with 100 mm outer diameter and 2 mm thickness), showed that no resonance effect would present at start–up and that the first mode shape presented at 387 Hz.

Guimaraes LNF et al. [136] deepened the work presented in [116], [121], developing a Tesla turbine for space application, claiming that this technology could be utilized both in Brayton and Rankine cycle, with the optimal characteristics which make it suitable for space application, such as low pressure drop and almost no maintenance required, as well as the possibility of using it with any kind of fluid.

Holland K [137] designed, built and tested a 92 mm rotor diameter Tesla turbine. The tests were carried out with air as working fluid and the maximum obtained efficiency was of 8.5% at 3 bar inlet total pressure and 10,000 rpm.

Kölling A et al. [138] applied the Tesla turbine concept to small–distributed power generation from biomass resources. Particularly, in the study, the design, construction and tests of a 175 mm rotor diameter Tesla turbine were presented. The maximum power obtained was of 1.4 kW when a saturated steam at 9 bar and 0.11 kg/s mass flow rate was utilized. The assessed isentropic efficiency was of about 30%.

Krishnan V [139] exploited the work presented in [103], [109], [120] providing a Matlab tool for generating the design of micro to small Tesla turbines. Analytical, computational and experimental results were obtained, demonstrating the soundness of concept of Tesla turbine for sub–Watt and Watt range applications.

Neckel AL and Godinho M [140] realized and tested ten convergent–divergent nozzles to improve the injection efficiency of the working fluid; different geometries were first investigated with one and two–dimensional approaches and then an experimental test campaign with air as working fluid was carried out.

Nedelcu D et al [141] performed a numerical simulation both on stress evaluation and the flow calculation of the Tesla turbine rotor. The aim was to develop and manufacture a turbine working with air for teaching application.

Raje a et al. [142] presented a review of the principle of operation, design consideration, performance parameters and possible applications of the Tesla turbine.

Ruiz M [143] applied the Tesla turbine concept to a completely different application, which does not involve power production, but instead utilized as a heat sink. Numerical as well experimental results were obtained both with single phase and two–phase conditions (water as working fluid). The milestone to be exploited for Tesla turbine power applications is the development of an accurate heat transfer model in two–phase flow conditions.

Ruiz M and Carey VP [144] presented the experimental results obtained when utilizing a Tesla turbine as a heat sink, employing the work developed in [143]. Heat transfer, as well as pressure drop of a micro tesla turbine with water as working fluid was analysed.

Schosser C and Pfitzner M [145] developed a throughout CFD analysis, focusing on the velocity profile of the flow inside a Tesla turbine with air as working fluids. Particularly, they stated that laminar CFD results were better approximated by a fourth order polynomial function, compared to parabolic profile.

Thawichsri K and Nilnont W [146] performed an experimental comparison between a centrifugal turbine and a Tesla turbine working with Isopentane at low temperature (70–90°C) heat resources. The experimental assessment demonstrated, from one point that the centrifugal turbine was on average 30% more performing than the Tesla turbine, but also that the Tesla turbine is a very cheap and easily to manufacture turbine. The maximum reached efficiency of the Tesla turbine was of about 12%, the specific power output of 35 kJ/kg and the cycle efficiency of 8.6%, when the heat source was 90°C.

2016

Bankar N et al. [147] designed a Tesla turbine for micro power application. Particularly, they called the new design approach as “hybrid Tesla turbine”, due to the introduction of some changes, such as the grooving of the disks and utilization of polycarbonate disks of thin thickness.

Herrmann–Priesnitz B et al. [148] developed a fluid dynamics model on the structure of the boundary layer of a Tesla disk turbine. Inviscid core region was coupled to boundary layer formulation in order to develop a sound analytical model, which was compared to numerical simulations run in OpenFoam environment.

Jose R et al. [149], [150] realized a comprehensive project on the design, theoretical and experimental analysis of a Tesla turbine utilizing water as working fluid. The effect of surface roughness, as well as disk spacing and number of disks was analysed. The experimental results highlighted that a spiral grooving on disks could enhance the turbine efficiency of about 5–6%.

Joshi KN et al. [151] coupled the Tesla turbine design configuration with a Pelton turbine, obtaining therefore a “hybrid Tesla wheel turbine”. A computational fluid dynamic assessment on Tesla and hybrid Tesla Pelton turbine was carried out. The Hybrid turbine allowed a 5% increase in efficiency compared to the bladeless turbine. A rapid prototyping technique was also showed as a possible solution for Tesla–Pelton turbine fabrication.

Qi W et al. [152] performed a numerical investigation on the influence of disk spacing on the performance of Tesla turbines. The analysis conducted considered 7 different spacing (from 0.1 to 1 mm) highlighting the changes in performance (power and efficiency), as well as on the mass flow rate of the turbine. Several rotational speeds were also considered and optimal values of disk spacing, as well dimensionless tangential velocities were obtained when air as working fluid was considered.

Schosser C et al. [153] performed a throughout investigation of the flow field inside a Tesla turbine with air as working fluid, through the means of a stereoscopic 3D–PTV measurement technique. The main result was the assessment of the laminar velocity profile inside the channels, which slightly differs from parabolic distribution and is better described by a 4^{th} order polynomial.

Schosser C [154] exploited the study presented in [145], [153] and carried out a throughout experimental and numerical investigation of a Tesla turbine working with air as working fluid. Analytical and numerical results were also compared and an efficiency prediction of over 50% was obtained.

Sengupta S and Guha A [155] investigated the performance of a Tesla turbine when nanofluids were utilized as working fluid; an increase of power output of 30% appears to be possible when the volume fraction of nanoparticles is increased from 0 to 0.05. Therefore, the maximum predicted efficiency was of about 56% when water based nanofluid with ferro–particles were utilized.

Zahid I et al. [156] analysed the performance of an air driven Tesla turbine. The claimed reached efficiency was of about 58% for a turbine with an external rotor diameter of 100 mm, run with an inlet pressure of 272 kPa.

2017

Alrabie MS et al. [157] applied an analytical solution in order to assess the performance of a small–scale hydro Tesla turbine. The design of experiment was carried out and the definition of the optimal prototype geometry was obtained, assessing various geometric parameters (inlet, outlet rotor diameters, disks spacing, nozzle number and location), as well as the most significant thermodynamic parameters (density, viscosity). Finally, an 80 mm rotor outer diameter turbine was selected as the proper design in order to obtain

0.47 W power output at 1197 rpm. Similarity scaling law equations were applied to assess the performance of a 3 mm rotor outer diameter turbine working with Ethylene Glycol.

Damodhar R et al. [158] designed and fabricated a cm–scale Tesla turbine utilizing water as working fluid. Design specifications were given; as well experimental tests were conducted. The maximum power obtained was of 0.12 W at 140 rpm, with a corresponding efficiency of 20.97%.

Guha A and Sengupta S [159] performed an optimization assessment of the Tesla turbine based on the non–dimensional scaling laws presented in [125]. The role of each non–dimensional parameter was assessed and the physical explanation of its effects on the performance of the turbine is given. As an illustrative example of the methodology applied, a turbine efficiency of 68.8% was designed when a tangential inlet velocity ratio (the ratio between tangential velocity and rotational speed at rotor inlet) of 1.45 was considered.

Li et al. [160] explored the performance characteristics of the Tesla turbine through experimental and numerical assessment. An 11 mm outer rotor diameter, with 1 mm disk spacing and a total of 13 disks, Tesla turbine was fabricated and tested with water as working fluid. The experimental assessment was carried out at various, rotational speeds, inlet pressures and mass flow rates; a maximum efficiency of about 8% was obtained. The numerical simulation assessed efficiencies higher than 40% for rotational speeds between 700 and 1000 rpm.

Lisker R et al. [161] developed an analytical model, which takes into account thin film condensation in a Tesla turbine rotor. The influence of thin film condensation on velocity fields and mass flow rate was highlighted when condensing steam was utilized as working fluid.

Mandal A and Saha S [162] investigated the performance of a cm–scale Tesla turbine for micro–air vehicles application. Numerical simulations on 20 disks, 0.1 m outer rotor diameter air Tesla turbine were performed. Different rotational velocities were assessed, obtaining maximum rotor efficiency of 89.56% for an inlet velocity of 10 m/s and a maximum power output of 21.3 W for an inlet velocity of 20 m/s at 1500 rpm.

Polisetti S et al. [163] fabricated and conducted a performance study on an air driven Tesla turbine. A 95 mm outer rotor diameter, 1.27 mm thick disks Tesla turbine was fabricated and various configurations were tested, varying number of disks, distance between the disks, number of nozzles and pressure at rotor inlet. The results were presented in the form of rotational speeds. The maximum reached rotational speed was 25,324 rpm for a 4 disks configuration at 6 bar inlet pressure.

Schosser C et al. [164] presented a comparison between analytical and numerical models on the flow field developing inside a Tesla turbine single channel. Several analyses were

conducted, showing the influence of non–dimensional parameters, such as dimensionless friction factor, inlet conditions and geometry parameters. Inflow effect was analysed, as the discrepancy between theoretical and numerical analyses was found to be relevant.

Shah V and Dhokai S [165] carried out experimental tests of an air driven Tesla turbine. The turbine was composed by 8 disks of 95 mm rotor outer diameter, with disk spacing of 1 mm. The maximum power obtained was of 137.83 W at 4500 rpm, with 4 bar of total inlet pressure.

Shah V et al. [166] conducted a literature review on the principle of operation and on the parameters affecting the performance of the Tesla turbine.

Song J and Gu CW [167] developed a 1D model of a Tesla turbine working with organic fluids. Furthermore, a thermodynamic analysis of an organic Rankine cycle utilizing R245fa as working fluid, exploiting the Tesla turbine as the expander was carried out. The assessed isentropic efficiency of the turbine reached a maximum value of 45% when a 15° oriented nozzle was utilized and an evaporation temperature of 370 K was taken into account. The maximum power output of 1.24 kW was obtained when the heat source temperature was of 355 K. The maximum thermal cycle efficiency obtained was of about 8%.

Song J et al. [168] improved and used the one–dimensional Tesla turbine model presented in [167] to predict the efficiency of a small scale ORC power plant adopting various working fluids and operating conditions: at design point, the ORC with R245ca released 1.25 kW power output at 4% thermodynamic efficiency.

Thiyagarajan V et al. [169] applied the Tesla turbine concept to solar power refrigeration. A prototype of 50 mm outer rotor radius was fabricated and some preliminary tests carried out. Based on the data obtained, the theoretical time to convert 1 kilogram of water in ice was calculated (6.5 hr).

Umashankar M et al. [170] assessed the possible application of the Tesla turbine in cogeneration of heat and power systems (CHP). Cogeneration concept and turbine analytical approach were assessed.

Variava JM and Bhavsar AS [171] performed an experimental and numerical analysis on Tesla turbine utilizing water as working fluid. The experimental investigation allowed assessing turbine efficiency as high as 60% with a 0.56 kg/s mass flow rate and a power output of 15.18 W.

2018

Sengupta S and Guha A [172] investigated the effect on non–uniform admission inside a Tesla turbine rotor, taking into account discrete inflows effect, finite disks thickness and

radial clearance. An extensive computational fluid dynamic assessment was carried out assessing both the variation in power and efficiency as function of the number of nozzles, clearance, rotational speed and disks thickness. Small disk thickness, straight disk edge, optimum radial clearance and high number of nozzle were recommended as an optimal design solution.

Song et al. [173] improved the one–dimensional model developed in [167], [168] and compared the predicted performances with the experimental results obtained by Rice [60] with air as working fluid.

Traum MJ et al. [174] extended the work developed by Carey VP [93] in order to assess the sensitivity of shaft power to a selected design variable. A differentiable closed form analytical model was applied, starting from the one developed in [93] and applying some substantial changes, such as: identifying model Reynolds number limitation; defining closed–form torque and power output expressions; introducing simple nozzle geometric height parameter and showing the importance of checking maximum turbine rotational speed.

SERG (Sustainable Energy Research Group) contribution to Tesla turbine state of the art

The SERG group of the department of Industrial Engineering of University of Florence contributed to the state of the art on Tesla turbines with the following research.

2017

Manfrida et al. [175] revisited the original concept presented by Tesla, improving the stator layout and applying a modular design to the turbine, increasing its flexibility. The evaluation of the turbine performance with two different organic working fluids (R245fa and n–Hexane) was also carried out, analysing the influence of the most significant turbomachinery non–dimensional parameters (n_s, d_s, ϕ, ψ). A preliminary design of a prototype was also presented, and the expected efficiency with the assessed working fluid highlighted. Maximum efficiency (about 40%) was obtained for n–Hexane as working fluid, for low mass flow rates.

2018

Manfrida G and Talluri L [176] revised the mathematical model of the Tesla turbine, upgrading the model presented in [93], [111], taking into account compressible real fluid properties. A performance analysis on the Tesla turbine rotor was presented, allowing the understanding of the principal parameters influencing turbine efficiency and reaching a design of an air Tesla turbine rotor with over 90% efficiency.

Manfrida G et al. [177] further polished the work conducted in [175], presenting an upgraded concept of the Tesla turbine for Organic Rankine cycle applications. Concept design and performance assessment of a manufactured prototype were performed. The fluid assessment comprehended 5 different organic working fluids: R245fa, R134a, SES36, n–Pentane, n–Hexane. High turbine efficiency (over 55%) can be reached for n–Hexane as working fluid. Higher power production was reached with refrigerant fluids, and SES36 resulted as the best compromise between power production and efficiency.

Talluri et al. [178] performed a design and optimization of Tesla turbine for ORC applications. An innovative rotor model was presented, as well as the assessment of each component losses was carried out. Not only the rotor, but also stator, still chamber and diffuser model were designed. As an outcome of the methodology process, three different turbine configurations were assessed; the maximum total to static efficiency assessed was of 64% when a 0.5 m rotor diameter was considered and n–Hexane was utilized as working fluid. The power production per single channel of such configuration was of 58 W, which allowed a very compact axial design.

Statistics

To conclude the literature review, a resume of the available literature is presented in Tab. 2.6. The previously described works were resumed highlighting the type of analysis that was carried out and which kind of fluid was considered.

Fig. 2.18 displays the number of publication on Tesla turbines (updated in August 2018). It has to be remarked how the trend is drastically increasing in the last few years; this is directly linked to the high attention that micro power generation gained on the energy market.

Fig. 2.19 collects the most active authors assessing the Tesla turbine. Rice W (Arizona State University, Tempe) is the author that most investigated the Tesla turbine, both from analytical and experimental point of view. Of particular relevance are also the work developed by Guha A and Sengupta S (Indian Institute of Technology, Kharagpur) and Carey VP (University of California, Berkeley), who developed analytical, computational and experimental research, properly explaining the flow behaviour inside a Tesla disk turbine.

Finally, Fig. 2.20 resumes the working fluids that have mainly been considered when developing a study on Tesla turbine. Air is the principal fluid investigated, but of particular importance is the emerging interest in recent years of the application of Tesla turbines in organic Rankine cycles.

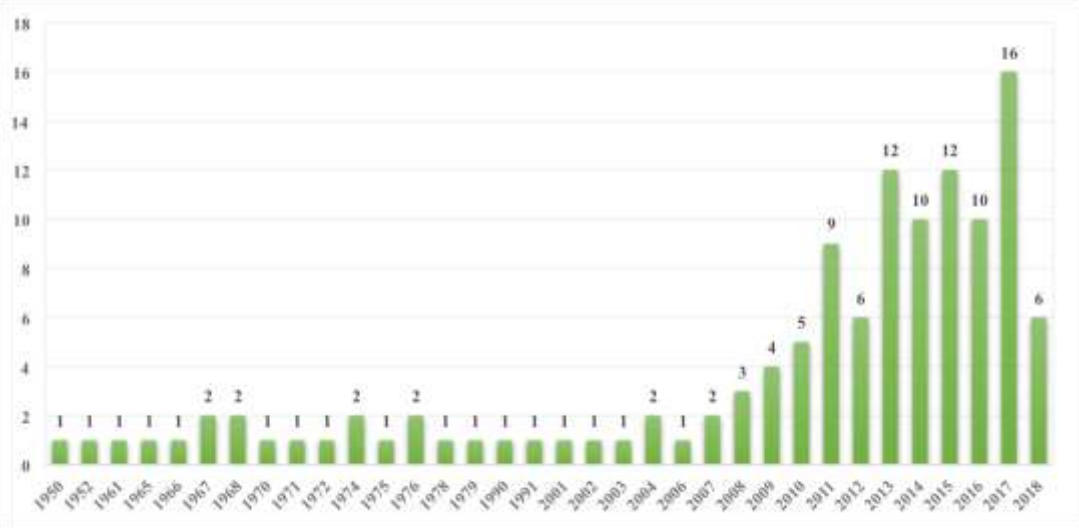

Fig. 2.18 Number of publications (Journal paper, conference paper, Ph.D. and M.Sc. available thesis) from 1950 to nowadays (updated in August 2018)

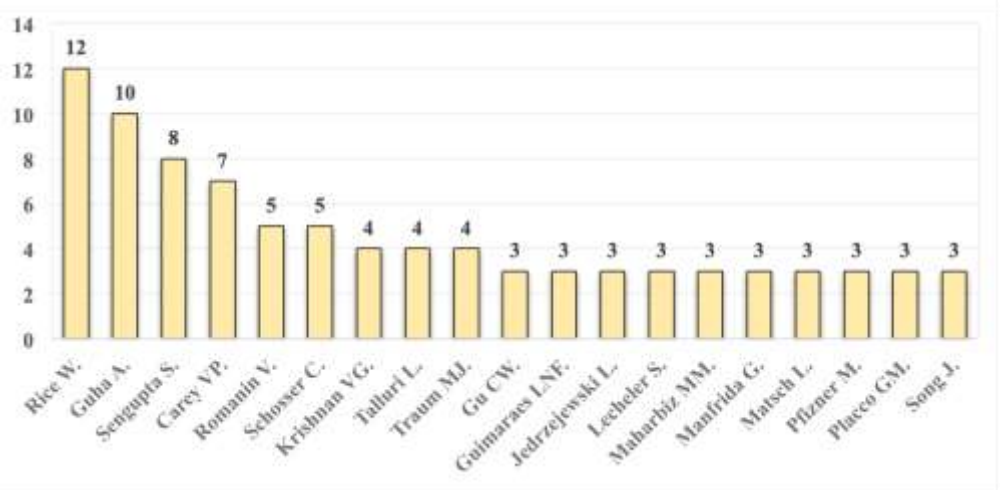

Fig. 2.19 Most active authors on Tesla turbine research

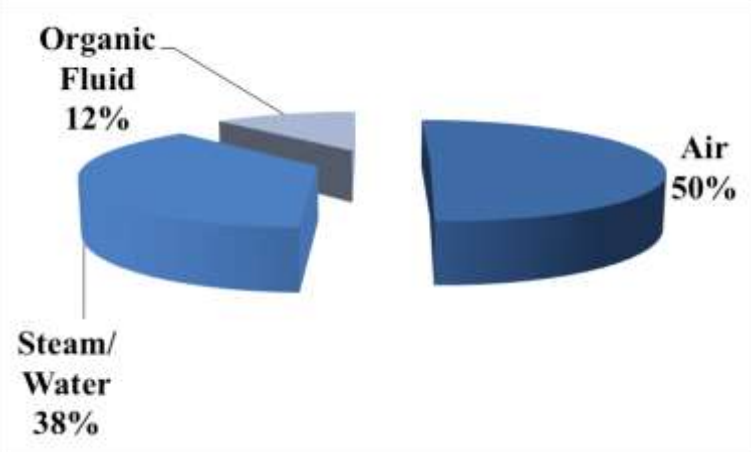

Fig. 2.20 Working fluid taken into account in literature studies

Table 2.6 Literature Review summary

Ref.	Year	Fluid considered	Focus of work	Ref.	Year	Fluid considered	Focus of work
[57]	1950	Air	Design/ experimental	[87]	2008	Air	Experimental/ Numerical
[58]	1952	Steam	Design/ experimental	[88]	2008	Hydrocarbon gases	Experimental
[59]	1961	Air	Numerical/ experimental	[89]	2009	Care30	Practical assessment
[60]	1965	Air	Analytical/ experimental	[90]	2009	Air	Experimental
[61]	1966	Air	Experimental	[91]	2009	Air	Experimental
[62]	1967	–	Analytical	[92]	2009	SES36	Numerical
[63]	1967	–	Analytical	[93]	2010	Steam	Analytical
[64]	1968	Air	Numerical	[94]	2010	Steam	Analytical/ Numerical
[65]	1968	–	Analytical	[95]	2010	Air	Experimental/ Mechanical
[66]	1970	Water – Ethylene Glycol	Experimental	[96]	2010	Water	Analytical/ Numerical
[67]	1971	–	Analytical	[97]	2010	Water/Steam	Numerical/ Experimental
[68]	1972	Hydrogen/ Sodium/ Glycerine	Performance assessment	[98]	2011	–	Analytical
[69]	1974	Water	Numerical	[99]	2011	Water	Numerical
[70]	1974	Water	Experimental	[100]	2011	R245fa/Steam	Design/ experimental
[71]	1975	Air	Analytical	[101]	2011	Air	Experimental/ Mechanical
[72]	1976	Air	Numerical	[102]	2011	Water	Performance assessment
[73]	1976	Water/Steam	Experimental	[103]	2011	Water	Experimental
[74]	1978	Steam with droplets	Numerical	[104]	2011	SES36	Numerical
[75]	1979	Air with solid particles	Numerical	[105]	2011	–	State of the art
[76]	1990	Air	Analytical	[106]	2011	Air	Analytical
[77]	1991	–	State of the art	[107]	2012	Water	Experimental
[78]	2001	Air + SO_2	Numerical	[108]	2012	Air/ Steam	Numerical/ Experimental
[79]	2002	Air/Steam	Experimental	[109]	2012	Water	Analytical
[80]	2003	Steam	Practical assessment	[110]	2012	Air / Water	Analytical/ numerical/ experimental
[81]	2004	Air	Numerical	[111]	2012	Air	Analytical
[82]	2004	Air	Numerical	[112]	2012	Air	Practical assessment
[83]	2006	Air/Water	Analytical	[113]	2013	Air/ R600/ R245fa/ R123	Numerical
[84]	2007	–	Analytical	[114]	2013	Air	Analytical/ Numerical
[85]	2007	Water	Design/ Experimental	[115]	2013	Air	Analytical
[86]	2008	Air	Practical assessment	[116]	2013	Air /Steam	Experimental

Ref.	Year	Fluid considered	Focus of work	Ref.	Year	Fluid considered	Focus of work
[117]	2013	–	State of the art	[148]	2016	–	Analytical/ numerical
[118]	2013	Water	Experimental	[149]	2016	Water	Numerical
[119]	2013	Air/ Water	Application assessment	[150]	2016	Water	Design/ experimental
[120]	2013	Water	Design	[151]	2016	Water	Numerical
[121]	2013	Air /Steam	Experimental	[152]	2016	Air	Numerical
[122]	2013	Air	Analytical/ numerical	[153]	2016	Air	Experimental
[123]	2013	Air	Experimental/ mechanical	[154]	2016	Air	Numerical/ experimental
[124]	2013	Air/ Water	Design/ experimental	[155]	2016	Water + solid ferro–particles	Analytical/ numerical
[125]	2014	Air/Water	Analytical	[156]	2016	Air	Experimental
[126]	2014	Air	Analytical	[157]	2017	Ethylene Glycol	Analytical
[127]	2014	Air	Numerical	[158]	2017	Water	Design/ experimental
[128]	2014	Water	Numerical	[159]	2017	Air	Analytical/ numerical
[129]	2014	Air	Experimental/ numerical	[160]	2017	Water	Experimental/ numerical
[130]	2014	Air	Design/ numerical	[161]	2017	Water/ Steam	Analytical
[131]	2014	Air	Numerical	[162]	2017	Air	Numerical
[132]	2014	–	Analytical	[163]	2017	Air	Experimental
[133]	2014	Isopentane	Experimental	[164]	2017	Air	Analytical/ numerical
[134]	2014	Air/ Water	Experimental/ numerical	[165]	2017	–	Experimental
[135]	2015	–	Mechanical/ numerical	[166]	2017	Air	State of the art
[136]	2015	Air/ Steam	Experimental	[167]	2017	R245fa	Analytical
[137]	2015	Air	Design/ experimental	[168]	2017	R123/ R600/ R600a/ R236ea/ R236fa/ R245ca/ R245fa	Analytical
[138]	2015	Steam	Design/ experimental	[169]	2017	Steam	Practical assessment
[139]	2015	Water	Numerical/ experimental	[170]	2017	–	Practical assessment
[140]	2015	Air	Experimental	[171]	2017	Water	Experimental
[141]	2015	Air	Mechanical/ numerical	[172]	2018	Air	Numerical
[142]	2015	–	State of the art	[173]	2018	Air	Analytical
[143]	2015	Water/Steam	Numerical/ experimental	[174]	2018	Water	Analytical
[144]	2015	Water	Experimental	[175]	2017	R245fa/ n–Hexane	Design/ analytical
[145]	2015	Air	Numerical	[176]	2018	Air	Analytical
[146]	2015	Isopentane	Experimental	[177]	2018	R245fa/ R134a/ SES36/ n–Hexane/ n–Pentane	Design/ Analytical
[147]	2016	Air	Design	[178]	2018	n–Hexane	Design/ analytical/ numerical

3 Methodology and Models

The methodology carried out in this research comprehends aspects of both analytical and numerical modelling, as well as a design process of prototypes and the mechanical analysis. The experimental setup of the test benches, as well as each developed numerical model are described in the next Sections.

Typical configurations and principle of operation

As discussed in Section 2.4.1, the first concept of the Tesla turbine was developed by Tesla in 1913 [56]. Conversely, to traditional turbomachines, which exploit the pressure difference that is produced when a fluid flows around a row of blades; the Tesla turbine generates power through the frictional interaction between the evolving fluid and the bladeless rotor. This peculiar rotor, characterized by the absence of blades, is the main feature of the Tesla turbine. Indeed, due to the configuration of the rotor, as well as to the principle of operation, the Tesla turbine is also called bladeless turbine, viscous turbine, boundary layer turbine or friction turbine.

Differently from conventional turbines, the rotor is composed by a series of parallel flat disks with a very small gap between them. The admission of the flow in the rotor occurs through one or more nozzles, which allows the fluid to enter from the external radius of the disks and to exit from the openings made on the disks at the inner radius. Inside the rotor, the fluid depicts a spiral centrifugal path, due to the interaction between the viscous forces and exchange of momentum. Typical configurations of the Tesla turbine consider only the rotor as part of the turbine, and often, nozzles are just converging pipes positioned tangentially to the rotor outer radius, as displayed in Fig. 3.1.

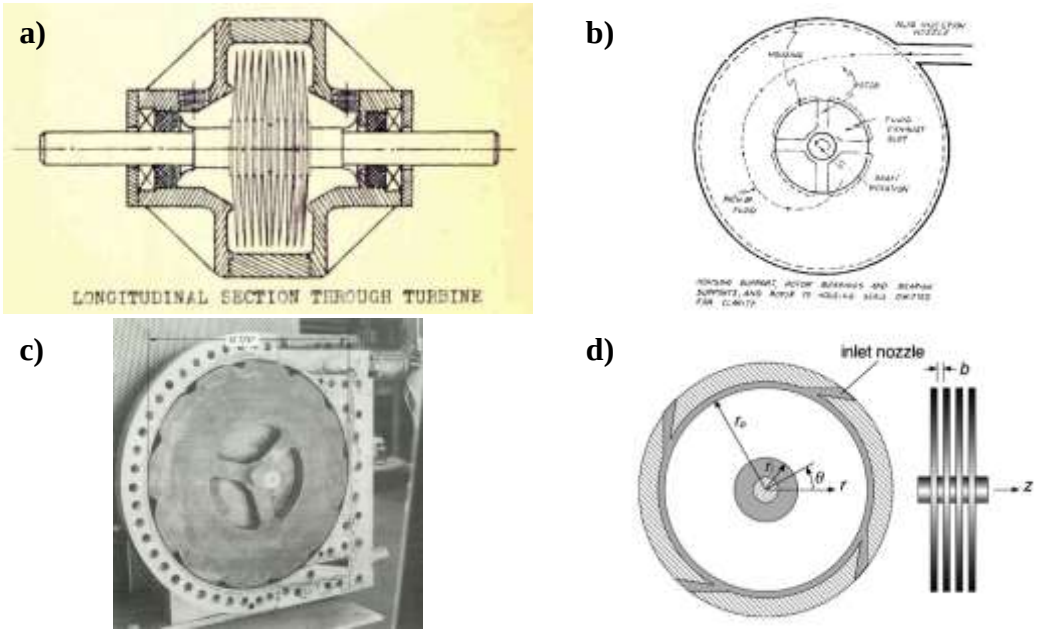

Fig. 3.1 Typical configuration of Tesla turbine a) [58], b) [60], c) [73], d) [93]

Conversely to the typical configurations, the Tesla turbine described and analysed in this work consists of several components: an external toroidal plenum chamber, a stator with fixed nozzles and a bladeless rotor composed by parallel thin disks fixed to the rotating shaft; Fig. 3.2 displays the schematic of the ORC prototype, nonetheless the same nomenclature is used for the air prototype.

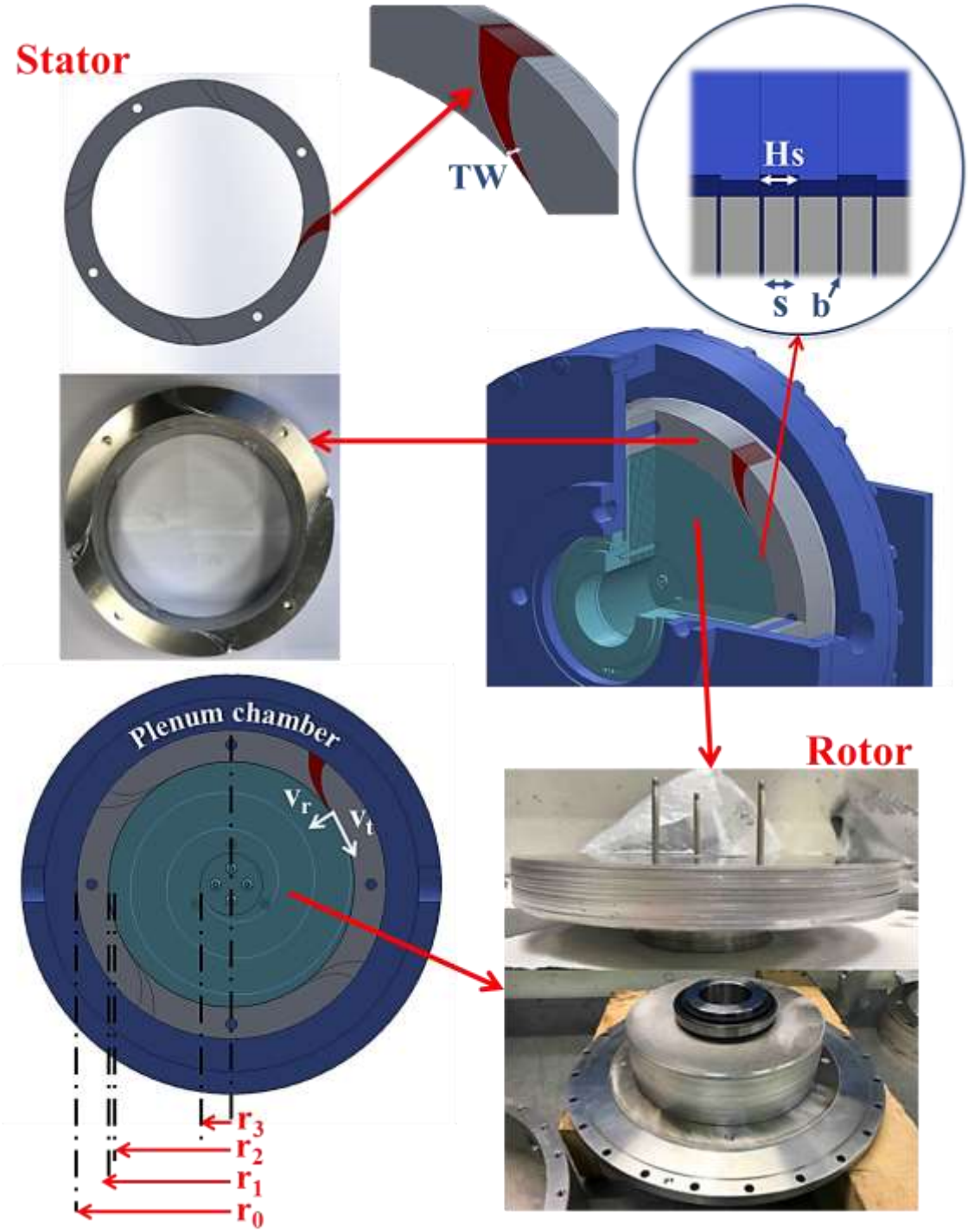

Fig. 3.2 Schematic of Tesla turbine

3.1 2D model developed in EES

A 2D thermo–fluid dynamic model was developed in Engineering Equation Solver [179]. Each procedure is thus explained.

3.1.1 Nozzle Design

Blade design is a procedure, which enables the definition of the stator geometry.

The stator is designed like a circular crown, of a certain thickness "*Hs*" in the axial direction, on which a series of channels ("or nozzles") are obtained, defined by the blades profile.

The required inputs for the procedure are:

- Outlet diameter of the stator (r_1);
- Inlet and outlet angles (α_0, α_1);
- Total length of the camber (m_{tot}), which can be determined imposing the inlet/outlet diameter stator ratio at 1.25 as suggested in [180], [181].

Another feature of the code is that the camber angle distribution can be adjusted changing the exponent *n* of a predefined power law.

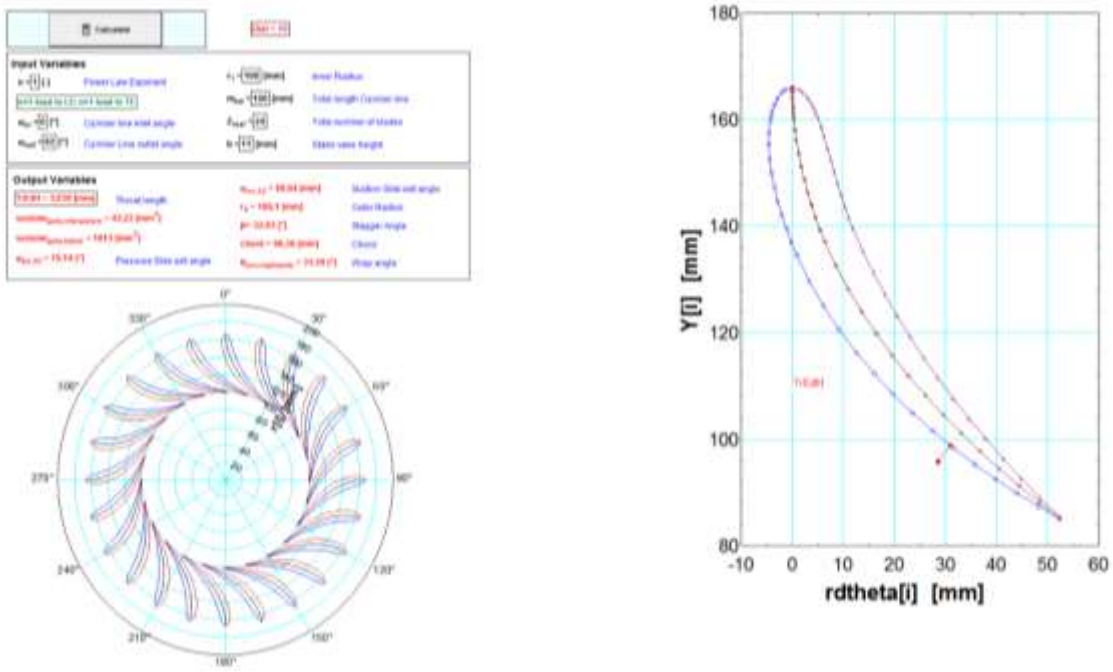

Fig. 3.3 Blade design code interface

Once all the inputs are fixed, the code draws blades on the circular crown, defining the main parameters such as width of the throat section, chord, pressure and suction side exit angles). The maximum feasible number of passages is then calculated (Z_{max}) and partialized (Z_s). The partialization consists of the occlusion of several volumes present between two blades, due to the low mass flow rate required by the turbine rotor. The final geometry of the stator is then obtained, composed by a small number of real channels, located inside a thick volume.

Specifically, the program can include the coordinates of NACA or any other blade profile, allowing the construction of pressure and suction sidewalls. The user can adapt the geometric inputs and the drawn profile will be visible both in the configuration of a single blade and as section of stator, as shown in Fig. 3.3.

Blade design main equations

In the lookup table, the coordinate of the selected NACA profile with chord value equal to 1 are stored. Absolute camber line values are thus determined:

$$m_i = \left(m_{r(i)} - m_{r(i-1)}\right) \cdot m_{tot} \tag{3.1}$$

Where:

m_i – absolute discretised value of camber line

$m_{r(i)}$ – relative discretised value of camber line

m_{tot} – total length of camber line

The camber line is then curved through an exponential law, which sets the local camber angle.

$$\alpha = \alpha_0 + (\alpha_0 - \alpha_1) \cdot m_r^n \tag{3.2}$$

In order to find the coordinate of each point of the camber line, trigonometry analysis is applied. From the law of cosines, it is possible to determine the radius and from the law of sines the wrap angle (Fig 3.4).

$$r_i = (r_{i-1})^2 + (m_i)^2 - (2 \cdot m_i \cdot r_{i-1} \cdot \cos(\alpha_i)) \tag{3.3}$$

$$\theta_i = \theta_{i-1} + \arcsin\left(\frac{m_i}{r_i} \cdot \sin(\alpha_i)\right) \tag{3.4}$$

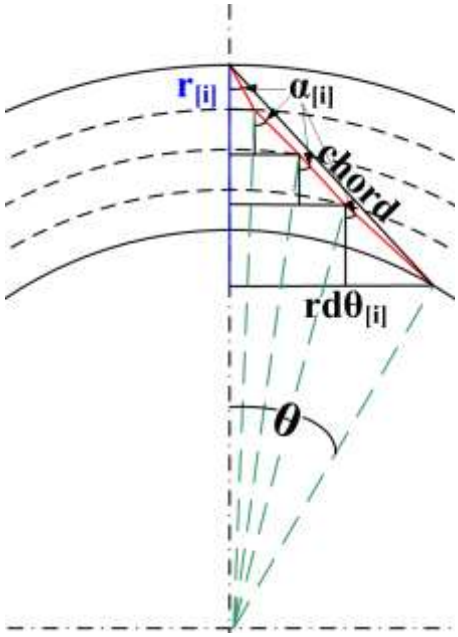

Fig. 3.4 Trigonometric representation of stator blade

It is then possible to find the Cartesian coordinate of the camber point with a simple coordinate transformation.

$$X_i = r_i \cdot \sin(\theta_i) \tag{3.5}$$

$$Y_i = r_i \cdot \cos(\theta_i) \tag{3.6}$$

The chord and stagger angle (the angle between the chord and radial direction) values are thus found:

$$\beta = \arctan\left(\frac{(X_0 - X_1)}{(Y_0 - Y_1)}\right) \tag{3.7}$$

$$\text{Chord} = \frac{X_0 - X_1}{\sin(\beta)} \tag{3.8}$$

The coordinate of suction and pressure side can be easily determined knowing the blade thickness (which is a function of the chord):

$$X_{i\,PS/SS} = X_i + \left(\frac{\left(\frac{t}{2}\right)_{PS}}{SS} \cdot \cos(\alpha_i)\right) \tag{3.9}$$

$$Y_{i\,PS/SS} = Y_i + \left(\frac{\left(\frac{t}{2}\right)_{PS}}{SS} \cdot \sin(\alpha_i)\right) \tag{3.10}$$

Once the coordinates of suction and pressure side of each blade are known, it is possible to determine the distance between two blades at each point and therefore to determine the throat length.

3.1.2 Stator model

As the most original component of a Tesla turbine is the bladeless rotor, simple nozzles are commonly used instead of properly designed stator vanes. The Tesla turbine stator purpose is to generate the necessary tangential flow stream at rotor inlet and to convert the pressure energy of the flow in the plenum chamber to kinetic energy at nozzles output. The reduction of cross sectional area for a subsonic flow produces a favourable pressure gradient and an acceleration of the fluid [182], avoiding wall separation; as a result, the efficiency of nozzles is usually very high, often exceeding 96% [183], [184]. Anyway, for small size nozzles, where the throat width is lower than 3 mm (as is the case for Tesla turbine), the boundary layer might occupy a significant portion of the cross sectional area [185], generating increased viscous losses. In these cases, the flow is laminar ($Re<10^5$) and the total pressure losses decrease with increasing the Reynolds number [185].

As discussed in several papers [58], [60], [90], [91], [140], the stator is commonly acknowledged to be one of the critical components of the Tesla turbine. It is indeed recognized among the main reasons for the low efficiency of the machine obtained in several experimental tests, as it is the source of high total pressure losses. Specifically, Guha and Smiley [91] carried out an experimental and computational study of the Tesla turbine nozzles and concluded that the stator is responsible for total pressure losses up to 35% of the total inlet conditions.

In the present study, the stator design follows the approach derived from radial expanders vaned stators [41]–[43], [186], [187], also accounting for partial admission due to the reduced flow rates. In [42], the design guidelines for a radial ORC turboexpander are defined using a zero dimensional model: an input dataset (thermo–fluid dynamic variables, dimensional and non–dimensional parameters) is provided by the designer, while the outputs of calculations are the basic geometry, velocity triangles and nozzle efficiency.

In order to carry out a parametric analysis, a set of geometric and thermodynamic parameters, needs to be defined. The formers are: stator blade angles, number of nozzles, length and height of the channel and nozzle geometry profile; which allow the definition of the full geometry (in particular the throat width and the chord length). The main thermodynamic conditions to be fixed are the inlet total pressure and temperature and the mass flow rate.

Two iterative processes were implemented, the former one on mass flow rate, the latter one on two stator loss coefficients. The static pressure at throat section is taken as the

iterative parameter for the matching of the mass flow rate, which will ultimately assume the imposed input mass flow rate.

The first loss coefficient (ζ_N) was taken from [43], [187], [188] and it is only dependent on Φ_n, which is the ratio between the real and isentropic velocity at stator exit. The range of this parameter is between 0.9 and 0.97. The second loss coefficient (ζ_R) [181] is on the other hand dependent on geometry values, such as chord, pitch, stator height and stator exit angle, as well as on the Reynolds number of the flow. The two coefficients are compared and until they are not equal, an iterative process on flow exit velocity runs.

Stator main equations

The thermo–fluid dynamic model for the calculation of the fluid behaviour into the Tesla turbine stator assumes real fluid Equations of State (EoS). For this reason, all the thermodynamic properties were evaluated as functions of couples of local variables (typically, *p* and *T*) using the Engineering Equation Solver (EES) EoS library data. Fig. 3.5 displays the enthalpy–entropy diagram of the Tesla expander stator and its nomenclature.

The thermodynamic of point 00 is defined from input values p_{00} and T_{00}. Point 0 is defined through iteration on density (first guess value is ρ_{00}) and application of mass flow rate definition in order to find v_0.

$$\dot{m} = v_0 \cdot \rho_0 \cdot A_0 \tag{3.11}$$

The root finding interpolation method was applied in order to find the correct expansion ratio in the stator. P_1 is taken as the variable for the interpolation method; convergence is reached when the imposed mass flow rate and the calculated one are equal, as shown in the diagram of Fig. 3.6. Eqns. (3.12) and (3.13) are main equations of the applied scheme. In order to set the right starting point, the upper bound for P_1 was assumed as equal to $P_0 - 100$ Pa; the lower bound was set assuming an incompressible flow expansion.

$$P_1(\text{up}) = P_1(\text{up}) + \frac{(\dot{m} - \dot{m}_{\text{up}})}{(\dot{m}_{\text{down}} - \dot{m}_{\text{up}})} \cdot (P_1(\text{down}) - P_1(\text{up})) \tag{3.12}$$

$$P_1(\text{down}) = P_1(\text{up}) + \frac{(\dot{m} - \dot{m}_{\text{up}})}{(\dot{m}_{\text{down}} - \dot{m}_{\text{up}})} \cdot (P_1(\text{down}) - P_1(\text{up})) \tag{3.13}$$

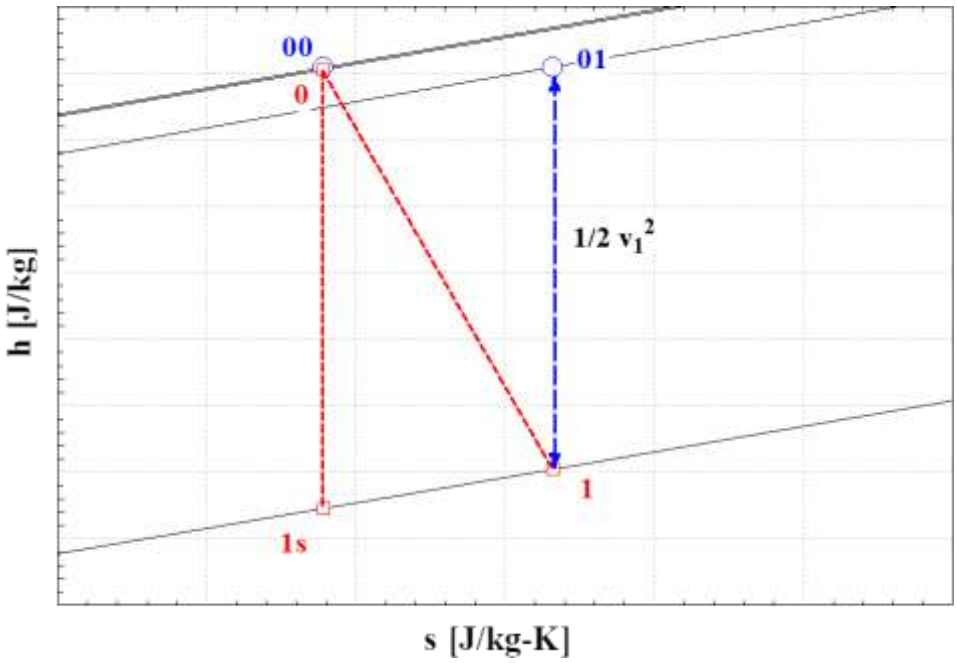

Fig. 3.5 Stator Enthalpy–Entropy diagram

An iterative process was also implemented on two loss coefficients ζ_N and ζ_R in order to assess the right velocity at stator outlet and therefore the efficiency of the nozzle. Eqns. (3.14) and (3.15) display the calculation of the loss coefficients.

$$\zeta_N = \frac{h_1 - h_{1s}}{\frac{1}{2}v_1^2} = \frac{1}{\phi_n^2} - 1 \tag{3.14}$$

$$\zeta_R = \frac{0.05}{Re^{0.2}} \cdot \left(3 \cdot \frac{\tan(\alpha_1)}{pitch/chord} + pitch \cdot \frac{\cos(\alpha_1)}{H_s}\right) \tag{3.15}$$

Where:

H_s– Blade height at stator outlet ; α_1– Absolute angle at stator outlet;

Re – Reynolds number (based on blade height and absolute velocity at stator outlet)

After the two iterative process point 1 and 01 are defined and, finally, stator efficiency is calculated as:

$$\eta_{st} = \frac{(h_{01} - h_1)}{(h_{01} - h_{1s})} \tag{3.16}$$

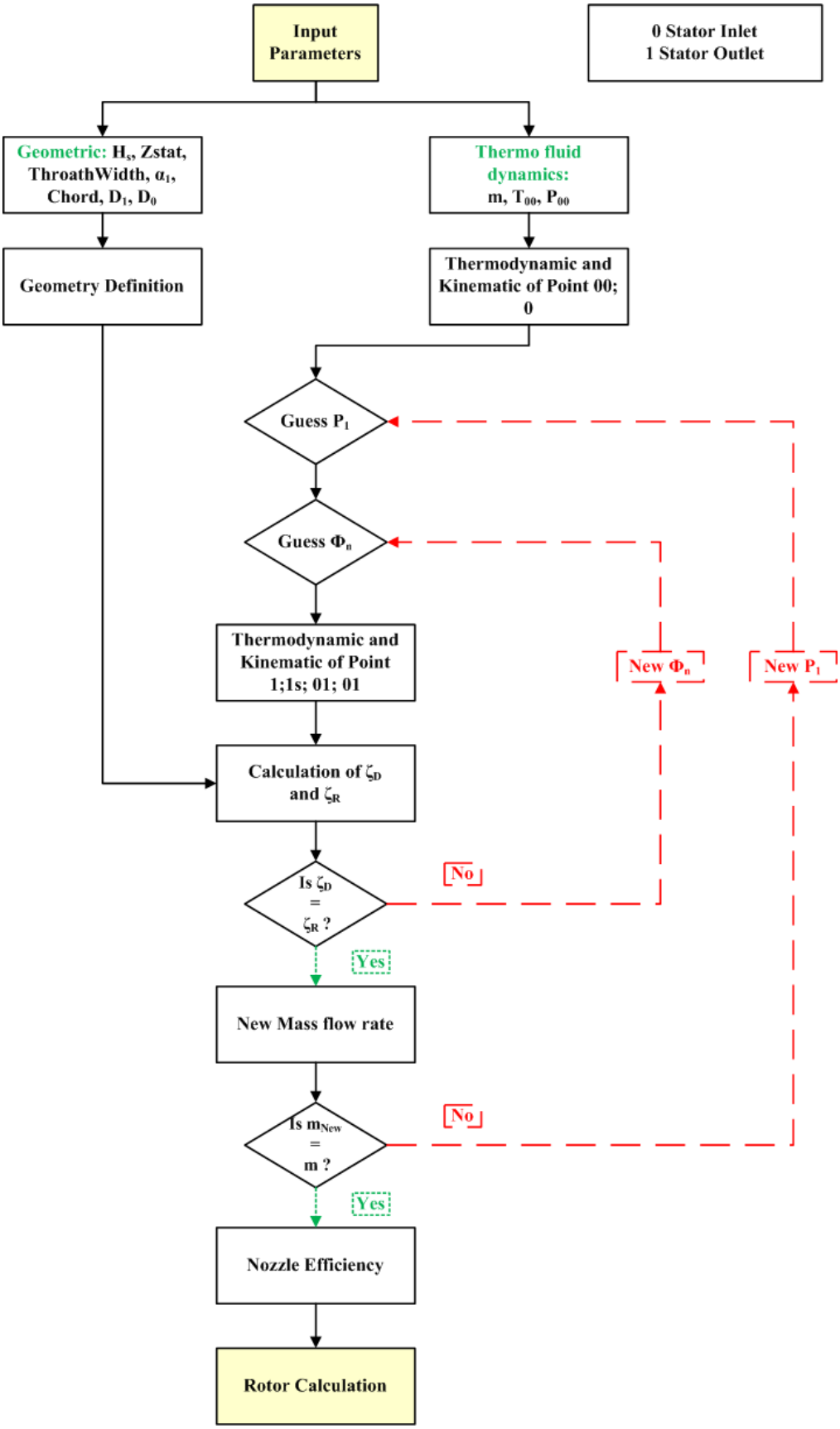

Fig. 3.6 Flow Diagram of Stator model

3.1.3 Stator–rotor coupling model

Assumptions

When connecting the three–separated developed flow models (stator, rotor and gap pressure losses), the following assumptions were applied:

- Conservation of total enthalpy between the stator outlet and the rotor inlet, because the transformation may be considered adiabatic and without any work transfer.
- Invariable static enthalpy, and consequently constant absolute velocity v_1, while the flow direction changes during the gap crossing. It means that the pressure losses may be treated like an isenthalpic throttling process into a valve.

Model characteristic

The stator and rotor models only take into account of the distributed pressure losses inside the components, but they do not consider those concentrated into the stator–rotor gap. The passage of the flow from the throat of the nozzle to the gap first and to the rotor channel later, involve an abrupt cross–section enlargement followed by a contraction and generates large flow pressure losses.

Both loss coefficient (abrupt enlargement and abrupt contraction) were obtained from standard incompressible flow loss treatment theory (Borda Carnot coefficient and polynomial fitting of empirical data [189]). In order to take into account compressibility effects, an iterative procedure was implemented in EES to compute average values of density between inlet and outlet sections.

Stator–rotor losses main equations

For an incompressible fluid, the concentrated pressure losses are calculated by the definition of a loss coefficient, depending on the system geometry and the flow conditions, which reduces the kinetic energy of the fluid [189]:

$$\Delta p_0 = \zeta \cdot \frac{1}{2} \rho v^2 \tag{3.17}$$

For the case of Tesla turbine, it can be written as:

$$\Delta p = \Delta p_{en} + \Delta p_{con} = \frac{1}{2}\zeta_{en}\rho v_1^2 + \frac{1}{2}\zeta_{con}\rho w_2^2 \tag{3.18}$$

Where Δp_{en} is the pressure loss occurring immediately after the throat section (abrupt enlargement) and Δp_{con} is the pressure loss related to the flow entering the rotor micro–

channels (relative flow contraction), while ζ_{en} and ζ_{con} are their respective loss coefficients.

The loss coefficient for abrupt enlargement (ζ_{en}) was modelled as an incompressible Borda–Carnot coefficient [189], according to Eq. (3.19):

$$\zeta_{\mathrm{en}} = (1 - \frac{\mathrm{A_{in}}}{\mathrm{A_{out}}})^2 \tag{3.19}$$

Where A_o is the throat cross section, here having rectangular shape:

$$\mathrm{A_{in}} = \mathrm{L_t} \cdot \mathrm{H_s} \tag{3.20}$$

A_{out} is the cross section on the disks (transversal) covered by the flow jet:

$$\mathrm{A_{out}} = \left\{[\frac{\mathrm{L_t}}{\tan\alpha_1} + \frac{\mathcal{G}}{\sin\alpha_1}]/\cos\alpha_1 - \mathcal{G} \cdot \tan\alpha_1 - \frac{\mathcal{G}}{\tan\alpha_{\mathrm{PS}}}\right\} \cdot \mathrm{H_S} \tag{3.21}$$

Eq. (3.19) can be used for a turbulent flow with a uniform velocity profile; when these assumptions aren't checked, some numerical and graphical correlations available in [189] can be used.

The total pressure loss for abrupt expansion can be calculated using the velocity immediately upstream the enlargement. A parametric analysis showed that the pressure loss is mainly influenced by the velocity v_1 (second order law), followed by the density and, finally, by geometric parameters (throat width TW and gap extension $\mathcal{G}$).

The loss coefficient for abrupt contraction (ζ_{con}) was obtained through a polynomial fitting of empirical data [189]:

$$\begin{aligned}\zeta_{\mathrm{con}} = &-0.126\left(\frac{\mathrm{A_{out}}}{\mathrm{A_{in}}}\right)^4 + 1.0296\left(\frac{\mathrm{A_{out}}}{\mathrm{A_{in}}}\right)^3 - 1.279\left(\frac{\mathrm{A_{out}}}{\mathrm{A_{in}}}\right)^2 \\ &- 0.1209(\frac{\mathrm{A_{out}}}{\mathrm{A_{in}}}) + 0.5\end{aligned} \tag{3.22}$$

Where A_{in} is the total cylindrical surface, including disks and channel surfaces:

$$\mathrm{A_{in}} = 2\pi\mathrm{r_2} \cdot \mathrm{H_s} \tag{3.23}$$

While A_{out} only takes into account the cylindrical surface of the channel:

$$A_{out} = 2\pi r_2 \cdot b \cdot n_{ch} \tag{3.24}$$

The velocity used in this case is the radial component of the relative velocity w_{r2} (normal to passage section), immediately after the contraction. The main geometric parameters influencing the pressure loss are the height of the nozzle throat, the thickness and the number of rotor channels. Generally, the pressure loss for abrupt enlargement is far higher than the one for abrupt contraction at rotor inlet, because the velocity v_1 influencing the former is higher (typically by a factor 10).

Eq. (3.18) could be used if the flow Mach number was less than 0.3, thus the flow could be treated as incompressible, but it is not applicable for the flow at nozzle output/rotor inlet sections. For this reason, two iterative calculations were implemented into the EES code in order to achieve average values of density between the input and the output sections (both for abrupt enlargement and abrupt contraction), which allows the recovery of compressibility effects.

3.1.4 Rotor model

The first developed model for the rotor flow was derived from [60], [93], applying some remarkable improvements. Specifically, real and compressible fluid behaviour was considered (rather than ideal and incompressible). The variable density and the other thermodynamic functions were taken as fluid properties, depending on the local variables (for example pressure and temperature). As for the stator model, the fluid properties were locally evaluated using EES EoS library data. The assumptions of steady, laminar and two–dimensional flow were kept, as well as the viscous forces treated as body forces acting on the flow at each position [93]. It allowed simplifying and thus numerically solving the fundamental Navier–Stokes equations, expressed in cylindrical coordinates.

Assumptions

When developing the first rotor model, the following assumptions were made:

a) Steady, laminar flow.

b) The viscous force is treated as a body force acting on the flow at each (r–θ) position.

c) Two–dimensional flow:

- $v_z = 0$;
- $v_r =$ constant across the channel ;
- $v_\theta =$ constant across the channel.

d) Radial symmetric flow field, uniform at the inlet ($r = r_0$). The flow field is thus the same for any θ, therefore the derivative $\partial/\partial\theta = 0$ for all flow variables.

e) $(\partial p/\partial\theta)$ negligible compared to wall friction forces.

General Flow Equations

Taking into account the above assumptions, the fundamental Navier–Stokes equations in cylindrical coordinates are reduced to:

Continuity

$$\frac{1}{r}\frac{\partial(r\rho v_r)}{\partial r} = 0 \tag{3.25}$$

Momentum, *r*–direction

$$v_r\frac{\partial v_r}{\partial r} - \frac{{v_\theta}^2}{r} = -\frac{1}{\rho}\left(\frac{\partial p}{\partial r}\right) + f_r \tag{3.26}$$

Momentum, θ–direction

$$v_r\frac{\partial v}{\partial r} + \frac{v_r v_\theta}{r} = f_\theta \tag{3.27}$$

Momentum, *z*–direction

$$-\frac{1}{\rho}\left(\frac{\partial p}{\partial z}\right) = 0 \tag{3.28}$$

The integration of the reduced continuity Eq. (3.25) results in $r\rho V_r = \text{costant}$. Furthermore, knowing the mass flow rate inside each channel, it follows that locally:

$$v_r = -\frac{\dot{m}_c}{2\pi r b\rho} \tag{3.29}$$

Formulation of the viscous shear stress

Considering a fluid element between the two disks defining the flow channel, a control volume V_e can be defined with base surface A_e and height b. The fluid wetted area is $A_w = 2A_e$. Therefore, the hydraulic diameter D_h is equal to $2b$. Consequently,

$$A_e = \frac{Ve}{b} = \frac{2Ve}{D_h} \qquad A_w = \frac{4Ve}{D_h} \tag{3.30}$$

For laminar flow, the wall shear effect can be expressed as a function of a friction factor ζ and of the relative velocity of the flow. Eq. (3.31) displays the expression of the wall shear stress, decomposing the relative velocity in its two components.

$$\tau_w = \frac{\zeta \rho}{2} w^2 = \frac{\zeta \rho}{2} [(v_\theta - \omega r)^2 + {v_r}^2] \tag{3.31}$$

Considering $U = (U_0 / r_0) \cdot r$ and $\zeta = 24 / Re$ as usual for laminar flow between parallel plates:

$$\zeta = \frac{24\mu}{\rho W D_h} = \frac{24\mu}{\rho W D_h} = \frac{24\mu}{\rho D_h \sqrt{(v_\theta - \omega r)^2 + {v_r}^2}} \tag{3.32}$$

So that:

$$\tau_w = \frac{12\mu}{D_h} \sqrt{(v_\theta - \omega r)^2 + {v_r}^2} \tag{3.33}$$

The force resulting from wall friction force is given by the product of the wall shear with the wetted area:

$$F = \frac{12\mu Ve}{b^2} \sqrt{(v_\theta - \omega r)^2 + {v_r}^2} \tag{3.34}$$

The wall friction force has a tangential and a radial component, which influence the torque and the radial pressure gradient, respectively.

Solution of the rotor flow

Fig. 3.7 shows the local velocity triangle of the fluid element inside the rotor.

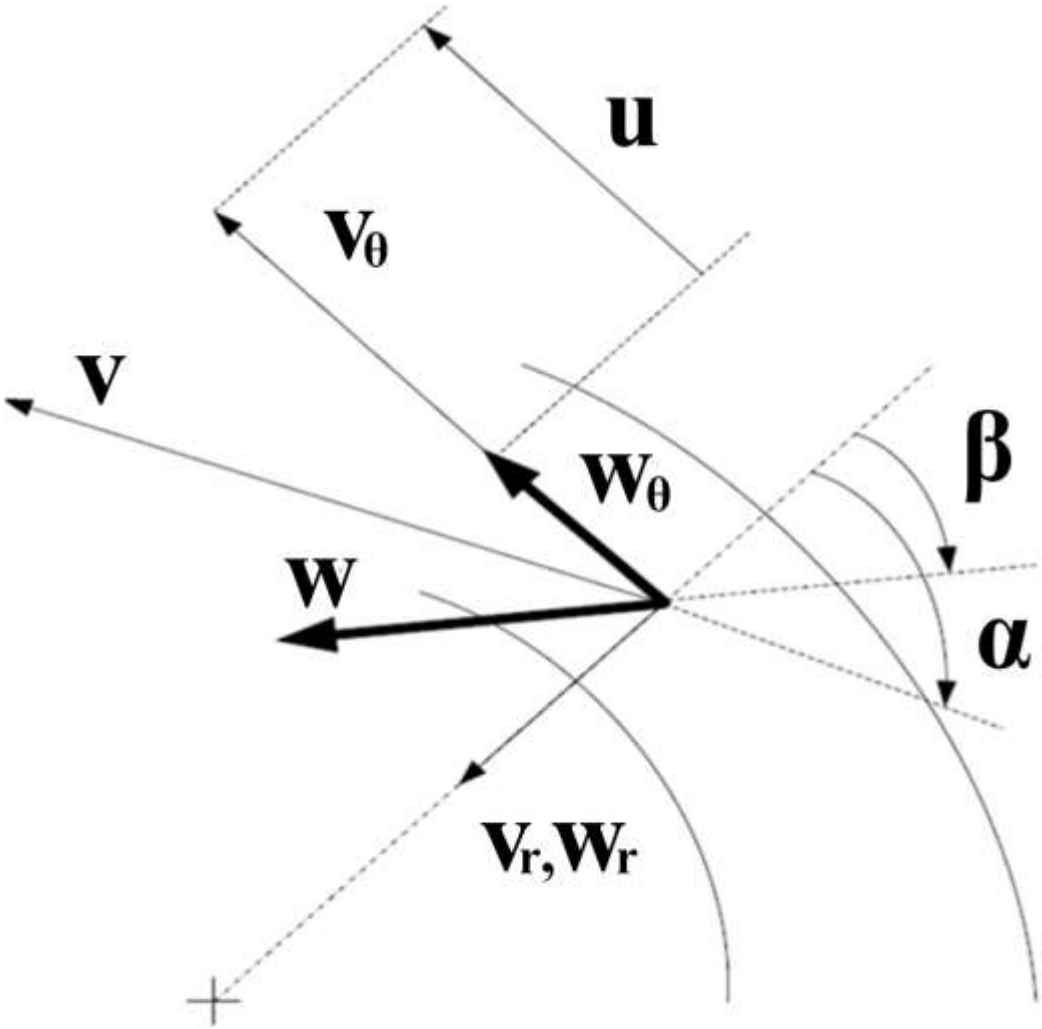

Fig. 3.7 Local velocity triangle

The radial component of the friction force is given by:

$$F_r = F\cos(\beta) \tag{3.35}$$

Where β is the angle between relative velocity and the radial direction. The value of $cos(\beta)$ can thus be calculated as:

$$\cos(\beta) = \frac{w_r}{w} = \frac{v_r}{\sqrt{(v_\theta - \omega r)^2 + {v_r}^2}} \tag{3.36}$$

Substituting Eq. (3.36) in Eq. (3.35), a compact expression of the radial force component is obtained:

$$F_r = \frac{12\mu Ve}{b^2} v_r \tag{3.37}$$

Dividing Eq. (3.37) by the mass of the fluid element between two disks, the body force term in the radial direction can be expressed as:

$$f_r = \frac{12\mu}{\rho b^2} v_r \tag{3.38}$$

Proceeding in the same way for the tangential direction, the wall friction force is given by:

$$F_\theta = -F \sin(\beta) \tag{3.39}$$

$$\sin(\beta) = \frac{w_\theta}{w} = \frac{(v_\theta - \omega r)}{\sqrt{(v_\theta - \omega r)^2 + {v_r}^2}} \tag{3.40}$$

Similarly, substituting Eq. (3.40) in Eq. (3.39), a compact expression of the tangential force is obtained:

$$F_\theta = -\frac{12\mu Ve}{b^2} (v_\theta - \omega r) \tag{3.41}$$

The body force in tangential direction is thus given by:

$$f_\theta = -\frac{3\mu}{\rho b^2} (v_\theta - \omega r) \tag{3.42}$$

In order to determine the local pressure, Eq. (3.38) is substituted in Eq. (3.26):

$$v_r \frac{\partial v_r}{\partial r} - \frac{{v_\theta}^2}{r} = -\frac{1}{\rho}\left(\frac{\partial p}{\partial r}\right) + \frac{12\mu}{\rho b^2} v_r \tag{3.43}$$

Using Eq. (3.29), the local derivative $(\partial v_r)/\partial r$ can be expressed as:

$$\frac{\partial v_r}{\partial r} = -\frac{1}{r} v_r \tag{3.44}$$

Finally, substituting Eq. (3.44) in Eq. (3.43), the pressure gradient in radial direction is given by:

$$\left(\frac{\partial p}{\partial r}\right) = -\frac{12\mu}{b^2}\left(\frac{\dot{m}_c}{2\pi r b \rho}\right) + \frac{\rho}{r}\left(\frac{\dot{m}_c}{2\pi r b \rho}\right)^2 + \frac{\rho}{r}{v_\theta}^2 \tag{3.45}$$

Likewise, in order to compute the tangential velocity, Eq. (3.42) can be substituted in Eq. (3.37):

$$v_r \frac{\partial v_\theta}{\partial r} + \frac{v_r v_\theta}{r} = -\frac{12\mu}{\rho b^2}(v_\theta - \omega r) \tag{3.46}$$

Obtaining finally:

$$\frac{\partial v_\theta}{\partial r} = \frac{24\mu\pi r(v_\theta - \omega r)}{b\dot{m}_c} - \frac{v_\theta}{r} \tag{3.47}$$

Which determines the profile of $v_\theta(r)$.

Eq. (3.47) was implemented in EES environment and numerically solved by applying a step forward method (centered finite difference): the rotor channel was discretized in radial direction with a predefined number of equal steps. Increasing the discretization steps allowed a higher accuracy prediction of the local thermodynamic variables; nonetheless, the increase of accuracy was obtained at the cost of an increased computational time. Therefore, two–hundred discretization steps were selected, as it was found as a reasonable compromise between accuracy of results and calculation time.

This equation set allows the calculation of the local values of pressure and velocity, both in absolute and relative coordinates. Finally, the rothalpy conservation Eq. (3.48) was applied to calculate the local value of static enthalpy:

$$h = I_1 - \frac{w^2}{2} + \frac{u^2}{2} \tag{3.48}$$

A further upgrade to the model, compared to [60], [93] was the assumption of variable viscosity in Eqns. (3.45, 3.47): it was locally evaluated as a flow property, as a function of temperature and pressure, using the EES fluid library data. The results obtained showed a limited reduction of the viscosity values (lower than 2%), because of the modest variation in fluid temperature. However, this upgrade allowed more accurate results at negligible additional calculation time.

The rotor model was completed by the calculation of the performance indicators like power output, total to static efficiency and the non–dimensional fluid dynamic parameters, such as load and flow coefficients.

Upgraded Rotor model

An upgraded model for the rotor flow was derived from [115]. The main difference compared to the previous model, was the assumption of viscous flow in place of the equivalent body forces along the radial and tangential directions. Adopting this new approach, the Navier–Stokes equations in cylindrical coordinates were simplified again; in this case, the body forces were assumed negligible, while the viscous terms were still present. Thus, the Navier–Stokes equations were reduced to:

Continuity equation:

$$\frac{1}{r}\frac{\partial(\rho r w_r)}{\partial r} = 0 \tag{3.49}$$

r–Momentum equation:

$$w_r\frac{\partial w_r}{\partial r} - \Omega^2 r - 2\Omega w_\theta - \frac{w_\theta^2}{r} = -\frac{1}{\rho}\frac{dp}{dr} + \nu\frac{\partial^2 w_r}{\partial^2 z} \tag{3.50}$$

θ–Momentum equation:

$$w_r\frac{\partial w_\theta}{\partial r} + \frac{w_r w_\theta}{r} + 2\Omega w_r = \nu\frac{\partial^2 w_\theta}{\partial^2 z} \tag{3.51}$$

z–Momentum equation:

$$\frac{\partial p}{\partial z} = 0 \tag{3.52}$$

The present model introduces an axial velocity profile, so that the relative velocities in *r* and *θ* directions may be expressed as:

$$w_\theta(r,z) = \bar{w}_{\theta_2}\zeta(R)G(z) \tag{3.53}$$

$$w_r(r,z) = \bar{w}_{r_2}\xi(R)H(z) \tag{3.54}$$

Where:

$$R = \frac{r}{r_2}; \qquad \zeta(R) = \frac{\bar{w}_\theta(r)}{\bar{w}_{\theta_2}}; \qquad \xi(R) = \frac{\bar{w}_r(r)}{\bar{w}_{r_2}};$$

$$G(z) = \frac{w_\theta(r,z)}{\bar{w}_\theta(r)}; \qquad H(z) = \frac{w_r(r,z)}{\bar{w}_r(r)}$$

G(z) and *H(z)* are the variations of tangential and radial velocities respectively along *z* direction within the boundary layers.

Following the procedure outlined in [115], it was initially assumed that the velocity profile of the fully developed flow was laminar, thus parabolic. Accordingly, *G(z)* and *H(z)* could be expressed as:

$$G(z) = H(z) = 6\frac{z}{b}\left(1 - \frac{z}{b}\right) \tag{3.55}$$

and:

$$w_r(r,z) = \bar{w}_r \cdot 6\frac{z}{b}\left(1 - \frac{z}{b}\right) \tag{3.56}$$

$$w_\theta(r,z) = \bar{w}_\theta \cdot 6\frac{z}{b}\left(1 - \frac{z}{b}\right) \tag{3.57}$$

Integrating the differential form of the *θ*–momentum and *r*–momentum equations between *z=0* and *z=b/*2, and applying the boundary conditions reported in [115], which assumed maximum velocity value at mid channel and zero velocity at the walls, it was possible to calculate the gradient of relative tangential velocity and static pressure in radial direction.

$$\frac{\partial w_\theta}{\partial r} = -\frac{5}{3}\Omega - \left(\frac{10\nu}{w_r b^2} + \frac{1}{r}\right) \cdot w_\theta \tag{3.58}$$

$$\frac{1}{\rho}\frac{dp}{dr} = -w_r\frac{\partial w_r}{\partial r} \cdot \frac{6}{5} + \Omega^2 r + 2\Omega w_\theta + \frac{w_\theta^2}{r} \cdot \frac{6}{5} - \nu w_r \cdot \frac{12}{b^2} \tag{3.59}$$

These equations were also implemented in EES environment and numerically solved by applying a step forward method (second–order centered finite difference).

In order to generalize the mathematical model of the flow, a coefficient for the parabolic velocity profile was defined, still under the assumption of laminar flow condition. Accordingly, *G(z)* and *H(z)* can be expressed as:

$$G(z) = H(z) = a\frac{z}{b}\left(1 - \frac{z}{b}\right) = a\frac{z}{b} - a\left(\frac{z}{b}\right)^2 \tag{3.60}$$

Where the coefficient "*a*" is set to 6 in [115].

Following the above calculation steps, the reduced θ and *r* momentum equations were achieved and implemented into the developed EES calculation code, in the same way as the previous case:

$$\frac{\partial w_\theta}{\partial r} = -\frac{10}{a}\Omega - \left(\frac{60\nu}{w_r a b^2} + \frac{1}{r}\right) \cdot w_\theta \tag{3.61}$$

$$\frac{1}{\rho}\frac{dp}{dr} = -w_r\frac{\partial w_r}{\partial r} \cdot \frac{a^2}{30} + \Omega^2 r + 2\Omega w_\theta \frac{a}{6} + \frac{w_\theta^2}{r} \cdot \frac{a^2}{30} - \nu w_r \cdot \frac{2a}{b^2} \tag{3.62}$$

In order to further generalize the mathematical model of the flow, a general law for the definition of the velocity profile for turbulent flows was introduced. The required constraints were the zero and maximum velocity at the walls and at mid channel height, respectively.

The turbulent flow velocity profile law is suggested in [190]; accordingly, the applied power law distribution was adopted for the definition of *G(z)* and *H(z)*:

$$G(z) = H(z) = \left(1 - \frac{z}{\frac{b}{2}}\right)^{\frac{1}{n}} \cdot \frac{(n+1)\cdot(2n+1)}{2n^2} \tag{3.63}$$

Following the previous calculation process, with the only difference in the integration of velocity distribution functions, it was possible to calculate the gradient of relative tangential velocity and static pressure in radial direction and to integrate them in the EES calculation code with a step forward method:

$$\frac{\partial w_\theta}{\partial r} = -4\Omega \cdot \frac{(n+2)\cdot n^2}{(n+1)^2(2n+1)} - \left(-\frac{\nu}{w_r} \cdot \frac{4(2n+4)n^2}{n^2 b^2 (n+1)(2n+1)} + \frac{1}{r}\right) w_\theta \tag{3.64}$$

$$\frac{1}{\rho}\frac{dp}{dr} = -w_r\frac{\partial w_r}{\partial r}\cdot\frac{n}{n+2}\cdot\frac{(n+1)^2*(2n+1)^2}{4n^4} + \Omega^2 r + 2\Omega w_\theta\frac{n}{n+1} \cdot\frac{(n+1)*(2n+1)}{2n^2} + \frac{w_\theta^2}{r}\cdot\frac{n}{n+2}\cdot\frac{(n+1)^2\cdot(2n+1)^2}{4n^4} + \nu w_r\cdot\frac{4}{nb^2}\cdot\frac{(n+1)\cdot(2n+1)}{2n^2} \quad (3.65)$$

For fully developed turbulent flow, *n=7* is the most used in literature. For this reason, the law is also called the *one–seventh power law velocity profile*.

Furthermore, for laminar flow profiles, reference [190] suggests the following expression for the functions *G(z)* and *H(z)*:

$$G(z) = H(z) = 2\cdot\left(1-\left(\frac{z}{\frac{b}{2}}\right)^2\right) \quad (3.66)$$

Which, after the required passages of integration and derivation, corresponds to the generalized parabolic formula when the coefficient "*a*" is equal to 8.

The last upgrade of the here proposed turbulent rotor model was the estimation of the right power law exponent: as reported in [190], for turbulent flows (generally Reynolds $>10^4$) it can be determined as a function of the Reynolds number. Rotor Reynolds number is calculated as: $Re = \frac{(w\cdot 2b)}{\nu}$ at each discretization step. In this way, a logarithmic law for n was implemented:

$$n = 0.7823\ln(Re) - 2.0013 \quad (3.67)$$

When the Reynolds number is lower than 2000, the laminar expression derived from [115] was adopted.

When the Reynolds number is between 2000 and 10^4, corresponding to a transitional flow regime, a parabolic distribution with lower value of coefficient "*a*" can be used rather than a power low equation, with the exponent *n* obtained from an approximate exponential law.

In Eq. 3.60, the coefficient "*a*" was introduced in the parabolic velocity profile in order to generalize the model. This coefficient is suggested to be set to 6 in [111], [115]. A more accurate match with CFD results was achieved for the fully developed region with "*a*" equal to 8, as suggested by [190].

Fig. 3.8 shows the effects of the "*a*" coefficient on the velocity profiles: high values of "*a*" determine pronounced parabolic distributions, typical of fully developed laminar flows, while low values are related to transitional and not fully developed laminar flows, characteristic of the entry region. In order to calculate the length of the entry region, Eq. 3.68 was applied [93].

$$S_e = \frac{b}{50}\left(\frac{b\rho v}{\mu}\right) \tag{3.68}$$

It was found with a comparison with CFD analysis that in the entry region the correct value of the "*a*" coefficient is around 4, as there, the flow is not fully developed. This has been confirmed in all analyses conducted, for all fluids (R404a, R134a, R245fa, R1233zd(E)) at various rotational speeds (1500, 3000, 4500) and total inlet temperatures (60, 80, 120, 140°C) at a total pressure inlet of 1.16. Nonetheless, in order to be certain that the "*a*" coefficient hold the proposed value, an extensive experimental campaign, involving visual measurements of the flow field inside a Tesla turbine would be required; however, in literature there are no available researches on this topic.

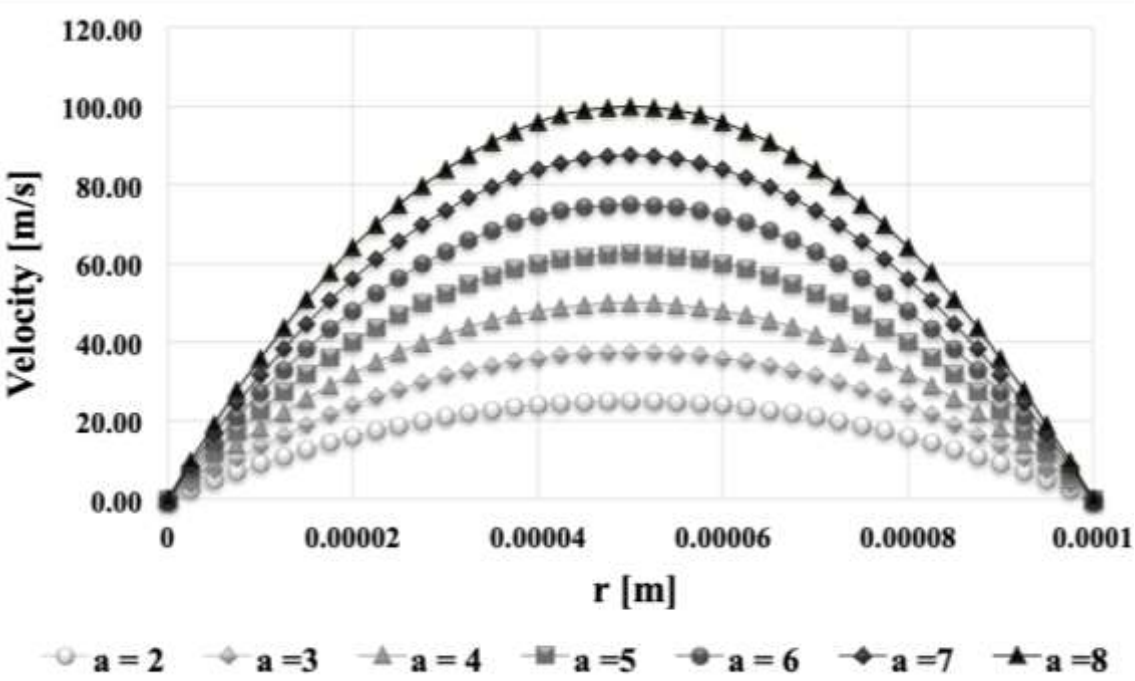

Fig. 3.8 Velocity distribution inside the channel for different values of the "*a*" coefficient

The infinitesimal length of the fluid trajectory can be assessed through (3.69).

$$ds = \sqrt{d\theta^2 + dr^2} \tag{3.69}$$

Where $d\theta = w_\theta \, dt$ is tangential component and $dr = w_r \, dt$ is the radial component, as shown in Fig. 3.9.

When $\sum_{i=0}^{NR} ds_i$ is lower than the entrance region length, the coefficient for not fully developed flow is used; when $\sum_{i=0}^{NR} ds_i$ is higher than the entrance region length, the laminar flow coefficient is adopted.

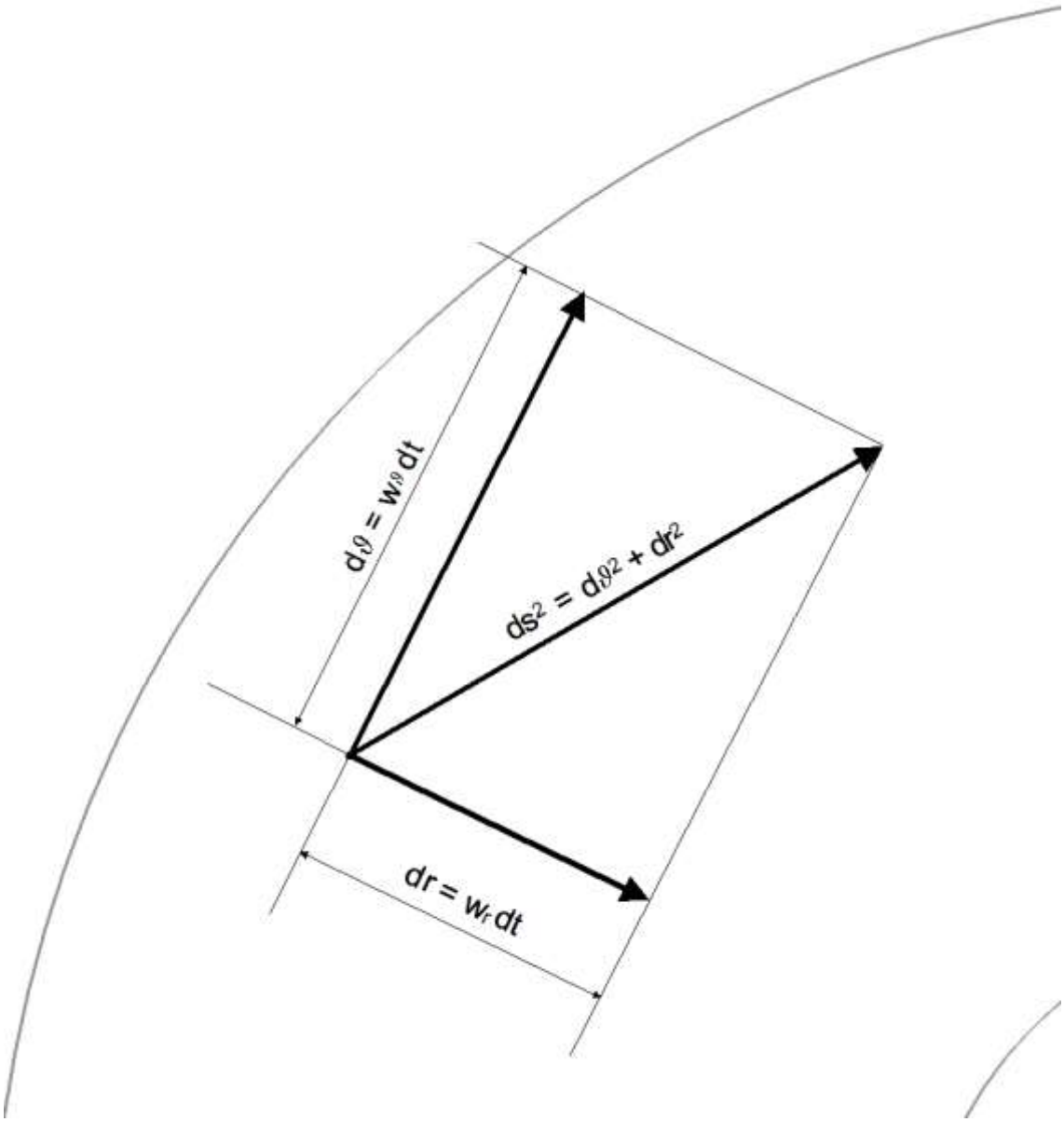

Fig. 3.9 Infinitesimal trajectory

Disk profiling

Another feature of the developed in–house code is the possibility of simulate disk profiling. Disk profiling refers to the potentiality of sharpen the outer section of the disk, in order to reduce the abrupt contraction losses.

An exponential law (3.70) has been implemented in order to simulate this feature. Another possibility in order to simulate disk profiling is to define a priori the profile of the disk and store it in lookup tables, which will be used as input in the procedure.

$$b_i = b_{min} + (b_{max} - b_{min}) * \left(\frac{r_i - r_{min}}{r_{man} - r_{min}}\right)^{ex} \tag{3.70}$$

The percentage of the disk, which will be sharpened, can be imposed in the code. After the sharpening of the edge, the disk maintains a constant profile.

Rotor Streamlines

In order to determine the trajectory of the flow inside the rotor, the velocity components in differential form must be considered:

$$r\, d\theta = v_\theta dt \tag{3.71}$$

$$dr = v_r dt \tag{3.72}$$

The combination of Eqns. (3.71) and (3.72) implies that:

$$\left(\frac{d\theta}{dr}\right) = \frac{v_\theta}{v_r \cdot r} \tag{3.73}$$

For the relative trajectory, following the same procedure, it can be found that:

$$\left(\frac{d\gamma}{dr}\right) = \frac{w_\theta}{w_r \cdot r} \tag{3.74}$$

The determination of the absolute and relative streamlines is of paramount importance, not only because it allows the visualization of the flow trajectory, but also because it is a way to assess the "filling" of the rotor channel (absolute streamlines in Fig. 3.10a) and to verify the eventual flow reversal (relative path lines in Fig. 3.10b). Specifically, the reverse flow condition occurs when the absolute tangential velocity is lower than the rotor peripheral velocity, resulting into a negative relative tangential velocity, as it is noticed on the red relative streamline in Fig. 3.10b.

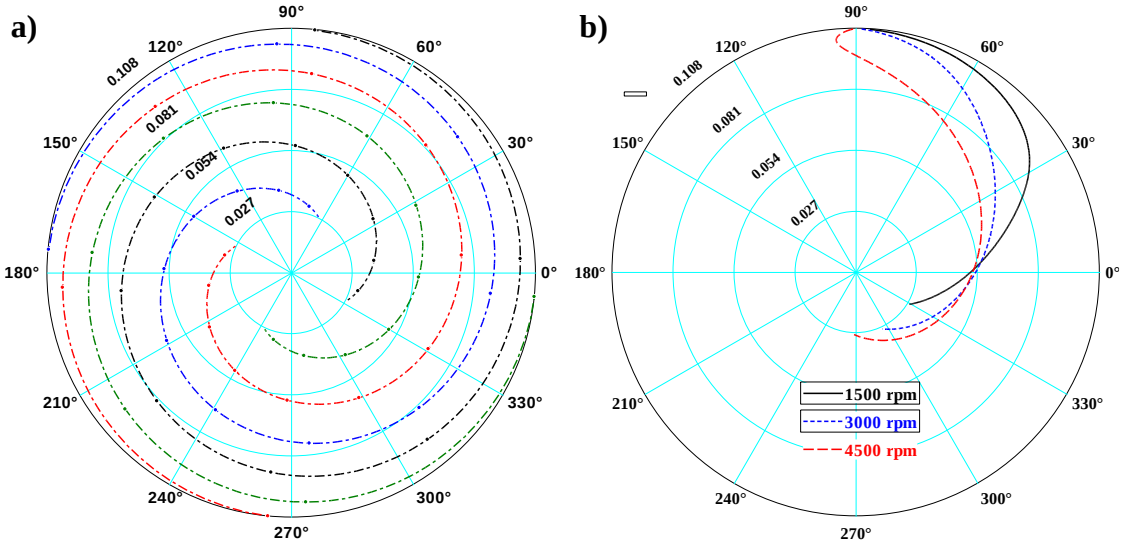

Fig. 3.10 Absolute and relative rotor streamlines with R404a working fluid: (a) Absolute at 1500 rpm, 4 nozzles; (b) Relative streamlines at various rpm

Non adiabatic model

Initially, Eq. (3.48) (rothalpy conservation) was applied in order to calculate static enthalpy at each discretization step. Indeed, in steady state operation, Tesla turbine can be considered as an adiabatic expander; however, for transient, and especially at start up condition, the turbine rotor cannot be considered as adiabatic. Therefore, Eq. (3.48) has been modified to Eq. (3.75).

$$I_2 = I_1 + \frac{\dot{Q}}{\dot{m}} \tag{3.75}$$

The heat transfer model in order to determine the heat exchanged between the disks and the fluid assumes a constant temperature of the disks. This assumption is reasonable, if one takes into account that the velocity at which the heat conduction takes place is extremely faster compared to the convection "velocity".

In order to determine the convection heat transfer coefficient, the correlations present in [191] for the internal laminar flows of rectangular shaped pipes were applied. Furthermore, the model, as for the viscous case, takes into account the thermal entry region. In this region, the Nusselt number, conversely to the fully developed laminar flow, is not constant, but it is a function of Reynolds and Prandtl numbers. The complete set of equation is therefore resumed in Eqns. (3.76) – (3.80).

$$\mathrm{Nu} = 2.98 \text{ for fully developed laminar flow} \tag{3.76}$$

$$\mathrm{Nu} = 2.98 + \frac{\left(0.065 * \mathrm{Re} \cdot \mathrm{Pr} \cdot \frac{\mathrm{Dh}}{\mathrm{L_t}}\right)}{1 + 0.04 * \left(\mathrm{Re} \cdot \mathrm{Pr} \cdot \frac{\mathrm{Dh}}{\mathrm{L_t}}\right)^{\frac{2}{3}}} \text{ for entry region} \tag{3.77}$$

$$\mathrm{h_i} = \frac{\mathrm{Nu} * \mathrm{k}}{\mathrm{D_h}} \tag{3.78}$$

$$\mathrm{dA} = \pi(\mathrm{r_{i-1}^2} - \mathrm{r_i^2}) \tag{3.79}$$

$$\mathrm{dQ} = \mathrm{h_i} * \mathrm{dA} * (\mathrm{T_i} - \mathrm{T_{disk}}) \tag{3.80}$$

For steady state flow, an iterative procedure has been implemented, which impose the temperature of the wall as the area weighted mean temperature of the fluid through the rotor.

$$\mathrm{T_{mean}} = \frac{\sum_{i=0}^{NR} \mathrm{T_i} * \mathrm{dA}}{\sum_{i=0}^{NR} \mathrm{dA}} \tag{3.81}$$

3.1.5 Diffuser

At the rotor outlet, the fluid trajectory is curved and the velocity mainly assumes an axial direction, while a considerable amount of the kinetic energy is lost. The presence of a diffuser can partially recover this energy through a gradual section enlargement, which is able to decrease the fluid velocity, thus converting a fraction of the kinetic energy into pressure. The typical solution is the installation of a conical diffuser at the turbine outlet. The design concerns the choice of the outlet diameter, the length and the diffusion angle; the latter is particularly important to reduce the pressure losses related to the wall separation of the fluid.

The model provides the calculation of the axial velocity at diffuser inlet through the continuity equation, while the tangential and radial components are conserved from the rotor to the diffuser output. Here, the continuity equation ensures the reduction of axial velocity due to the increased cross–section, while the radial and tangential components were calculated by assuming the conservation of their angle with the axial velocity. These velocity components are responsible for a 3D swirled flow.

Inside the diffuser, the total enthalpy is conserved, while the total pressure is reduced due to the wall friction inside the diffuser:

$$\mathrm{p_{05}} = \mathrm{p_{04}} - \zeta_{\mathrm{diff}} \frac{1}{2} \rho_4 \mathrm{v_4^2} \tag{3.82}$$

This equation is similar to the one used for the abrupt enlargement, but the loss coefficient ζ_{diff} was obtained through a polynomial fitting of experimental data available in [189] as a function of the diffuser in/out area ratio and the diffusion angle.

$$\zeta_{diff} = (1 - \frac{A_{in}}{A_{out}})^2 \tag{3.83}$$

A further step was the assumption of swirled flow: in [192], a large number of diffusers were analysed and tested to evaluate the influence of vorticity on the performance, concluding that swirled flow could increase the diffuser efficiency. Therefore, an incremental coefficient, which depends on the inlet/outlet area ratio of the diffuser, on the swirl ratio (i.e. the ratio between tangential and axial velocity), and on the diffuser angle, can be applied to the efficiency, defined as:

$$\eta_{diff} = \frac{p_5 - p_4}{\frac{1}{2}\rho_4 v_4^2} \cdot \zeta_{swirl} \tag{3.84}$$

The pressure recovery and the outlet static pressure are increased due to the swirled flow.

Therefore, when the velocity, total pressure and total enthalpy are known, it is possible to completely define the fluid state at inlet and outlet of the diffuser.

3.1.6 Performance indicators

In order to assess the performance potential of a Tesla turbine, the right design parameters need to be defined. Non–dimensional parameters were selected, following common practice in turbomachinery [187], [188]. Therefore, the flow and load coefficient can be expressed as:

$$\phi = \frac{v_{r1}}{U_1} \tag{3.85}$$

$$\psi = \frac{work}{U_2^2} = \frac{V_{\theta 2} U_2 - V_{\theta 3} U_3}{U_2^2} \tag{3.86}$$

The specific speed and the non–dimensional specific diameter are given by:

$$N_s = rpm * \frac{\left(\frac{\dot{m}}{\rho_2}\right)^{0.5}}{\left((h_2 - h_3) + \frac{v_2^2}{2}\right)^{0.75}} \tag{3.87}$$

$$D_s = D_2 \cdot \frac{\left(\frac{(h_2 - h_3) + \frac{v_2^2}{2}}{g}\right)^{0.25}}{\left(\frac{\dot{m}_c}{\rho_2}\right)^{0.5}} \tag{3.88}$$

The total to static efficiency of the turbine is defined as:

$$\eta = \frac{work}{\Delta h_{0s}} = \frac{V_{\theta 2} U_2 - V_{\theta 3} U_3}{(h_{00} - h_{3ss})} \tag{3.89}$$

Moreover, critical design parameters for the Tesla turbine were identified in the geometrical ratios (D_3/D_2) and (b/D_2); for output conditions the exit kinetic energy and the absolute flow angle, which should be as low as possible, were identified as critical performance indicators. The exit kinetic energy is presented in non–dimensional form as:

$$\xi_3 = \frac{E_{kin,3}}{\Delta h_{0s}} = \frac{\frac{v_3^2}{2}}{(h_2 - h_3) + \frac{v_3^2}{2}} \tag{3.90}$$

And the exit fluid angle can be calculated as:

$$\alpha = \tan^{-1}\left(\frac{V_{\theta 3}}{V_{r3}}\right) \tag{3.91}$$

3.2 Mechanical Design

3.2.1 Static analysis

Plenum chamber

The thickness of the plenum chamber is calculated assuming it as a cylinder and applying therefore the theory of thin pressure vessels, assuming that the thickness is significantly less than the diameter. Eq. (3.92) allows obtaining the minimum thickness that the plenum chamber has to have; provided that the inner radius, the operating pressure and the permissible load are fixed.

$$t_{min} = \frac{P_{amm} \cdot r_{int}}{\sigma_{amm}} \tag{3.92}$$

Rotor disks

In order to verify the mechanical resistance of the rotor disks, rotating disks theory was employed, considering that centrifugal, thermal and pressure forces act on them. These forces act both radially and tangentially; however, since the maximum stresses develop within the internal radius, the former are zero, while the latter are maximum. In addition to the geometrical and thermo–fluid dynamic parameters of the machine, it is necessary to know the main characteristics of the material, in this case aluminium; these are resumed in Tab. 3.1.

Table 3.1 Aluminium properties (at 20°C)

Density [kg/m^3]	Poisson ratio	Young module [GPa]	Thermal expansion coefficient [°C^{-1}]	Yield tension [MPa]
2700	0.33	70	0.0000234	180

The equations provided by rotating disk theory for the calculation of the tangential forces are reported. For the stresses due to inertial effects, or centrifugal force, Eq. (3.93) is applied [193].

$$\sigma_c = \frac{3+\nu}{8}\rho\omega^2\left(r_2^2 + r_3^2 - \frac{r_2^2 r_3^2}{r^2} - \frac{1+3\nu}{3+\nu}r^2\right) \tag{3.93}$$

For stresses related to the thermal gradient along the disk Eq. (3.94) is employed [193].

$$\sigma_c = \frac{E\alpha}{3}\frac{T_2 - T_3}{r_2^3 - r_3^2}\left(r_2^2 + r_3^2 + r_2 r_3 + \frac{r_2^2 r_3^2}{r^2} - 2r\,(r_2 + r_3)\right) \quad (3.94)$$

For stresses linked to boundary conditions, i.e. pressure inside and outside the disk, Eq. (3.95) is used [193].

$$\sigma_c = -\frac{p_2 r_2^2}{r_2^2 - r_3^2}\left(\frac{r_3^2}{r^2} + 1\right) \quad (3.95)$$

These formulas do not take into account a safety coefficient, so values of temperature and pressure higher than the possible achievable conditions during tests have been considered, both for the air (10 bar and 150°C) and the ORC (25 bar and 200°C) prototypes.

Power shaft

The power transmission shaft has to be dimensioned in order to withstand the torsional forces; the shaft is therefore schematised as a solid cylinder subjected to torque. The torque defined by the ratio between power and rotation speed, as shown in Eq. (3.96).

$$T = \frac{\text{Power}}{\omega} \quad (3.96)$$

The shear stress acting on the shaft is given by Eq. (3.97) [193].

$$\tau = \frac{16 \cdot T}{\pi \cdot D^3} \quad (3.97)$$

This value (further multiplied by a safety coefficient) has to be lower than the maximum allowable tangential stress, which, according to the Tresca criterion, is obtained from the yield strength as reported in Eq. (3.98) [193].

$$\tau_{sn} = \frac{1}{2}\sigma_{sn} \quad (3.98)$$

Shaft screws

A further mechanical sizing concerns the screws connecting the shaft to the outer plate, which in turn is connected by threaded cylinders to the disks; these screws are passing through the disk and are captive on the shaft, therefore they are loaded by compression as most of the screws used for these purposes. However, unexpected shaft tightening

could lead to the severing of the screws; to avoid this risk, their sizing is done following shear theory and particularly the theory of bolted unions.

The tangential stress associated with the torque is calculated through Eq. (3.99).

$$\tau = \frac{F_b}{n_b \cdot n_{pt} \cdot A_b} \tag{3.99}$$

Where F_b is the exchanged force, n_b the number of bolts, n_{pt} the number of cutting planes and A_b the resistant area of the screw.

This tension (again multiplied by a safety coefficient) has to be lower than the tangential stress leading to yield, calculated through Tresca criterion.

Plenum chamber screws

The external case was sized to withstand the pressure inside it, but the number and size of the screws needed to keep it close still have to be defined. The screws can be dimensioned for static failure or for separation, and this last condition being more stringent than the first one is preferred for the selection of the screws.

The dimensioning of a threaded connection is obtained through Eq. (3.100).

$$A_t = n_s \cdot \frac{1 - C}{K} \cdot \frac{F}{\sigma_p} \tag{3.100}$$

The left term indicates the overall section of the bolts; while in the right term there are the force (F) acting on the screws, the admissible load (σ_p) and the coefficients K and C. The force is calculated by multiplying the internal pressure by the section of the box, while the admissible load is known from the type by the class of screws used (usually 8.8) and by the safety coefficient (1.25). The standards [193] suggest to assume a coefficient K=0.75, while the coefficient C is calculated through Eq. (3.101).

$$C = \frac{E_b}{8\,E_e + E_b} \tag{3.101}$$

Where E_b=E_e represents Young's modulus of steel, so C=1/9.

3.2.2 Dynamic analysis

As thermodynamic conditions, as well as the maximum rotational speed of the air Tesla turbine during tests condition were not planned to reach critical conditions, dynamic analysis has been carried out only for the ORC Tesla prototype.

Simplified Rotor Geometry

In order to reduce the computational cost of the simulations, a simplified rotor geometry has been considered. Particularly, the simplified geometry has been built with the same dimension of the disks (outer diameter of 0.216 m, inner diameter of 0.055 m) and shafts of the real prototype, but with a reduced number of disks (from 60 to 11), as shown in Fig. 3.11. The real geometry of the prototype will be throughout discussed in Section 3.3.2.

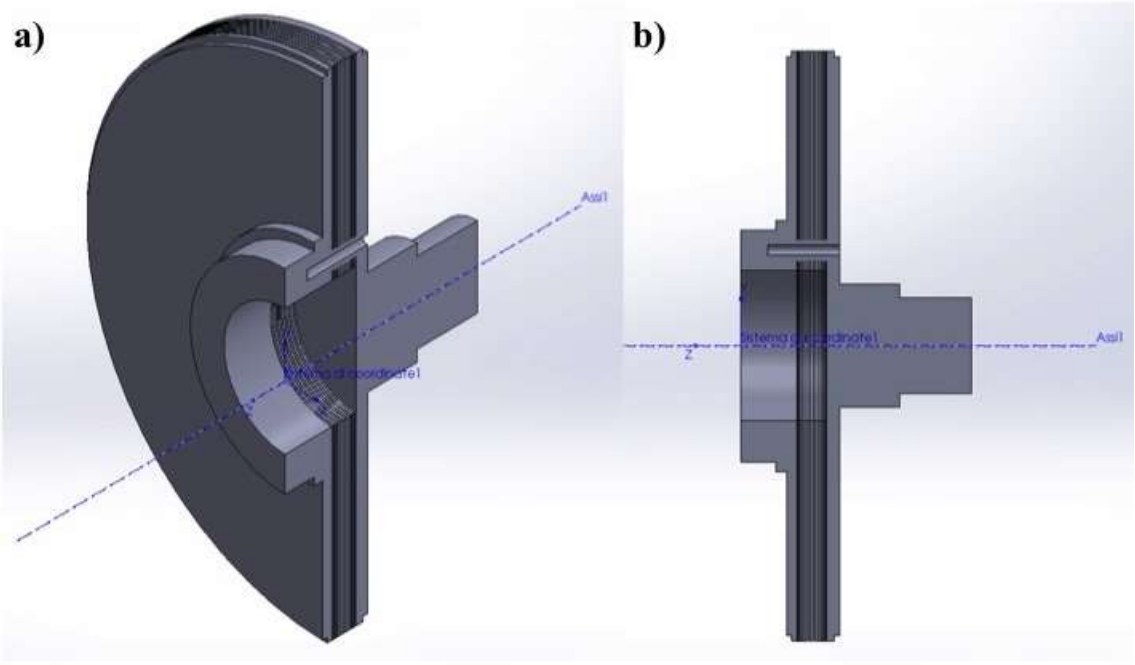

Fig. 3.11 Simplified Tesla rotor geometry

Calculation model in SolidWorks Software – Ideal Bearings Hypothesis

The calculation of the simplified rotor geometry was performed using SolidWorks Simulation frequency analysis tool. The main mesh and solver parameters are shown in Tab. 3.2 and Fig. 3.12. Several meshes were created, with the objective of investigating the effects of elements size on the obtained results. In order to attain a proper compromise between accuracy and computational time, the 228,738 nodes mesh was finally selected.

A material selection process for the prototype was carried out. Stresses on rotating disks were evaluated through the application of Eqns. (3.93) – (3.95). An aluminium alloy

(7075) was finally selected. This was mainly due to the lower weight compared to iron cast alloys.

Table 3.2 Settings used for Software calculations

Solver Settings	Direct Sparse Solver + Soft Spring stabilization
Mesh parameters	Solid Mesh – Parabolic tetrahedral solid elements
Number of elements	115663
Number of Nodes	228738
Mass Properties	
Model Mass [kg]	0.77
Moment of inertia Ixx [kg*mm^2]	2134
Moment of inertia Iyy [kg*mm^2]	2134
Moment of inertia Izz [kg*mm^2]	4035

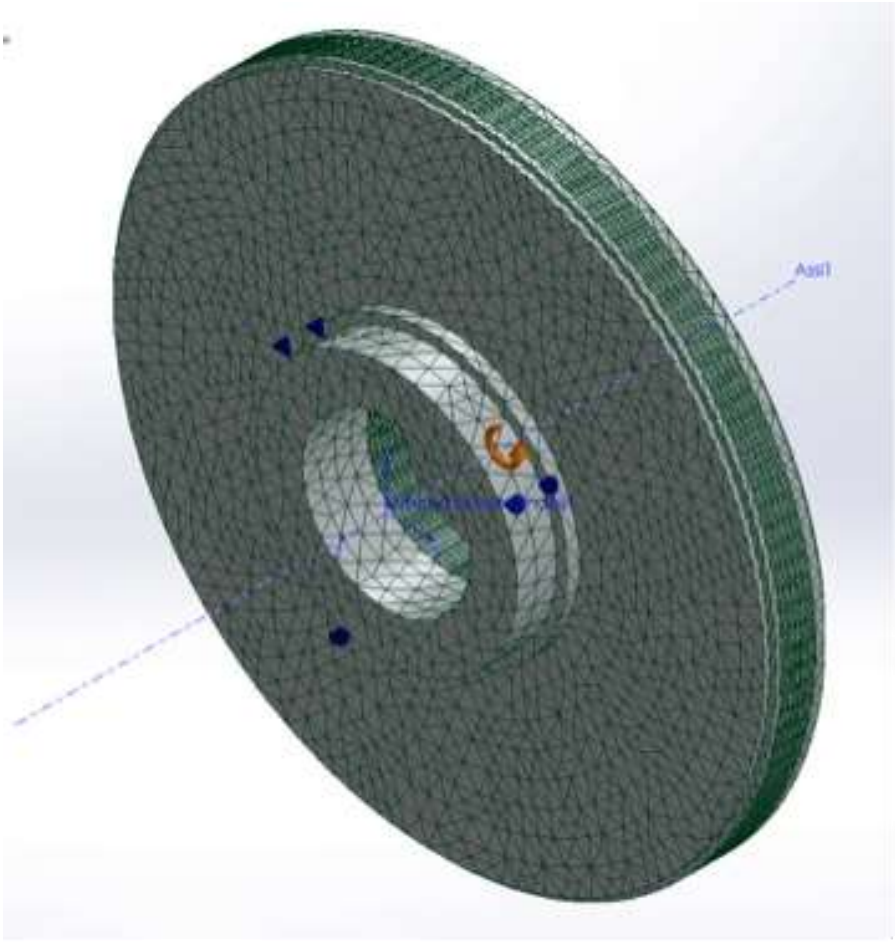

Fig. 3.12 Mesh distribution of simulated simplified rotor geometry

Fig. 3.13 displays the resulting total amplitude for the first mode. Particularly, Fig. 3.13 a–c is obtained for 3 different velocities of the expander (3000, 4500 and 6000 rpm). As it can be noted, if the first mode frequency is reached, the total deformation of one of the central disposed disk (different for each rotational speed) would be too high and therefore it would break. The positive trait is that the resonance frequency rises with rotational speed; therefore, for the assumed test conditions the resonance frequency is not reached. (The issues arise for rotor velocities values between 12000 and 15000 rpm.)

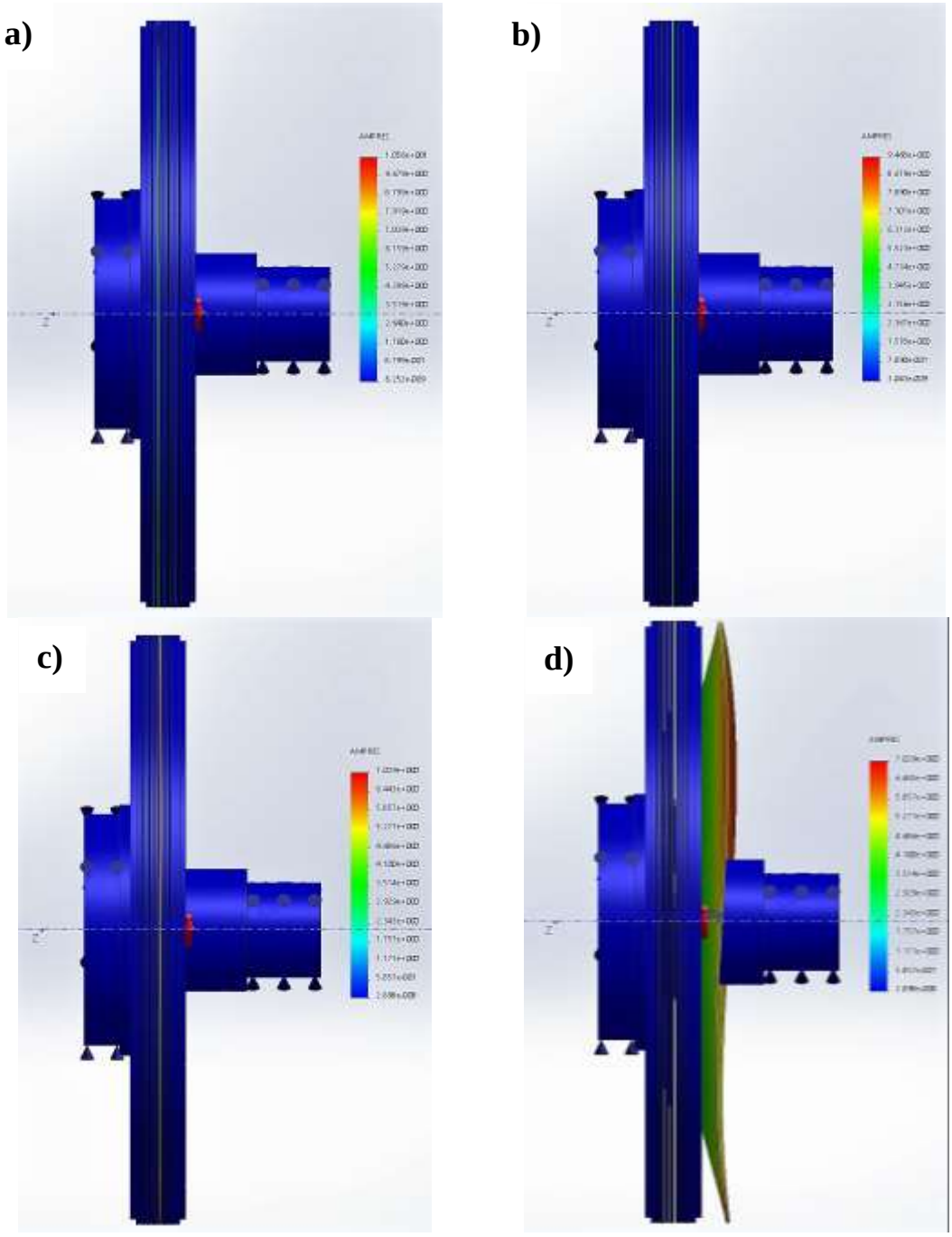

Fig. 3.13 Total Amplitude for ideal bearing stiffness; a) 3000 rpm; b) 4500 rpm; c) 6000 rpm; d) twisted result of first mode at 6000 rpm

Ball bearing stiffness model

The radial deep groove ball bearing stiffness was determined through the application of the model presented in [194], which was developed in [195].

$$k_r = 0.0325E06 \cdot \sqrt[3]{D \cdot F \cdot Z^2 \cdot (\cos\alpha)^5} \tag{3.102}$$

Where:

- k_r is the Radial Stiffness in [N/m];
- F is the external radial force in [N];
- D is the ball diameter in [m];
- Z is the number of rolling elements;
- α is the contact angle in [rad].

On the other hand, the double row angular ball bearing stiffness was determined on the basis of the model developed by Guay P. and Frikham A. [195].

The model is based on the calculation of the ball stiffness, which is built on Hertz theory [196]. Therefore, the developed model starts from the preliminary calculation on curvature to finally obtain the ball stiffness.

Particularly, the curvature parameters required are shown in Tab. 3.3.

Table 3.3 Curvature parameters

Parameter	Symbol/Equation
Ball Diameter	D
Raceway groove curvature radius	r
Raceway conformity	$f = \frac{r}{D}$
Contact angle	α
Pitch Diameter	d_m
Dimensionless parameter γ	$\gamma = \frac{D \cdot \cos\alpha}{d_m}$
Equivalent curvature radius	
Inner raceway	Outer raceway
$R_{xi} = (1-\gamma) \cdot \frac{D}{2}$	$R_{xe} = (1+\gamma) \cdot \frac{D}{2}$
$R_{yi} = \frac{f_i \cdot D}{(2f_i - 1)}$	$R_{ye} = \frac{f_e \cdot D}{(2f_e - 1)}$

Applying Hamrock and Anderson model [197], [198] for a simplified solution of the ellipse elongation, it is possible to calculate all the parameters required for the ball

stiffness calculations. Eqns (3.103) to (3.105) are used for calculating ellipse elongation, elliptic integral of the first and second kind, respectively.

$$\kappa = 1.18 \cdot \rho^{0.598} - 0.19 \tag{3.103}$$

$$F(\kappa) = \frac{\pi}{2} + q \cdot (1 + \ln(\rho)) \tag{3.104}$$

$$S(\kappa) = 1 + \frac{q}{\rho} \tag{3.105}$$

Finally, the stiffness of ball/raceway contact, as well as the ball stiffness, can be found respectively from Eq. (3.106) and Eq. (3.107).

$$K = \frac{\pi}{3} \cdot \kappa \cdot E. \sqrt{\frac{2Sr}{F^3}} \tag{3.106}$$

$$K_n = \left(\frac{1}{K_i^{\frac{2}{3}}} + \frac{1}{K_e^{\frac{2}{3}}} \right)^{-\frac{3}{2}} \tag{3.107}$$

Where *e* and *i* suffixes are used for external and internal raceways.

Axial and radial stiffness can thus be computed applying Eq. (3.108) and Eq. (3.109), with the assumption of constant contact angle. The assumption of constant contact angle is justified for contact angles higher than 25° [195].

$$k_a = \frac{3}{2} \cdot Z \cdot K_n \cdot (\sin \alpha)^{\frac{5}{2}} \cdot \left(\frac{e}{2}\right)^{\frac{1}{2}} \tag{3.108}$$

$$k_r = \frac{3}{2\sqrt{2}} \cdot Z \cdot K_n \cdot (\cos \alpha)^{\frac{5}{2}} \cdot (e \cdot \tan \alpha)^{\frac{1}{2}} \tag{3.109}$$

For paired bearing the axial stiffness is worth twice the single bearing axial stiffness, therefore Eq. (3.108) should be multiplied by 2.

Tab. 3.4 resumes the main characteristics, while Tabs. 3.5 and 3.6 display the values of radial and axial stiffness for the Tesla prototype bearings. In Tab. 3.4, the preload of the bearing has been calculated as suggested in [199]; that is taking the minimum load on ball bearing as *0.01C*, where *C* is the basic dynamic load rating. In Tab. 3.6, very low

preload value, of 50 N, has been considered in order to evaluate the effect of preload on modes frequencies.

Table 3.4 Bearings main parameters [200]–[201]

Deep groove ball bearing	SKF 61817–2RZ
Pitch diameter dm	97.5
Ball diameter D	7.14
Number of rolling elements Z	24
Double row angular contact ball bearing	SKF 3207 A–2ZTN9/MT33
Pitch diameter dm [mm]	53.5
Ball diameter D [mm]	11.11
Contact angle [°]	30
Number of rolling elements Z	18

Table 3.5 Bearings stiffness for ORC Tesla prototype; preload = 0.01C

Deep groove ball bearing	SKF 61817–2RZ
Axial Stiffness k_a [N/m]	–
Radial Stiffness k_r [N/m]	2.36E+08
Double row angular contact ball bearing	SKF 3207 A–2ZTN9/MT33
Axial Stiffness k_a [N/m]	3.62E+08
Radial Stiffness k_r [N/m]	5.44E+08

Table 3.6 Bearings stiffness for ORC Tesla prototype; preload = 50 N

Deep groove ball bearing	SKF 61817–2RZ
Axial Stiffness k_a [N/m]	–
Radial Stiffness k_r [N/m]	6.95E+07
Double row angular contact ball bearing	SKF 3207 A–2ZTN9/MT33
Axial Stiffness k_a [N/m]	8.41E+07
Radial Stiffness k_r [N/m]	1.26E+08

Calculation model in SolidWorks Software –Bearings with Real Stiffness

Same settings as the ones used for ideal bearing stiffness calculations were used also for the case with real bearing stiffness. Figs. 3.14 and 3.15 display the resulting total amplitude for the first mode, when real bearing stiffness is applied (Fig. 3.14 with *P = 0.01 C* and Fig. 3.15 with *P = 50 N*). Particularly Figs. 3.14 and 3.15 are the analogue of

Fig. 3.13. As can be noted from the comparison of Figs. 3.13, 3.14 and 3.15, the effect of real bearing stiffness model slightly influences the resonance frequency as well as the shape of deformations. The only significant change is that more disks display high deformation, even if with a lower amplitude. The preload value slightly affects the modes frequency values.

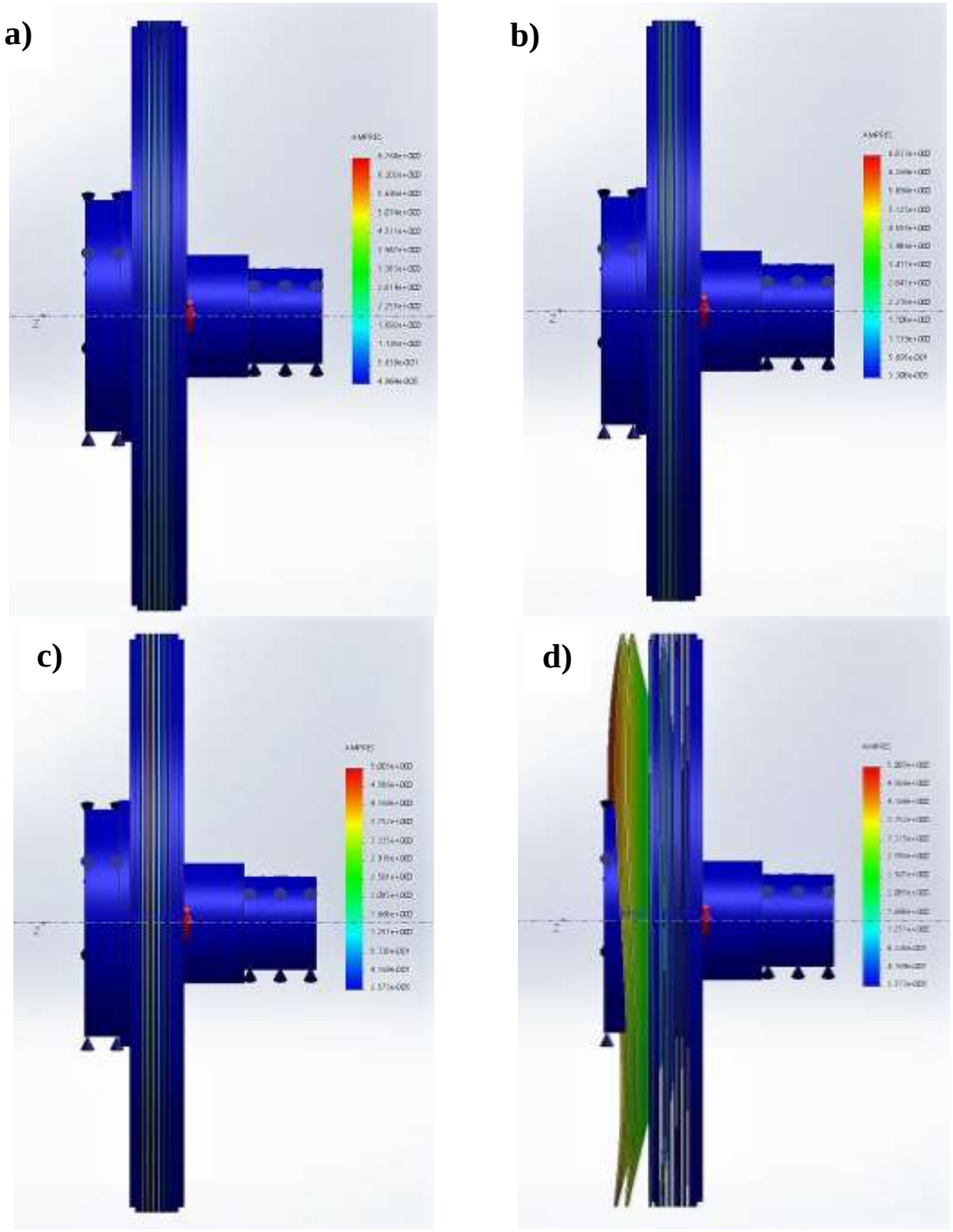

Fig. 3.14 Total Amplitude for real bearing stiffness; a) 3000 rpm; b) 4500 rpm; c) 6000 rpm; d) twisted result of first mode at 6000 rpm

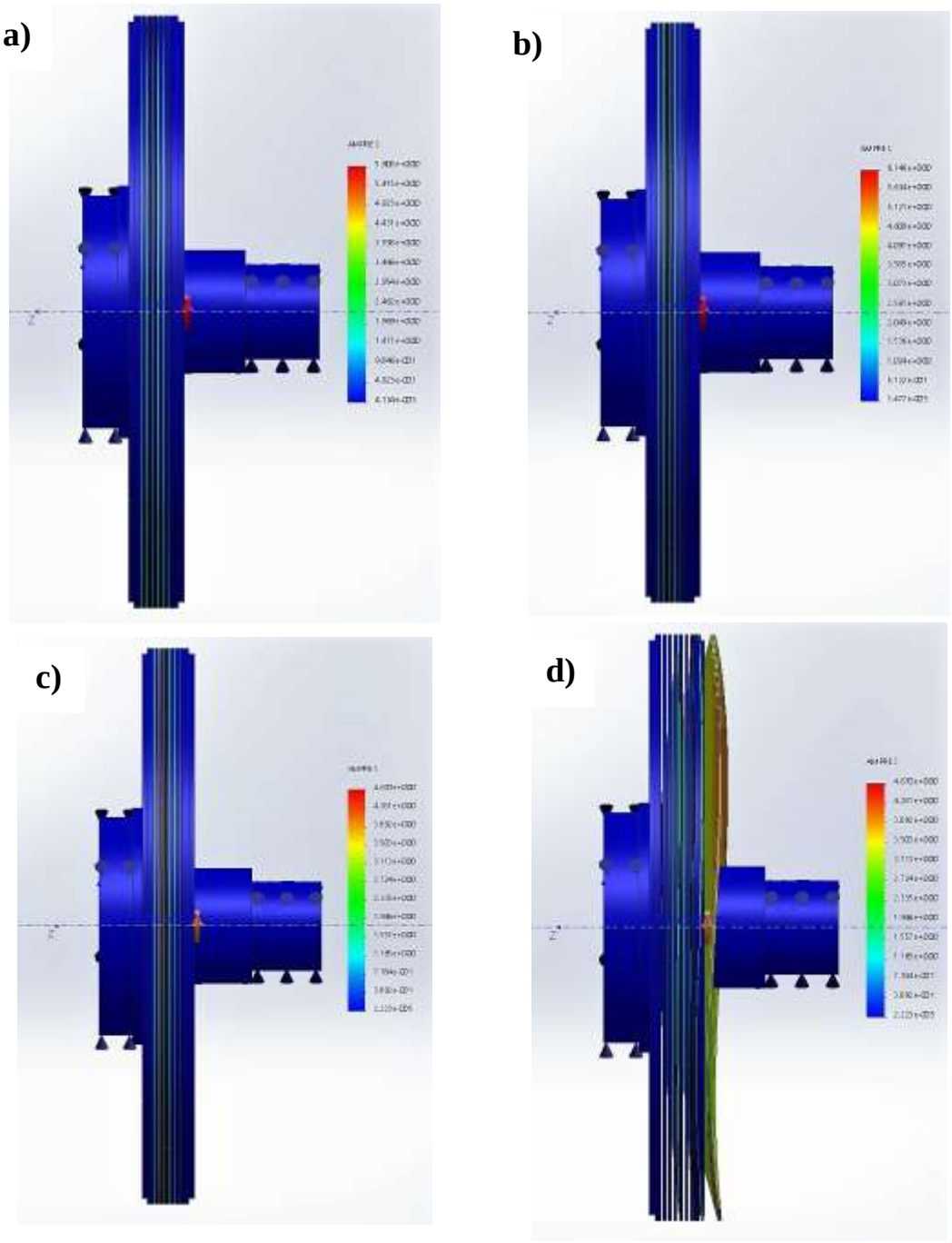

Fig. 3.15 Total Amplitude for real bearing with low stiffness; a) 3000 rpm; b) 4500 rpm; c) 6000 rpm

Fig. 3.16 displays the comparison between ideal and real bearing stiffness modes frequencies. For low rotational speeds the frequencies obtained are very close, for higher rotor velocities, the influence of bearing stiffness is more marked, as it slightly lower the modes frequency values.

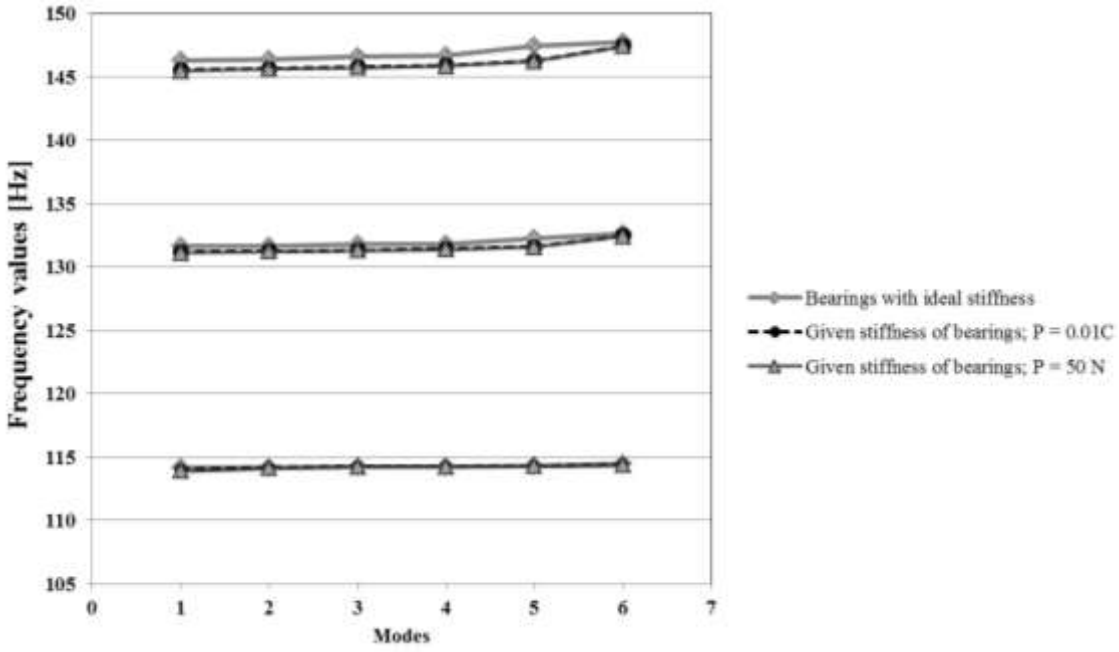

Fig. 3.16 Ideal vs. real bearing stiffness modes frequencies

The modal analysis of the rotor of the ORC Tesla turbine prototype, through the meand of a commercial solver (Solidworks simulation) was performed; first assuming perfect bearing stiffness, after, a simplified model to assess the stiffness of the selected bearings has been developed. The modal analysis has been carried out for different rotational speeds, both for ideal and real stiffness values. Two different stiffness values have been obtained, one with a preload value recommended by the bearings manufacturer and another with a very low preload. The influence of preload in the modal analysis is negligible. Frequency of the modes calculated with real bearings stiffness are very close to the ones calculated with ideal bearing stiffness. To conclude, for test case conditions (velocities lower than 9000 rpm), the design prototype seems not to be experiencing resonance.

3.3 Prototypes design: from thermodynamic considerations to realization

In order to reach the final prototypes geometry, various factors were taken into account. First thermodynamic optimization was carried out, but without forgetting to perform a mechanical analysis of the optimal thermodynamic configuration, choosing therefore the right compromise and also keeping in mind manufacturing process and test benches limitations.

3.3.1 Air Tesla turbine

Design constraints and limitations

The air Tesla turbine prototype parts were built through different processes. Particularly, the stator was made with a 3D printing technique in ABS material. Therefore, one of the boundary conditions of the design was the printable area of the 3D printer.

3D printer and ABS material

3D printing is a technique based on the overlapping of layers of plastic material heated to relatively high temperature. At the proper temperature, the material becomes malleable, and therefore it is deposited on a plate, layer after layer, in order to produce the desired piece. The contact with air provides the cooling and therefore the stiffening of the material, returning it to solid state.

The printer used to make the stator of the air Tesla prototype is the Anet A8 model manufactured by Prusajr (Fig. 3.17). Tab. 3.7 resumes its main specifications.

Table 3.7 3D Prusajr Anet A8 characteristics

Printing Area [mm]	Max. nozzle Temperature [°C]	Max plate temperature [°C]	Nozzle diameter [mm]	Printing velocity [mm/s]	Possible printing materials
220x220x240	250	100	0.4	100	PLA, ABS, TPU, PVA, PP

The main boundary condition given by the 3D printer was the maximum printing area. It was found while using the 3D printer that, in order to have a good quality of the printed stator, the maximum external stator diameter had to be of about 150 mm.

The material used for printing the stator is ABS, an acronym for acrylonitrile–butadiene–styrene, a thermoplastic polymer frequently used in industry and, thanks to its thermal and mechanical properties, particularly suitable for three–dimensional moulding. ABS in fact has a melting point of 100°C, which allows the resistance of the printer to work at a temperature between 215°C and 250°C, and the material to cool rather quickly once

deposited. ABS has good impact resistance, high toughness and rigidity. Thermal resistance is good a low temperature, however, for power production it determines a limitation, as it fluid inlet temperature affects the machine performance. Manufacturers recommend using ABS at temperatures below 85°C, which prevents the air from being heated to higher temperatures. The main properties of ABS are resumed in Tab. 3.8.

Table 3.8 Main ABS properties (at 20 °C)

Density [kg/m^3]	**Poisson ratio**	**Young module [GPa]**	**Yield strength [MPa]**	**Bending strength [MPa]**
1060	0.35	2500	45	70
Friction coefficient on steel	**Melting temperature [°C]**	**Temperature range of operation**	**Thermal expansion coefficient[°C^{-1}]**	**Relative permittivity**
0.5	85 / 130	-40 / 80	0.00005	3.5

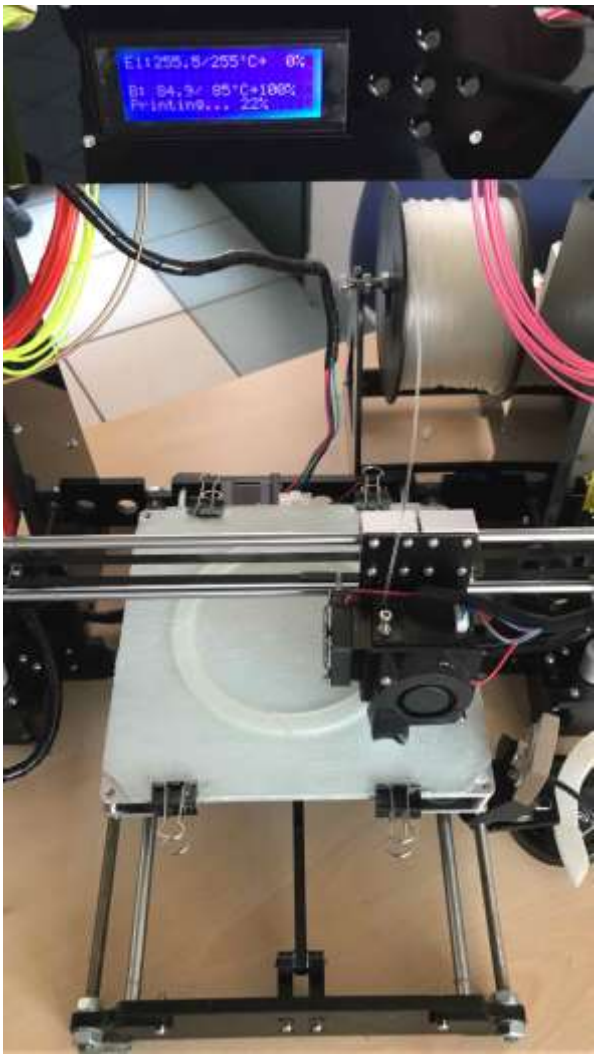

Fig. 3.17 3D Prusajr Anet A8

The other parts of the air Tesla turbine prototype were built through the different processes. The outlet casing is made by Plexiglas material and it has been made through a milling process. The rotor disks are made of aluminium through laser cutting and the shaft are made of steel (through turning). The reason for choosing metal materials for the rotor lies in the greater stresses and deformations to which is subjected; in particular, the disks, due to their limited thickness and the mechanical and thermal loads (even if limited) to which they are subjected, could run the risk of undergoing high deformations (verified through the application of the model discussed in Section 3.2.1), altering the shape of the channels. Nonetheless, the choice of these materials allowed not having further restrictions given by the materials or the manufacturing process.

Test bench

The air Tesla turbine prototype was designed to a specific test bench, which comprised a centrifugal compressor (MICO 90/8 model produced by SAVIO SRL), whose speed can be regulated with a variable–frequency inverter. Fig. 3.18 shows the performance curves of the centrifugal compressor. As can be noted, the reachable pressure is not high (max 1.85 bar), therefore while designing the turbine, this had to be taken into account.

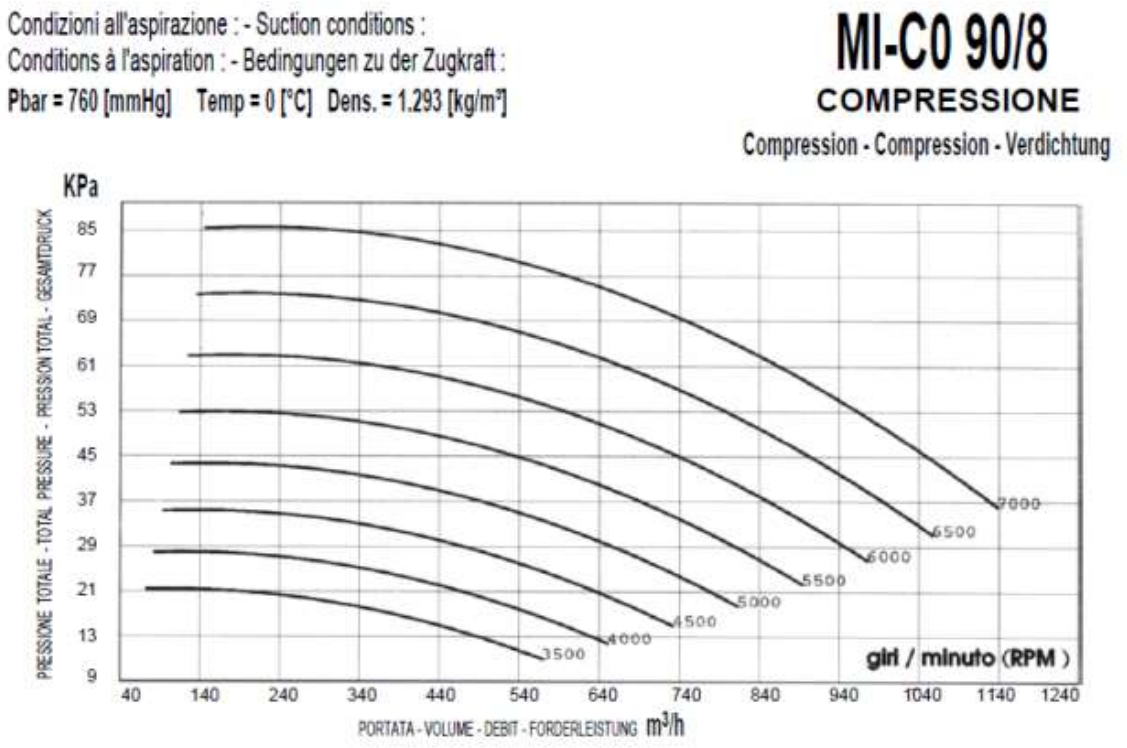

Fig. 3.18 Centrifugal compressor performance curves

The turbine furthermore needs to be connected to an electric motor (brushless type) that controls the rotational speed through a servo drive. By means of a continuous exchange of electricity between the electric motor and the grid, the brushless is able to operate as

generator or as brake, according to the power produced by the turbine. The maximum allowable rotational speed by the generator is 3000 rpm. The torque and, consequently, the power produced by the turbine is measured by a torque meter (Lorenz, nominal torque 10 Nm) connected between the turbine and the brushless motor through flexible couplings.

The limitation on rotational speed is an important feature to take into account, as the Tesla turbine prototype, and generally Tesla turbines, as it will be discussed deeply in the results Section, perform well at relatively high rotational speeds.

Design objectives

Taking into account the boundary conditions provided by materials, manufacturing processes and test bench, some design objectives where selected in order to have significant tests results. Particularly, a 10% thermodynamic efficiency and a 100 W power output have been taken as reachable objectives. Having therefore stated the limitations and objectives, the proper dimensioning of the turbine can be carried out.

Plenum chamber

The turbine entry is made by 4 different “Rilsan pipes” in order to have a homogeneous distribution inside the plenum chamber. The toroidal plenum chamber allows having low velocities at stator inlet, which, as demonstrated in [91], [140], are beneficial to the turbine efficiency.

The mass balance equation states that for a fixed mass flow rate and thermodynamic conditions, in order to have low velocities, a wide area is required. The first thing to dimension is therefore the required section area of the plenum chamber, which will allow the flow to slow down, passing from 4 circular duct of 3/4" to a toroidal chamber of greater section. As the lower boundary of the plenum chamber is given by the external diameter of the stator, the first geometry parameter that has to be defined is the height of the plenum chamber (which will determine the internal radius of the carter). Assuming the maximum achievable mass flow rate of 60 g/s at 1.8 bar and 60°C, the velocity at entry of the plenum chamber is 28 m/s. In order to have velocities in the plenum chamber lower than 1.5 m/s the height of the plenum chamber should be around 35 mm. Therefore, assuming maximum external stator diameter achievable with the 3D printer, an internal carter diameter of 0.22 m is required.

The thickness of the external carter is sized by the theory of thin pressure vessels; assuming that its value is significantly lower than the diameter. Eq. (3.92) allows obtaining the minimum thickness that the component must have. From Eq. (3.92), the minimum required thickness for the test conditions would be of 3 mm. Nonetheless, it was decided to design the turbine in order to withstand 10 bar of internal pressure, in case future tests in other test benches could be run. Therefore, the minimum required thickness

obtained from Eq. (3.92) is of 13 mm and taking into account the diameter of the screws, the final minimum radial thickness of the plenum chamber was set at 20 mm.

Table 3.9 Final external carter dimensions

Carter external dimensions [m]	Carter internal radius [m]	Carter radial minimum thickness [m]	Height of plenum chamber [m]
0.26x0.26x0.1	0.11	0.02	0.035

Fig. 3.19 displays the Solidworks drawing and the realized carter of the prototype in PMMA material, while Tab. 3.9 resumes the carter dimensions.

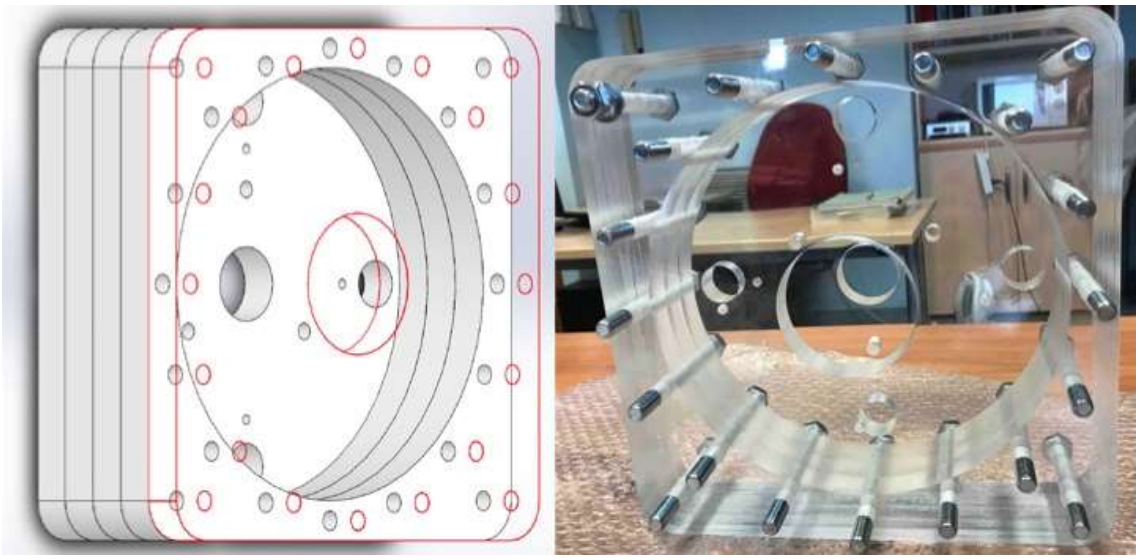

Fig. 3.19 External carter of the turbine, SolidWorks drawing and real prototype

Stator

The design of the stator, due to the external diameter limitations has been quite straightforward. Indeed, applying the inlet/outlet diameter ratio recommended by [180], [181], it has been possible to select the internal diameter, which allows highest efficiencies.

Knowing internal and external radius of the stator, the last and most important things to determine are number of nozzles, the height and width dimensions, as well as the exit angle. The nozzle exit angle has been taken as the maximum that the manufacturing process could achieve, or 85°. Indeed, in order to obtain maximum efficiencies, a completely tangential fluid to the rotor is required. The 3D printing limited the throat width at 0.8 mm, as the uncertainty of the printing process is of 0.2 mm.

Therefore, the last dimensions to determine have been stator height and number of nozzles. Tesla turbines efficiency is high when high Mach number and low mass flow rates are reached. Particularly, increasing height of the nozzle, as well as the number of nozzles, would bring to a penalty in efficiency. Nonetheless, low number of channels would not guarantee and homogeneous flow; therefore 4 nozzles per stator have been selected. Nozzle number optimization is being further assessed in Section 4.1.1.2.

The stator height has been defined so that each stator would provide the flow to ten channels; therefore, the height of the stator is obtained from the sum of 9 disks thickness plus 10 rotor channels width. Tab. 3.10 resumes the main dimensions of the nozzle and Fig. 3.20 displays the Solidworks drawing and the realized stators of the prototype in ABS material.

Table 3.10 Final stator dimensions

Stator external diameter [m]	**Stator internal diameter [m]**	**Chord length [m]**	**Number of nozzles**
0.152	0.126	0.018	4
Stator inlet angle [°]	**Stator outlet angle [°]**	**Nozzle throat width [m]**	**Nozzle throat height [m]**
0	85	0.0008	0.012

Fig. 3.20 Turbine stator, SolidWorks drawing and real prototype

Rotor

Larger is rotor diameter, higher is the power produced par channel, therefore, the maximum possible rotor diameter, taking into account a 1 mm gap between stator and rotor was chosen.

Once the diameter is chosen, in order to optimize the rotor, two main parameters have to be selected, the rotor outlet/inlet diameter ratio and the width of the channels; furthermore, the total number of disks has to be defined as well.

The most significant parameter of a Tesla turbine is the width of the rotor channels, which deeply influences the performance of the machine. Particularly, tight gaps are required for high efficiency and performance. Therefore, an analysis on the performance of the machine varying rotor gap at various inlet conditions was carried out.

Fig. 3.21 display the variations of total to static efficiency (a–c–e) and power production par channel (b–d–f), for three different mass flow rates and four different total inlet pressures. At low pressure and mass flow rate optimal channel width is a bit larger (in the range of 0.4–0.5 mm), but as pressure and mass flow rate increases, a tighter gap is preferred (in the order of 0.3 mm). Higher pressure allows higher total to static efficiency at fixed geometry and mass flow rate. This is directly linked to the velocity decrease at nozzle stator exit. Indeed, higher pressure means higher density values, and accordingly to mass balance equation, in order to maintain the same mass flow rate at fixed section, velocity has to be decreased.

Theoretically, Tesla turbines work better at high velocities, but it has to be kept in mind that the maximum reachable rotational speed is limited to 3000 rpm, therefore, optimal tangential velocity ratio is not optimized.

Power produced per channel is directly linked by throat Mach number value. Particularly, as the throat section is defined as the sum of the disks thickness plus the channels width, increasing the gap between the channels directly augment the throat section and therefore lower throat Mach number values are reached. Consequently, in order to have a proper power production, tight channels are preferred.

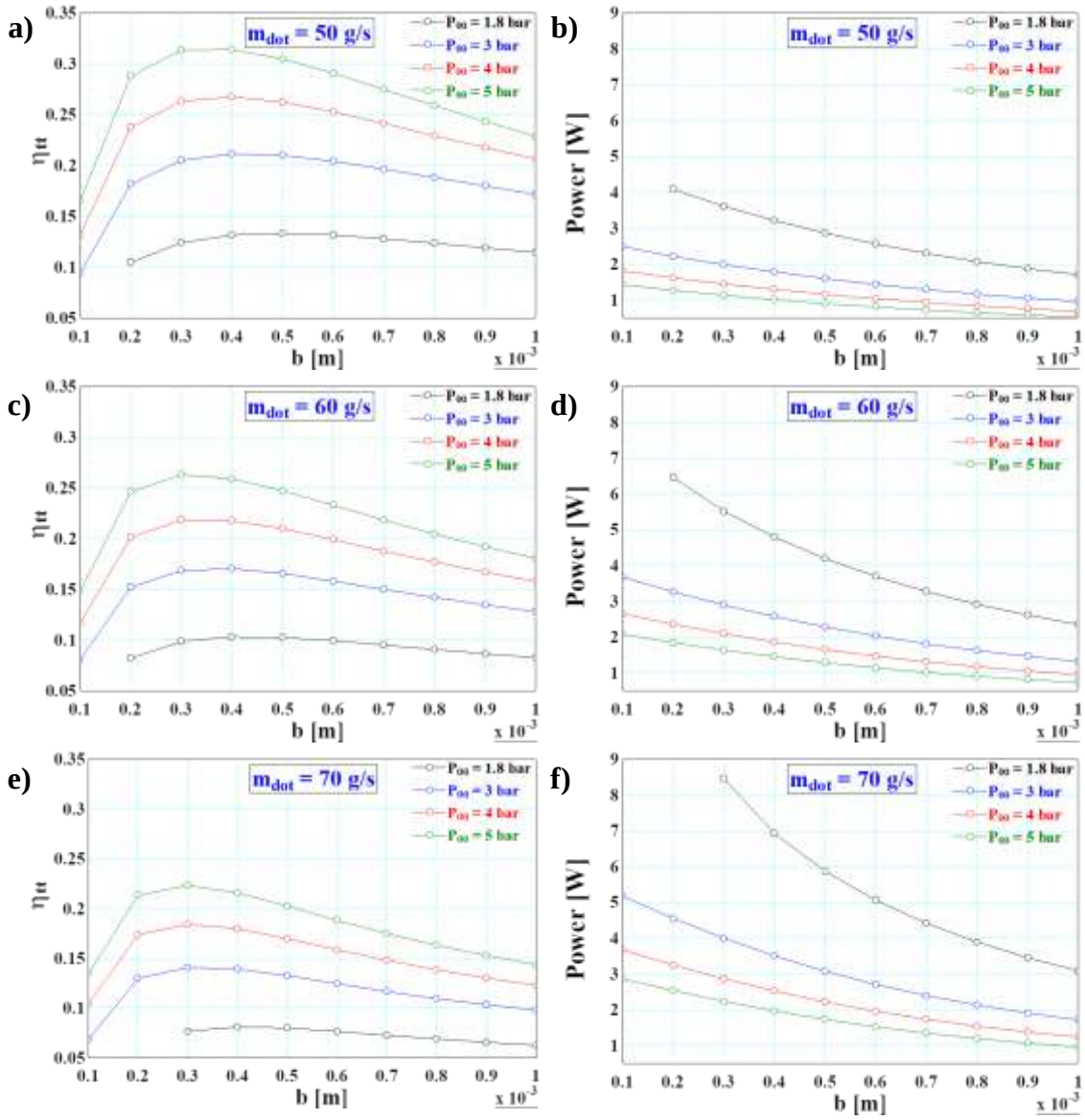

Fig. 3.21 Efficiency (a–c–e) and power par channel production (c–d–f) for a Tesla turbine working with air at various pressure and mass flow rates, as function of channels width

The other fundamental parameter of Tesla turbine rotor is the ratio between rotor inlet and outlet radius. Fig. 3.22 displays the efficiency (a–c–e) and the power produced per channel (b–d–f), at various mass flow rate and total inlet pressures, as function of the rotor outlet/inlet radius ratio. Optimal values of efficiency are reached for a rotor radius ratio of about 0.4, for all mass flow rates and pressures. On the other hand, the power produced per channel is increasing as the rotor radius ratio decreases, as it implied that the exchange area is increased. Therefore, for optimal efficiency a rotor radius ratio of 0.4 has to be chosen, while for maximum power a rotor radius ratio of 0.1 is preferred. Taking into account these considerations, the selected design ratio chosen was of 0.25, for two main reasons: (i) to have high efficiency with relatively high power production;

(ii) to not have bearings at turbine outlet with high diameter, as low diameter bearings produce lower mechanical losses.

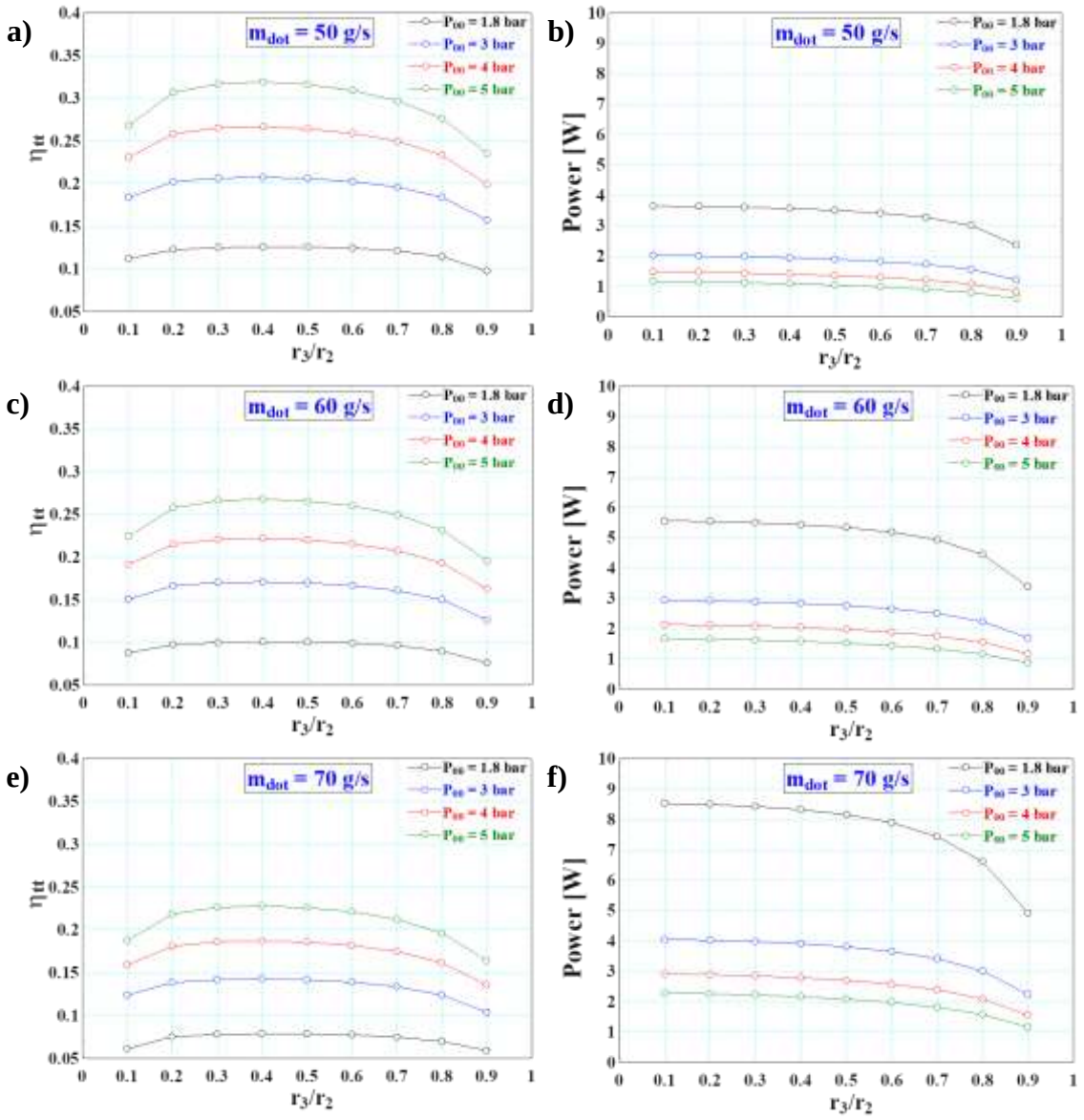

Fig. 3.22 Efficiency (a–c–e) and power per channel production (c–d–f) for a Tesla turbine working with air at various pressure and mass flow rates, as function rotor outlet/inlet radius ratio

Finally, the total number of channels had to be chosen. At design condition (60 g/s at 1.8 bar inlet pressure), the power produced per channel resulted of 5.5 W. Therefore, in order to obtain the desired value of 100 W, 20 channels would be enough. Nonetheless, taking into account mechanical losses, and keeping in mind the possibility of further tests at higher pressure, double the number of the minimum channels was selected (40). Tab. 3.11 resumes the main dimensions of the rotor and Fig. 3.23 displays the Solidworks drawing and the realized rotor of the prototype in aluminium and steel materials.

Table 3.11 Final rotor dimensions

Rotor inlet diameter [m]	Rotor outlet diameter [m]	Channel width [m]
0.125	0.031	0.0003

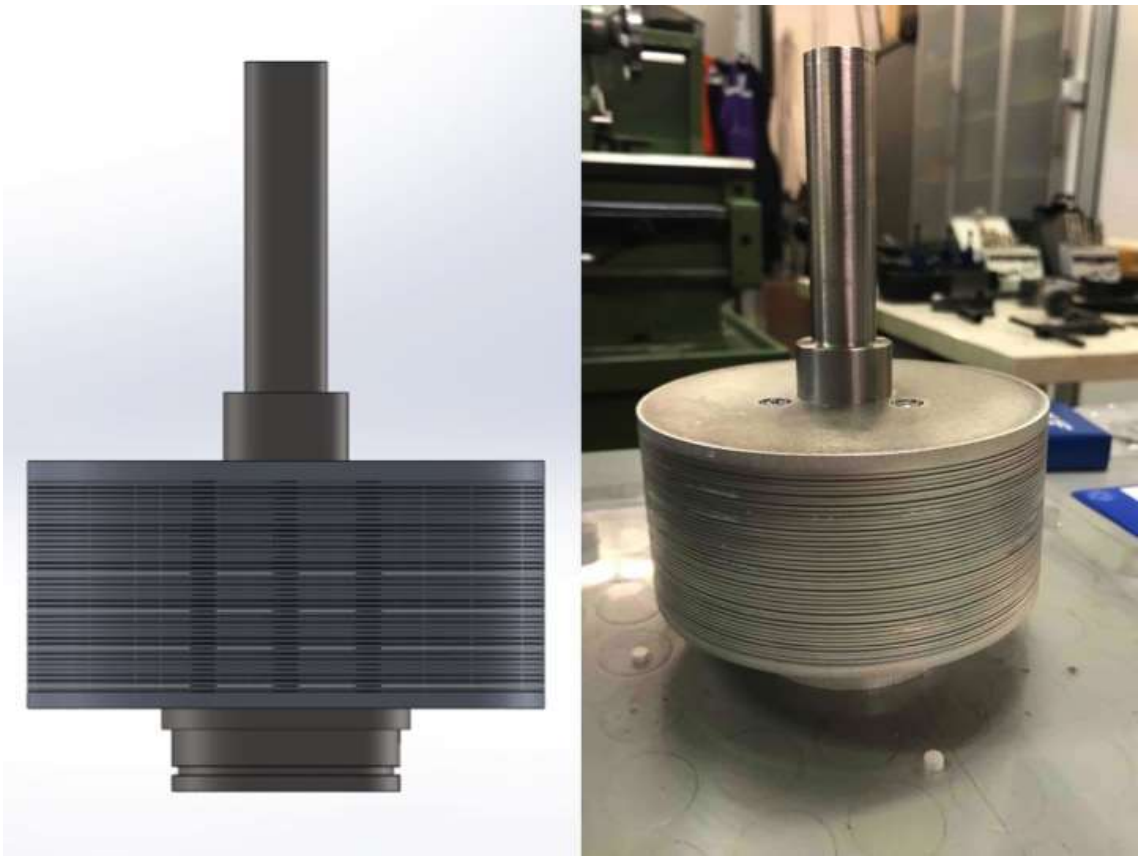

Fig. 3.23 Turbine rotor, SolidWorks drawing and real prototype

Full assembly

Once the three main parts of the machine have been dimensioned, all other components needed to be assessed, from the rotor shafts, to the bearings, and the screws of the carter. Each component has been verified according to the formula displayed in Section 3.2.1 and the final dimensions of each component have been resumed in Tab. 3.12.

Finally, each drawn component has been assembled in a final assembly, as shown in Fig. 3.24, in order to verify if some inconsistencies were present. Once the final drawing was completed, all components were ordered and assembled in Linea Laboratory of University of Florence.

Table 3.12 Final prototype dimensions

Bearings	**Total number of channels**	**Gap Stator/Rotor [m]**	**Power shaft diameter [m]**	**Washers dimensions**
SKF 1205 EKTN9 SKF 61811 – 2RZ	40	0.001	0.02	0.003x0.006x0.0003
Fluid side shaft diameter	**Rotor screws**	**Disks–shaft screws**	**Carter screws**	**Sheet gasket thickness**
0.055	M3	M5	M10	0.00015

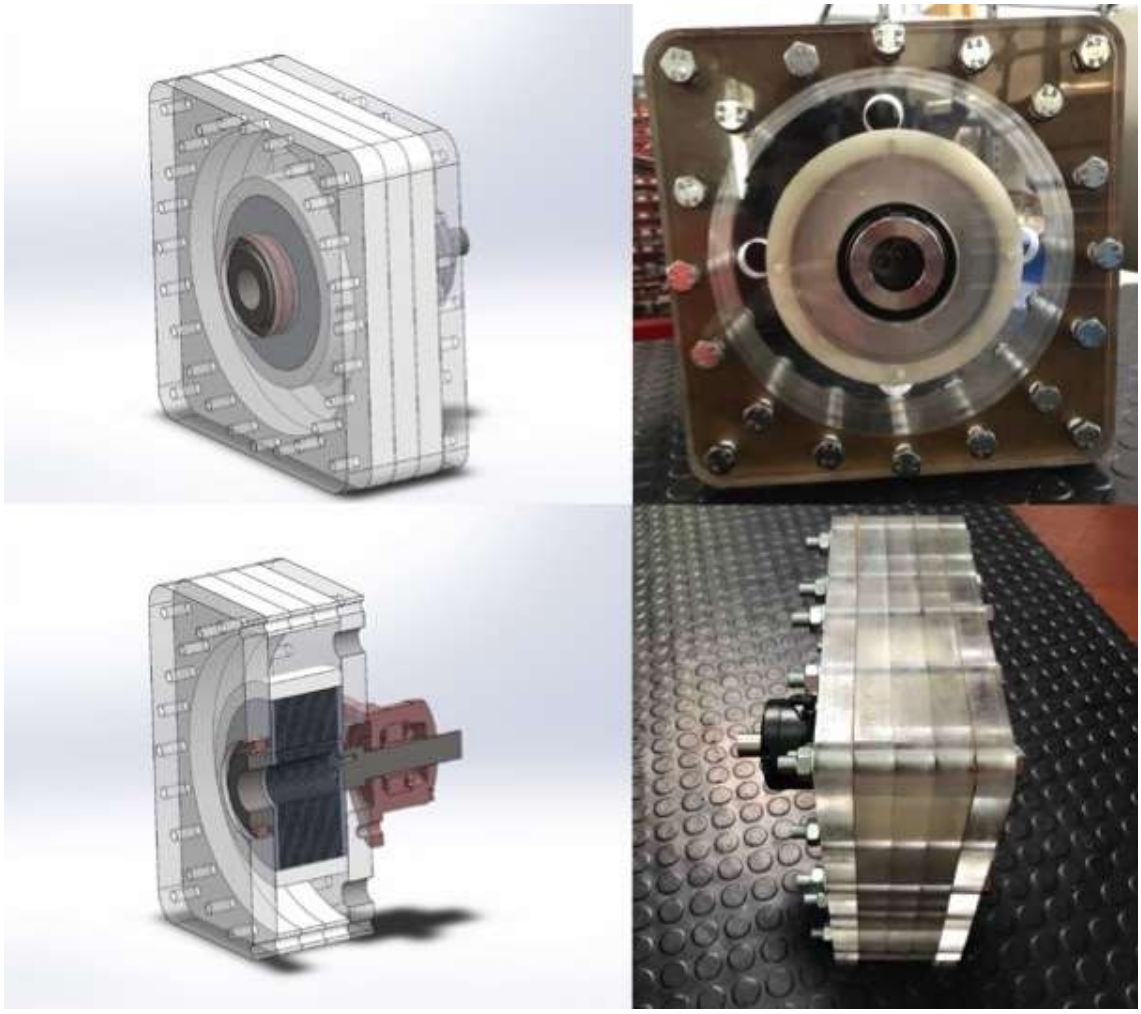

Fig. 3.24 SolidWorks drawing and real prototype

3.3.2 ORC Tesla turbine

As for the air case, in order to proceed to the design of the ORC prototype, the boundary conditions have to be firstly analysed. The limitations on the turbine design in case of the ORC prototype were given mostly by the test bench and by manufacturing issues when dealing with nozzle outlet width.

Test bench

The ORC prototype was designed in order to work in a test bench available in University of Florence (Linea Laboratory) working with R404a as working fluid. The scheme of the test bench is showed in Fig. 3.25.

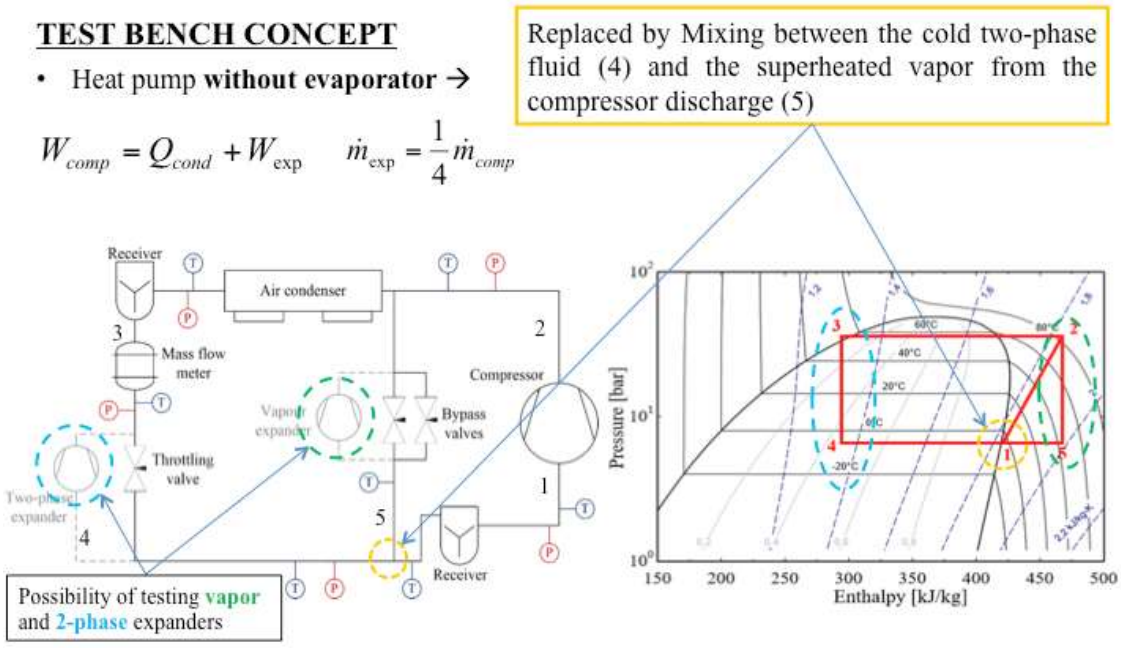

Fig. 3.25 Scheme of University of Florence Test bench (Linea Laboratory)

The test bench is composed by the following components:

- A volumetric compressor of the H5 series, model H3400CC manufactured by Dorin, which has the task of compressing the vapour of the working fluid to the required pressure; as known, once the rotational speed is set, the volumetric compressors are able to compress a constant volumetric flow of gas over a wide range of compression ratios. The model used, operating at a frequency of 50 Hz, is able to process a flow rate of 102.35 m^3/h absorbing a maximum electrical power of 35.2 kW; these limits have to be kept in mind when assessing the mass flow that will evolve in the turbine and the maximum inlet pressure to the expander.

- The expander to be tested, placed in parallel to a bypass valve for hot gases. The torque meter used to measure the torque is the same as that used in the air test bench, therefore the torque must be less than 10 Nm to avoid damage to the instrument; the brushless motor will also have the same limit as seen in the analysis of the air machine (3000 rpm). However, in this test a speed reducer will be placed in series that will allow the machine to operate up to 4500 rpm, allowing to obtain a greater production of power and a better efficiency. Finally, the axial thrust will influence the choice of bearing type and size.
- An air–cooled condenser, i.e. a gas–air heat exchanger capable of cooling the vapour of the working and bringing it to saturated liquid conditions. The condenser is designed to exchange a maximum amount of heat of 25 kW, while the use of air in ambient conditions (approximately 15°C), requires that the saturation temperature is at least 5–10°C higher, to which is associated a minimum value of saturation pressure: the diagram *T–s* in Fig. 3.26 shows that, at a saturation temperature of 23°C corresponds a pressure of 12 bar, which will constitute the minimum value of P_{00}.

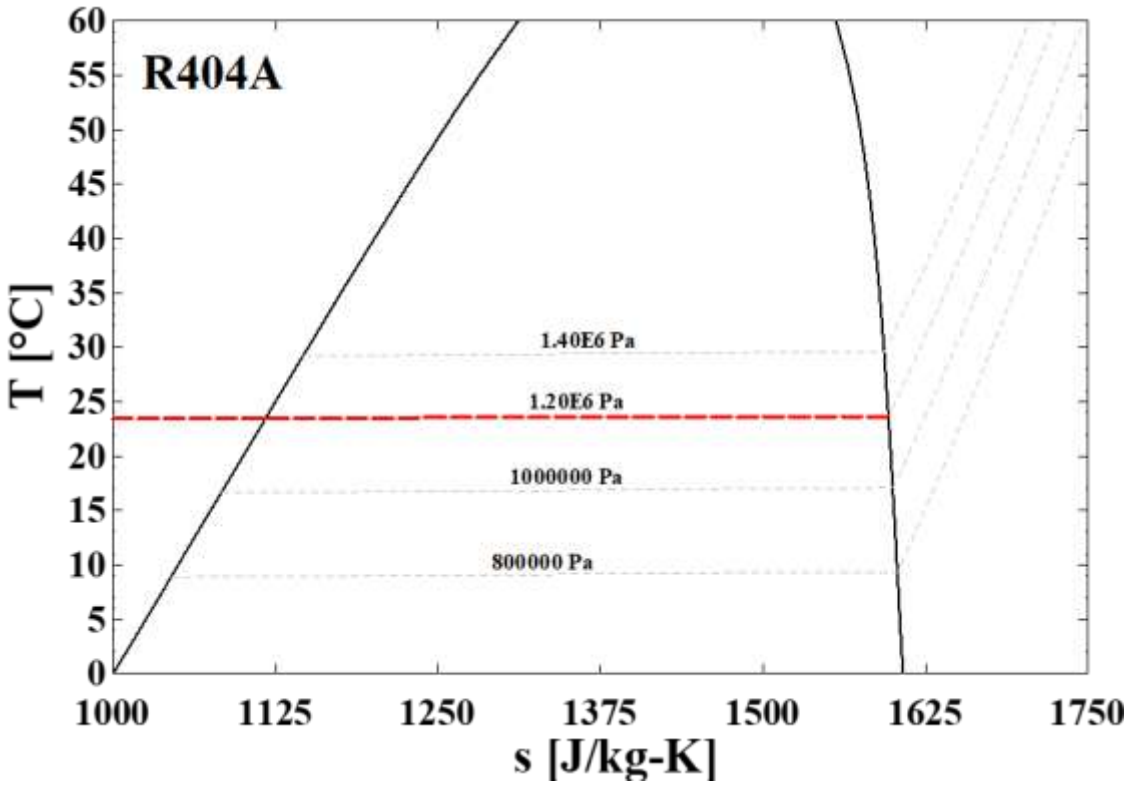

Fig. 3.26 R404 Temperature–Entropy diagram, highlighting saturation pressure (12 bar) at 23°C

- A throttling valve, through which the cooled vapour is expanded and brought back to the same pressure conditions as the fluid expanded in the turbine.
- A storage tank, where the flows of the two branches mix and exchange heat.

The test bench (Fig. 3.27) compresses the entire flow of fluid to a minimum pressure of 12 bar, after which the flow is separated into two currents: the former expands into a turbine, making the required pressure drop, the latter is cooled and condensed under saturated liquid conditions, then expanded into a throttling valve to the turbine discharge pressure and finally mixed. The hottest fluid leaving the turbine will return the entire flow rate to conditions of overheating, ensuring a temperature of about 10°C higher than saturation conditions, in order to ensure the absence of small droplets at the entrance of the compressor.

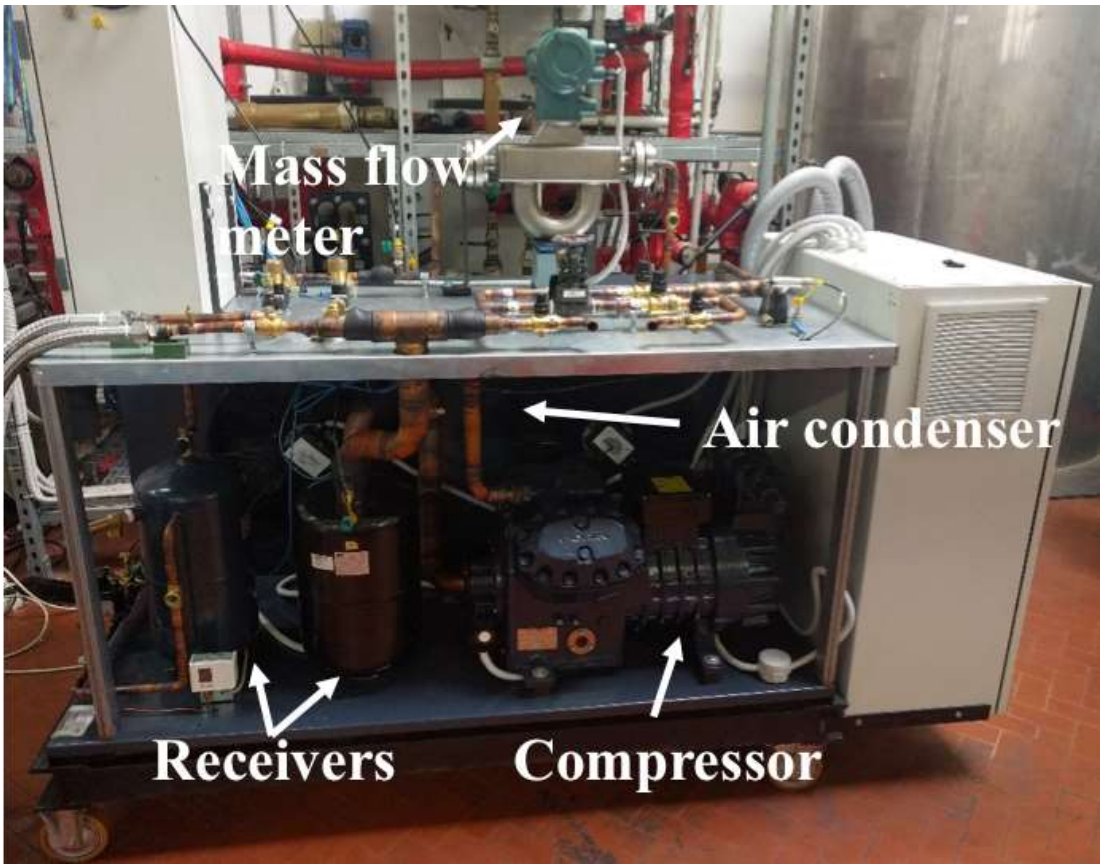

Fig. 3.27 University of Florence Test bench (Linea Laboratory)

Therefore, once the upper and lower pressure levels are fixed, the efficiencies of the two machines and the flow rate of fluid required in the turbine are determined; using a code developed in EES environment, it is possible to obtain the total flow rate processed by the compressor, the power absorbed and the heat exchanged in the condenser. It is thus possible to evaluate whether the experimental conditions respect the limitations imposed by the test bench; the program has also been implemented in such a way that, once the diameters of the ducts are known, it is possible to calculate the relative speeds and pressure losses through an appropriate internal EES function which determines pressure drops.

Developing a parametric analysis varying the three fluid dynamic parameters (upper and lower pressure and mass flow rate), it is possible to obtain the operating range of the turbine: for each inlet pressure the machine discharge pressure and the evolving flow rate are varied, the results are excluded for which the heat exchanged in the condenser exceeds 25 kW and the work carried out by the compressor is greater than 35 kW. Fig. 3.28, referring to an inlet pressure of 12 bar, shows the trend of the flow rate processed by the compressor as a function of the discharge pressure (or equivalent, the compressor inlet pressure) and the flow rate used in the turbine; the green curve, on the other hand, refers to the maximum flow rate that the compressor is able to dispose of, calculated as a product between the volumetric flow rate ($\dot{V}$ =102.34 m^3/h) and the density of the inlet refrigerant, a function of pressure. This line defines the operating range in which the test bench is able to operate, thus identifying a minimum limit to the turbine exhaust pressure; this limit is more stringent the greater the flow rate processed by the expander.

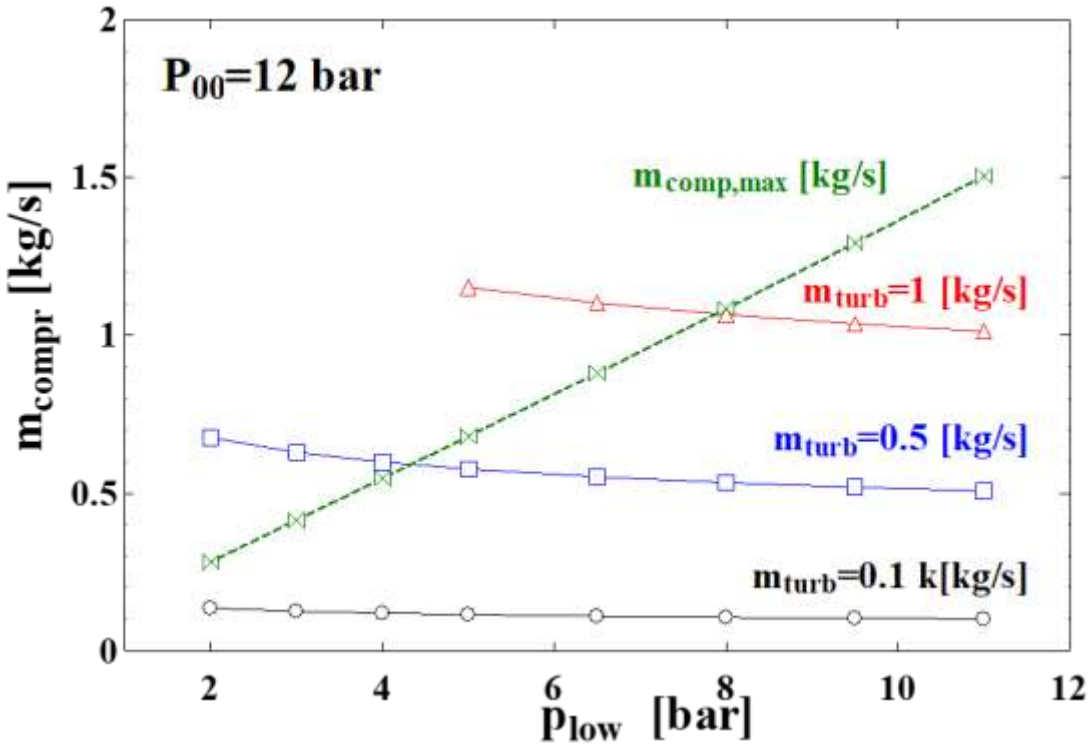

Fig. 3.28 Max. and actual compressor flow rate, as function of turbine mass flow rate and lower pressure of the test bench for an upper pressure (P_{00}) of 12 bar

When higher inlet pressures are considered, such as the case presented in Fig. 3.29, by operating the turbine with a flow rate of 0.1 kg/s, the fluid could expand up to atmospheric pressure, while a flow rate of 1 kg/s could expand only up to 8 bar, limiting the pressure drop to 4 bar. At higher inlet pressures, the flow rate of fluid elaborated by the compressor does not change for the same value of (m_{turb}); however, the limits linked to the maximum heat exchanged in the condenser are more stringent, so much so that in the graph of Fig.

3.29, referring to an upper pressure (P_{00}) of 24 bar, there is no intersection between the operating lines.

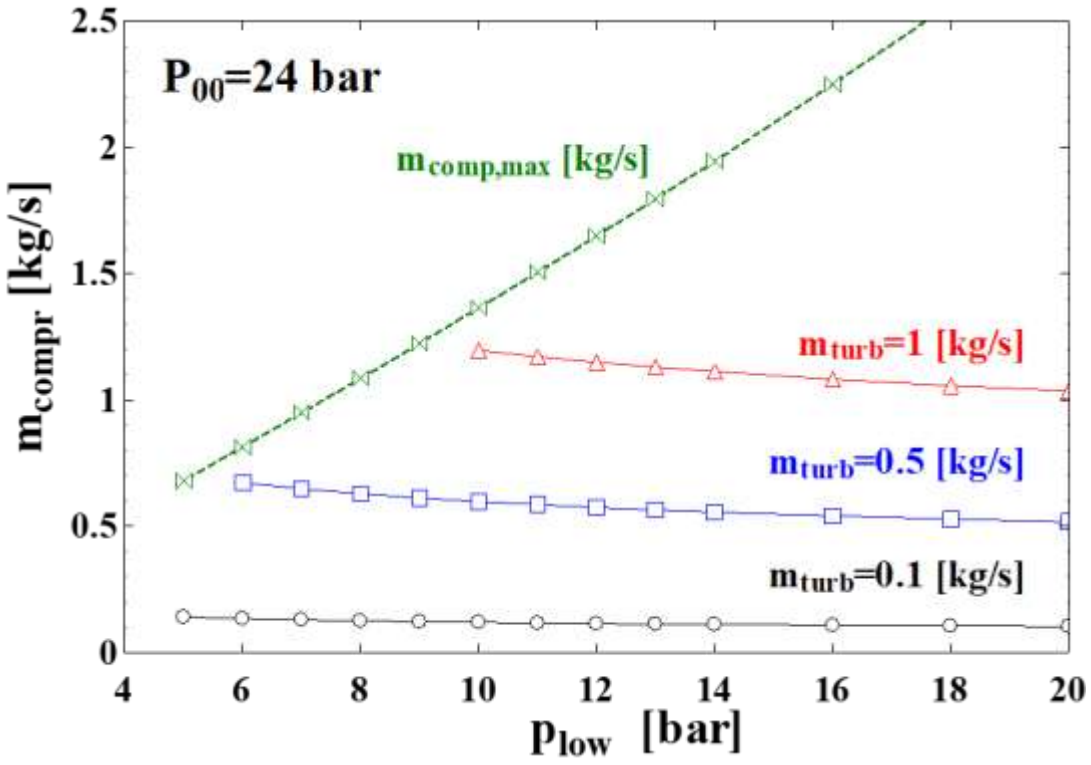

Fig. 3.29 Max. and actual compressor flow rate, as function of turbine mass flow rate and lower pressure of the test bench for an upper pressure (P_{00}) of 24 bar

Design objectives

As for the air expander design, the boundary conditions have been taken into account, considering materials requirements, manufacturing processes and test bench operation range; therefore, some design objectives have been selected in order to obtain significant tests results. Particularly, a 40% thermodynamic efficiency and a 500 W power output have been taken as reachable objectives. Having therefore stated the limitations and objectives, the proper dimensioning of the turbine can be carried out.

Components design

The design of each component was carried out with the same procedure applied to the air Tesla turbine prototype. Tesla turbines, as will be further assessed in the result Section, produce high power when inlet rotor diameter is greater, while keeping high efficiency level if proper thermodynamic conditions are provided. The aim of the design was to manufacture an efficient turbine with relatively limited dimensions. The maximum possible outer dimension that could not be exceeded by the casing was of 0.4 m, imposed by test bench characteristics. The dimensioning of the turbine, keeping in mind the maximum allowed outer casing diameter started from the rotor.

Rotor

The design of the rotor started from the evaluation of the external diameter. Various total inlet pressures, mass flow rates and rotational speeds were assessed, in order to find an optimal configuration, which could comply with the test bench and the set objectives. As shown in Figs. 3.30 and 3.31, efficiency and power per channel are higher at low pressure and high rotor diameter. Furthermore, at a fixed mass flow rate, a higher rotational speed allows to achieve higher efficiency at lower rotor inlet diameter. The power developed par channel is fairly low for the mass flow rate considered, while the efficiency values are in the range of the other competing technologies for micro power generation. The external rotor diameter has thus been selected trying to have a relatively high power production at limited dimension and high efficiency.

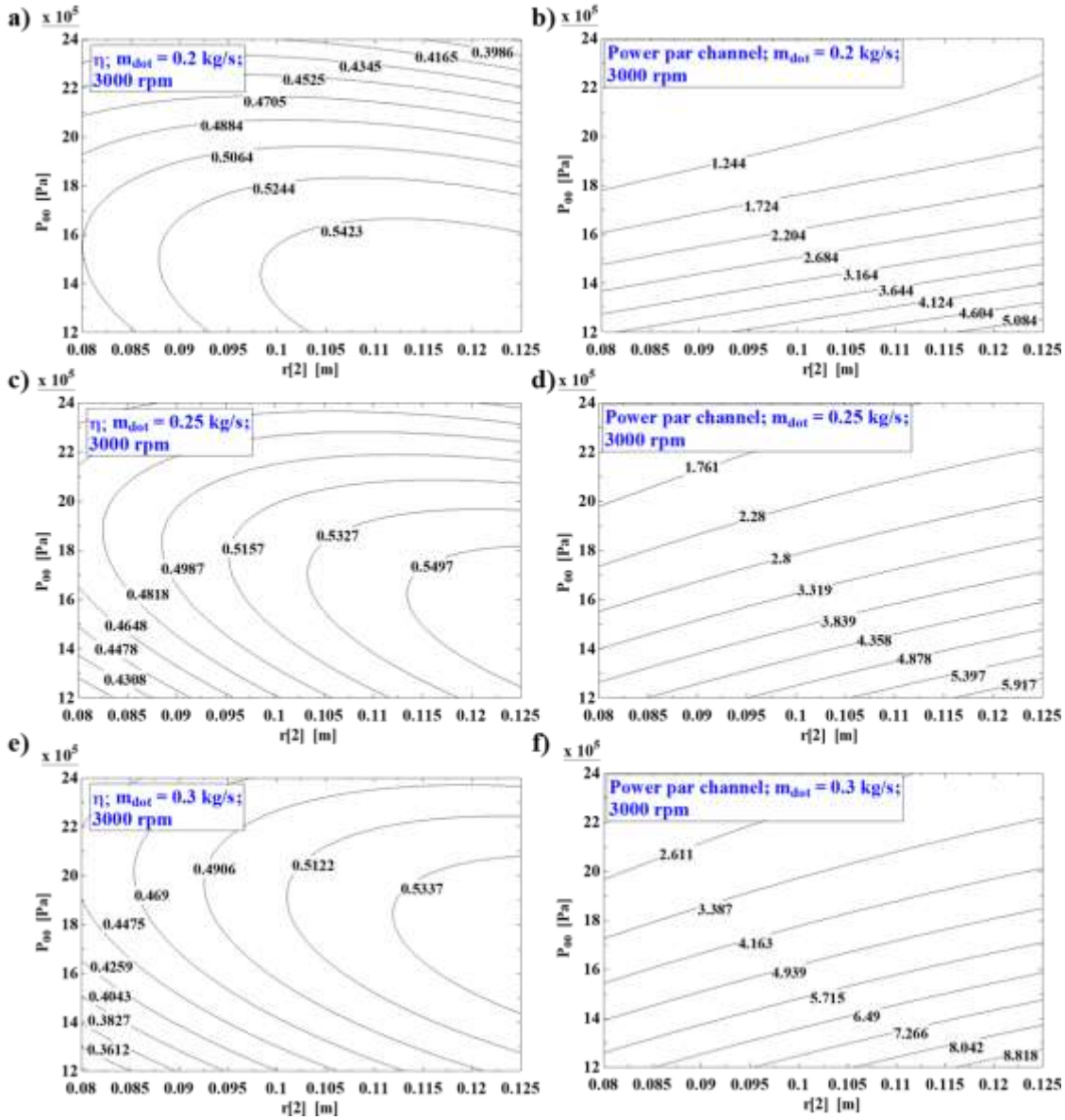

Fig. 3.30 Efficiency and power per channel of a Tesla turbine working with R404a, as function of total inlet pressure and external rotor diameter, for a rotational speed of 3000 rpm

The design point conditions have been taken to be a rotational speed of 4500 rpm and a mass flow rate of 0.25 kg/s. Considering therefore these conditions, the balanced selection of the radius was a value of 0.108 m, which could guarantee an efficiency over 40% for a very wide test range, with a power production close to 500 W at 12 bar of total inlet pressure, when a total of 60 rotor channels is considered.

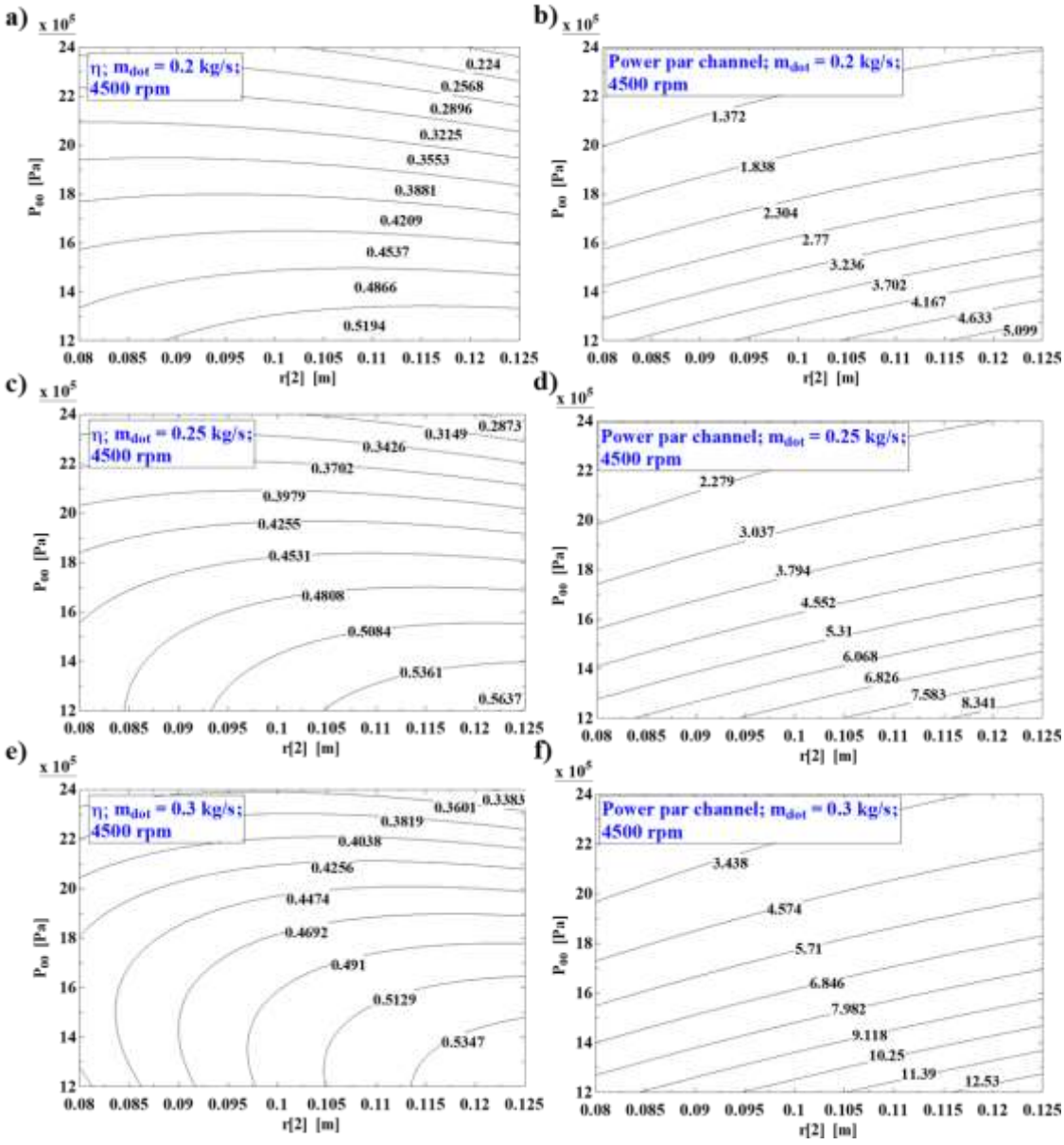

Fig. 3.31 Efficiency and power per channel of a Tesla turbine working with R404a, as function of total inlet pressure and external rotor diameter, for a rotational speed of 4500 rpm

After selecting the outer rotor diameter, the other fundamental parameters, as for the air Tesla prototype are the width of the rotor channels and the rotor outlet/inlet radius ratio. Fig. 3.32 displays the efficiency (a) and the power produced per channel (b), at various total inlet pressures, as function of the rotor channel width. Optimal values of efficiency and power per channel are reached for the smallest assessed width (0.08 mm);

nonetheless, after a market assessment, spacers of 0.08 mm were hard to find, therefore a rotor channel width of 0.1 mm was selected, as it still guaranteed high efficiency and high power par channel. Fig. 3.32 also displays the efficiency (c) and the power produced per channel (d), at various total inlet pressures, as function of the rotor outlet/inlet radius ratio. Optimal values of efficiency are reached for a rotor radius ratio between 0.25 and 0.4, tending to the lower value when total inlet pressure increases. On the other hand, the power produced per channel is steadily increasing as the rotor radius ratio and the pressure decrease; which is directly linked to the increase in exchange area. Therefore, for optimal efficiency a rotor radius ratio of 0.25 has to be chosen, while for maximum power a rotor radius ratio of 0.1 is preferred. Taking into account these considerations, the selected design ratio chosen was of 0.25, for the same main reasons discussed for the air Tesla turbine prototype: (i) to have high efficiency with relatively high power production; (ii) to not have bearings at turbine outlet with high diameter, as low diameter bearings produce lower mechanical losses.

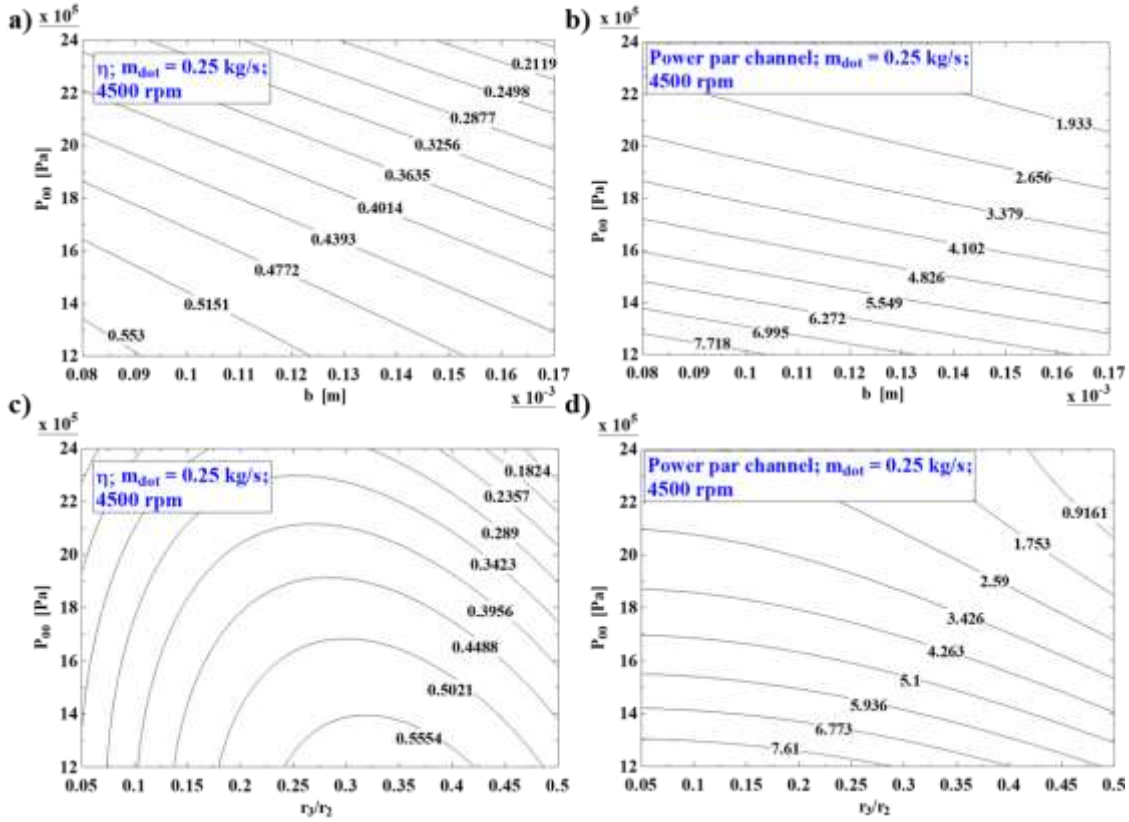

Fig. 3.32 Efficiency and power per channel of a Tesla turbine working with R404a, as function of total inlet pressure and (a–b) rotor channel width, (c–d) outlet/inlet rotor radius ratio, for a rotational speed of 4500 rpm

Finally, Tab. 3.13 resumes the main dimensions of the realized rotor, while Fig. 3.33 displays the Solidworks drawing and the realized rotor of the prototype in aluminium and steel materials.

Table 3.13 Final rotor dimensions

Rotor inlet diameter [m]	Rotor outlet diameter [m]	Channel width [m]
0.216	0.055	0.0001

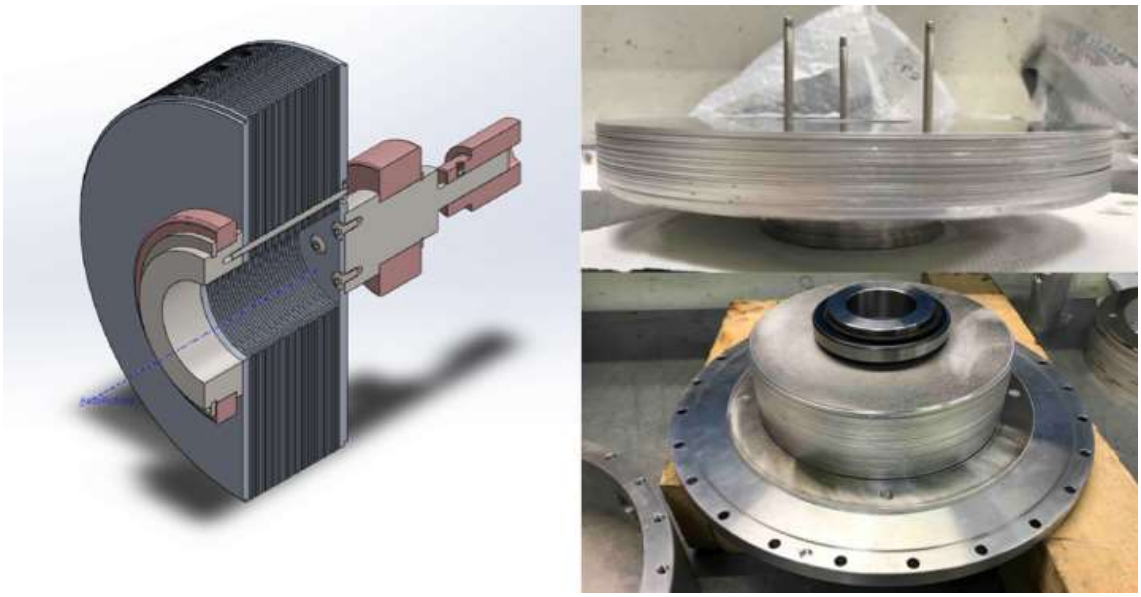

Fig. 3.33 ORC Turbine rotor, SolidWorks drawing and real prototype

Stator

As for the design of the air Tesla prototype, the stator geometry is straightforwardly defined once the geometric and fluid–dynamic boundary conditions are imposed. The design hypotheses are summarised briefly below:

- Inlet/outlet diameter ratio = 1.25, as recommended in [180], [181];
- Nozzle exit angle = 85° (maximum achievable due to manufacturing process);
- Throat section = 1 mm (maximum achievable due to manufacturing process).

The actual number of channels is chosen maximizing the velocity ratio φ_n (Section 3.1.2): in the case of the air prototype, the φ_n coefficient was constantly decreasing as the number of channels increased, reducing the stage efficiency. In this case φ_n is initially increasing until the number of nozzles is equal to 5 and then it decreases in a monotonous way, as shown in Fig 3.34. Therefore, in order to optimize stator efficiency, the five channels configuration would be the optimal one; nonetheless, the minimum flow rate is reached using two nozzles. A compromise between stator and rotor efficiency, as well as considerations related to uniformity, symmetry and distribution of the jet, it was decided to adopt a stator with four channels, with nozzles placed at an angular distance of 90° and a coverage degree (ratio between the segment of input to the rotor multiplied by four and the entire circumference) of 10%.

Tab. 3.14 resumes the main dimensions of the stator and Fig. 3.35 displays the Solidworks drawing and the realized stators of the prototype in aluminium material.

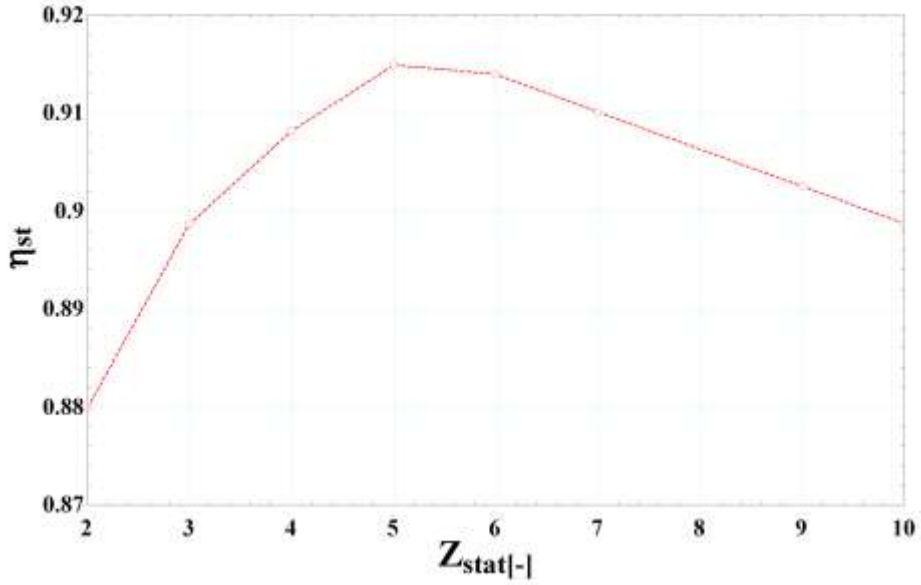

Fig. 3.34 Stator efficiency as function of total number of nozzles

Table 3.14 Final stator dimensions

Stator external diameter [m]	Stator internal diameter [m]	Chord length [m]	Number of nozzles
0.272	0.217	0.059	4
Stator inlet angle [°]	**Stator outlet angle [°]**	**Nozzle throat width [m]**	**Nozzle throat height [m]**
0	85	0.001	0.001

Fig. 3.35 ORC Turbine stator, SolidWorks drawing and real prototype

Plenum chamber

The turbine entry is made by 2 1–inch pipes in order to obtain a uniform distribution inside the plenum chamber. The required section area of the plenum chamber, which allows the flow to slow down, passing from 2 circular duct of 1" to a toroidal chamber of greater section has to be defined. As for the air Tesla prototype, the lower boundary of the plenum chamber is given by the external diameter of the stator, therefore, the height of the plenum chamber (which will determine the internal radius of the carter) has to be determined. Assuming the maximum achievable mass flow rate of 1 kg/s at 12 bar and 80°C, the velocity at entry of the plenum chamber is 22 m/s. In order to have velocities in the plenum chamber lower than 1.5 m/s the height of the plenum chamber should be around 19 mm, which is lower than 1". Therefore, the selected internal carter diameter has been of 0.33 m, in order to have a small space on both sides of the 1" entrances.

The thickness of the external carter is sized by the theory of thin pressure vessels; assuming that its value is significantly lower than the diameter. The minimum thickness is obtained from Eq. (3.92) taking into account maximum achievable test conditions (25 bar), and it was found to be of 10 mm. Considering also the diameter of the screws and a safety coefficient, the final minimum radial thickness of the plenum chamber was set to 20 mm. Fig. 3.36 displays the Solidworks drawing and the realized carter of the prototype in aluminium material, while Tab. 3.15 resumes the carter dimensions.

Table 3.15 Final external carter dimensions

Carter external dimensions [m]	Carter internal diameter [m]	Carter radial minimum thickness [m]	Height of plenum chamber [m]
Φ0.37 x 0.07	0.33	0.02	0.03

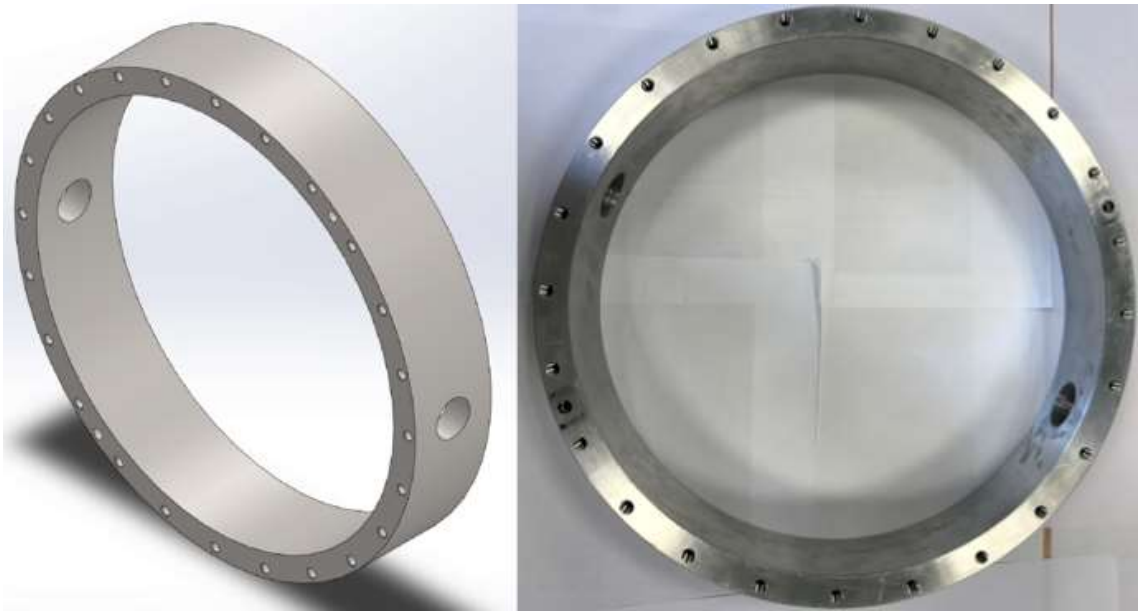

Fig. 3.36 ORC External carter, SolidWorks drawing and real prototype

Full assembly

As for the air Tesla prototype, once rotor, stator and plenum chamber dimensions were defined, all other components needed to be assessed, such the rotor shafts, the bearings and the screws of the carter.

A particular feature, which differentiates the air and ORC expanders, is the magnetic coupling of the latter one. Indeed, in order to have a completely sealed turbine configuration, the power shaft has been designed in order to convey power through a magnetic coupling.

Each designed component has successively been verified according to the formula displayed in Section 3.2.1 and the final dimensions of each part have been resumed in Tab. 3.16.

Finally, each drawn component has been put together in a final assembly, as shown in Fig 3.37, in order to verify if some inconsistencies were present. Once the final drawing was completed, all components were ordered and assembled in Linea Laboratory of University of Florence.

Table 3.16 Final ORC prototype dimensions

Bearings	**Total number of channels**	**Gap Stator/Rotor [m]**	**Power shaft diameter [m]**	**Washers dimensions**
SKF 61817–2RZ SKF 3207 A–2ZTN9/MT33	60	0.001	0.035	0.004x0.008x0.0001
Fluid side shaft diameter	**Rotor screws**	**Disks–shaft screws**	**Carter screws**	**O–ring section [m]**
0.085	M4	M5	M8	0.00262

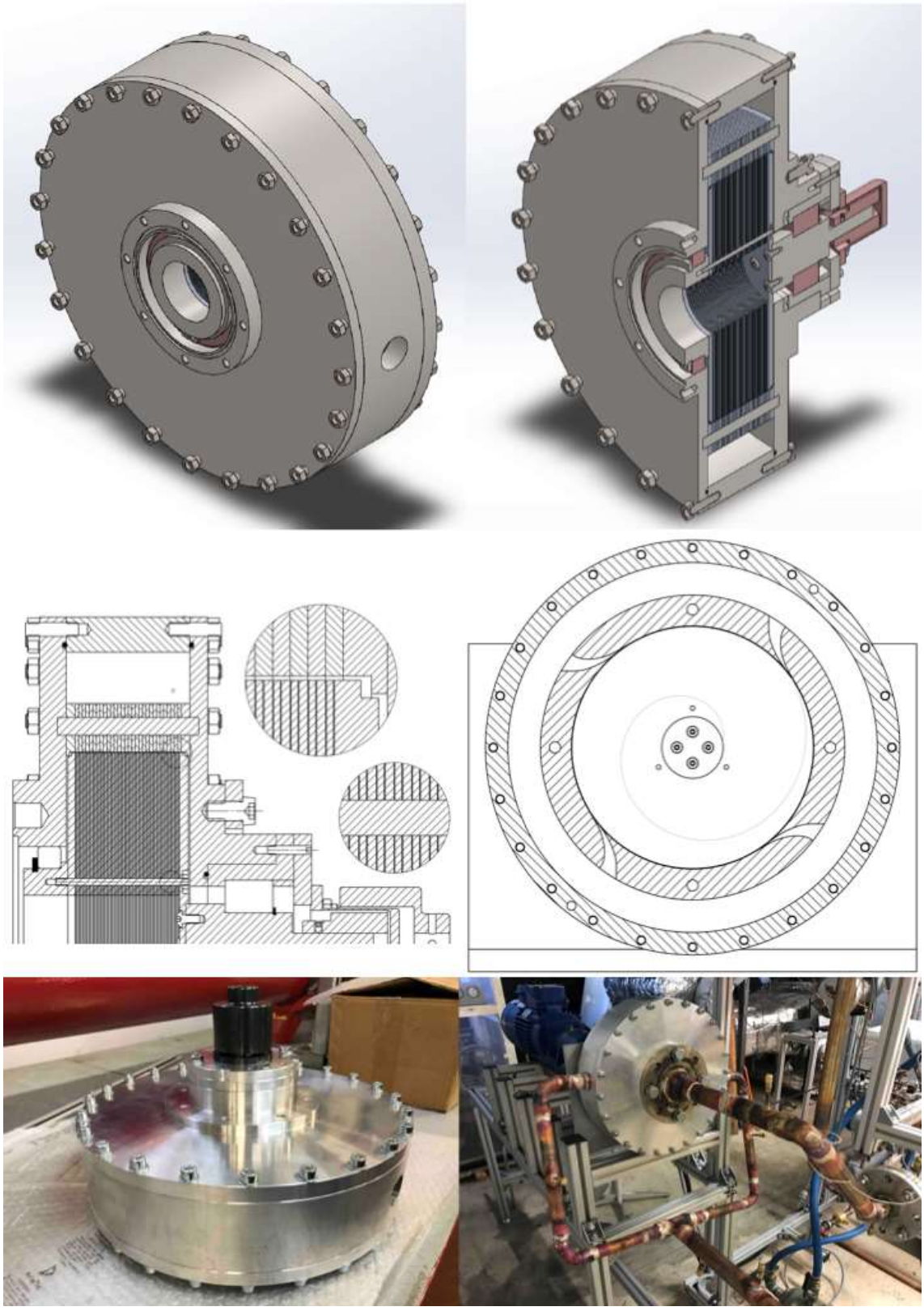

Fig. 3.37 SolidWorks drawing and real ORC Tesla prototype

3.4 3D CFD Model

The fluid behaviour inside the Tesla turbine rotor of both prototypes was analysed through the means of computational fluid dynamics; while only for the ORC configuration stator–rotor coupled simulations were carried out.

The study of the real gas flow through the rotor of the Tesla turbine was performed with three–dimensional CFD simulations, based on compressible Reynolds averaged Navier–Stokes equations by the ANSYS Fluent software. The spatial discretization method utilized is finite volume with cell–centered approach and the mesh generated is hexahedral with local refinement.

3.4.1 Air Tesla turbine

The CFD analyses were performed in order to determine the flow field within the disks of the air Tesla turbine prototype. For this purpose, three–dimensional, double precision, pressure based, steady and implicit simulations were set. Velocity formulation was considered in the absolute frame and both laminar and transitional k–kl–omega models were analysed. The k–kl–omega was selected as turbulence model in order to evaluate the transitional behaviour of the flow, given that in this scheme transition is not fixed but triggered by velocity fluctuations in the boundary layer.

The pressure–velocity coupling scheme was set as SIMPLE, with second order upwind scheme for momentum and PRESTO! scheme for pressure equation. The geometry of the model was created with the software ICEM on a disk with outer diameter 125 mm, inlet diameter 32 mm and gap between disks of 0.3 mm. A real fluid model was considered for air, with Peng–Robinson scheme enabled.

The parameters set for the developed simulations are summarized in Tab. 3.17 and the computational domain is shown in Fig. 3.38 where the inlet, the outlet, and the periodic boundary conditions are specified. The inlet mass flow was imposed as boundary conditions on the inlet, setting also the inlet flow angle. Pressure field was imposed on the outlet. The rotation feature of the rotor was applied by considering frame motion with fixed frequency of rotation.

Table 3.17 Parameters set for ANSYS simulations of air Tesla prototype.

Fluid	Air (real)
Channel mass flow rate	0.001119 [kg/s]
Outlet Pressure	131234 [Pa]
Rotational velocity	18000 [rpm]
Inlet flow angle	87 [°]

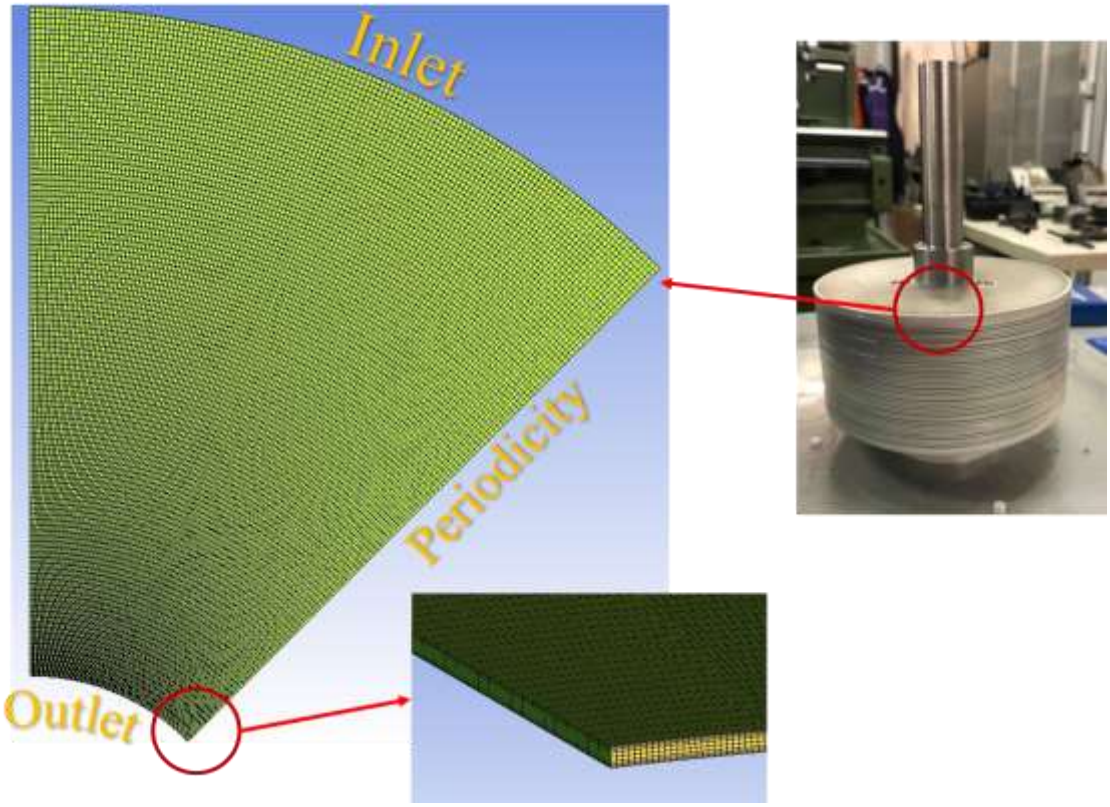

Fig. 3.38 Three–dimensional computational domain of the Air Tesla turbine rotor (very coarse mesh)

A mesh sensitivity analysis was carried out for CFD simulations, using both laminar and k–kl–omega turbulence models. Several meshes were created, with the objective of investigating the effects of elements size and local refinement. In each case, the y^+ was selected to be lower than 1 for being able to evaluate transition effects when the suitable turbulence model is applied; the mesh was refined in particular at inlet and near walls, where the laminar separation was expected to occur. The imposed cell growth ratio was always set to be lower than 1.1.

Tangential velocity was selected as parameter for mesh independence assessment, as this parameter proved to be the most affected by the grid characteristics, especially for transitional simulations (Fig. 3.39, where only significant meshes are displayed for the sake of clarity). In Fig. 3.39c, it is noticeable that a mesh with at least 800000 nodes ensures grid independence, while coarser meshes determine errors in absolute tangential velocity computation, both at inlet and at outlet.

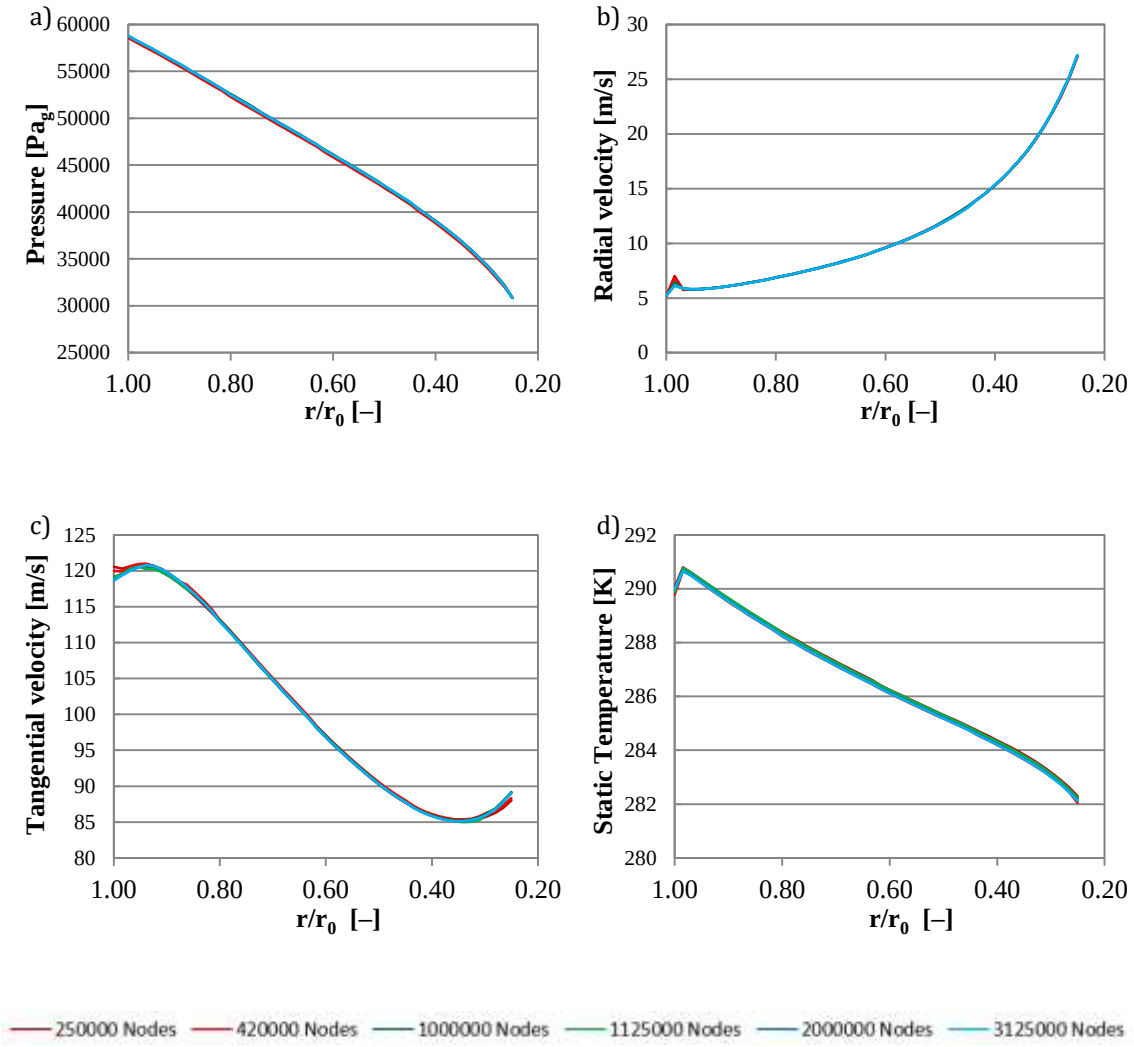

Fig. 3.39 Results of the mesh sensitivity analysis performed on simulations with transitional turbulence model

3.4.2 ORC Tesla turbine

Rotor analysis

As for the air Tesla turbine, the CFD analyses were performed in order to assess the flow field behaviour within the disks of the ORC Tesla turbine prototype The governing reduced Navier–Stokes equations are discretized with a cell–centered method with PRESTO! scheme for pressure, third order MUSCL scheme for density, momentum and energy and second order upwind for turbulent kinetic energy, specific dissipation rate and momentum thickness. To compute the variable gradients, both the Green–Gauss cell–based and the least–squares cell–based methods were applied. The turbulence closure was done both with the laminar model and the Langtry–Menter transitional shear stress transport model (SST) with second order discretization.

In this case k–kl–omega model could not be applied due to the sharp pressure gradients at rotor inlet. The equations were implicitly solved by applying the SIMPLE approach as pressure correction scheme.

The gas density was calculated by Helmholtz Free Energy (FEQ) EOS, which is valid for different fluids [202]–[205]. The properties of mixtures like R404a were calculated on the basis of those of each single component by using the ideal mixing rules; the properties of pure fluids R134a, R245fa and R1233zd(E) were obtained from literature [202], [205], [206]. The main properties of pure fluids are summarized in Tab. 3.18.

Table 3.18 Main properties of the pure fluids

Fluid	MW [kg/kmol]	T_c [K]	P_c [Pa]	ρ_c [kg/m^3]
R134a	102.03	374.21	$4.06 \cdot 10^6$	511.90
R143a	84.04	345.86	$3.76 \cdot 10^6$	431.00
R125	120.02	339.17	$3.62 \cdot 10^6$	573.58
R245fa	134.05	427.16	$3.65 \cdot 10^6$	516.09
R1233zd(E)	130.5	438.8	$3.57 \cdot 10^6$	478.9

The computational domain is shown in Fig. 3.40 where the inlet, the outlet, and the periodic boundary conditions are specified. The inlet velocity and the outlet pressure fields were imposed as boundary conditions on the inlet and the outlet, respectively. The periodic boundary conditions were introduced for the sidewalls of half a quarter of a cylindrical domain in order to speed up computations. The rotation feature of the rotor was applied by considering frame motion with fixed frequency of rotation.

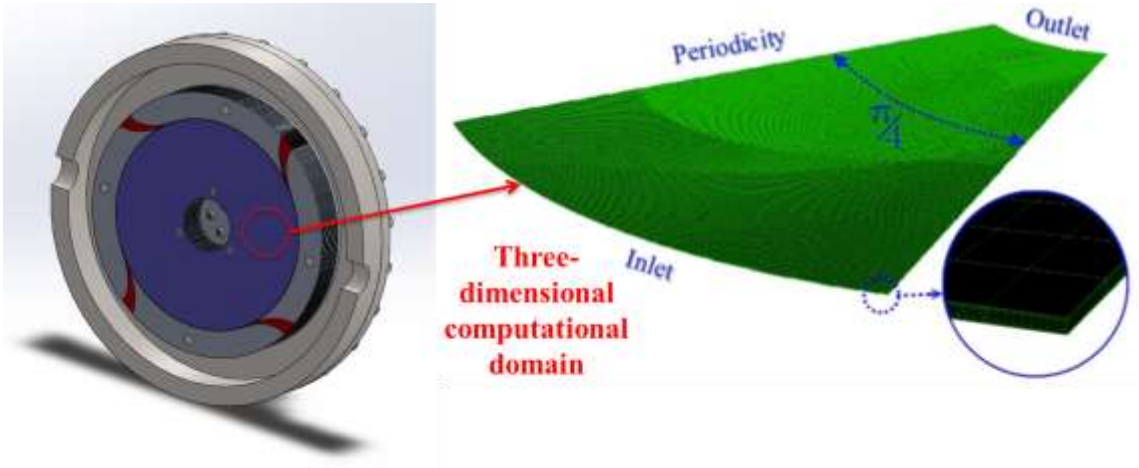

Fig. 3.40 Three–dimensional computational domain of the Tesla turbine rotor

Several diverse meshes, differing on the number of nodes (from 37000 to 1.87 million), were examined in order to assess the mesh independency of computational results. Since tangential velocity is the parameter which is the most dependent on mesh size, particularly at domain inlet, Fig. 3.41 resumes the results of the mesh sensitivity analysis in terms of inlet tangential velocity and computational time ratio versus computational cell number. In order to attain a proper compromise between accuracy and computational time, the 273000 nodes mesh was finally chosen.

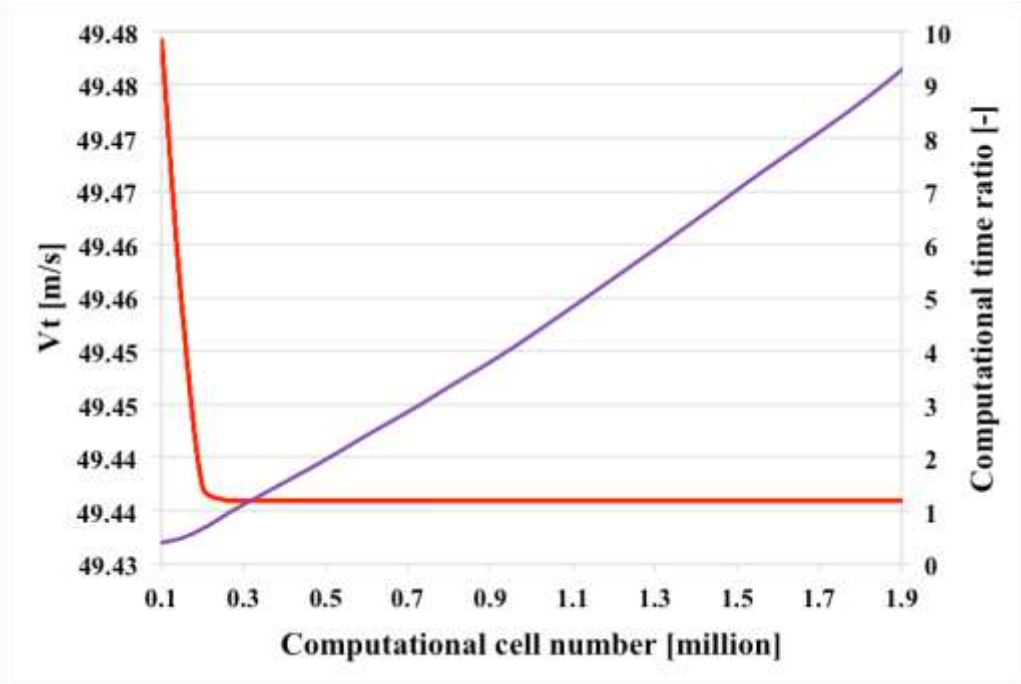

Fig. 3.41 Mesh sensitivity of inlet tangential velocity at rotor inlet and computational cost of accuracy

Stator – Rotor analysis

In order to assess the interaction between stator and rotor, as well as to analyse the sources of inefficiency that are triggered in the gap between them, a separated approach analysis does not provide accurate results; therefore, a coupled stator–rotor simulation was set.

The numerical analyses of the Tesla turbine with coupling of stator and rotor were performed with the same settings specified for the single rotor analyses. The turbulence closure was still obtained with the Langtry–Menter transitional shear stress transport model (SST) with second order discretization. The computational domain is displayed in Fig. 3.42. The rotor still presents the same outlet and periodic boundary conditions, while the inlet has been specified in the plenum chamber. Indeed, the geometry is composed by the stator, the rotor, the plenum chamber and the gap between stator and rotor. The inlet and the outlet pressure fields were imposed as boundary conditions. The periodic boundary conditions were introduced for the sidewalls of a quarter of a cylindrical domain

in order to speed up computations. The rotation feature of the rotor was applied by considering frame motion with fixed frequency of rotation.

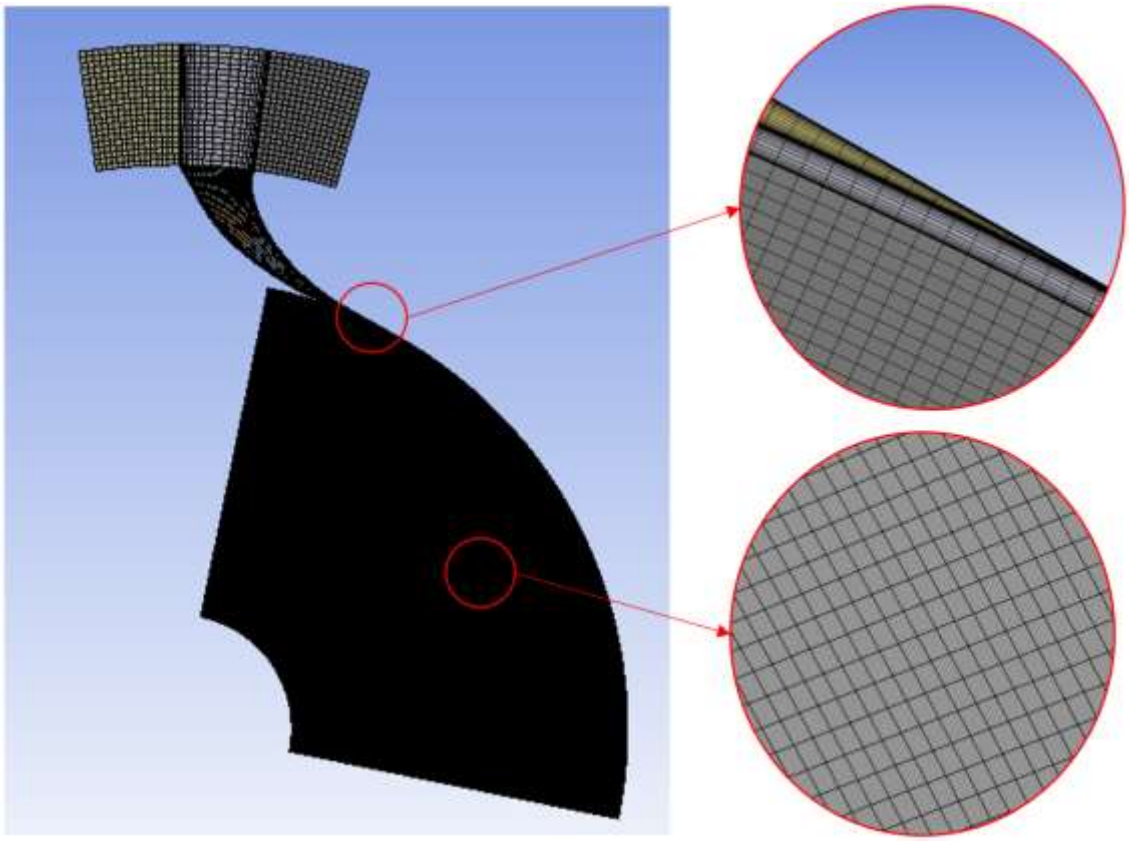

Fig. 3.42 Three–dimensional computational domain of the stator–rotor configurations

Several diverse meshes, differing on the number of nodes (from 108,100 to 4.45 million), were examined in order to assess the mesh independency of computational results. With the aim to achieve the optimum grid size as a compromise between accuracy and computational time, the 3.23 million nodes mesh was finally selected, by fulfilling the minimum change of rotor inlet tangential velocity of $1*10^{-3}$ m/s.

3.5 Test benches setup

3.5.1 Air Tesla turbine

In order to test experimentally the performance of the air Tesla turbine, it was arranged on a test bench (Fig. 3.43a) equipped with several measurement sensors. The turbine was connected to an electric motor (brushless type) that controlled the rotational speed during the tests through a servo drive. By means of a continuous exchange of electricity between the electric motor and the grid, the brushless motor was able to operate as generator or as brake, according to the power produced by the turbine. The torque and, consequently, the power produced by the turbine was measured by a torque meter (Lorenz, nominal torque 10 Nm, 0.2% FS) connected between the turbine and the brushless motor through flexible couplings.

The Tesla turbine was tested with air as working fluid elaborated by a centrifugal compressor, whose speed could be regulated with a variable–frequency inverter. Fig. 3.43b shows the schematic of the air test rig composed by the compressor, the Tesla turbine and the measuring instruments.

The thermodynamic conditions upstream the Tesla turbine were measured by installing a T–type thermocouple and a pressure transducer (Honeywell, 100 psi, 0.1% FS) in the space between the casing and the stators. At the outlet, another thermocouple was installed to measure the temperature downstream the turbine, whereas the pressure was imposed as the ambient pressure due to the direct discharge in the environment. The mass flow rate was measured by using a calibrated flange directly connected to the pipeline between the compressor and the Tesla turbine. The temperature before the flange was measured by a T–type thermocouple (copper and constantan wires, uncertainty of ± 0.5 K) and the pressure difference across the flange was acquired by a Setra pressure transducer (–5 to 5 PSID, 0.1% FS).

The experimental measurement chain, the data acquisition and control system are showed in Fig. 3.44. All signals were acquired by a National Instruments Field Point and processed by a software specifically developed in LabView® environment, which was also used to control the servo drive and set the Tesla rotational speed.

In addition to obtain the thermodynamic boundary conditions, the software computed the power produced by the expander by the measured torque and the imposed rotational speed. The mass flow rate was obtained by elaborating the measured pressure difference across the calibrated flange and the temperature upstream by using the equations implemented in the software after a previous calibration of the flange.

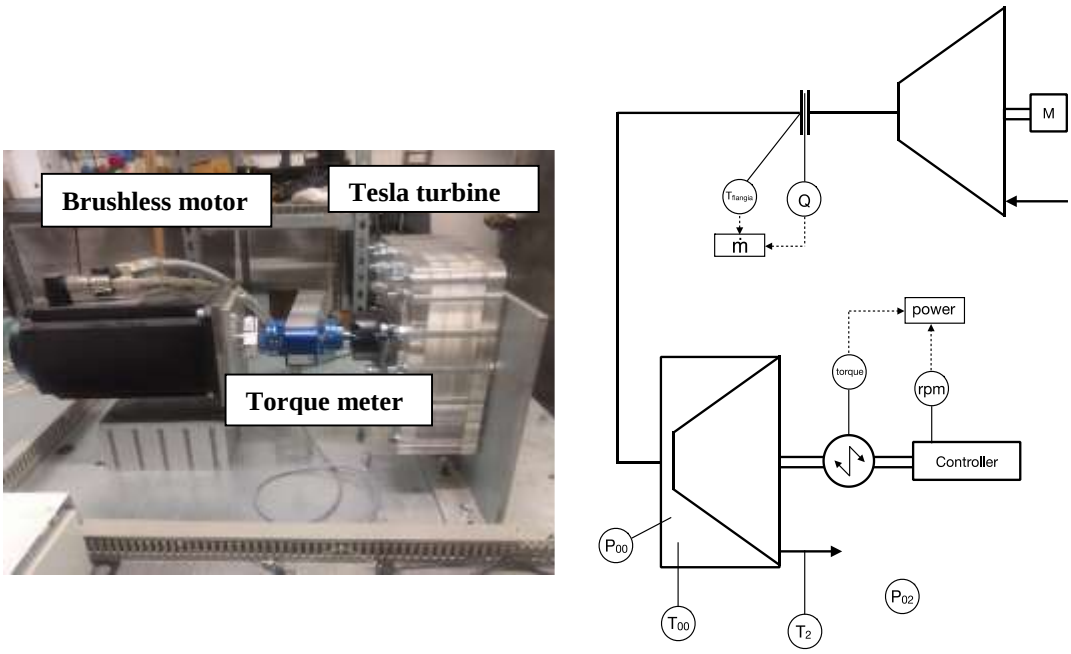

Fig. 3.43 Test bench setup: a) Mechanical connection; b) Test rig schematic

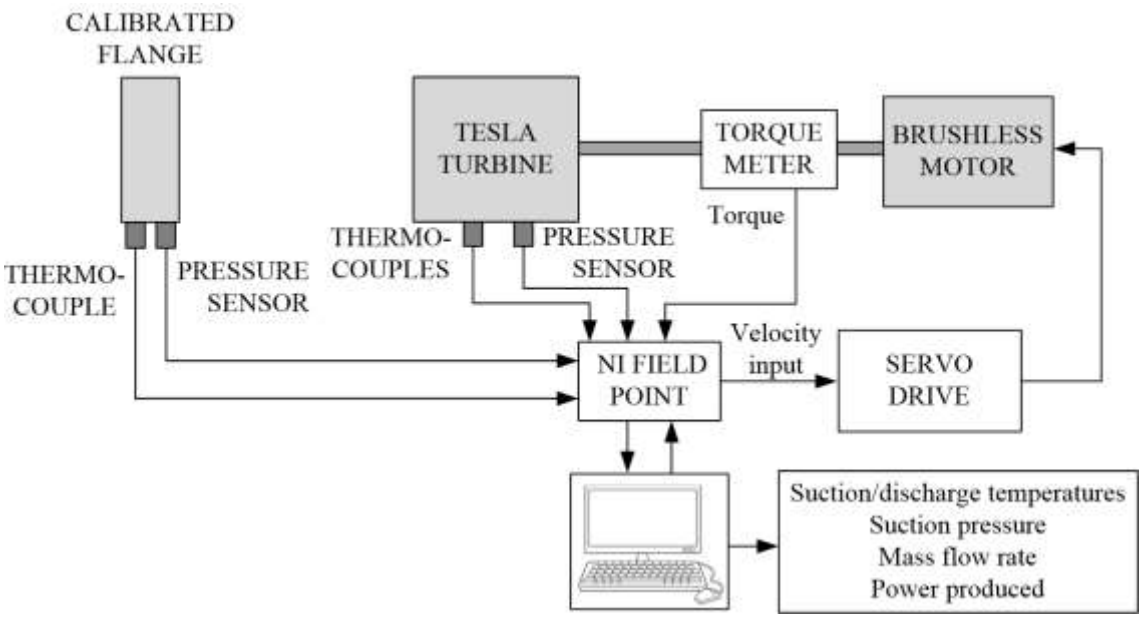

Fig. 3.44 Measurement chain and control system of the test rig

3.5.2 ORC Tesla turbine

Université de Liège test bench

The schematic of test bench of *Université de Liège* is displayed in Fig. 3.45. It is basically a recuperative organic Rankine cycle, utilizing R1233zd(E) as working fluid. It was constructed using standard mass produced components from the HVAC industry, as well as from some specific industrial prototypes, such as the evaporator. The test bench consists of an evaporator, a condenser, a brazed plate recuperator (which however was by–passed during these tests), a pump and a liquid receiver. The pump is a Wanner Hydra–Cell piston pump, which is controlled via a frequency inverter. The maximum volume flow rate and outlet discharge pressure are 30.6 l/min (at 1450 rpm) and 103 bar (at 750 rpm), respectively. The heat source is an industrial heater, which allowed a maximum heat input of about 150 kW.

The thermodynamic conditions upstream and downstream the Tesla turbine were measured by installing T–type thermocouples (copper and constantan wires, very stable measuring range between −200 °C and 200 °C, with a maximum error of ± 0.5 K) and piezoresistive pressure transducers (Keller, 30 bar, 0.25% FS). The mass flow rate was measured by using a precision Coriolis Krohne Optimass 1400Cr flow meter.

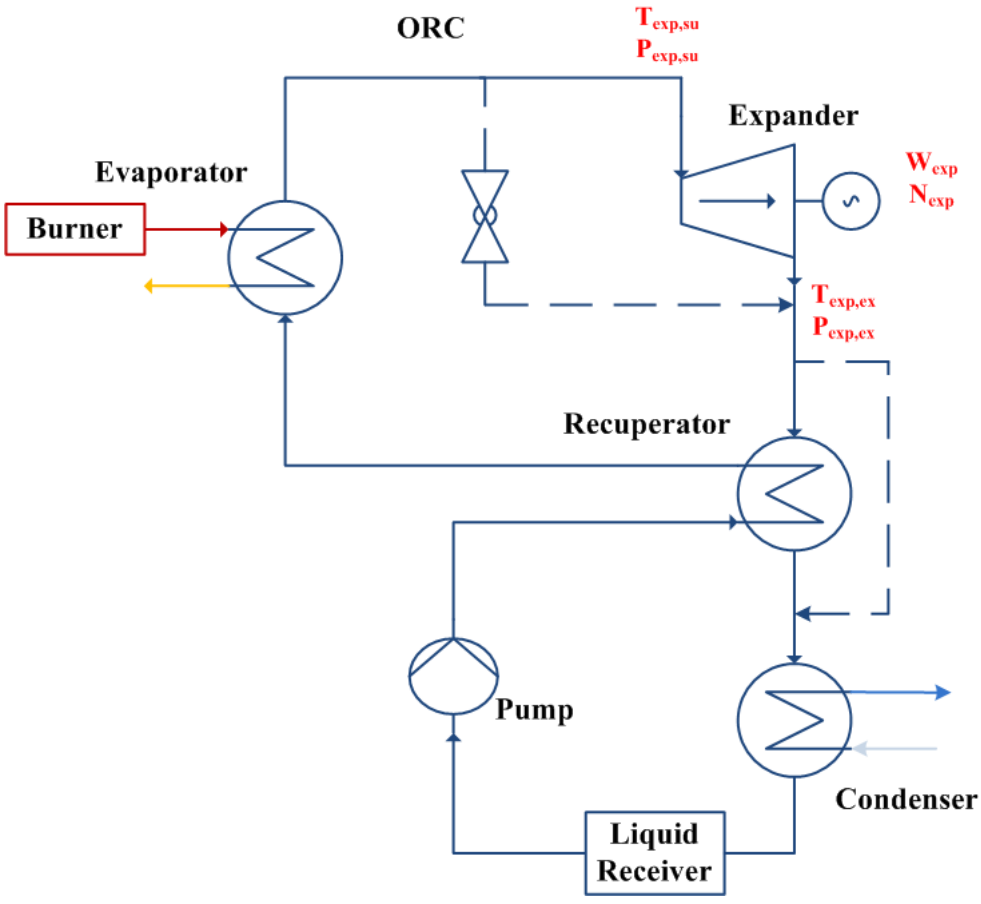

Fig. 3.45 Schematic of *Université de Liège* test bench (recuperative ORC)

The turbine was connected to an electric motor (Perske D 6800 Mannheim 1) that controlled the rotational speed during the tests through a four–quadrant frequency inverter (ABB ACS501–01). The torque and, consequently, the power produced by the turbine was measured by a torque meter (Messtechnik DRBK, nominal torque 50 Nm, 0.5% FS) connected between the turbine and the motor through flexible couplings, as displayed in Fig. 3.46. All signals were acquired by a National Instruments® platform and processed by a software specifically developed in LabView® environment. Tab. 3.19 resume the measurements ranges and accuracy of the sensors.

Table 3.19 Sensors ranges and absolute accuracies

Quantity	Unit	Range	Maximum error (full scale)
Temperature	[K]	73–473	0.5
Pressure	[bar]	0–30	0.3
Mass flow rate	[kg/s]	0–1	2.0 E–3
Torque	[Nm]	0–50	0.25

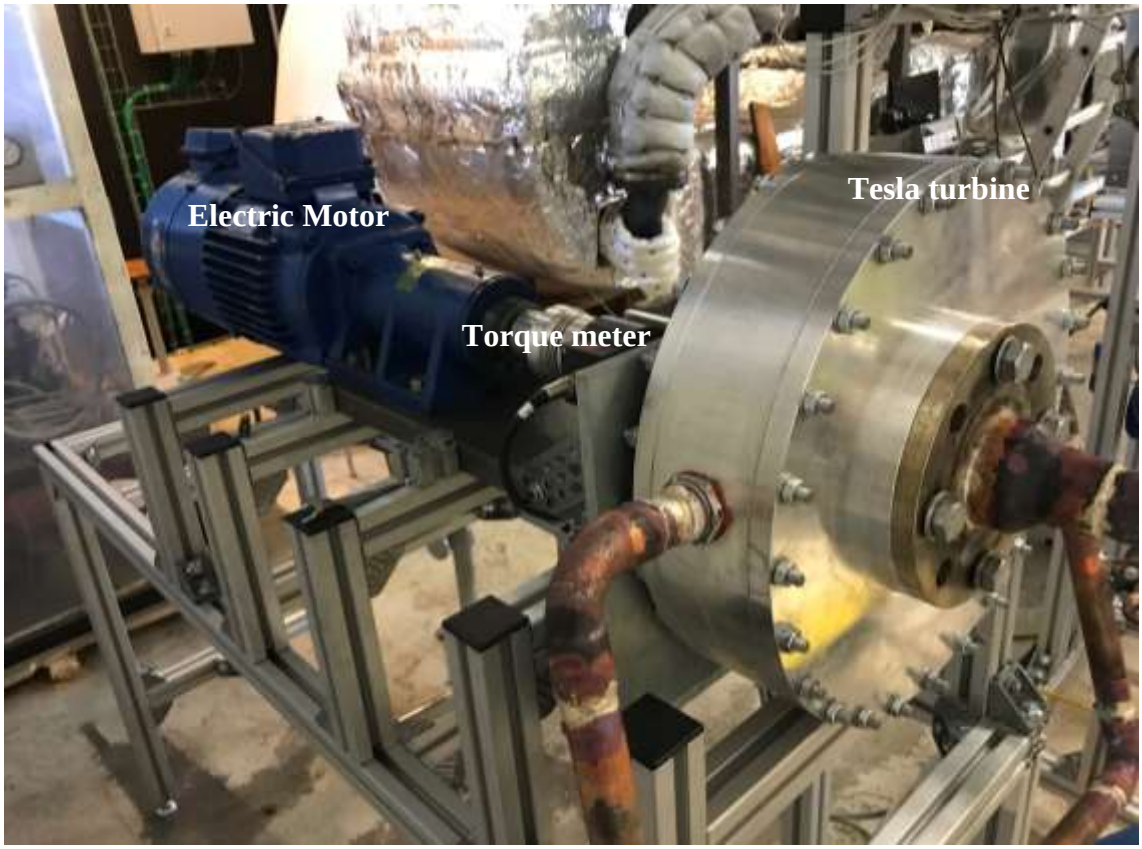

Fig. 3.46 Mechanical connection of ORC Tesla turbine to electric motor

4 Analysis of Results

The results obtained in this project are resumed in this chapter. The chapter is organized in three main Sections, (i) 2D EES model, (ii) computational fluid dynamics and (iii) experimental results.

All types of analysis are fundamental for understanding the principle of operation, as well as the research and industrial prospects of the Tesla turbine. The numerical model developed in EES allows evaluating the performance, varying lots of degree of freedom of the turbine, such as the geometry or the thermodynamic conditions. Computational fluid dynamics permits to understand flow characteristics, which are difficult to simulate in a 2D code; while experimental results are the true litmus paper in order to confirm the validity and the perspectives of an emerging technology.

4.1 2D model Results

4.1.1.1 Air Tesla turbine

The results obtained with air as working fluid have been computed in order to assess the performance potential of the rotor, as the parametric study displaying each component influence on the turbine efficiency and power will be deeply developed in the next Section, when organic working fluids will be considered. Nonetheless, a parametric analysis on the performance of air Tesla turbines as function of the main design variables, which are non–dimensionalized following common practice in turbomachinery [187], [188], has been carried out.

Rotor output/input diameter ratio (D_3/D_2) and rotor channel width over inlet rotor diameter (b/D_2) were recognized as the most significant design parameters for the Tesla turbine. Exit kinetic energy and absolute exit flow angle, which should be as low as possible, were identified as two critical parameters to assess as they deeply influence the performance of the turbine. The trend of rotor efficiency η as function of (D_3/D_2) and (b/D_3) is shown in Fig. 4.1.

Rotor efficiency η is notably affected by different values of outlet/inlet diameter ratio. With decreasing D_3/D_2, the larger kinetic energy at discharge, due to the higher axial component of velocity, appears to be somewhat compensated by the larger rotor surface available for momentum exchange between the fluid and the disks. Nonetheless, an optimizing configuration can be selected. Indeed, values of D_3/D_2 close to 1 do not allow the complete conversion of work, while values of D_3/D_2 close to 0.1 increase kinetic energy losses at discharge. The right trade–off is therefore necessary.

The channel width over rotor inlet diameter (b/D_2) parameter strongly affects the efficiency of the rotor. This is due to the influence of the Reynolds number in the laminar

flow regime, which can be best explained re–arranging its definition and remembering that $b = D_h/2$ (Eq. 4.1).

$$\mathrm{Re} = \frac{\rho * v_r * D_h}{\mu} = \frac{\dot{m}_c}{2\pi r b \rho} \cdot \frac{\rho * D_h}{\mu} = \frac{\dot{m}_c}{\pi r \mu} \tag{4.1}$$

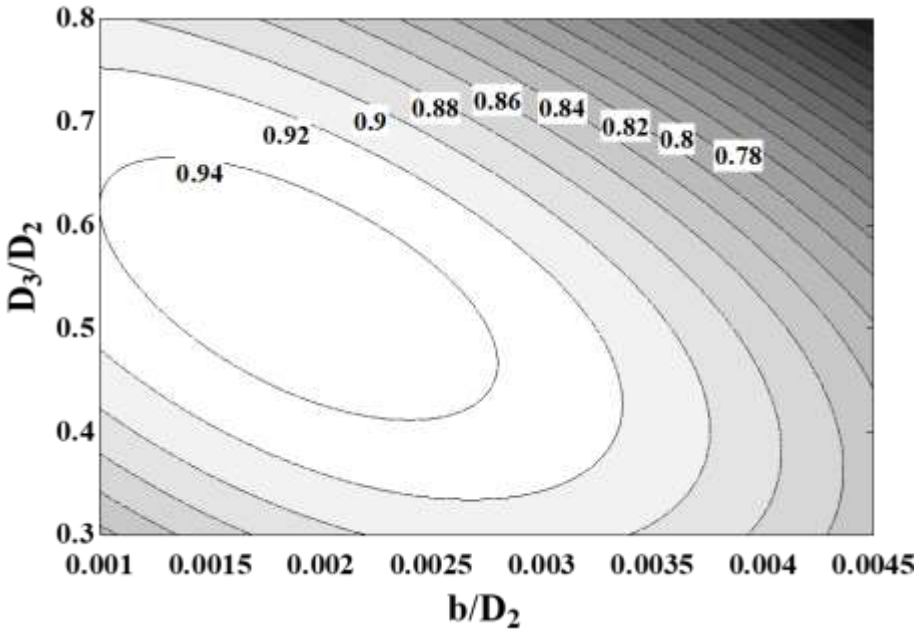

Fig. 4.1 Rotor Efficiency η vs D_3/D_2 and b/D_2

The load coefficient behaviour Ψ as function of (D_3/D_2) and (b/D_2) is shown in Fig. 4.2. The inlet rotor diameter (b/D_2) strongly affects the load coefficient Ψ; furthermore, the load coefficient is also sharply influenced by (D_3/D_2). The momentum exchange is favoured as the wet area is increased (values of D_3/D_2 close to 0.1); nevertheless, the exit diameter should not exceed a certain limit, the penalty being an increase of the residual tangential velocity, leading to higher discharge losses. From the points of view of rotor efficiency η and load coefficient Ψ, values of $0.35 < (D_3/D_2) < 0.45$ and $0.005 < (b/D_2) < 0.015$ appear therefore recommendable.

Another essential parameter, which is definitely influenced by the gap between disks, is the absolute exit angle (Fig. 4.3). Lower absolute exit angles are desired in order to have an efficient recovery of discharge kinetic energy. A reduction of the gap between the disks is certainly beneficial to this end. The decrease of α_3 for smaller values of b is due to the reduction of the tangential component, as well as to the increase in the radial component of absolute velocity. The reduction of tangential velocity, as can be noted from Eq. (3.47), is due to the increase of viscous momentum transfer for small values of b. On the other hand, the radial velocity increases because of the continuity (Eq. 3.25).

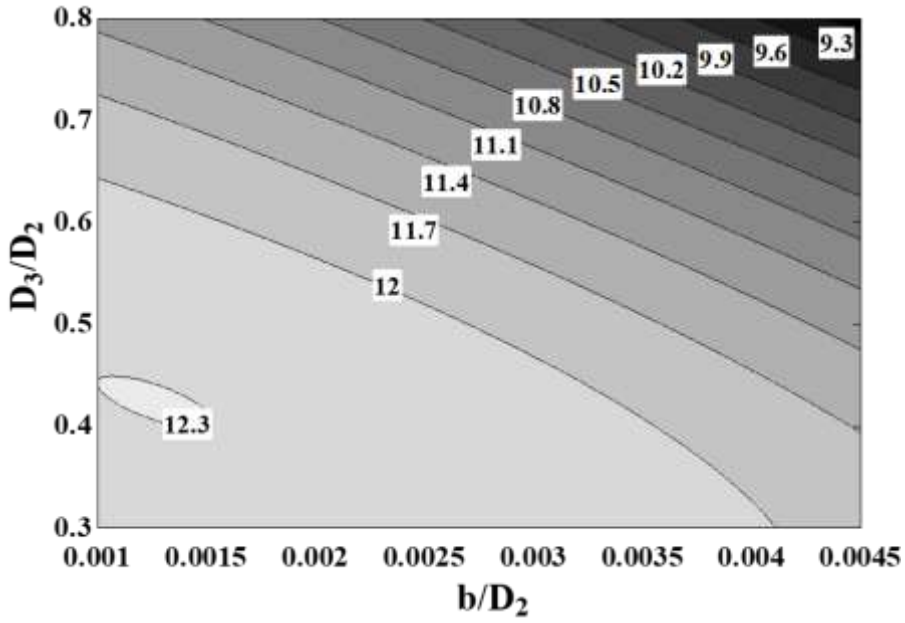

Fig. 4.2 Rotor Load Coefficient Ψ vs D_3/D_2 and b/D_2

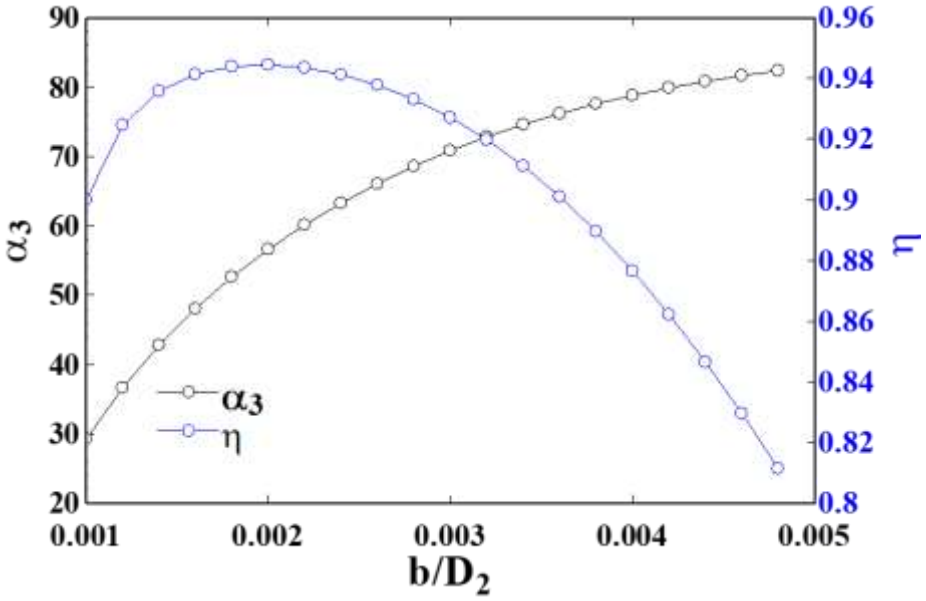

Fig. 4.3 Exit fluid angle α_3 and efficiency of the turbine vs b/D_2, for $D_3/D_2 = 0.44$

The trend of the absolute velocity and of its components with variable gap is showed in Fig. 4.4. The absolute exit velocity displays a minimum, which is determined by opposite trends of the two components of velocity (radial and tangential) as a function of b/D_2. The minimum of the exit kinetic energy E_{kin3} corresponds to the maximization of the rotor efficiency.

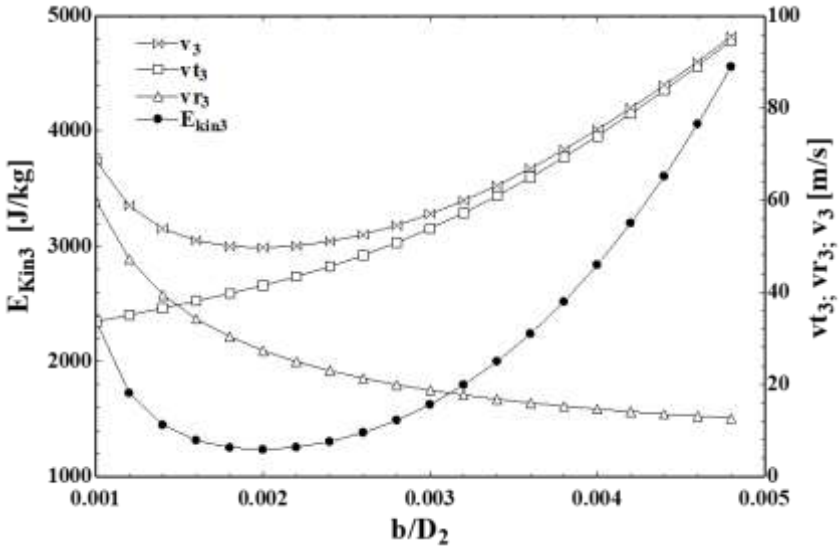

Fig. 4.4 Exit kinetic energy vs non dimensional gap

Fig. 4.5 displays the absolute exit angle and the efficiency behaviours against the flow coefficient Φ. An increase in the flow coefficient leads to a decrease of the absolute exit angle. This is due to an increase of the radial component of the fluid, which therefore turns the fluid in the axial direction. If values of exit flow angles below 50° are sought, then a flow coefficient in the range $\Phi = 0.2$ should be selected; under these conditions, the rotor efficiency is still high – in the range of 0.94.

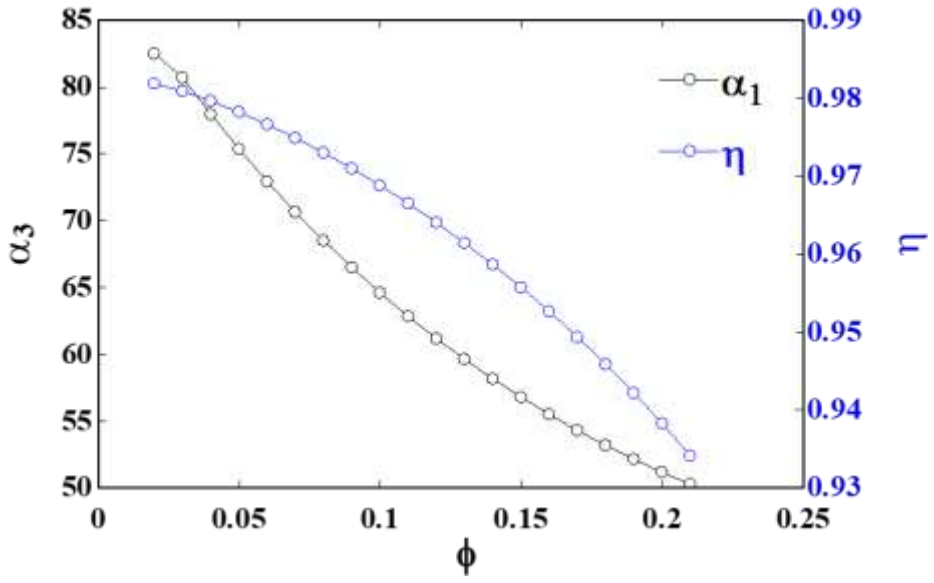

Fig. 4.5 α_3 and η versus Φ

The analysis of the rotor utilizing air as working fluid allowed confirming the possibility of achieving high efficiencies when the turbine is properly designed. Next Section will be focused on the influence of not only the rotor but also of the other components on the performance of the turbine, taking n–Hexane as working fluid.

4.1.1.2 ORC Tesla Results

4.1.2 Component analysis

In order to assess the performance potential of the Tesla turbine for organic Rankine cycle applications, several parametric analyses were carried out: the performance parameters were evaluated as functions of the main geometric variables and operating conditions. The n–Hexane was adopted as the working fluid for the investigation of each component influence on the performance of the turbine, due to its favourable low expansion ratio and the well suitable thermodynamic critical conditions (e.g. low critical pressure 3.034 MPa and high critical temperature 234.67 °C [207]). Furthermore, hydrocarbons are among the best compromises between environmental constraints (having zero ODP and GWP and fairly low toxicity [207]), and good thermodynamic cycle features for use in ORCs. The only drawback might be the flammability, but the rapidly increasing safety standards, coupled to typically small or micro sizes for which Tesla expander technology is generally conceived, make hydrocarbons particularly attractive for these applications. Initially, single variable optimization was carried out, in order to determine the most critical parameters for the Tesla turbine; successively combined parameters optimization was performed, to understand the mutual influence of the most meaningful parameters both on efficiency and power.

Individual variables optimization

In this Section, the influence of each single parameter on the performance of the turbine is analysed, while keeping constant all the other geometric and thermodynamic parameters.

Rotor inlet diameter

The rotor inlet diameter is one of the most significant parameters, as it plays a primary role on both the power production and the size of the machine. When fixed thermodynamic conditions and velocity are assumed at the stator output, a higher rotor diameter is associated to a larger throat section. Therefore, according to continuity equation, a higher mass flow rate is obtained. The increased of mass flow rate is also responsible for an increase of velocity at rotor output (as radial velocity will strongly increase as is progress to the exit). It leads to higher kinetic energy losses, which become unbearable when the outlet Mach number value overcomes the inlet one. High kinetic energy losses are not acceptable; therefore, the value of D_2 is limited. The work output per unit mass of the expander is defined by the Euler equation Eq. (4.2).

$$\text{Work} = v_{t2} \cdot u_2 - v_{t3} \cdot u_3 \tag{4.2}$$

Since both the first and second terms increase with larger rotor diameter (increase in peripheral velocity), the specific work output presents an optimization value, while the overall power output, mainly influenced by the mass flow rate, has a monotonically increasing trend. The rotor and the total efficiencies are affected by increasing the rotor isentropic enthalpy drop and mass flow rate, thus their values decrease increasing rotor diameter, as shown in Fig. 4.6.

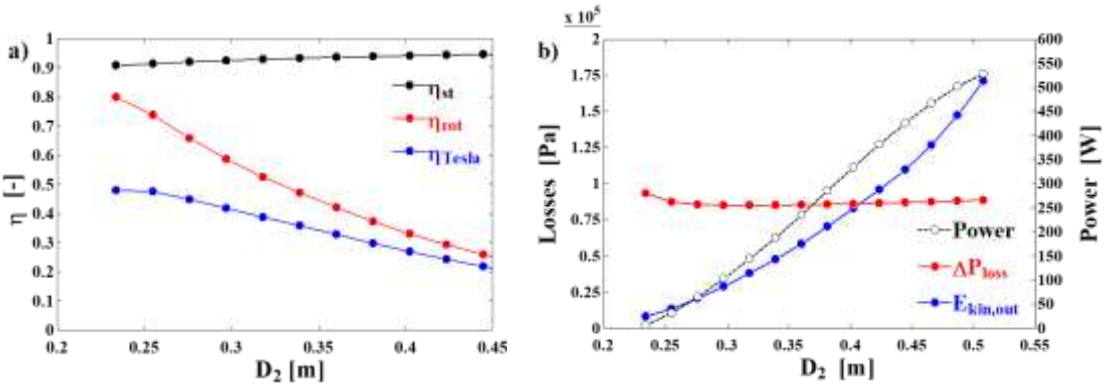

Fig. 4.6 Turbine efficiency a) and turbine power and losses b), versus rotor inlet diameters

Camber line length

The length of the camber line in the stator channel is another parameter that affects turbine performance. An increase of the camber line, while keeping the other geometrical parameters fixed, is responsible for the reduction of the throat section width and, consequently, of the mass flow rate. According to Eq. (4.2), the flow velocity at the rotor outlet decreases and generates a higher work output. Therefore, an increase in the length of the camber line has the same effect of a reduction of the rotor inlet diameter (Fig. 4.7).

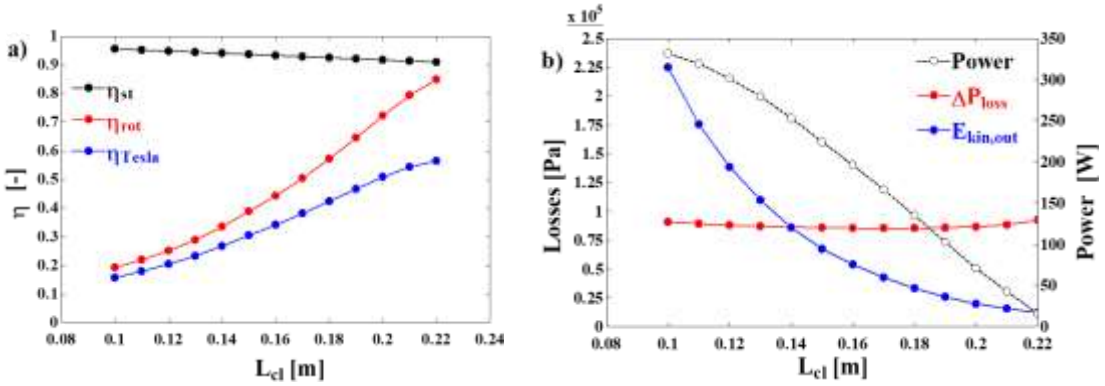

Fig. 4.7 Turbine efficiencies a) and power and losses b), versus length of nozzle camber line

Height and width of the nozzle throat section

The height and the width of the throat section directly influence the geometry and the variables at the stator output, especially the mass flow rate, which shows a linear trend. The maximum value of mass flow rate is determined by the sonic condition at the throat section: decreasing the height of the rectangular area, the continuity equation ensures a reduced flow rate and, consequently, a lower expansion rate inside the rotor. The velocity components are both proportional to the flow rate, Eqns. (3.25) – (3.27), so the Mach number increases rapidly, thus increasing the overall efficiency (Fig. 4.8).

The reduction of throat width is responsible for a more than linear decrement of flow rate and velocity at rotor outlet that results in a reduction of power output and kinetic energy losses at rotor exit, whereas the expander efficiency shows a linear increment.

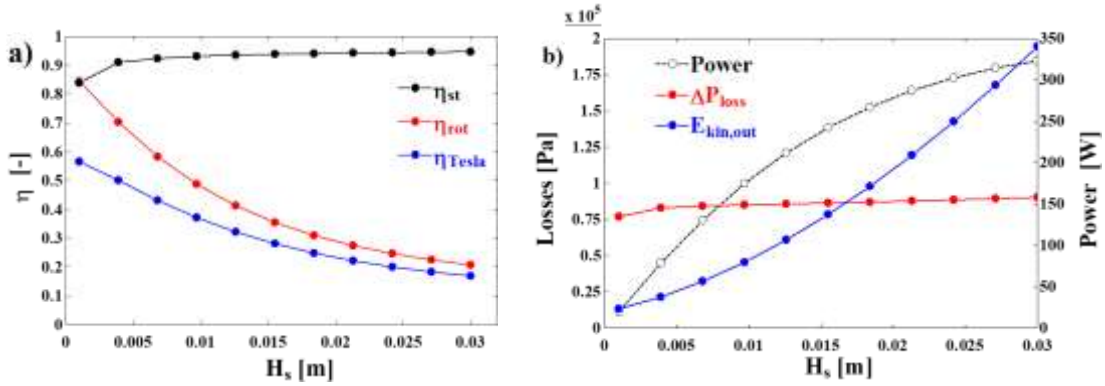

Fig. 4.8 Turbine efficiencies a) and power and losses b), versus height of the throat section

Rotor Channel height

The channel height, which is present in Eq. (3.27), is directly proportional to tangential velocity and inversely proportional to radial velocity. It leads to a maximization of the rotor outlet Mach number and, accordingly, to a minimization of outlet rotor pressure. This value of channel height corresponds to the one optimizing both rotor and turbine efficiency, as lower velocities are associated to lower kinetic energy losses (Fig. 4.9).

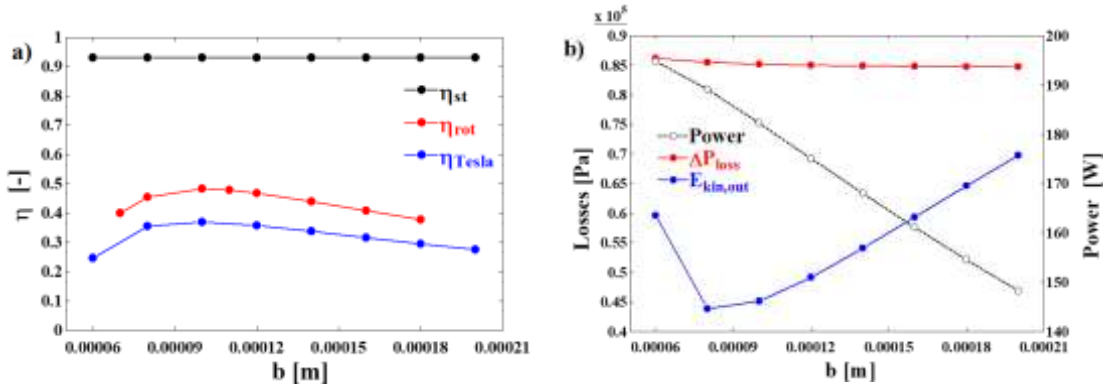

Fig. 4.9 Turbine efficiencies a) and power and losses b), versus disk channel height

Outlet rotor diameter

The variation of D_3 presents a significant minimum value of tangential velocity at rotor outlet, as can be deducted from Eq. 3.27. Similarly to the previous analyses, the optimizing value of outlet/inlet rotor diameter ratio D_3/D_2 is characterized by the minimum energy loss and, therefore, the maximum turbine efficiency (Fig. 4.10).

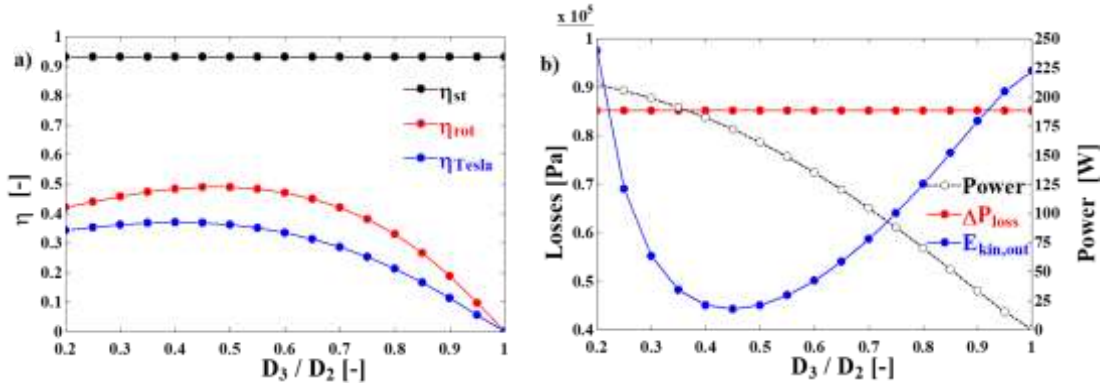

Fig. 4.10 Turbine efficiencies a) and power and losses b), versus in/out rotor diameters ratio

Thermodynamic conditions

The effects of the thermodynamic conditions on the turbine performance were also considered; particularly, total conditions at the stator inlet, for a determined superheating level were evaluated. High pressures correspond to high flow rates (conversely to high temperature, which partially reduce it due to a decrease in the fluid density) and subsequently to high expansion rates. As reported in [111], there are specific thermodynamic conditions, which generate negative relative velocities at rotor inlet, then a flow reversal (these are linked to the actual velocity at throat section). Therefore, for a particular value of inlet total pressure P_{00}, the relative velocity becomes zero. In this condition, the rotor inlet radial velocity component V_2 has the minimum value and maximizes turbine efficiency (Figs. 4.11a and 4.11c).

The static pressure at the stator output determines the pressure range into the convergent channel and the mass flow rate. The effect of increasing P_2 (which correspond to lowering the mass flow rate) is the same as a reduction of P_{00}, therefore an efficiency optimizing working point for the machine can be found (Figs. 4.11b and 4.11d).

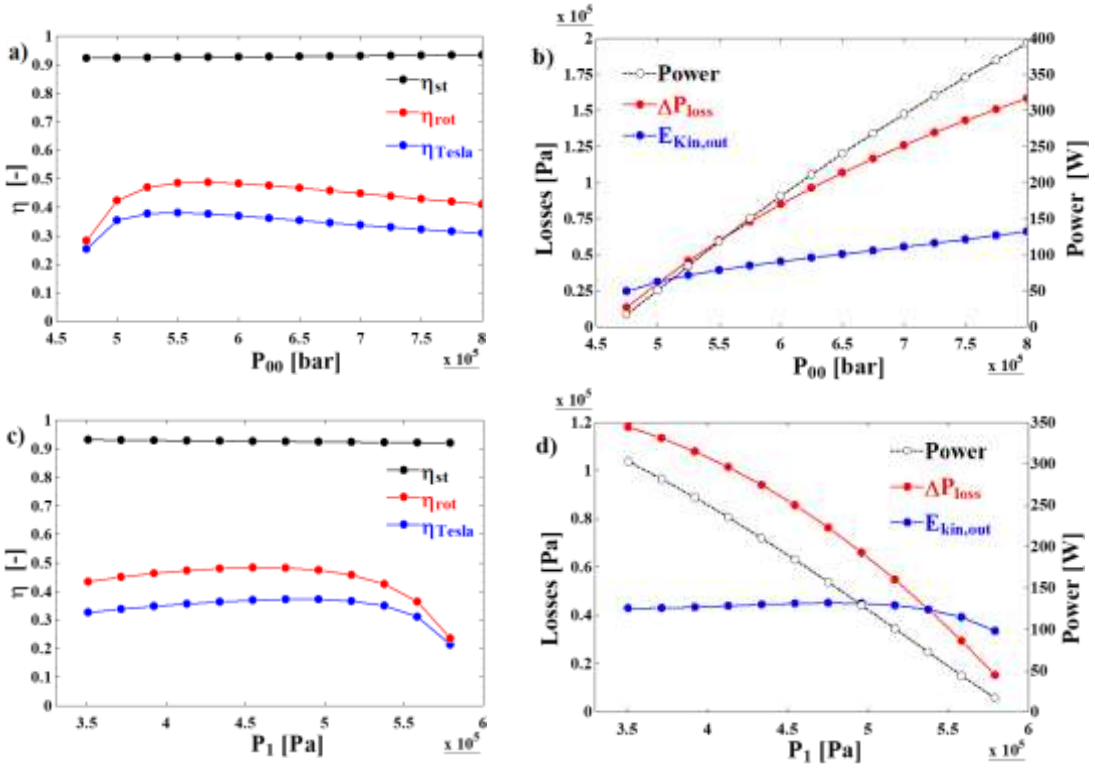

Fig. 4.11 Turbine efficiencies versus a) Total inlet pressure, c) Stator outlet static pressure and power and losses at various b) Total inlet pressure; d) Stator outlet static pressure

Rotor peripheral speed

The variation of the rotor peripheral speed influences the relative tangential velocity w_{t2}, thus a value of peripheral speed above which a reversal flow condition is generated exists. At disk exit, the pressure decreases when the rotational speed increases, due to momentum equilibrium in radial direction (similar to the behaviour of pumps where $H \equiv rpm^2$). Rotational speeds in the range between 4000 and 6000 rpm seemed to guarantee an optimised value of the expander efficiency, as displayed in Fig. (4.12).

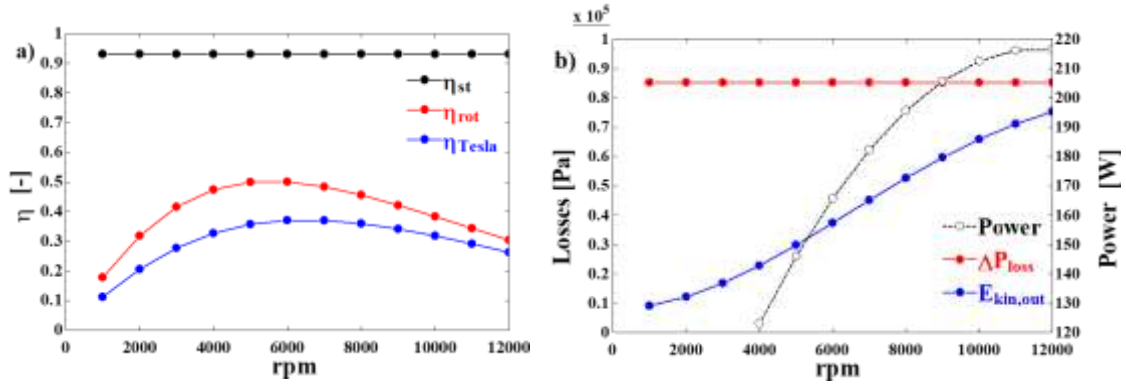

Fig. 4.12 Turbine efficiencies a) power output and losses b), versus rotational speed

Combined variables

Single parameter optimization is necessary in order to understand the influence of each element on turbine performance, but it is not enough in order to achieve a complete optimization procedure due to the mutual influence of each variable. As reported in Fig. 4.13, the combined assessment of both inner and outer disk diameter displays an improvement of the expander efficiency (η) at reduced values of stator outlet diameter D_1 and rotor outlet diameter D_3. This trend is directly linked to the reduction of the mass flow rate; power output conversely exhibits an opposite behaviour.

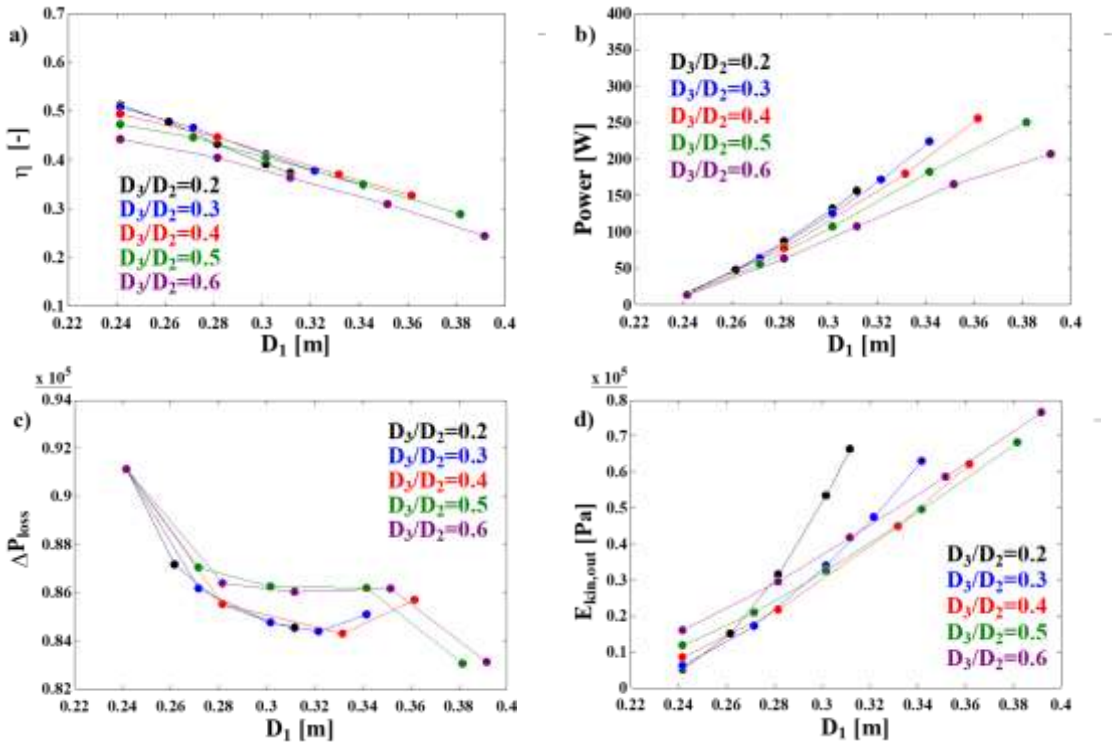

Fig. 4.13 Turbine efficiency a), power output b), between stator–rotor losses c) and kinetic energy at rotor outlet d) versus stator output diameter at variable in/out rotor diameter ratio

A further assessment was developed taking into account the influence of the diameters and adding an additional parameter, namely the camber line length, which is directly linked to the external radius value. In agreement with previous results, the efficiency is maximised when the throat section is at the minimum value; it can also be pointed out that long camber lines allow better results when coupled with low D_3/D_2 (Fig. 4.14). These conditions allow the achievement of relatively high overall turbine efficiency (over 60%).

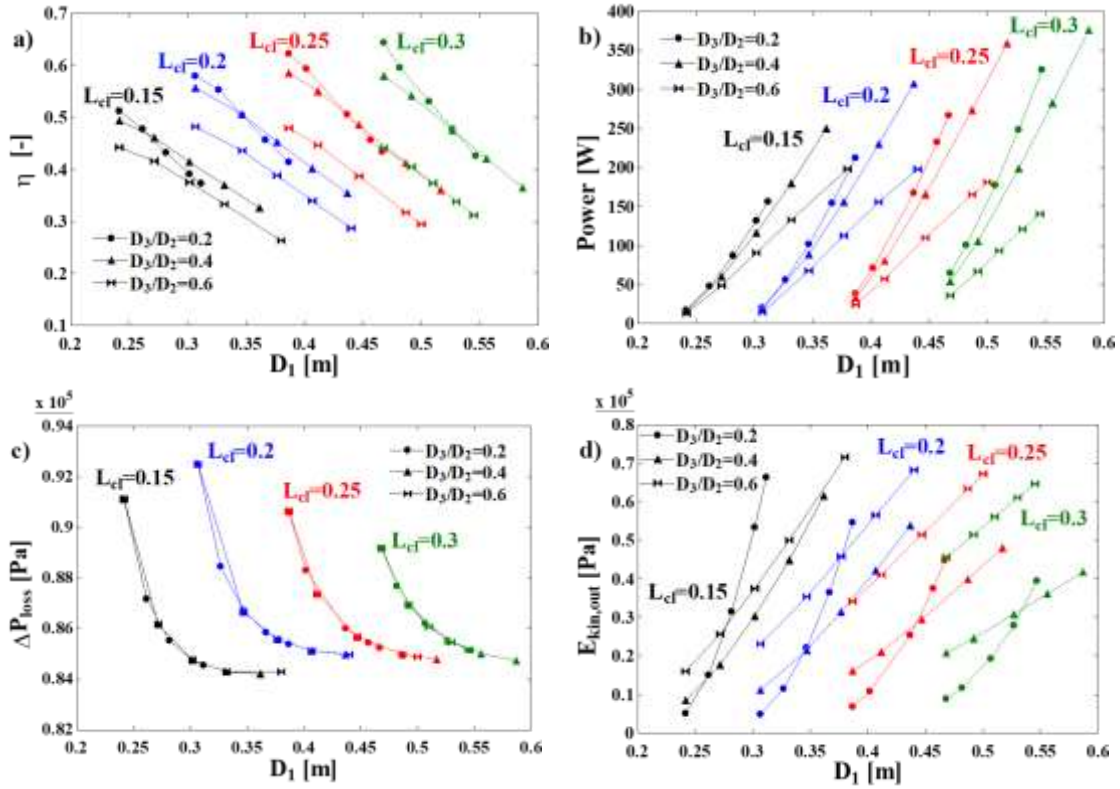

Fig. 4.14 Turbine efficiency a), power output b), stator–rotor losses c), and kinetic energy at rotor output d) versus stator exit diameter, for different rotor in/out diameter ratio and camber line length

A comprehensive study of the stator should also include the camber line length, the throat length (which are function of the total maximum number of feasible channels Z_{max}) and the actual number of channels (Z_s). The throat section is directly linked to the total number of channel, decreasing quadratically as Z_{max} increase. The curves in Fig. 4.15 show that the optimal conditions are obtained for higher turbine dimensions (r_0 and D_1), due to a reduction of the throat section (because the number of channels is maintained constant) and therefore a reduction of mass flow rate. Furthermore, Fig. 4.15 displays that for a fixed external 0.35 m diameter, the maximum efficiency can be kept constant by reducing both the external radius (larger turbine size), and the length of the camber line (therefore keeping constant the throat section). As discussed, this is due to the counterbalancing effects, which maintain the mass flow rate constant. In this way, a Tesla turbine may achieve a more compact shape and the throat length can be reduced. A higher number of stator channels (Z_S in Fig. 4.15) is responsible for steeper curves and lower global efficiency at fixed values of r_0 and Z_{max}.

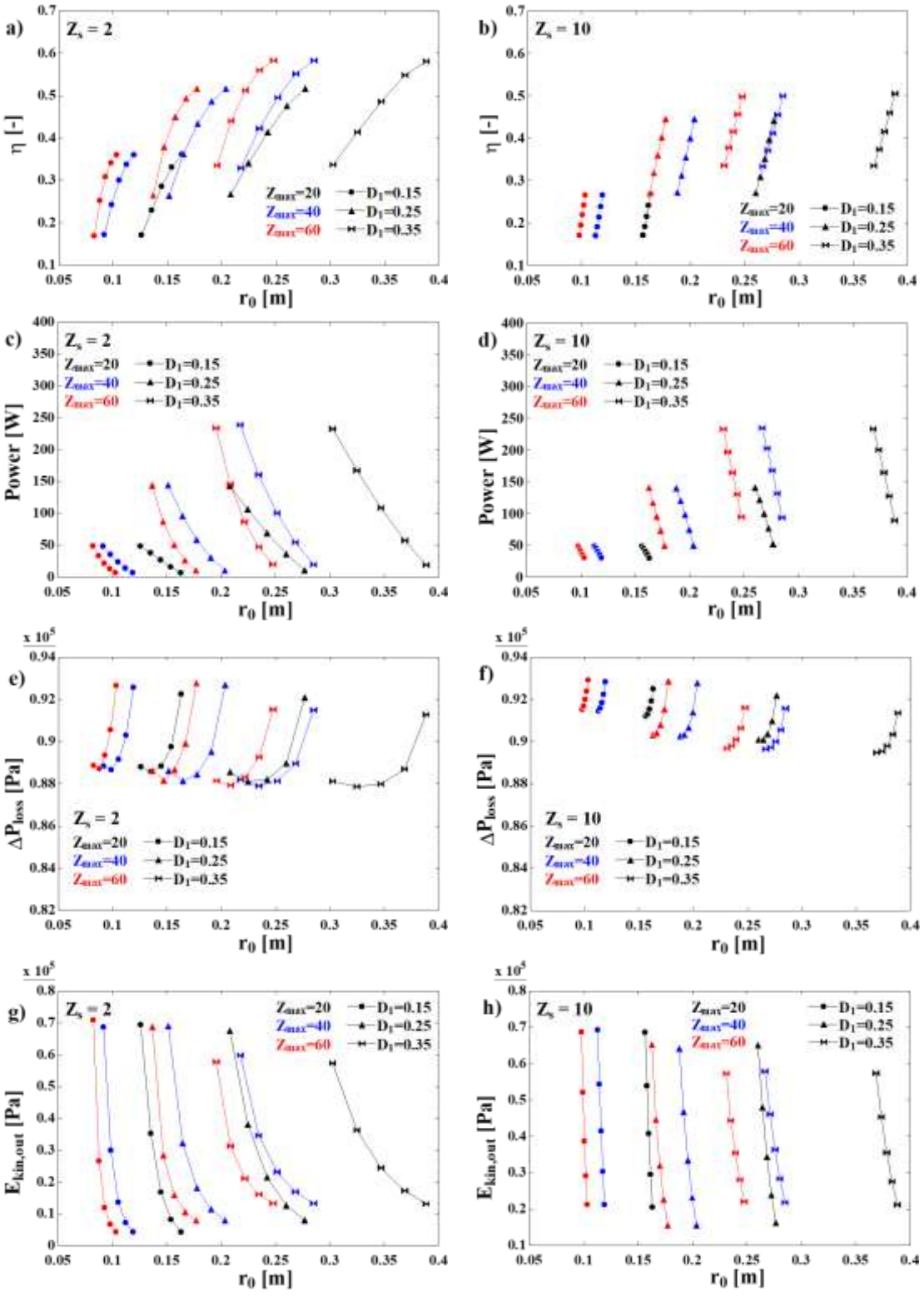

Fig. 4.15 Turbine efficiency, power, losses between stator and rotor, kinetic energy at rotor outlet at different stator inlet and exit diameters, with 2 nozzle channels (a, c, e, g) and 10 nozzle channels (b, d, f, h)

The analysis of the nozzle throat height can be performed while taking also into account the rotor channels height *b* and the thickness of the disks *s*. This study was performed using a constant value of throat width (*TW*=1 mm) and 10 channels in the rotor. The minimum values of *b* and *s* were chosen taking into account potential economical manufacturing processes and possible structural issues. The curves present a turbine efficiency optimizing value as function of b for both the analysed rotor diameters (0.8 mm for D_1=0.15 m and 1 mm for D_1=0.35 m), while the increase of disks thickness is responsible for a wider throat section and a higher mass flow rate (higher power output), which entail a reduction of turbine efficiency η (Fig. 4.16).

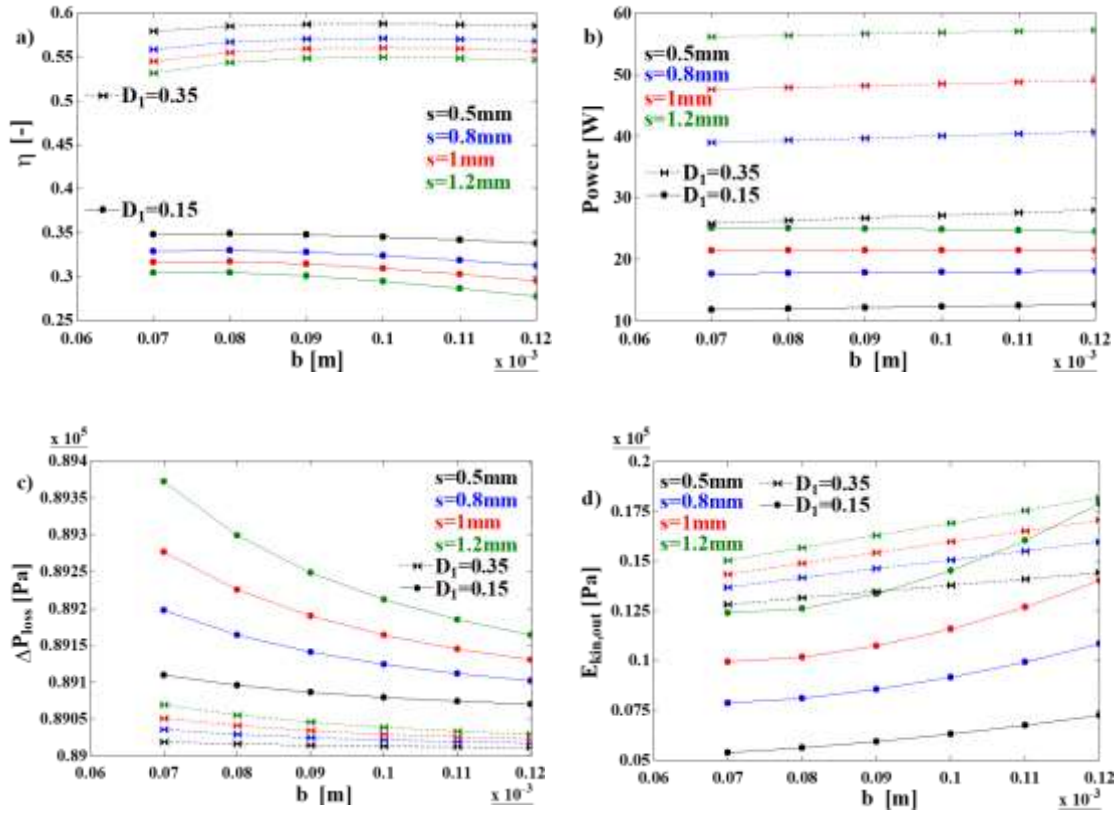

Fig. 4.16 Turbine efficiency a), power output b), stator–rotor losses c), kinetic energy at rotor outlet d) at various channel height b for different values of plates thickness s

The change of the number of rotor channels (and consequently H_s) does not modify the behaviour of the curves and the optimising value of *b*, although a reduction in the number of rotor channels n_{ch} can significantly improve the overall efficiency of the turbine (Fig. 4.17). This is directly linked to a reduction of throat section; therefore, lower mass flow rates are obtained at fixed thermodynamic conditions. The use of just 2 channels for every module allows reaching efficiency values (η) near 60%, also reducing the influence of the disks thickness. On the other hand, the reduction in number of channels implies a drop of power output, which can be counterbalanced by utilizing a higher number of modules.

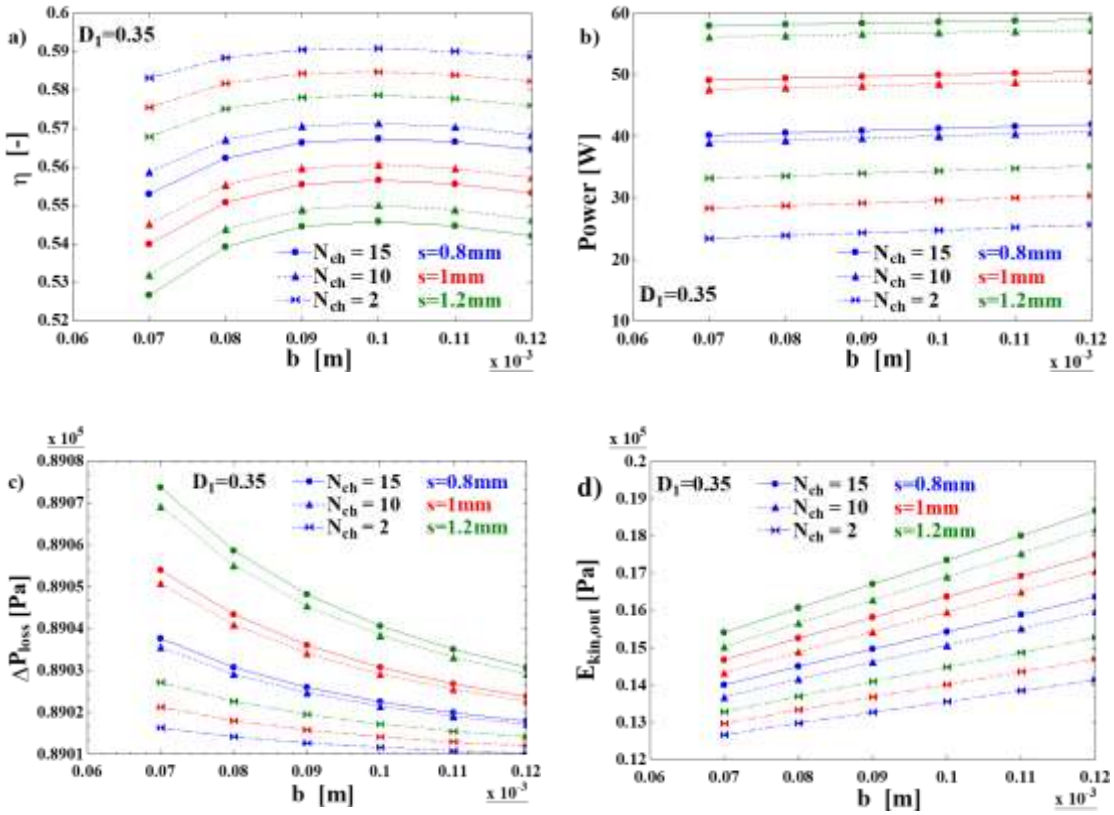

Fig. 4.17 Turbine efficiency a), power output b), stator – rotor losses c), kinetic energy at rotor outlet d) at various plates thickness s for different channel heights b and three configurations with different total number of channels N_{ch}

Collecting the result of the performed sensitivity analysis guidelines for design of an optimized and balanced Tesla turbine can be drawn; these may be summarised in the following:

- ***Stator***, 4 convergent nozzles with a squared throat section (1x1 mm);
- ***Rotor***, 10 channels 0.1 mm wide each; disks diameters ratio around 0.4; the external radius was not fixed, in order to evaluate the effects of the turbine size.

After fixing the geometry of the turbine a sensitivity analysis as function of expander operating conditions was carried out. Originally, the superheating temperature and the pressure drop ΔP inside the stator were fixed: the minimum value of total pressure P_{00} and total temperature T_{00} were set, in order to avoid sonic condition at the stator outlet. An optimal value of P_1 was found, as the turbine efficiency is affected both by the mass flow rate and the enthalpy of the fluid: the former decreases with reducing P_{00} (leading to a positive effect on the turbine efficiency η), whereas the latter has the same effect of T_{00} (positive when the temperature increases). The same considerations can be extended to the power output, which shows an optimizing value at lower total inlet pressure, due to the increasing density and mass flow rate (Fig. 4.18a).

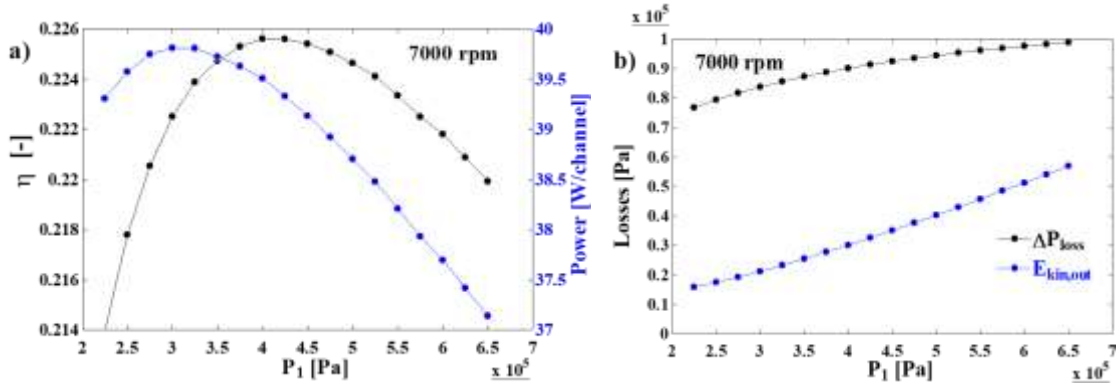

Fig. 4.18 Turbine efficiency and power output a) and losses b) versus static pressure at stator outlet (D_1= 0.15 m)

The sensitivity analysis to the rotational velocity showed that the expander efficiency η and power increase at higher speeds, with a slight peak placed at lower pressure (the limited extension of the curve at higher rpm is due to the high Mach number reached at the rotor outlet, Fig. 4.19).

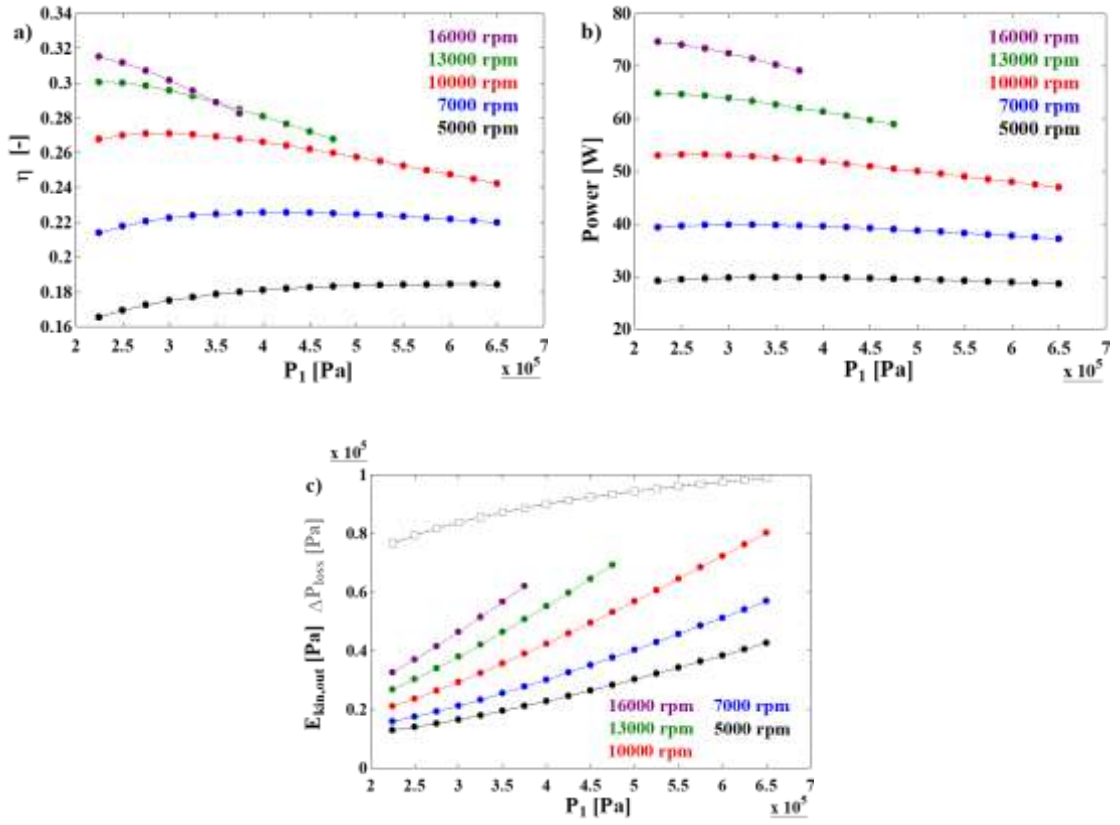

Fig. 4.19 Turbine efficiency a), power output b), and losses c) versus static pressure at stator outlet for variable rotational speed (D_1 = 0.15 m)

In Fig. 4.20, the expander efficiency and the power output are presented as function of rotational speed and stator inlet total pressure P_{00}. For all different P_{00}, an optimised value

of rpm is always present, lower at higher total inlet pressure; efficiency is enhanced at lower P_{00}, due to higher rotational speed and lower absolute tangential velocity at rotor outlet, which imply higher work production. The presence of a maximum may be explained through the momentum balance: higher velocity increases the work output, but, at the same time, also the expansion ratio and the enthalpy drop through the rotor are enhanced. In this way, from the definition of total to static efficiency $\eta = \frac{work}{h_{00}-h_2}$, the appearance of an optimised value is present.

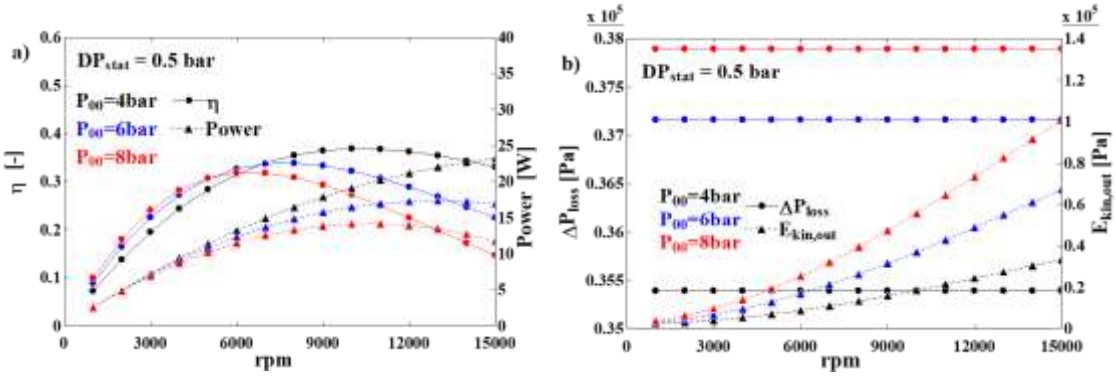

Fig. 4.20 Turbine efficiency and power output a), losses b) versus rotational speed at variable stator static pressure drop (D_1 = 0.15 m)

The superheating temperature level does not have a strong influence on Tesla turbine efficiency η when compared to the effects provided by pressure and rotational speed.

A further analysis, which needs to be carried out, is the one to assess the influence of up–scaling the Tesla turbine dimensions (for example doubling the diameter), while keeping the outlet/inlet rotor diameters ratio and throat section width fixed. The performance curves obtained show a very close behaviour to the one, which resulted, from the previous results (Figs. 4.19 and 4.20) but with improved values (Figs. 4.21 and 4.22). It was found that the up–scaled expander holds an optimized efficiency value for a static outlet pressure P_1 of 3.3 bar and a rotational speed of 10,000 rpm.

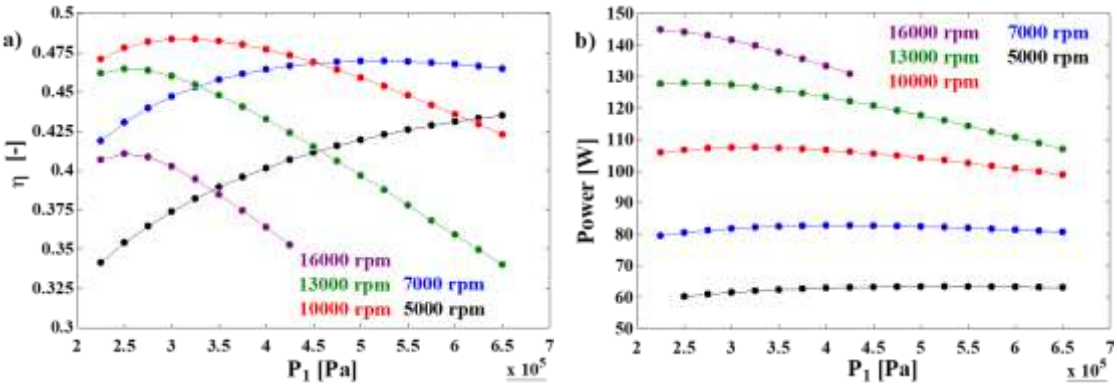

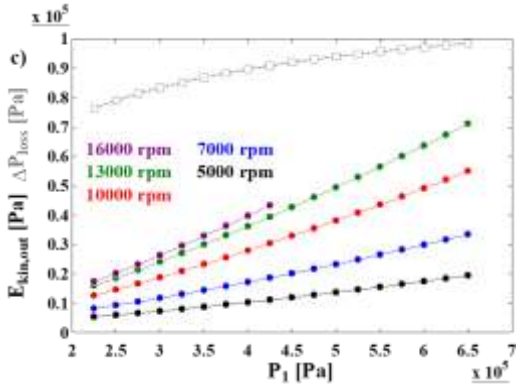

Fig. 4.21 Turbine efficiency a), power output b) and losses c) versus static pressure at stator output, at variable rotational speed for the up–scaled expander (D_1 = 0.3 m)

A very small stator static pressure drop ΔP_{stat} (in this case 0.5 bar) allows the reduction of inlet total pressure, optimising rotational speed and, on the whole, an increase of the turbine efficiency η up to 51%.

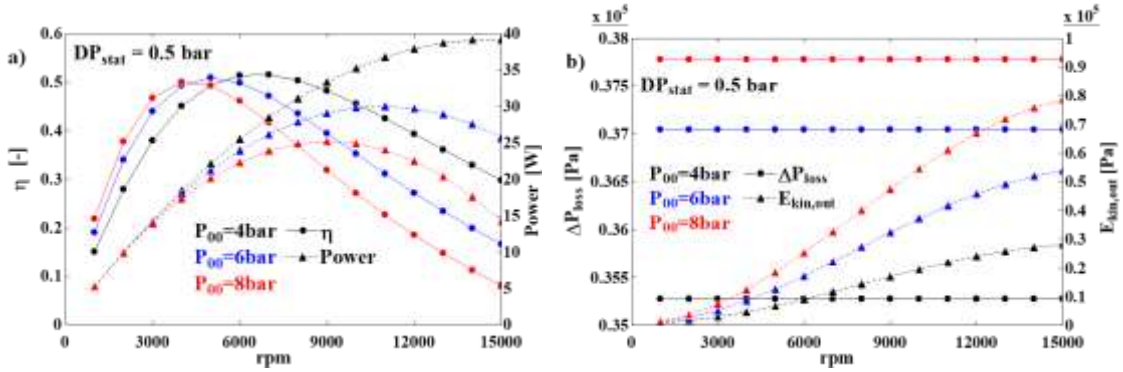

Fig. 4.22 Turbine a) efficiency and power output, b) losses versus rotational speed rpm at various total inlet pressure, for the up–scaled (D_1= 0.3 m) expander

Finally, taking into account the developed sensitivity analyses, it was possible to point out some useful guidelines for design and optimization of a Tesla turbine utilizing n–Hexane as working fluid:

- The expander efficiency, power output, mass flow rate and expansion ratio are in close relation: low mass flow rates $\dot{m}$ are connected to high efficiency and lower power output and vice versa, in agreement to the statement claimed in [58], [60].
- The length of the camber line L_{cl} and the number of the nozzles Z_s are fundamental geometric parameters, as they directly influence the mass flow rate, while the rotor variables (b and D_3/D_2) influence the variation of tangential velocity Δv_t and therefore the power production and the performance of the expander. They can be optimized in order to achieve optimal performances.

- Generally, the best performance of the Tesla expander is achieved with low inlet pressure and limited mass flow rates. Through all conditions, an optimised value of rotational speed is present (the one which allows inlet tangential relative velocity close to 0). The performance is not significantly affected by inlet temperature.

Full design procedure example

In this Section, an example of a Tesla turbine design procedure is displayed. The first matter to take into account, in order to achieve a complete and proper design, are the boundary conditions of the geometric parameters; particularly:

- Balanced stator size ($D_0/D_1 \leq 1.5$);
- Stator output angle $\alpha \leq 85°$;
- Throat section length $\geq$ 1mm;
- Rotor channel width $\geq$ 0.1 mm and disks thickness $\geq$ 0.5 mm.

Even the fluid conditions have constraints:

- $Ma_1 \leq 1$ in the throat section and $Ma_3 < Ma_2$.

Applying the considered boundary conditions and selecting disks with an external diameter D_2=0.30 m, best efficiencies were obtained with a reduced throat section length (1 mm) and with a limited number of statoric nozzles (Z=2). Nonetheless, this choice leads to low power output values and a not uniform flow distribution at rotor inlet. Due to the applied conditions, the shape and the length of the statoric channels require an inlet/outlet diameter ratio D_0/D_1 equal to 1.48, while the need of a tangential flow is favoured by a relatively large stator outlet angle. The parametric analysis suggested b=0.12 mm and s=0.5 mm as the optimum rotoric channel width and disks thickness respectively, in order to maximize turbine efficiency. In this way, if the rotor is made of 5 disks, the throat section height is 2.6 mm, while the diameter ratio is set to 0.2.

A parametric study was thus carried out varying total inlet pressure P_{00}, static stator outlet pressure P_1 and rotational speed. Efficiency was maximised at very low inlet pressure (4 bar) and stator pressure drop (0.5 bar) and with a rotational speed of 10,000 rpm. These operating conditions are close to the incipient flow reversal at rotor inlet. This occurrence sets a limit on the values of rpm and ΔP_{stat}, which, therefore, actually reduce the operating range. Nonetheless, very close values of efficiency can be achieved with lower inlet total pressure (3 bar) at higher rpm (Fig. 4.23).

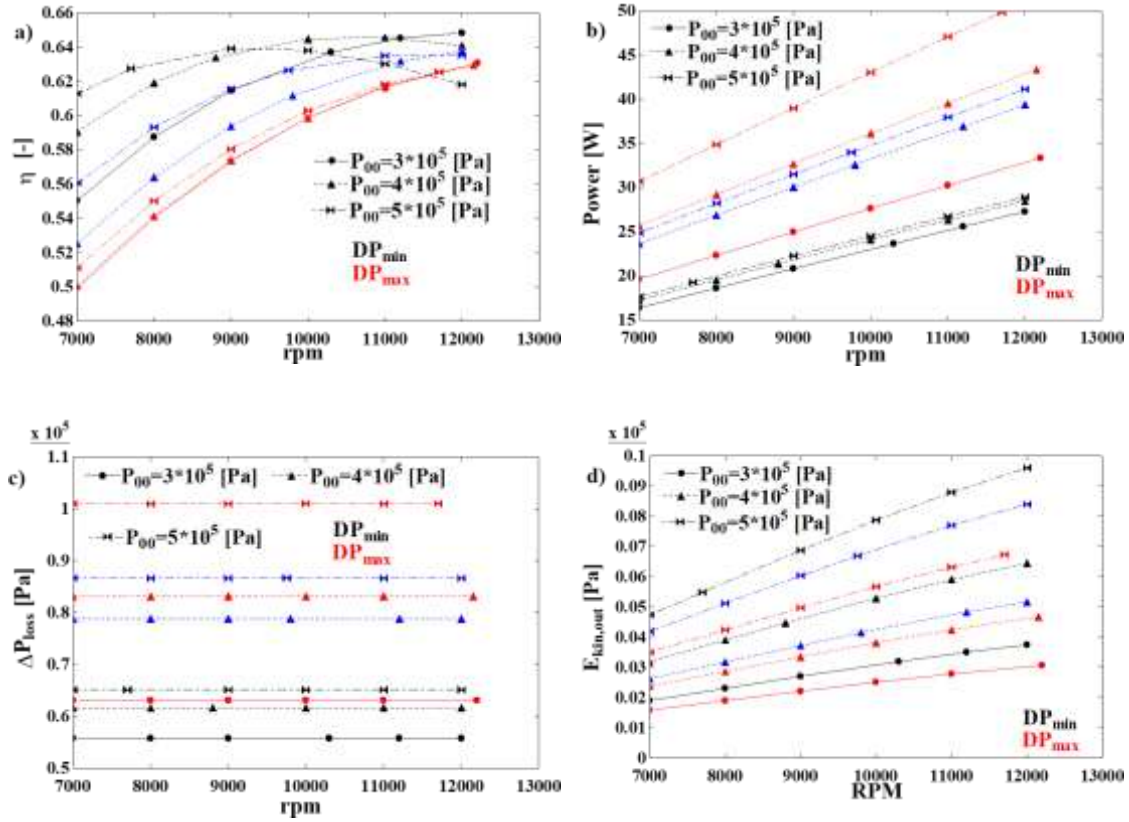

Fig. 4.23 Operating map of the Tesla expander: a) efficiency, b) power output, c) stator–rotor losses, d) kinetic energy at rotor outlet versus rotational speed at variable static pressure drop in the stator and total inlet pressure

The curves show that the maximum achievable value of efficiency is close to 64%, achievable at various combinations of total inlet pressures and rotational speeds. In particular, raising the total inlet pressure allows lower rotational velocities in order to achieve the same efficiency levels. The effects of the inlet temperature are not very relevant and efficiency is roughly constant versus temperature (Fig. 4.24). The modest variation is only due to the higher–pressure losses in the gap between stator and rotor.

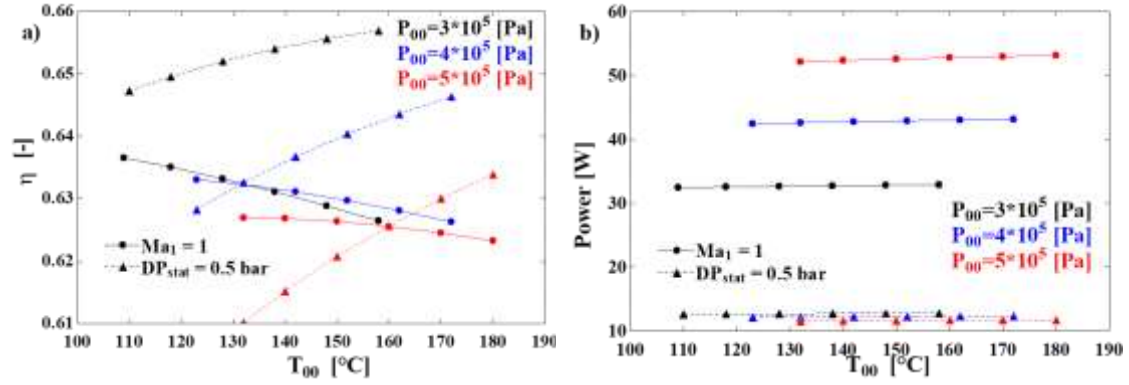

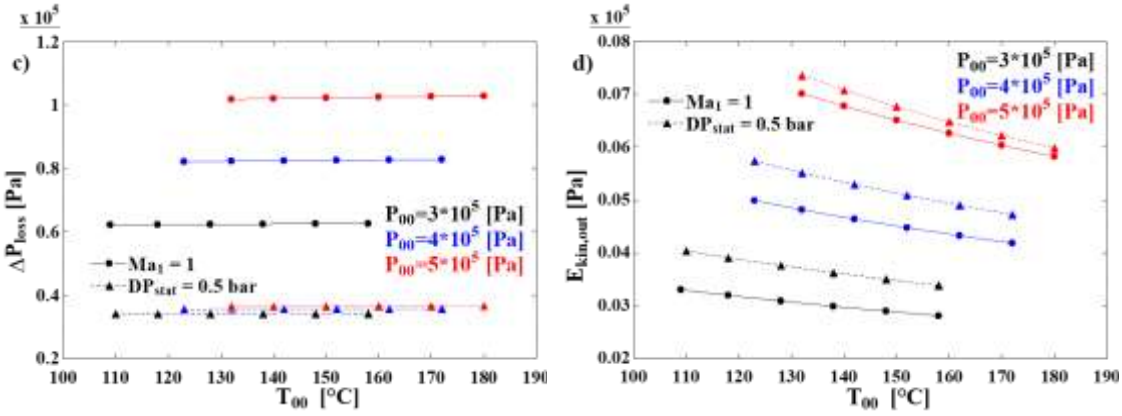

Fig. 4.24 Tesla expander operating map: a) efficiency, b) power output, c) losses stator–rotor, d) kinetic energy at rotor outlet versus inlet total temperature at different total inlet pressure

In the present assessed case, an inlet 5 bar total pressure and the related saturation temperature are optimised conditions, while the static stator pressure drop ΔP_{stat} should be set at the value allowing the sonic condition in the throat section. The rotational speed showed an optimised value at 11,700 rpm. Under these design conditions, the Tesla expander achieves 54 W power output per channel and 61% isentropic efficiency.

Down–scaling or up–scaling the Tesla turbine by modifying only the outer stator diameter D_1, while fixing all the other geometric design parameters, changed slightly the turbine performance, as shown in Tab. 4.1. Particularly, efficiency increased due to the increase of power production and the decrease of the non–dimensional channel width ratio (b/D_2). The most important feature to remark is the behaviour of optimised rotational speed when changing the diameter of the turbine. Particularly, high turbine diameters allow a reduced value of rotational speed. This matter is really important for some specific applications, (such as distributed power generation), as where the velocity could be limited for various reason (direct coupling to network frequency, noise, ecc.). The increase in diameter allows also a higher power production per channel, requiring therefore a limited axial extension of the expander in order to provide relatively high power.

Table 4.1 Performance and geometric parameters of the assessed turbines

D_1 [m]	**0.15**	**0.3**	**0.5**
L_{ts} [mm]	1	1	1
H_s [mm]	1.2	1.2	1.2
Z_s [–]	2	2	2
b [mm]	0.1	0.1	0.1
D_3/D_2 [–]	0.25	0.25	0.25
RPM	23400	11700	7000
Φ	0.03	0.02	0.01
Ψ	0.86	0.92	0.93
N_s	0.029	0.013	0.008
D_s	9.07	80.08	34.16
η [%]	52	61	64
Power per channel [W]	41	54	58

4.1.3 Turbine geometric assessment

Once the influence of each parameter, and an optimization procedure for the design and optimization of the turbine were developed, it was questioned if the main parameters could be linked together, in order to obtain geometric scaling laws, which are necessary when executing a performance assessment which aims to be independent from the size of the turbine. All the main geometric parameters have therefore been analysed in order to obtain maximum turbine total to total efficiency. The scaling laws have been developed in order to link every geometric parameter to external rotor radius.

The main considered parameters were found to be:

- Stator inlet/outlet diameter ratio (D_0/D_1);
- Gap between stator and rotor ($\mathcal{G}$);
- Rotor channel width (b);
- Rotor outlet/inlet diameter ratio ($R = D_2/D_3$);
- Throat width ratio ($TWR = \frac{TW*H_s*Z_{stat}}{2*\pi*r_2*b*n_{disk}}$).

Stator inlet/outlet diameter ratio

The stator inlet/outlet diameter ratio was fixed at 1.25. This value was assumed as suggested in [180], where a consolidated practice relying on geometric definitions was carried out.

$$D_0 = D_1 \cdot 1.25 \tag{4.3}$$

Thus, the outlet diameter of the stator comes out:

$$D_1 = D_2 + 2 \cdot \mathcal{G} \tag{4.4}$$

Gap between stator and rotor

The gap was chosen as small as possible but limited by the thermal expansion of the disks:

$$\mathcal{G} = 1.5 \cdot (r_2 - r_3) \cdot \lambda \cdot (T_{00} - T_{amb}) \tag{4.5}$$

Where λ is the thermal expansion coefficient, T_{00} the total temperature at stator inlet (conservative assumption) and T_{amb} is the ambient temperature (this is a conservative assumption, actually in/out rotor temperature should have been used). Therefore, the calculated value represents the linear thermal expansion of the disk, actually augmented by a 1.5 safety factor.

Rotor channel width

The rotor channel width was defined as a function of the external rotor diameter, by the means of an extensive parametric analysis. Fig. 4.25a shows the total to total efficiency of the turbine vs. channel width, at fixed 100°C total inlet temperature and total inlet

pressure corresponding to a 10 K super heating level (or, in other words, at 90°C saturation pressure; in order to compare all the different investigated fluids at the same low temperature level). For the sake of clarity, Fig. 4.25a shows the results for a fixed 0.2 throat Mach number and a 0.4 rotor outlet/inlet ratio. The throat width ratio is fixed at 0.02 at 100°C temperature. Nonetheless, the analysis was performed at various throat Mach numbers (0.2, 0.3, 0.6, 0.9), various rotor diameter ratios (0.2, 0.4, 0.6) and throat width ratios (0.02, 0.04). The effect of throat Mach number, rotor diameter ratio and throat width ratio do not remarkably influence the position of the best efficiency, but only the value (Fig. 4.25a). Therefore, Fig. 4.25b shows the loci of best efficiency ($\eta = \frac{W}{\Delta h_{os}} = \frac{v_{\theta 2} u_2 - v_{\theta 3} u_3}{(h_{00} - h_{3ss})}$) achieved by interpolation of the rotor channel width as a function of rotor outlet diameter at highest efficiency.

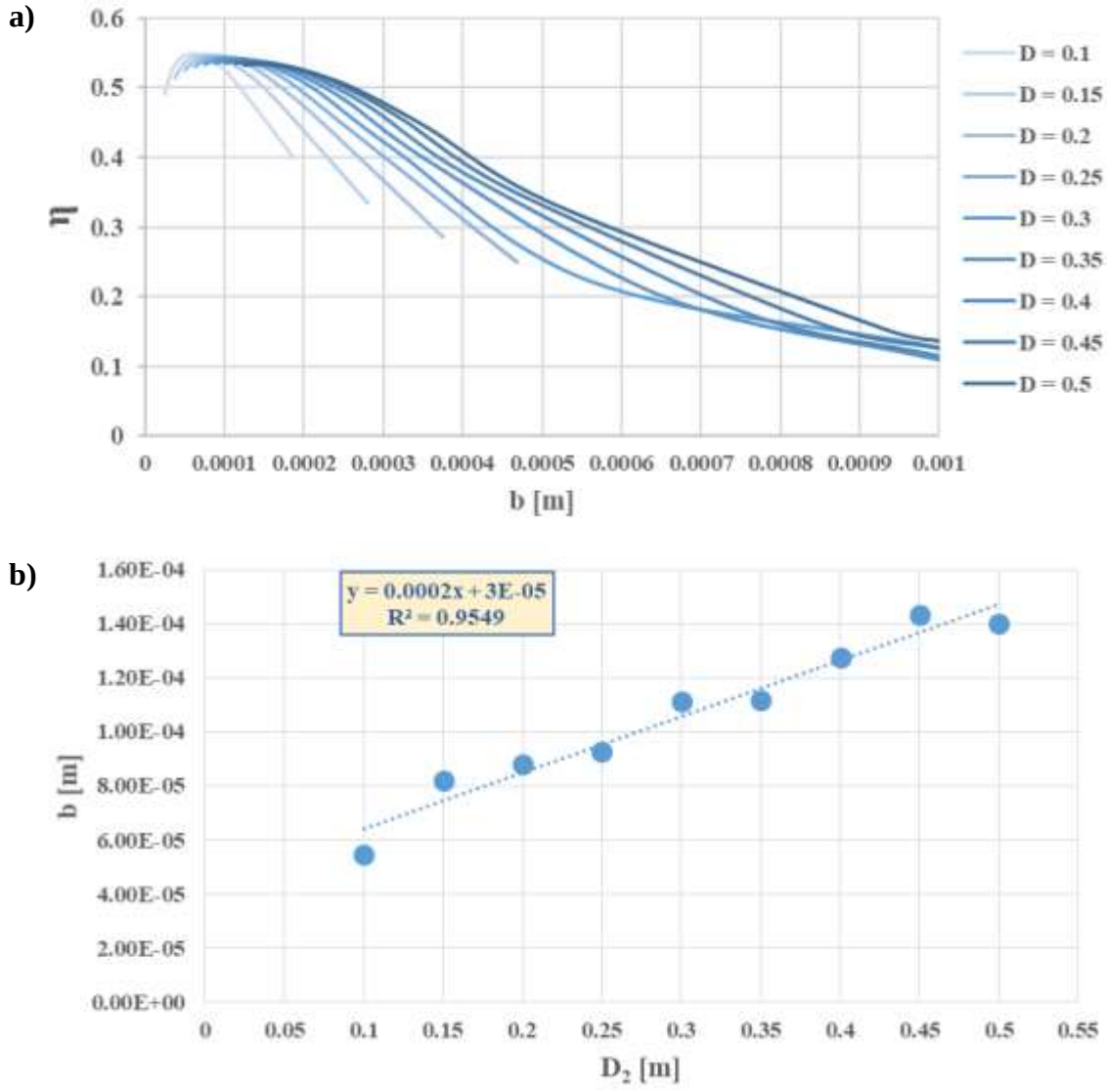

Fig. 4.25 a) Total to total efficiency against channel width. b) linear interpolation of channel width against rotor external diameter at highest efficiency value

The linear interpolated equation for the determination of the rotor channel width b, which allows achieving the highest efficiency vs. rotor outer diameter D_2 is reported in Eq. (4.6) for r1233zd(E) (equations for different fluids are presented in the following Sections).

$$b = 0.0002 \cdot D_2 + 3 \cdot 10^{-05} \quad (4.6)$$

Furthermore, the pressure effects are also assessed, in order to investigate the influence of pressure on efficiency and suitable rotor channel width. Specifically, the super heating level is fixed at 10K and the total inlet temperature is changed from 75 to 175°C. At low temperature, and therefore at low pressure, the rotor channel width allowing best efficiencies is larger compared to what is required at high temperature (and therefore high pressures). This is directly related to the mass flow rate. Indeed, high pressure corresponds to high mass flow rates, which requires narrower rotor channel width in order to achieve high efficiency. Narrower rotor channels favour viscous entrainment, while higher mass flow rates enhance momentum balance. Therefore, in order to have a suitable power extraction, tight channels are required at high mass flow rates; otherwise, an enhancement of kinetic energy loss is present. Nonetheless, the difference in rotor channel width is quite small and values between 0.00005 and 0.0001 m are recommended, in practice for all conditions. In order to have a comparable condition, the selected reference case is the one at 100°C for all the analysed fluids.

Rotor outlet/inlet diameter ratio

The best conditions for the rotor outlet/inlet diameter ratio (R) were evaluated running several parametric analyses (determining different Mach number conditions). It was found that when the optimal channel width correlation is applied, the best value for practically every turbine size is always in the range from 0.3 to 0.4, with the lower bound corresponding to low Mach number (0.3) and the higher bound to relatively high Mach number, close to 1. Fig. 4.26 displays the total to total efficiency as a function of R at various Ma numbers (0.3, 0.6 and 0.9) for the lower (0.08 m) and upper (0.44 m) diameter range bounds considered in this analysis. Smaller turbines can achieve higher efficiency at the price of a lower power production and higher rotational speeds. In the present case study, a value of R = 0.35 is selected, which guarantees good efficiencies at every investigated Mach number.

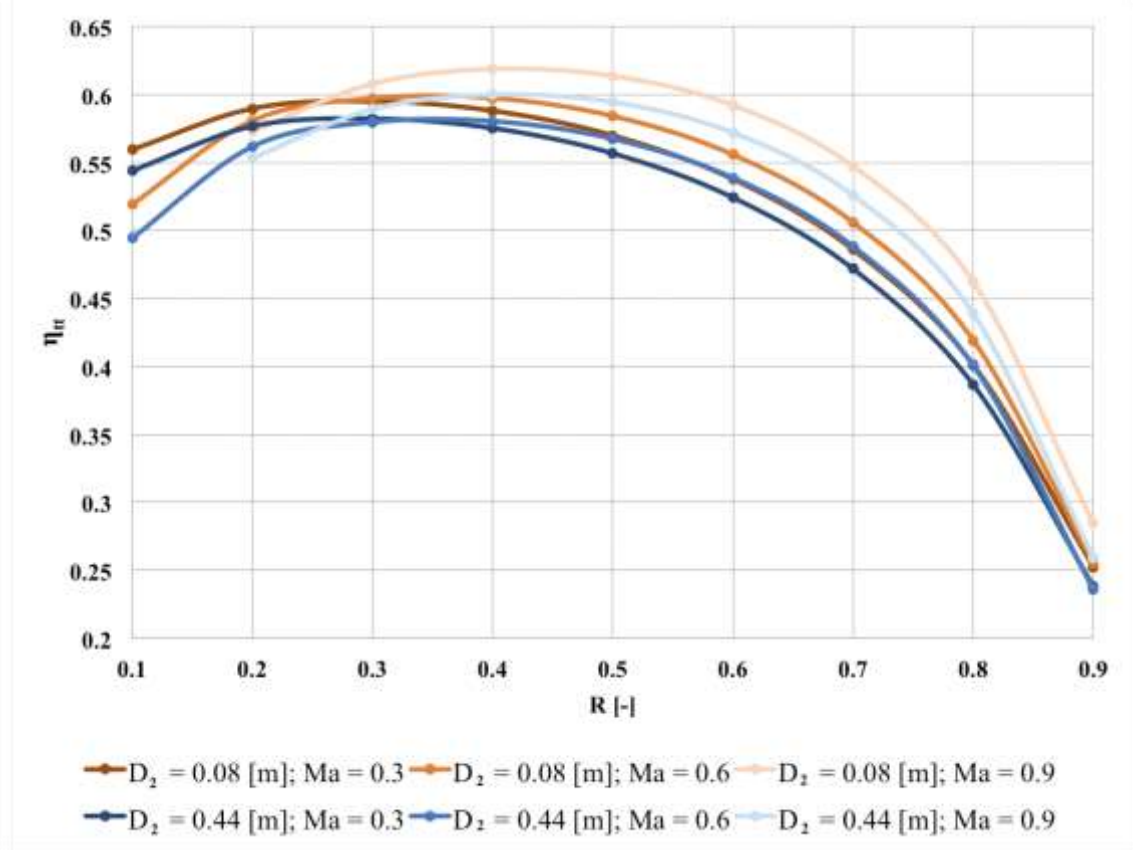

Fig. 4.26 Total to total efficiency against rotor outlet/inlet diameter ratio

Throat/width ratio

The throat–width ratio was determined as the ratio between stator outlet area and rotor inlet area, as shown in Eq. (4.7).

$$\mathrm{TWR} = \frac{\mathrm{TW}\cdot \mathrm{H_s}\cdot \mathrm{Z_{stat}}}{2\cdot\pi\cdot \mathrm{r_2}\cdot \mathrm{b}\cdot \mathrm{n_{disk}}} \tag{4.7}$$

Where *TWR* is the throat width, H_s is the throat height, Z_{stat} is the number of nozzles; n_{disk} is the number of rotor channels per each single stator.

It was found that the total to total efficiency increases monotonically with reducing *TWR* (Fig. 4.27). Actually, at lower *TWR* corresponds higher velocities at the throat, which are beneficial for rotor efficiency. On the other hand, the power output shows an opposite behaviour, steadily increasing with widening *TWR*. Therefore, a balanced solution was selected, that is, *TWR*=0.02. The balanced solution takes into account both thermodynamic matters (high efficiency at a suitable power) and manufacturing issues: in fact, lowering *TWR* implies dealing with manufacturing of very small stator channels, with a relatively complex geometry and compactness of the expander. Indeed, a very low *TWR* would certainly increase the efficiency, but would require a large expander: compactness factor *CF = Power/Volume* lower than 0.3 W/cm^3 were assessed for *TWR* = 0.01.

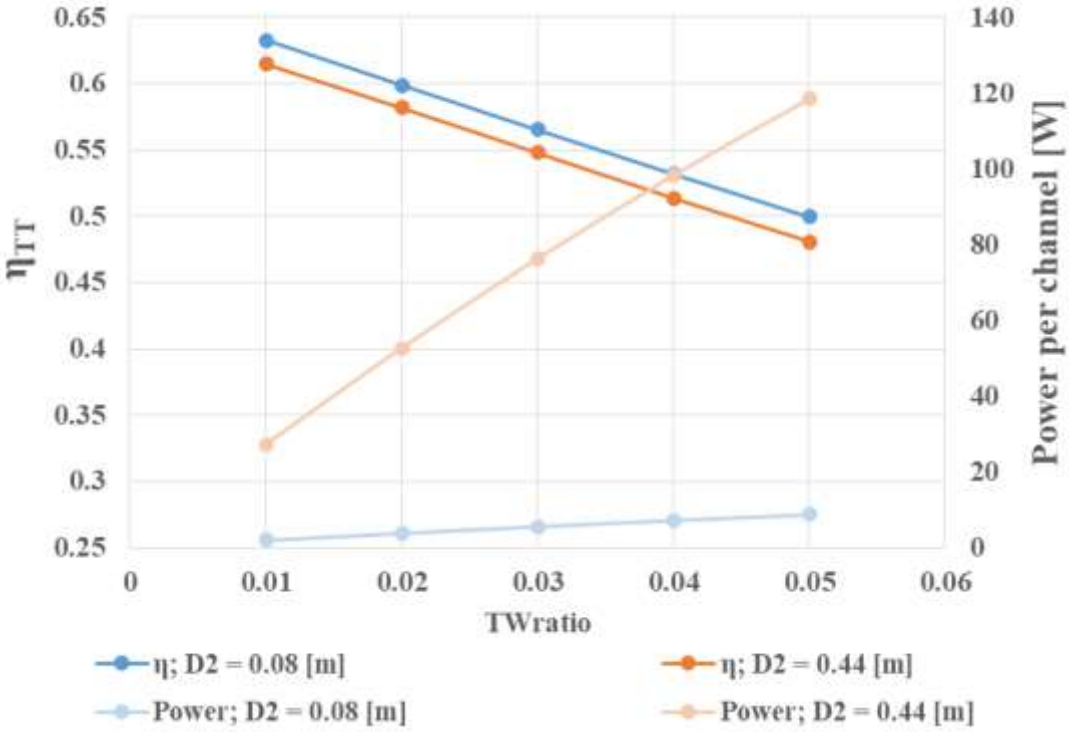

Fig. 4.27 Total to total efficiency and Power vs TW ratio for various Tesla turbine dimensions

Fluid dynamics assessment

Besides the investigation of geometric parameters, a fluid dynamics assessment in order to achieve best efficiencies was performed. The assessment of each thermodynamic parameter was set in terms of non–dimensional charts, which facilitate the methodological approach to the design of a Tesla turbine.
The main considered parameters were:

- Throat Mach number at stator outlet (and consequently mass flow rate);
- Tangential velocity over rotational speed at rotor outer diameter (or rotor inlet).

Throat Mach number

Once the geometry assessment was carried out, increasing throat Mach number allowed an improvement of both efficiency and power. The increase in efficiency is moderate, whereas the power increase is quite relevant, as shown in Fig. 4.28.

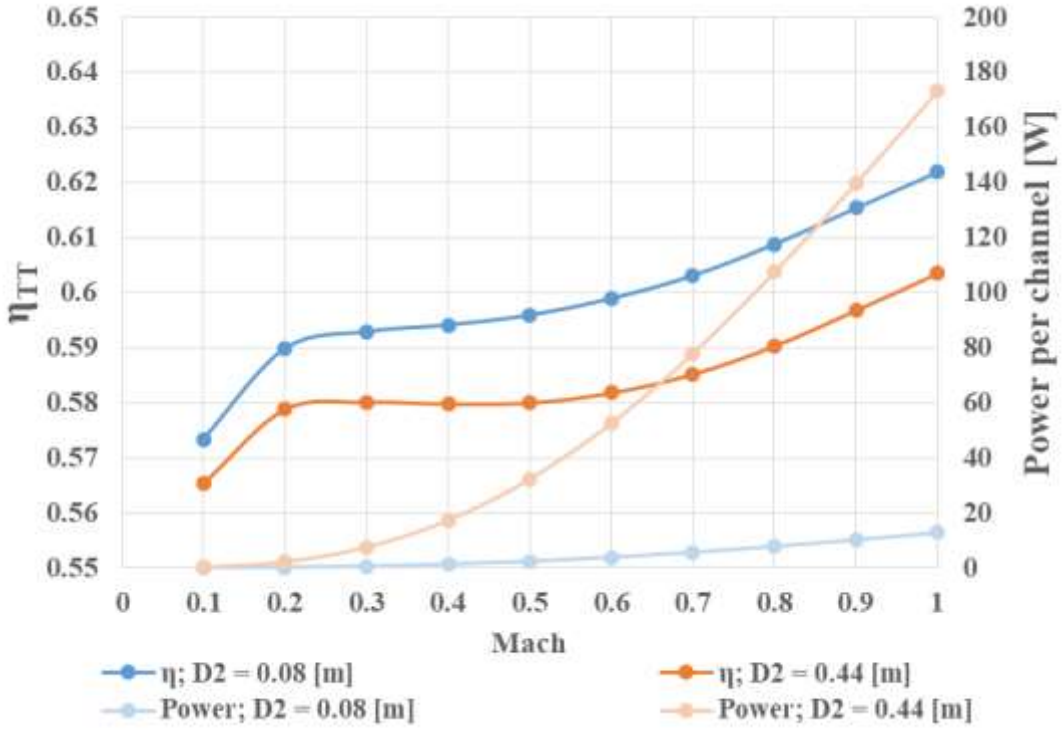

Fig. 4.28 Total to total efficiency and Power vs throat Mach number for various Tesla turbine dimensions

Tangential velocity ratio

The tangential velocity ratio ($\sigma = \frac{v_{t2}}{u_2}$) is one of the most important parameters for Tesla turbine optimization. The right matching of rotor inlet tangential velocity and peripheral speed is of paramount importance to achieve a high efficiency. In practise, the total to total efficiency is at its highest at $\sigma = 1$, or very close to 1 (Fig. 4.29). This is due to the right value achieved by the inlet tangential relative velocity in this condition, which is very close to zero. At higher value of σ, the fluid–machine work transfer would not be optimal, as the velocity would drop drastically at rotor inlet, dissipated into heat and not usefully transmitted to the rotor by the viscous forces. On the other hand, if a value lower than 1 is considered, a reversal flow conditions would be triggered. Indeed, if the absolute tangential velocity is lower than the rotational speed, a negative relative tangential velocity would be obtained at rotor inlet, so that the turbine would behave as a compressor at least in that region. Nonetheless, values only little lower than 1, but close to 1 may be considered to achieve high efficiency levels. Indeed, if the flow reversal region is very limited, the higher power produced by the remaining inner region of the rotor, operating at a higher rotational speed, while keeping all other parameters unchanged, counterbalances the negative effect of the flow reversal. Therefore, best values of the tangential velocity ratio σ were found in the range from 0.9 to 1.

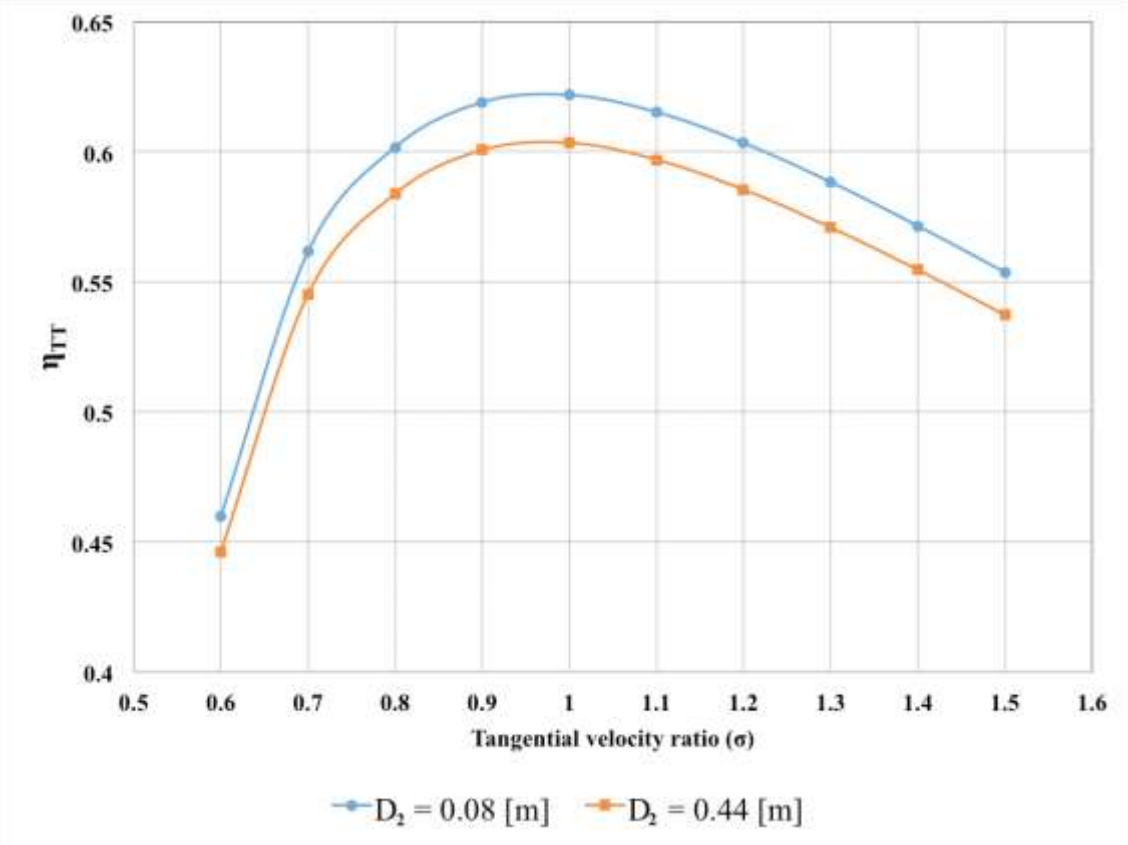

Fig. 4.29 Total to total efficiency vs. tangential velocity ratio for various Tesla turbine dimensions

Compactness and rotational speed

As discussed in the previous Section, the right matching between inlet tangential velocity in the rotor and rotational speed is of paramount importance to achieve high turbine performances. In order to have the proper match, the rotational speed needs to be adapted to the rotor external diameter. Specifically, the smaller the rotor, the higher the rotational speed required for best efficiency (Fig. 4.30). The machine compactness (i.e. power output per unit volume of the turbine) is another fundamental parameter, depending on the specific requirements of the field of application, and is clearly related to the rotational speed. For example – referring to expanders in the power range from 1 to 30 kW – for the automotive sector, compactness is a fundamental parameter, and therefore a small, fast–turning Tesla turbines would be preferable; on the other hand, for domestic application, the Tesla concept offers – with respect to other possible expanders, such as centripetal turbines – the attractive possibility of direct coupling with a 3000 rpm generator and a low noise emission factor; for these applications compactness of the machine could be sacrificed.

The compactness factor *CF* is the ratio between the power and the total volume of the turbine, expressed in W/cm^3 [208]; the calculated values of *CF* are shown together with

the rotational speed as a function of the rotor size in Fig. 4.30, where T_{00} = 100°C, P_{00} = 8.33 bar and mass flow rates between 0.08 and 1.1 kg/s were considered.

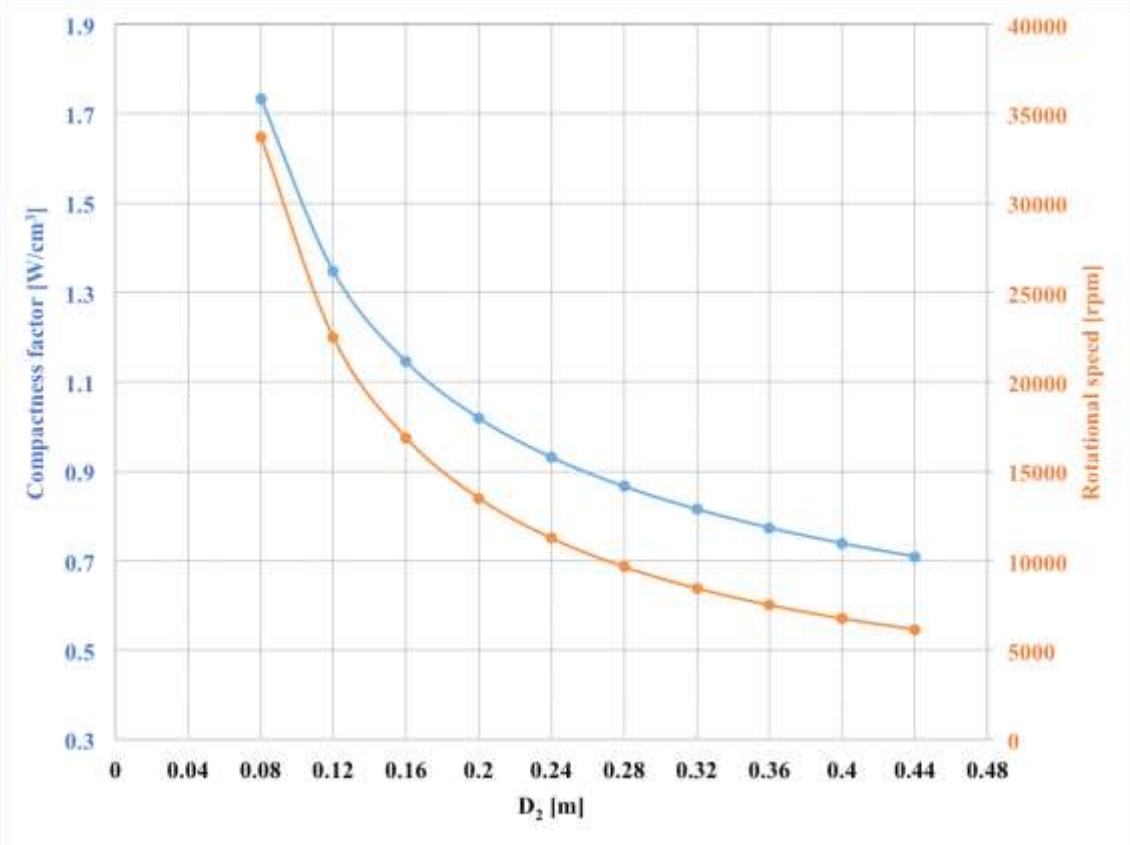

Fig. 4.30 Compactness factor and rotational speed for optimized Tesla turbine geometry (Ma_1 = 1; $\boldsymbol{\sigma = 1}$; $\boldsymbol{0.04 < r_2 < 0.22}$)

Tesla turbine geometry assessment

The obtained geometry as a function of rotor outer diameter for each fluid showed the same range of design configuration; that is quite similar in terms of rotor outlet/inlet diameter ratio (0.3 < *R*< 0.4), throat width ratio (*TW* = 0.02), throat Mach number (Ma_1 = 1) and tangential velocity ratio ($\sigma = 1$); nonetheless, the most important parameter is the rotor channel width b, which is different for each fluid (Tab. 4.2). Referring to ORC applications of the Tesla turbine, even if an optimal value of *b* results is present for each working fluid, values around 0.1 mm are required in order to obtain high efficiency. Lower rotor channel width values are beneficial for refrigerants, and especially for fluids with low critical temperature and high critical pressure (such as R1234yf). Conversely, hydrocarbon fluids such has n–Hexane, allow higher rotor channel width, due to their critical properties, which are opposite of refrigerants. That is, coupling a high critical temperature and low critical pressure. Furthermore, as discussed in the previous Section, high Mach numbers (in the range of 1) are beneficial for turbine efficiency, as they improve the power production and the efficiency. Nonetheless, the tangential velocity

ratio is the most important parameter when designing a Tesla turbine. High values of this parameter correspond inappropriate work transfer between the fluid and the rotor; on the other hand, values lower than 1 imply a reverse flow region at inlet. This feature was verified for all the examined working fluids.

Table 4.2 Calculated values of rotor channels width for the investigated fluids

Fluid	Rotor channel width [m]
R1233zd(E)	$0.0002 \cdot D_2 + 3 \cdot 10^{-05}$
R245fa	$0.00015 \cdot D_2 + 3 \cdot 10^{-05}$
R1234yf	$0.0001 \cdot D_2 + 2 \cdot 10^{-05}$
n–Hexane	$0.0003 \cdot D_2 + 5 \cdot 10^{-05}$

When constrained rotational velocity applications are considered, high expander efficiencies are directly related to the accurate selection of the rotor diameter. Indeed, as shown in Fig. 4.31, fixing the rotational speed implies assuming an inlet tangential velocity ratio (at fixed thermodynamic conditions); it can be observed that efficiency is higher when the inlet tangential velocity ratio σ gets close to 1. Furthermore, it should also be noticed that the highest expansion ratio of the machine β is achieved when σ approached unity (keeping the fixed condition of unit Mach number at the throat section).

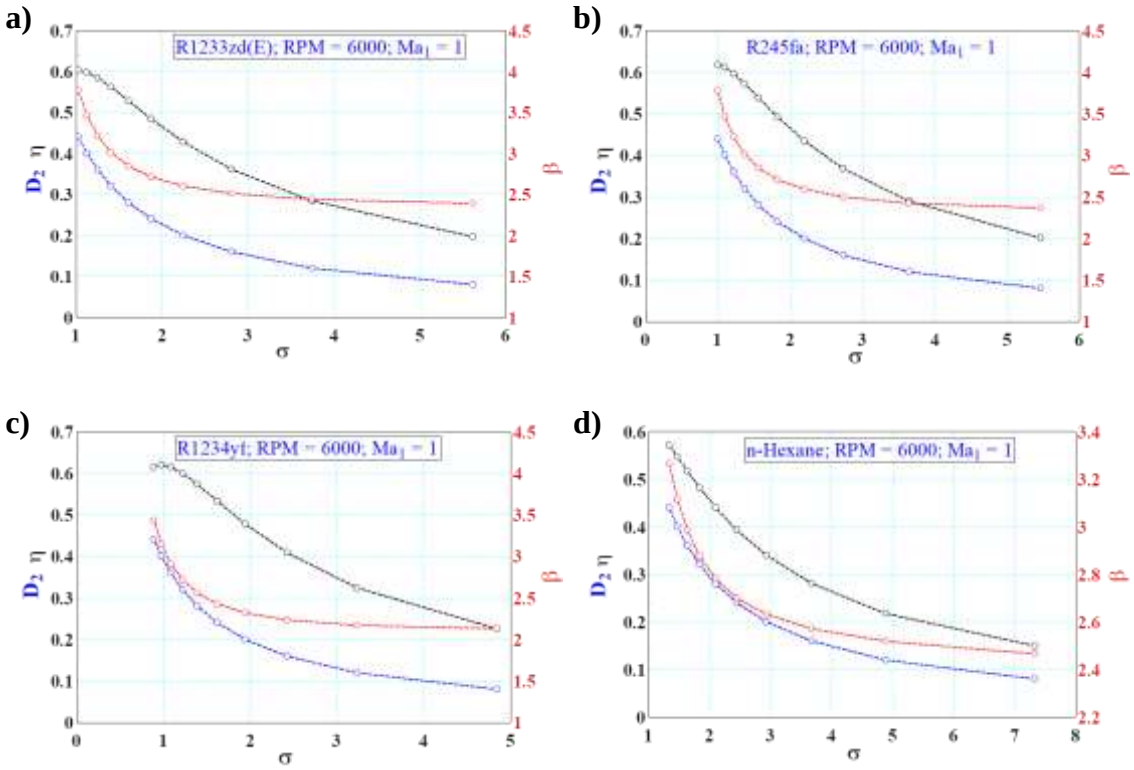

Fig. 4.31 Tangential velocity ratio, efficiency and expansion ratio at a fixed rotational speed of 6000 rpm ($Ma_1 = 1$; $\mathbf{0.04 < r_2 < 0.22}$)

Joint analysis: Efficiency versus Power and Expansion Ratio

The most suitable range of Tesla turbine design expansion ratio is between 3.5 and 5.5, depending on the working fluid. The power range, which depends on the number of channels of the manufactured turbine, is between few Watts and 30–35 kW (considering configurations in a range 2 and 100 rotor channels). At high–pressure ratio, the turbine is subjected to large pressure losses, thus undergoing to an efficiency penalty, mainly due to the stator – rotor gap and to the high kinetic energy loss at expander output. Fig. 4.32 displays the total to total efficiency of a 100–channels Tesla turbine as a function of power and expansion ratio. It is important to notice that the maximum efficiency level is almost the same for all the considered fluids and lies between 0.609 and 0.626. Also the expansion ratio in order to achieve best efficiency values is similar to all fluids (between 3.5 and 5.5), but shows some sensitivity to the different fluid characteristics. With reference to the here considered fluids, R1233zd(E) and R245fa (very similar for thermodynamics properties) hold the same optimizing range of expansion ratio, i.e. between 4 and 5. On the other hand, R1234yf holds higher pressure at the same temperature level, and then shows optimal conditions between 3 and 4. Conversely, n–Hexane, achieving the lowest efficiency at the fixed 100°C temperature level, requires higher expansion ratios, between 4.5 and 6. Furthermore, best efficiency conditions are achieved at low power output, especially in the case of hydrocarbon fluids.

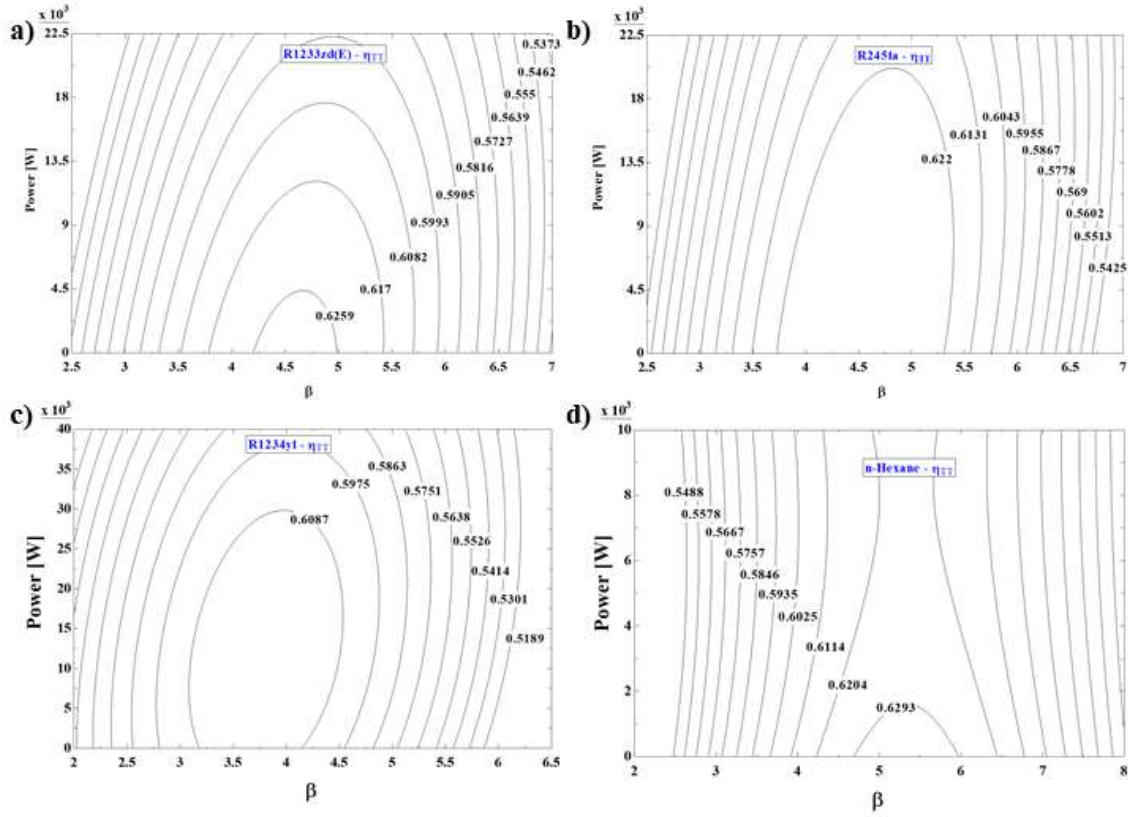

Fig. 4.32 Efficiency as function of power and expansion ratio for a) R1233zd(E), b) R245fa, c) R1234yf; d) n–Hexane (Ma_1 = 1; $\mathbf{0.9 < \sigma < 2.25}$; $\mathbf{0.04 < r_2 < 0.22}, \boldsymbol{n = 100}$)

Compactness and power (optimized speed)

Fig. 4.33 displays the behaviour of the compactness factor [208]. It is a fundamental indicator when selecting a micro expander. As can be noted from Fig. 4.33, this Tesla turbine configuration can be quite bulky (*CF* <1) when large rotor diameters are considered, especially for fluids with low pressure levels such as n–Hexane (Fig 4.33d). On the other hand, it can become quite compact (*CF* >1.5) when high power production is achieved through the utilization of refrigerants fluids with high pressure conditions (such as R1234yf, Fig 4.33c). Indeed, high pressure conditions mean that the mass flow rate elaborated by the turbine is higher and, consequently, the power output increases. Therefore, a compact turbine utilizing a refrigerant fluid can be suggested for applications where the compactness of the expander is the most important parameter, such as in automotive.

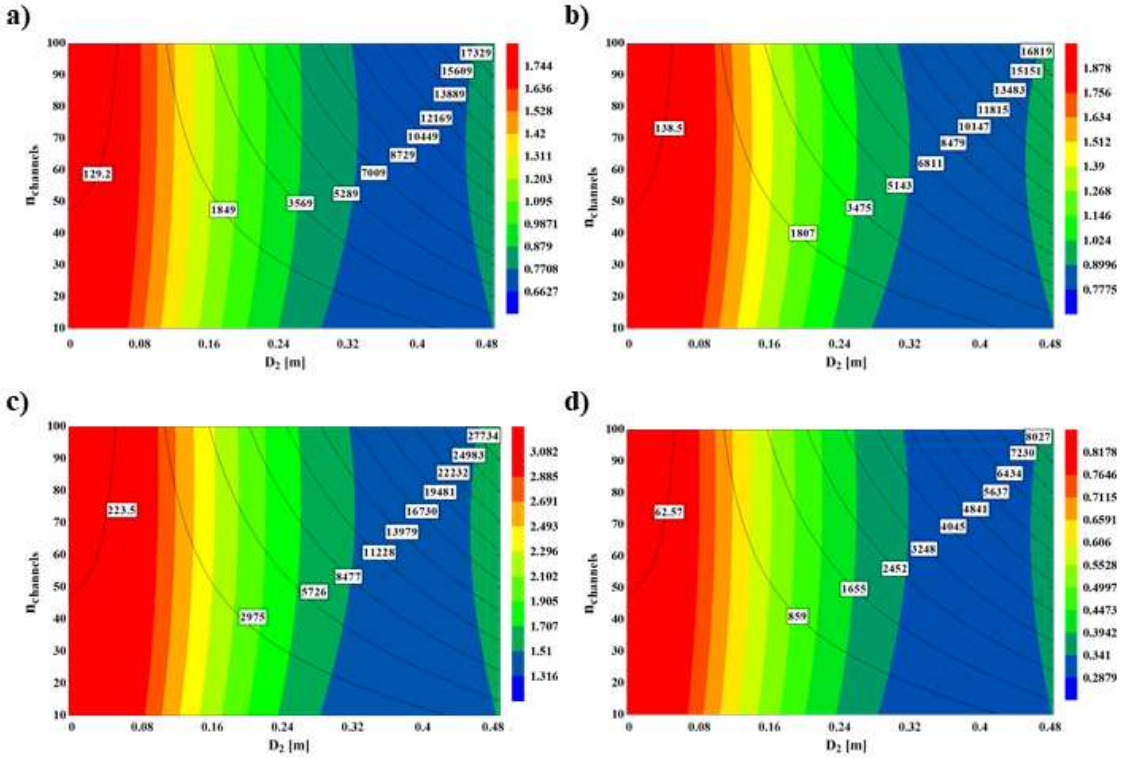

Fig. 4.33 Compactness (colour legend) and power (black lines on the graphs with corresponding caption) as function of turbine dimensions, channel and rotor diameter, for a) R1233zd(E), b) R245fa, c) R1234yf; d) n–Hexane ($Ma_1 = 1$; $\boldsymbol{\sigma = 1}$)

Fig. 4.33 shows also the power range for each considered fluid as a function of rotor diameter and number of channels. The Mach number was fixed at 1 in order to achieve the maximum possible expansion ratio. As expected, higher rotor diameters and higher number of channels allow higher power production at the price of a bulkier expander. Anyway, the right compromise between compactness and power production depends on the selected fluid, but certainly rotor diameters between 0.16 and 0.24 m guarantee a compact machine with reasonable power output levels. It should be remarked that a high–

pressure condition, as in the case of R1234yf, allows achieving very high power and compact expander (almost 30 kW with a *CF* >1.3). Furthermore, as was displayed in Fig. 4.30, compactness factor can be enhanced by selecting low rotor diameters and high rotational speeds.
Comparing the obtained compactness factor with those of from volumetric expanders [208], it seems that the Tesla turbine may be in the same range of roots and piston, and really close to scroll expanders. Nonetheless, it would certainly be always bulkier than screw expanders, having a very high value of *CF* (up to 20).

Inlet total pressure and degree of superheating – Effects on Efficiency and Power

Finally, a parametric investigation of the analysed Tesla turbines (working at T_{00} = 100°C as thermodynamic design point) was carried out for efficiency and power production par channel. These fundamental performance parameters were evaluated as functions of total pressure and superheating level at turbine inlet.
The 4 analysed fluids show the same trend of power output (Fig. 4.34). The power production gets higher at high–pressures and high superheating levels. On the other hand, the efficiency shows a different behaviour, depending on the working fluid. Specifically, for R1233zd(E), R245fa and n–Hexane, high efficiency conditions are achieved at low pressures and moderate super heating levels. Conversely, R1234yf presents optimised values for high pressures and moderate super heating level. This behaviour is mainly due to the very different thermodynamic properties of the fluids. R1234yf requires relatively large pressures in order to work with high temperature levels. This means that when pressure is low, also the considered temperature is quite low (for example, for the lower pressure case of 6 bar, with a 5 K super heating level, the total inlet temperature of the turbine is 25.5°C). With a reduction of the temperature, the density increases and the velocities at stator outlet decrease; therefore, the rotor efficiency is reduced. High superheating levels are not really fundamental, as they produce higher velocities at rotor outlet, thus increasing the kinetic energy losses at the turbine discharge.

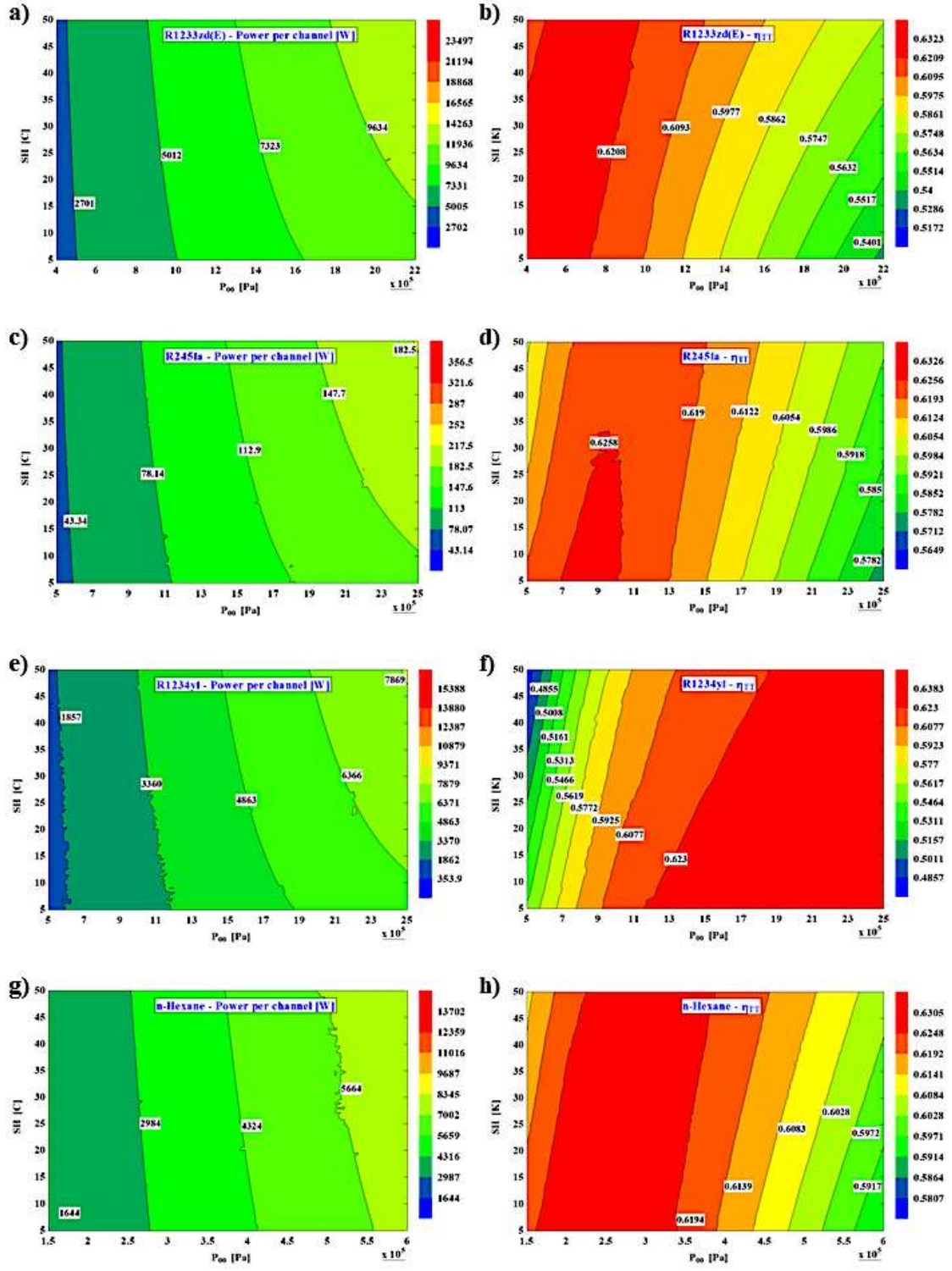

Fig. 4.34 Efficiency and power as function of pressure and super heating level for a–b) R1233zd(E), c–d) R245fa, e–f) R1234yf; g–h) n–Hexane ($Ma_1 = 1$; $\boldsymbol{\sigma = 1}$; $\boldsymbol{0.04 < r_2 < 0.22}$)

4.1.4 Comparison with Volumetric expanders

Power range, operating conditions, efficiency are the main parameters that need to be taken into account when proper selecting an expander for micro–small ORC. Tab. 4.3 summarises the main characteristics of the principal volumetric expanders compared to Tesla turbines. It is important to note that the Tesla turbine seems to be a direct competitor of scroll, roots and piston expanders, while for higher power ranges, screw expanders will still probably be the reference. According to the results obtained by the model predictions (deeply discussed in the next Sections), the possible reachable isentropic efficiency for Tesla turbines seems to be around 62%, therefore considering a typical value for mechanical efficiency of axial turbines of 0.95 [209], the overall expander efficiency would results in the order of 59% with an expansion ratio in the range between 3.5 and 5.5. Furthermore, it results that the proper power range for this expander extends from a few Watts (for very small rotor diameter configurations) to some tens of kW (for the largest diameter configurations). These evaluations rely on a proper balance of rotational speed, maximum power and temperature, rather than imposing absolute limits to one specific parameter. Rotational speed is a linear function of the rotor diameter, therefore the smaller the diameter the higher the required rotational speed for a reasonable efficiency. This favours mechanical design, as mechanical issues could arise for high rotor diameters, but not for small, compact disks. The Tesla turbine is claimed to be suitable for handling two–phase fluids [60]. Indeed, in [73] a Tesla turbine for geothermal application was tested in two–phase flow conditions, nonetheless, further research on this topic is still required.

Table 4.3 Comparison of technical data between volumetric expanders and Tesla turbine [60], [73], [208]

Parameter	Scroll	Piston	Screw	Roots	Tesla
Power [W]	0.005 – 10,000	0.001 – 10,000	2,000 – 200,000	1,000– 30,000	0.005 – 30,000
Max Rotational Speed [rpm]	10,000	3000 (swashplate: 12,000)	21,000	20,000	–
Built in volume ratio	1.5–4.2	2–14	8	~1	–
Maximum Pressure [bar]	~40	70	–	–	–
Maximum Temperature [°C]	250	560	–	–	–
Two–phase flow handling	Yes	Low	Yes	Yes	Yes [60], [73]
Isentropic efficiency	87	70	84	47	59

The main advantage of a Tesla turbine would be its low cost, but in order to perform a sound comparison with volumetric expanders this parameter cannot really be taken into account, as the cost depends not only on the complexity of the machine and on the manufacturing process, but is also linked to the maturity of the technology and market development. Concentrating on technical aspects, Tab. 4.4 compares the main parameters, which are of paramount importance when selecting an expander; capability of operating at high pressure and temperature, compactness and efficiency. There is not an absolute best choice when selecting and expander for micro–ORC, as it deeply depends on the operating conditions of the specific application. Particularly, it seems that scroll expanders present higher efficiency values when compared to the other technologies, but still they are not suited to high pressure and temperature applications, conversely to the piston expander. Screw, scroll and roots appear to be adaptable to wet expansion applications, while piston would be penalized. Screw expanders are the most flexible between the compared technologies, as they allow high efficiency in an extended power range. Furthermore, screw expanders are very compact. The Tesla turbine does not outstand in any of the analysed categories, but on the other hand it has still all positive "marks", as it is a quite efficient, reliable and flexible expander, suitable for a wide variety of applications.

Table 4.4 Comparison of advantages and drawbacks between volumetric expanders and Tesla turbine

	High Pressure and temperature	**Wet Expansion**	**Compactness**	**Flexibility**	**Efficiency**
Piston	++	–	+	+	+
Screw	–	+++	+++	+++	++
Scroll	–	+++	++	++	++
Roots	–	+++	+	–	–
Tesla	+	+ [60]	+	+	+

Based on a literature review [48]–[51] and on the results provided in this research, it is possible to compare the Tesla turbine with volumetric machines and traditional bladed turbines. From this analysis, it appears that, even if the Tesla expander is intrinsically a turbine, it presents several similarities with volumetric expanders, which makes it a "hybrid" technology between the two main categories of expanders. In terms of power range, pressure and temperature levels, the Tesla turbine presents characteristics similar to volumetric expanders. However, the very moderate dependence of the pressure ratio to rotational speeds makes Tesla expanders similar to traditional bladed turbines. In conclusion, this type of turbine is an interesting option with unique characteristics, which makes it suitable and attractive for application in the field of low and micro power (<30 kW), pressure ratios between 2 and 6, where keeping low costs is mandatory.

Furthermore, it is remarked that, conversely to volumetric expanders, the Tesla turbine does not have any requirement for internal lubrication, which represents a great simplification of the whole circuit.

Fig. 4.35 highlights the main characteristics of volumetric expanders, Tesla turbines and axial and radial turbines. Of particular interest is that Tesla turbine characteristics are closer to those of volumetric expander such as rotational speed, power, pressure and temperature operational ranges; with the only exception of the quasi–independency of pressure ratio with rotational speed, proper of dynamic machines.

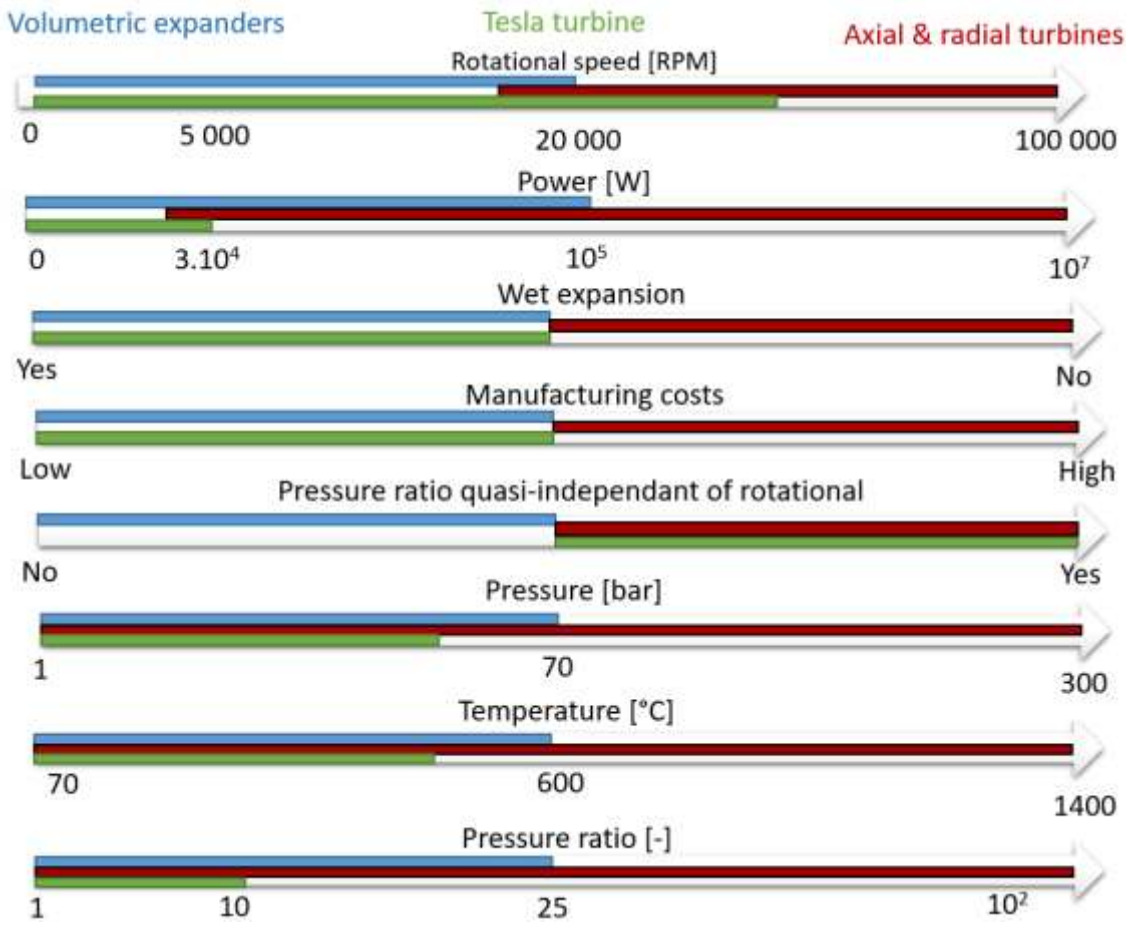

Fig. 4.35 Comparison of volumetric expanders, Tesla turbine and classical turbines

4.1.5 Prototypes performance maps

Performance maps of the real prototypes were developed. Particularly, the air prototype results are displayed as function of the main Turbomachinery parameters, while for the ORC, a deeper assessment on various fluids has been carried out.

4.1.5.1 Air Tesla turbine

Performance assessment

The performance assessment was carried out first varying the Mach number at nozzle throat outlet and the tangential velocity ratio at rotor inlet ($\sigma = \frac{vt_2}{u_2}$) at fixed thermodynamic conditions (total inlet pressure of 1.5 bar and total inlet temperature of 100°C); then the thermodynamic conditions were varied, fixing the Mach number at stator outlet at 0.4 and the tangential velocity ratio at 1.

The tangential velocity ratio at rotor inlet is a fundamental parameter for optimization of Tesla turbines. Particularly, as shown in Fig. 4.36 optimal efficiency is reached when $\sigma = 1$ or even a bit lower than one. If σ is lower than one, at rotor inlet there will be a region of reverse flow, which will therefore be a loss for the turbine. Nonetheless, values of σ between 0.8 and 1 are still recommended, as the penalty by the reverse flow is counterbalanced by the higher power production at higher rotational speeds.

Tesla turbine optimal efficiency is reached for low mass flow rates, and therefore or small values of the flow coefficient. Fig. 4.37 displays the $\phi - \psi$ diagram of the prototype. Particularly, the suggested range of operation would be: $0.05 < \phi < 0.08$ and $0.6 < \psi < 1$. The optimal specific speed and diameter are displayed in Fig. 4.38. Fig. 4.38 was obtained changing both Mach number and sigma, for a fixed geometry of the turbine, this means that the variations in specific diameter is due by the changing of both mass flow rate and rotational speed. The optimal operation range for this turbine prototype would be: $10 < d_s < 12$ and $0.16 < n_s < 0.18$. Fig. 4.39 assesses the reduced mass flow rate – expansion ratio curve at various reduced speeds. It is important to note that the shape of the curve, as expected, is the same of a "traditional" turbine, with expansion ratio between 1 and 3.5 and reduced mass flow rate between $1{\cdot}E^{-5}$ and $5{\cdot}E^{-5}$.

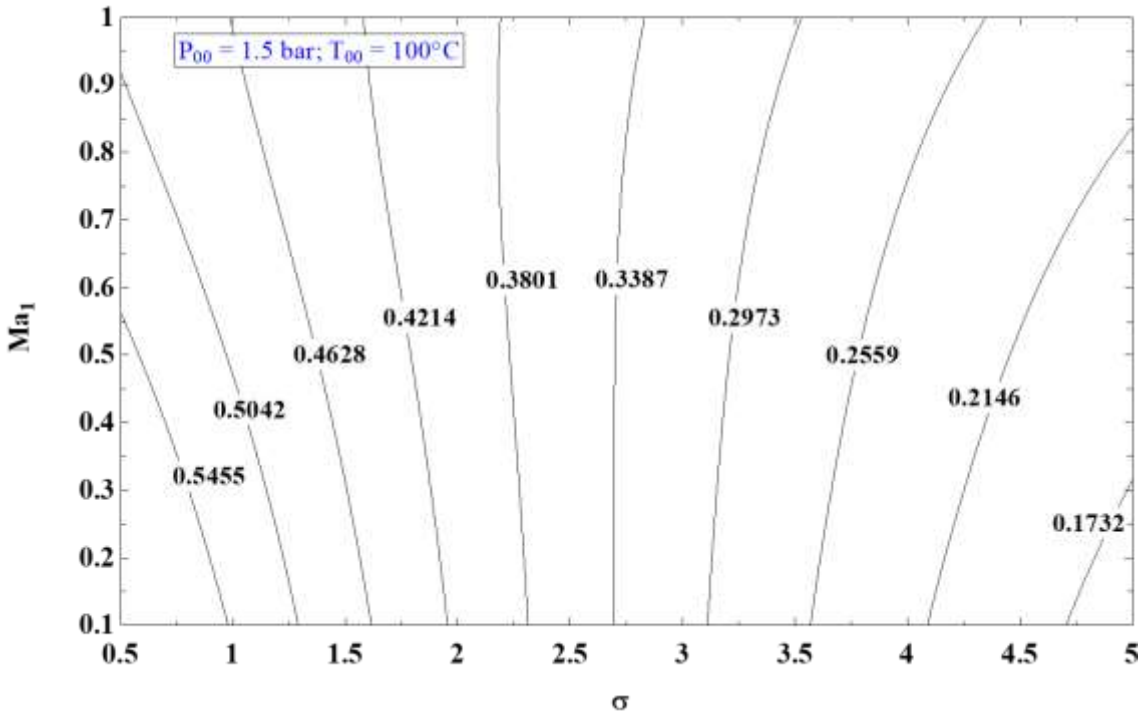

Fig. 4.36 Total to total efficiency of turbine prototype against $\boldsymbol{\sigma}$ and Ma_1

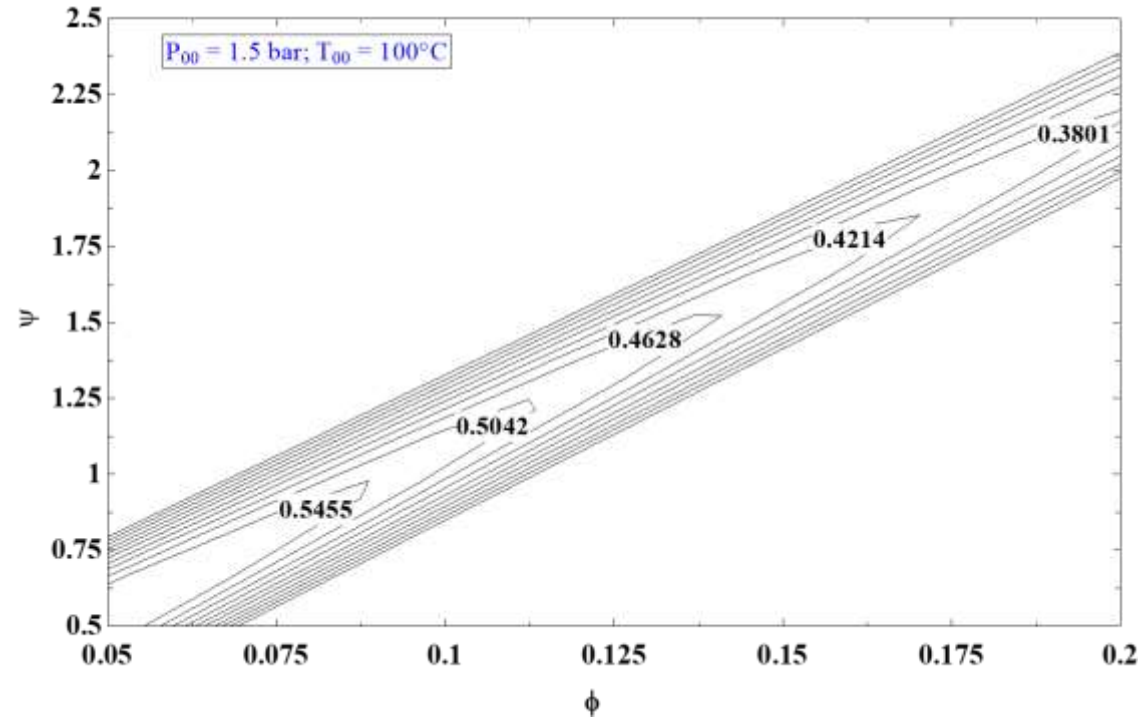

Fig. 4.37 $\boldsymbol{\phi - \psi}$ diagram of air Tesla turbine prototype

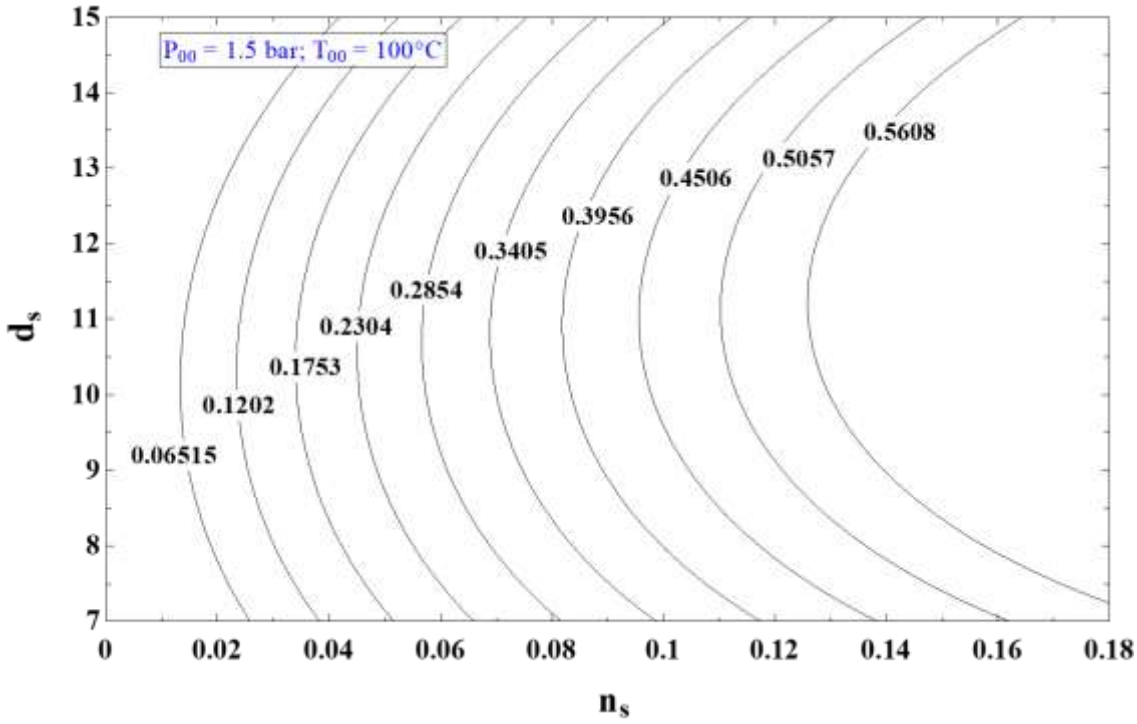

Fig. 4.38 n_s–d_s diagram of air Tesla turbine prototype

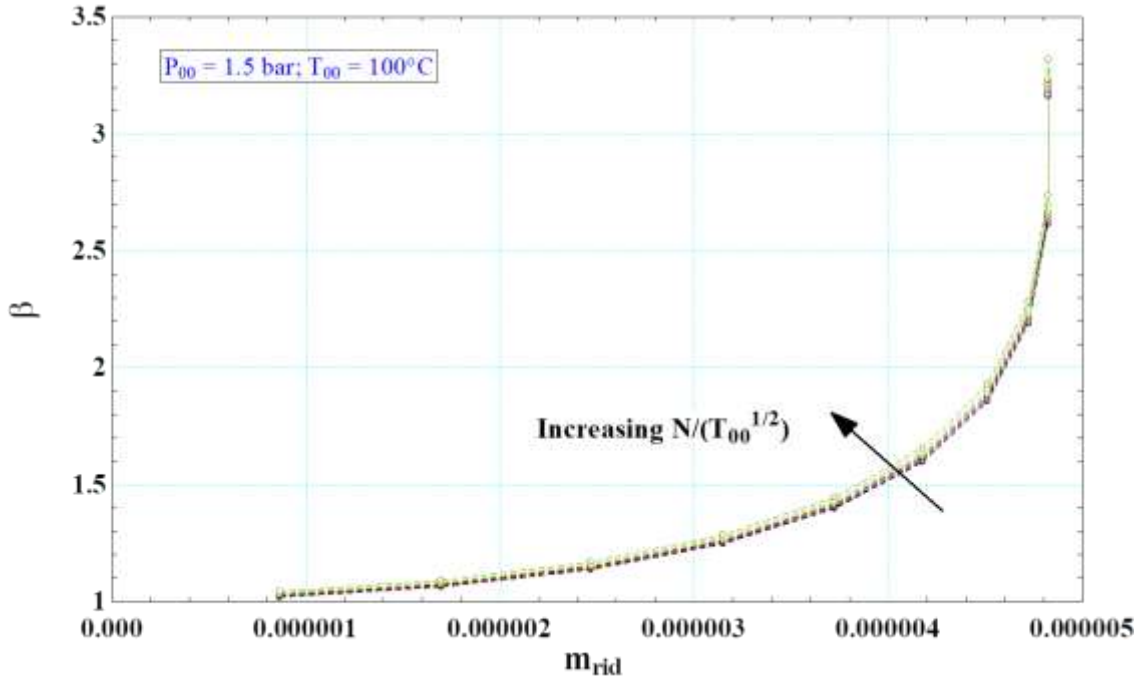

Fig. 4.39 m_{rid}– **β** diagram of air Tesla turbine prototype

The thermodynamic analysis assessment results are displayed in Fig. 4.40 (a–d). It is important to note the contrasting behaviour of efficiency (4.40a) and power (4.40c). Tesla turbine optimal efficiency is reached for very low mass flow rates (4.40d), which are reached for low pressures and high temperature, if the Mach number at stator outlet and

the rotational velocity ratio are fixed. The developed prototype, provided the right conditions, could therefore reach a power as high as 2,200 W, with a rotational speed of over 24,000 rpm.

Fig. 4.40b displays the compactness factor, as defined in [208], which could be a fundamental parameter for the selection of a micro expander. The compactness factor is the ratio between the power and the total volume of the turbine, expressed in W/cm^3. As can be noted from Fig. 4.40d, this Tesla turbine prototype is quite bulky (CF <1) when high efficiency range is concerned, on the other it is quite compact (CF >1.5) when high power production is achieved. It seems therefore, that in order to design properly a Tesla turbine, it is necessary to keep in mind the specific application requirements.

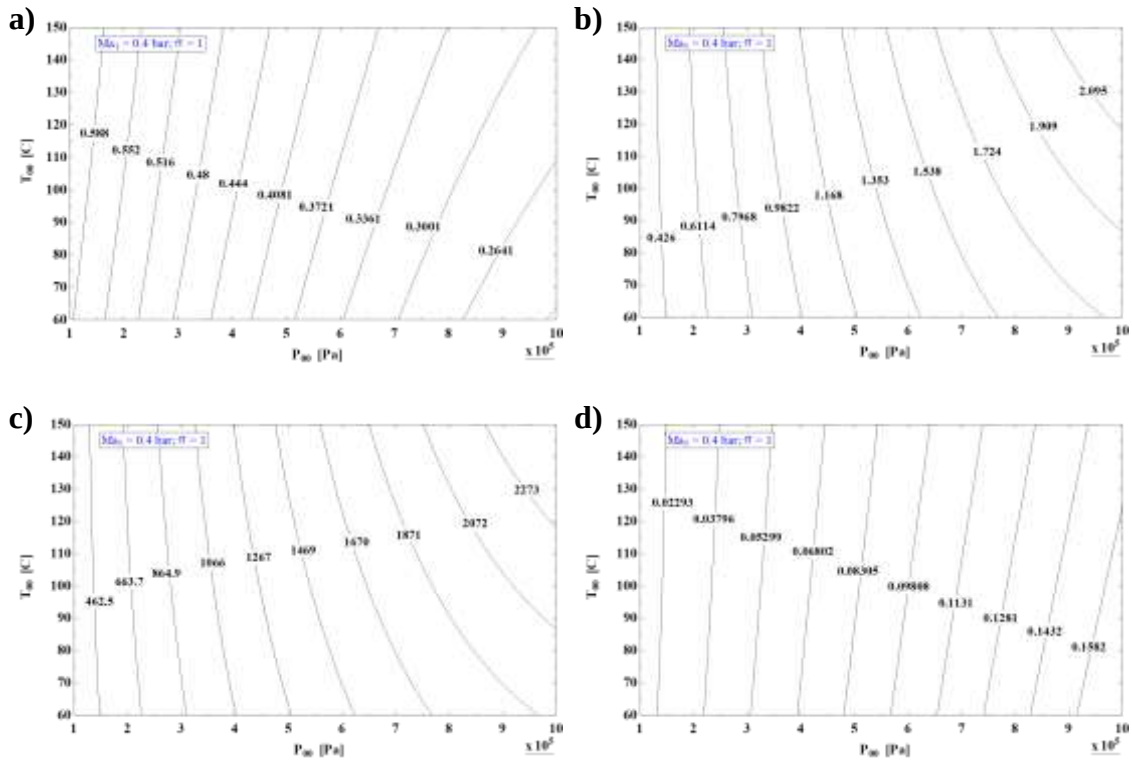

Fig. 4.40 a) η_{TT} b) Compactness factor c) Power d) Mass flow rate of air Tesla turbine prototype against total inlet pressure and temperature

4.1.5.2 ORC Tesla turbine

Before performing experimental investigation, it was important to assess the power and efficiency, which could be reached by the prototype depending on possible working fluid selection. This assessment was carried out on the geometry outlined in Section 3.3.2.

The fluids here analysed are R1233zd(E), R245fa, R134a, R1234yf, SES36, n–Hexane and n–Pentane. R134a and R245fa are considered as references in literature, because as hydrocarbon substitutes they allow to achieve the best efficiency levels. R1233zd(E) and R1234yf are the cleaner fluids which are going to substitute R245fa and R134a, respectively. N–Hexane and n–Pentane are on the other hand adopted as reference hydrocarbons, due to their favourable thermodynamic critical conditions (particularly, by the low critical pressure when compared to refrigerants). Finally, SES36 is chosen, as it is an azeotropic mixture, behaving like a single substance, showing very convenient features for the Tesla turbine, as it allows lower pressure levels at higher temperatures when compared to R134a and R245fa. R404a was not taken into account in this analysis, as the temperature levels are not appropriate for this fluid, nonetheless a performance analysis on this fluid is presented at the end of this Section.

As low–temperature resource applications are the most likely for this expander, two reference total inlet temperatures, T_{00} = 100°C and T_{00} =150°C, were considered. The total pressure at inlet is different for the fluids and it was selected, for both temperatures, in order to have superheated vapour 10°C above saturation temperature; the only exception are the cases for R134a and R1234yf at 150°C, which means superheating about 50°C as the critical temperatures of the fluid are 101 and 94.7 °C, respectively; a subcritical inlet pressure of 3.9 and 3.0 MPa were selected in these cases. The main parameters evaluated for all simulations are the power per channel, as well as the expander total to static efficiency. The calculations were performed varying the specific speed and the stator outlet Mach number, which is considered a fundamental parameter for the Tesla turbine [91].

Low turbine entry temperature (100°C)

The power of the Tesla turbine, such as conventional turbines, increases as the flow coefficient Φ is increased. The increase in flow coefficient (and hence in mass flow rate) is reflected by the increase in nozzle throat Mach number. Higher throat Mach numbers correspond to large flow coefficients and high mass flow rates. The increase in the flow coefficient on one hand increases power, but on the other it decreases the total to static efficiency (remembering that the geometry and the specific speed are fixed).

An increase in specific speed n_s allows obtaining a higher power production. Nonetheless, due to the characteristics of the machine, and especially of the conversion of power mechanism, the specific speed cannot reach exceedingly high values. This is caused by

the increase of the absolute velocity at rotor exit, which after a certain rotational speed would be higher than the value at rotor inlet, with considerable kinetic energy losses at exhaust. This behaviour is especially relevant for refrigerant fluids and in particular for R134a at high specific speeds.

Higher efficiencies and lower power are reached with hydrocarbons when compared to refrigerants. This is mainly due to the different turbine inlet pressure. Typical values of turbine inlet pressure for R245fa, R1233ZD(E), R134a and R1234yf are higher than 1 MPa; on the other hand, the inlet pressure for n–Hexane and n–Pentane is much lower (0.18 MPa – 0.47 MPa). Lower pressures mean lower densities; therefore, sonic conditions are reached at the nozzle throat for lower mass flow rates. As shown in [176], low mass flow rates are beneficial for the turbine efficiency, but on the other hand are adverse for power production.

SES36 seems attractive for the Tesla turbine, as it combines relatively low–pressure levels with comparably high temperatures. This feature combines the good traits of refrigerants (high power to density ratio) with those of the hydrocarbons (high efficiencies), allowing the design of a high power density machine at desirable efficiencies (~50%).

Fig. 4.41 displays the rotor and stator efficiency separately. Of particular importance is the trend of stator efficiency, which is almost flat with values around 90%. This is possible thanks to the vaned configuration. The rotor efficiency, on the other hand, is deeply influenced by the flow condition and it is the main responsible for the trend of total to static efficiency. It has to be also remarked that the total pressure losses between stator and rotor play a fundamental contribution in lowering the expander efficiency. Specifically, the total pressure loss in the turbine is in the order of 20–30% of the overall pressure drop, with higher values connected to high nozzle Mach numbers and low specific speeds. Therefore, it is important to rightly design the dimensions of the stator–rotor interface.

The main performance parameters of the assessed Tesla with various workings fluids for a turbine inlet temperature of 100°C, are resumed in Tab. 4.5.

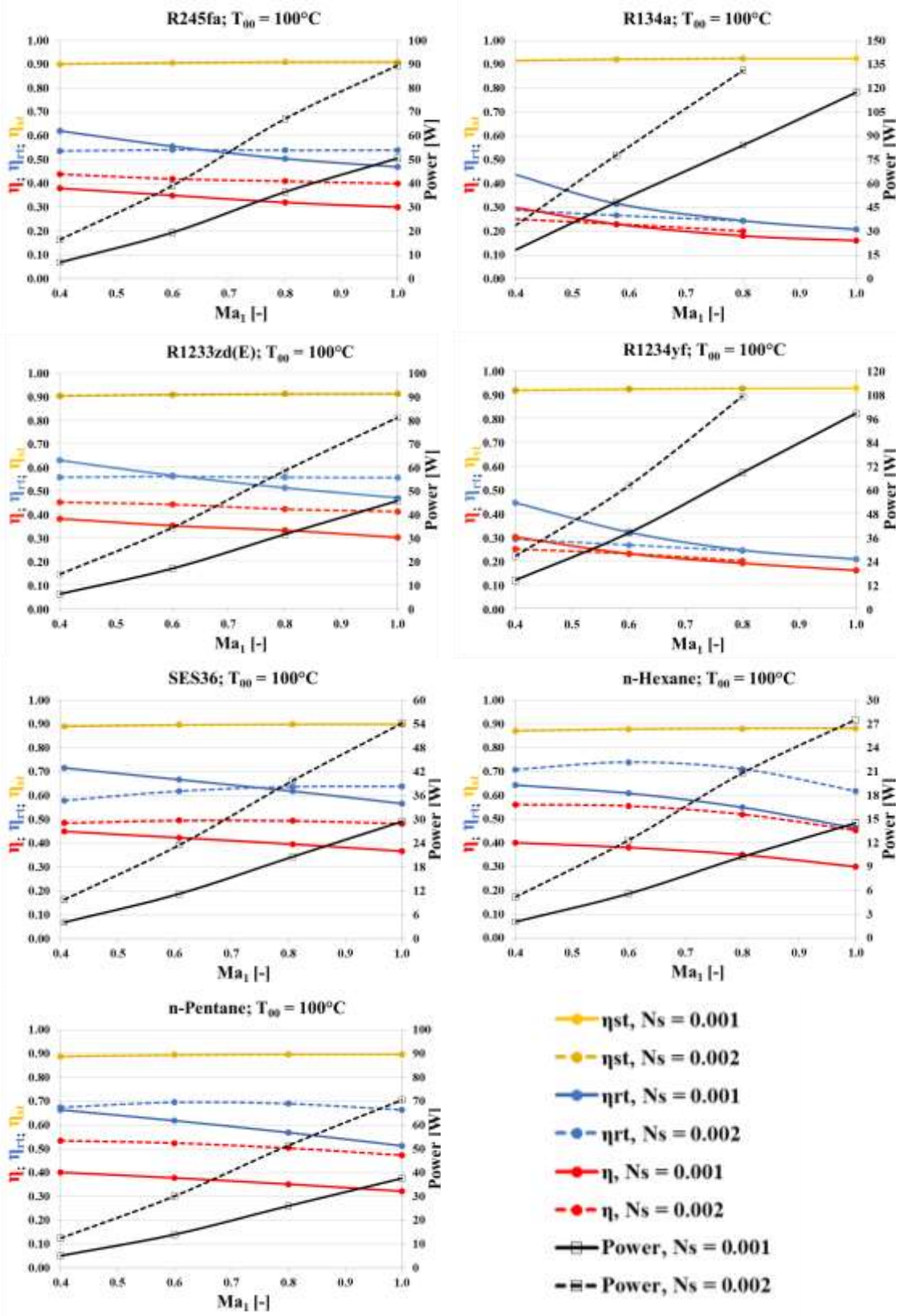

Fig. 4.41 Efficiency and power vs. stator outlet Mach number for low turbine entry temperature case (T_{00} =100°C)

Table 4.5 Parametric analysis of selected fluids for total inlet temperature T_{00} =100 [°C]

	R245fa – P_{00} = 1.009 [MPa]				R134a – P_{00} = 3.247 [MPa]			
	n_s = 0.001							
Parameter	Ma_1= 0.4	Ma_1= 0.6	Ma_1=0.8	Ma_1= 1	Ma_1 =0.4	Ma_1 =0.6	Ma_1 =0.8	Ma_1 =1
Ma_2	0.13	0.22	0.30	0.36	0.25	0.47	0.67	0.84
Ψ	3.62	3.90	4.36	4.87	3.18	3.38	3.93	4.83
ϕ	0.06	0.07	0.09	0.11	0.06	0.07	0.10	0.13
D_s	38.17	35.42	32.21	29.52	38.03	33.78	28.74	24.19
rpm	2393	3328	4021	4420	2357	3186	3629	3811
p_2/p_0	0.83	0.66	0.48	0.35	0.82	0.63	0.41	0.25
	n_s = 0.002							
Ma_2	0.35	0.49	0.59	0.65	0.58	0.80	0.99	*Not*
Ψ	1.07	1.46	1.89	2.29	0.91	1.33	1.82	*reached*
ϕ	0.02	0.03	0.04	0.06	0.02	0.04	0.05	–
D_s	40.01	33.91	29.22	26.10	37.57	30.35	24.74	*chocked*
rpm	6772	7705	8284	8582	5963	6459	6658	*rotor*
p_2/p_0	0.69	0.51	0.35	0.25	0.65	0.47	0.28	*exit*

	R1233zd(E) – P_{00} = 0.833 [MPa]				R1234yf – P_{00} = 3.080 [MPa]			
	n_s = 0.001							
Parameter	Ma_1= 0.4	Ma_1= 0.6	Ma_1=0.8	Ma_1= 1	Ma_1 =0.4	Ma_1 =0.6	Ma_1 =0.8	Ma_1 =1
Ma_2	0.13	0.21	0.29	0.36	0.24	0.46	0.66	0.82
Ψ	3.66	3.95	4.42	5.05	3.21	3.38	3.87	4.72
ϕ	0.06	0.07	0.09	0.12	0.06	0.07	0.10	0.13
D_s	38.14	35.41	32.22	28.96	38.10	34.03	29.11	24.62
rpm	2460	3410	4110	4580	2080	2840	3300	3530
p_2/p_0	0.83	0.66	0.48	0.33	0.83	0.64	0.43	0.27
	n_s = 0.002							
Ma_2	0.34	0.47	0.57	0.64	0.57	0.78	0..96	*Not*
Ψ	1.10	1.48	1.91	2.40	0.90	1.30	1.77	*reached*
ϕ	0.02	0.03	0.04	0.06	0.02	0.04	0.05	–
D_s	40.02	33.99	29.31	25.58	37.82	30.74	25.19	*chocked*
RPM	6950	7930	8520	8850	5330	5830	6110	*rotor*
p_2/p_0	0.69	0.50	0.35	0.23	0.67	0.48	0.31	*exit*

SES36 – P_{00} = 0.496 [MPa]				
n_s = 0.001				
Parameter	Ma_1= 0.4	Ma_1=0.6	Ma_1=0.8	Ma_1= 1
Ma_2	0.13	0.20	0.27	0.33
Ψ	3.00	3.27	3.65	4.15
ϕ	0.05	0.06	0.08	0.10
D_s	38.45	35.47	32.16	28.78
rpm	2656	3647	4383	4867
p_2/p_0	0.81	0.64	0.46	0.31
n_s = 0.002				
Ma_2	0.32	0.44	0.54	0.62
Ψ	0.92	1.23	1.56	1.94
ϕ	0.02	0.03	0.04	0.05
D_s	40.38	33.61	28.52	24.44
RPM	7420	8604	9320	9665
p_2/p_0	0.63	0.45	0.30	0.19

	n–Hexane – P_{00} = 0.185 [MPa]				n–Pentane – P_{00} = 0.469 [MPa]			
	n_s = 0.001							
Parameter	Ma_1= 0.4	Ma_1= 0.6	Ma_1=0.8	Ma_1= 1	Ma_1 =0.4	Ma_1 =0.6	Ma_1 =0.8	Ma_1 =1
Ma_2	0.09	0.14	0.19	0.27	0.10	0.16	0.22	0.28
Ψ	3.54	3.92	4.38	5.00	3.68	4.01	4.46	5.05
ϕ	0.06	0.07	0.09	0.11	0.06	0.07	0.09	0.12
D_s	38.83	35.94	32.64	28.60	38.33	35.70	32.70	29.44
rpm	3498	4755	5707	6302	3491	4818	5831	6525
p_2/p_0	0.81	0.64	0.46	0.28	0.83	0.66	0.49	0.33
	n_s = 0.002							
Ma_2	0.21	0.27	0.34	0.43	0.25	0.34	0.42	0.48
Ψ	1.16	1.55	1.94	2.43	1.17	1.55	1.94	2.39
ϕ	0.02	0.03	0.04	0.06	0.02	0.03	0.04	0.06
D_s	41.00	35.31	30.50	25.52	40.57	35.00	30.53	26.63
rpm	9722	11255	12225	12480	9784	11413	12447	13000
p_2/p_0	0.69	0.51	0.34	0.20	0.70	0.53	0.37	0.24

Medium turbine entry temperature (150°C)

Higher temperature levels imply a larger power production. This is true also for the Tesla turbine. Indeed, with an increase of 50°C (as well as with an increase of the pressure levels) the power produced per channel reaches almost doubled values compared to the 100°C case.

Nonetheless, if efficiency is considered, the trend is opposite. This behaviour is due to the corresponding increase of pressure. As stated above, the Tesla turbine reaches high efficiencies at low mass flow rate and with high nozzle throat velocities. For a fixed geometry and mass flow rate, high velocities are reached for low density values (that is, at low pressures and high temperatures); when using refrigerants as working fluids (as an alternative to hydrocarbons) at high temperature, it is necessary to work at relatively high pressure and this is the reason for the larger efficiency penalty which can be noticed comparing Figs. 4.41 and 4.42. At high temperature and pressure, higher rotor exit velocities are also reached, which again impairs the turbine efficiency.

In this range of temperature, it seems that n–Hexane would be the most suitable fluid for the Tesla turbine, as it can guarantee relatively high efficiency, with quite high power production par channel. This feature is guaranteed by the much lower total inlet pressure of n–Hexane when compared to all other fluids.

The performance parameters values of a Tesla turbine are in the same range of those of volumetric expanders or drag turbines, corresponding to relatively high specific diameters and low specific speeds [210], as resumed in Tab. 4.6. Due to the nature of the turbine, a low flow coefficient is needed to determine good rotor efficiency (Φ = 0.01–0.1). On the other hand, the work coefficient Ψ can be very high (over 3–4), especially at low specific speeds (n_s = 0.001). Values of Ψ between 1 and 1.6 are recommended for higher specific speed (n_s = 0.002).

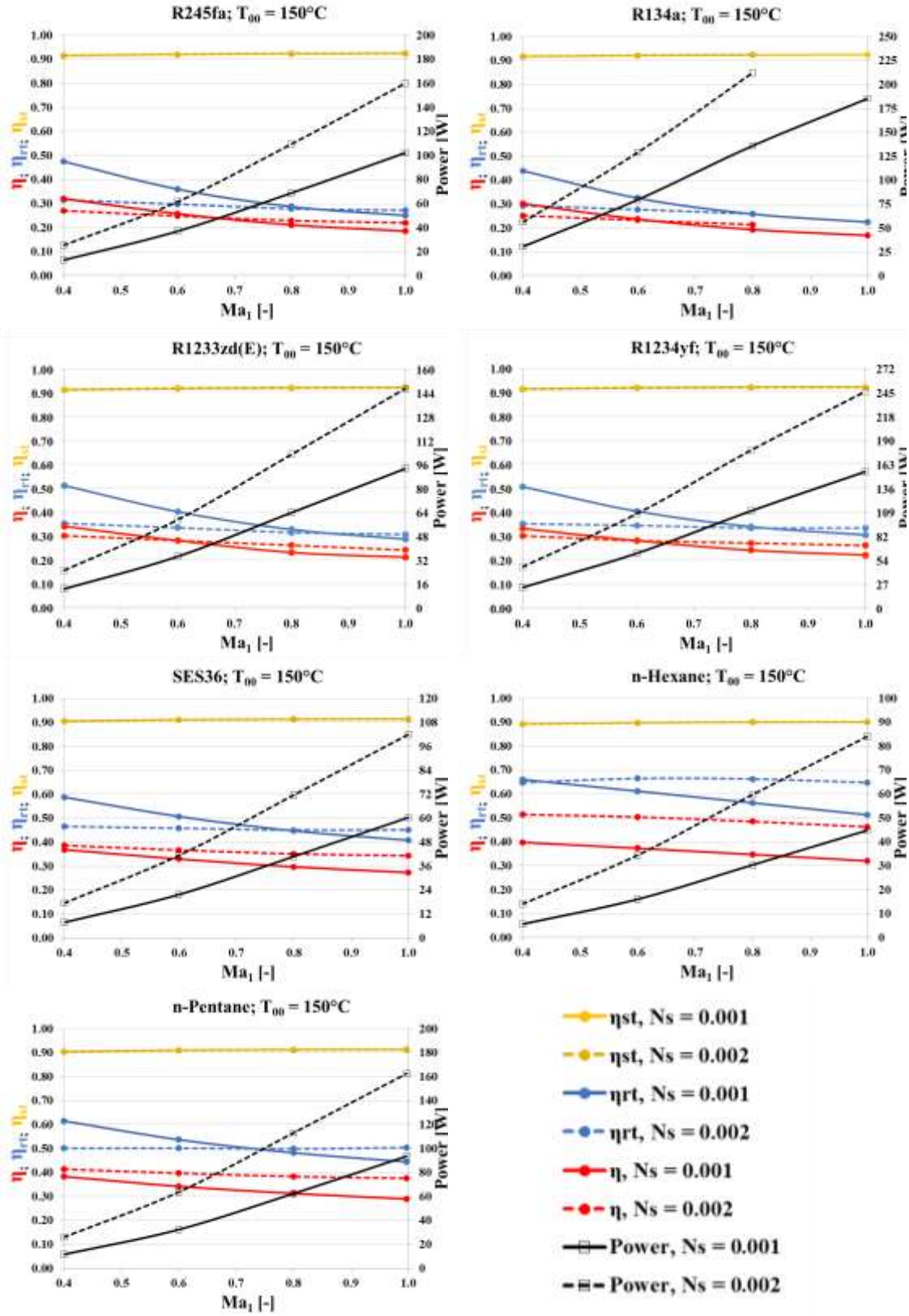

Fig. 4.42 Efficiency and power vs. stator outlet Mach number for medium turbine entry temperature case (T_{00} =150°C)

Table 4.6 Parametric analysis of selected fluids for total inlet temperature T_{00} =150 [°C]

Parameter	Ma_1= 0.4	Ma_1= 0.6	Ma_1=0.8	Ma_1= 1	Ma_1 =0.4	Ma_1 =0.6	Ma_1 =0.8	Ma_1 =1
	R245fa – P_{00} = 2.815 [MPa]				R134a – P_{00} = 3.975 [MPa]			
	n_s = 0.001							
Ma_2	0.22	0.41	0.59	0.73	0.25	0.47	0.66	0.82
Ψ	3.26	3.40	3.90	4.68	3.19	3.41	4.01	4.93
ϕ	0.06	0.07	0.09	0.12	0.06	0.07	0.10	0.14
D_s	38.21	34.52	30.03	25.80	38.05	33.79	28.78	24.34
rpm	2107	2960	3492	3822	2924	3914	4401	4567
p_2/p_0	0.84	0.65	0.45	0.28	0.80	0.58	0.38	0.23
	n_s = 0.002							
Ma_2	0.54	0.73	0.90	1	0.59	0.81	1.00	*Not*
Ψ	0.90	1.30	1.75	2.35	0.92	1.36	1.89	*reached*
ϕ	0.02	0.03	0.05	0.07	0.02	0.04	0.05	–
D_s	38.44	31.47	26.07	21.84	37.46	30.17	24.57	*chocked*
rpm	5587	6182	6570	6757	7375	7890	8012	*rotor*
p_2/p_0	0.68	0.49	0.32	0.20	0.62	0.42	0.26	*exit*
	R1233zd(E) – P_{00} = 2.290 [MPa]				R1234yf – P_{00} = 3.080 [MPa]			
	n_s = 0.001							
Ma_2	0.2	0.36	0.53	0.66	0.21	0.37	0.53	0.64
Ψ	3.37	3.56	4.02	4.77	3.36	3.59	4.11	4.89
ϕ	0.06	0.06	0.09	0.12	0.06	0.07	0.09	0.13
D_s	38.16	34.75	30.50	26.41	38.14	34.59	30.33	26.39
rpm	2230	3100	3700	4050	2800	3820	4440	4760
p_2/p_0	0.84	0.66	0.46	0.29	0.81	0.62	0.42	0.27
	n_s = 0.002							
Ma_2	0.50	0.70	0.86	1.00	0.53	0.72	0.87	0.99
Ψ	0.94	1.34	1.80	2.37	0.94	1.38	1.87	2.47
ϕ	0.02	0.03	0.05	0.07	0.02	0.03	0.05	0.07
D_s	38.71	31.85	26.51	22.33	38.38	31.41	26.15	22.24
rpm	6010	6640	7030	7210	7500	8100	8400	8450
p_2/p_0	0.68	0.49	0.32	0.20	0.63	0.44	0.29	0.18

Parameter	Ma_1= 0.4	Ma_1=0.6	Ma_1=0.8	Ma_1= 1
	SES36 – P_{00} = 1.462 [MPa]			
	n_s = 0.001			
Ma_2	0.15	0.26	0.36	0.44
Ψ	3.55	3.80	4.26	4.90
ϕ	0.06	0.07	0.09	0.12
D_s	38.13	35.22	31.77	28.36
rpm	1976	2757	3331	3726
p_2/p_0	0.84	0.67	0.49	0.33
	n_s = 0.002			
Ma_2	0.41	0.56	0.68	0.77
Ψ	1.02	1.42	1.85	2.35
ϕ	0.02	0.03	0.05	0.06
D_s	39.61	33.22	28.37	24.59
rpm	5550	6240	6693	6990
p_2/p_0	0.69	0.51	0.35	0.23

Parameter	Ma_1= 0.4	Ma_1= 0.6	Ma_1=0.8	Ma_1= 1	Ma_1 =0.4	Ma_1 =0.6	Ma_1 =0.8	Ma_1 =1
	n–Hexane – P_{00} = 0.601 [MPa]				n–Pentane – P_{00} = 1.329 [MPa]			
	n_s = 0.001							
Ma_2	0.11	0.17	0.23	0.29	0.14	0.24	0.33	0.40
Ψ	3.67	3.99	4.42	4.99	3.46	3.83	4.27	4.88
ϕ	0.06	0.07	0.09	0.11	0.06	0.07	0.09	0.12
D_s	38.32	35.75	32.80	29.64	38.27	35.49	32.26	29.02
rpm	3248	4524	5520	6240	3320	4539	5563	6285
p_2/p_0	0.84	0.67	0.50	0.34	0.85	0.68	0.50	0.34
	n_s = 0.002							
Ma_2	0.27	0.37	0.45	0.52	0.37	0.51	0.62	0.70
Ψ	1.14	1.52	1.91	2.34	1.03	1.42	1.84	2.32
ϕ	0.02	0.03	0.04	0.06	0.02	0.03	0.04	0.06
D_s	40.59	34.97	30.51	26.66	40.09	33.88	29.13	25.43
rpm	9185	10745	11775	12480	9185	10505	11415	12025
p_2/p_0	0.71	0.54	0.38	0.25	0.70	0.52	0.36	0.24

Performance assessment

The performance assessment of the ORC prototype was carried out for two working fluid: R404a and R1233zd(E). The first one is the fluid, which is available at the test bench of University of Florence, the second one, is on the other hand, the one available at the test bench of University of Liège.

As for the air Tesla prototype performance assessment, first Mach number at nozzle throat outlet and the tangential velocity ratio at rotor inlet ($\sigma = \frac{vt_2}{u_2}$) at fixed thermodynamic conditions (total inlet pressure of 12 bar and total inlet temperature of 60°C for R404a and a total inlet pressure of 8.33 bar and a total inlet temperature of 100°C for R1233zd(E)) were changed to see their influence on the efficiency and power of the turbine; then the thermodynamic conditions were varied, fixing the Mach number at stator outlet at 0.4 and the tangential velocity ratio at 1 for both fluids.

R404a

Fig. 4.43 displays the change in total to total efficiency of the Tesla turbine prototype when a total inlet pressure of 12 bar and a total inlet temperature of 60°C are considered. As discussed in the previous Sections, the optimal efficiency is reached when $\sigma = 1$ or close to one. High efficiency is reached when relatively low Mach number and proper tangential velocity ratio are achieved. Increasing the tangential velocity ratio will bring to a very drastic drop in efficiency.

As was the case for the air prototype, even for the ORC Tesla turbine prototype optimal efficiency is achieved through low mass flow rates, and therefore of small values of the flow coefficient. Fig. 4.44 displays the $\phi - \psi$ diagram of the ORC prototype (with R404a as working fluid for the above stated fixed thermodynamic conditions). Particularly, the suggested range of operation would be the same as the air prototype or: $0.05 < \phi < 0.08$ and $0.6 < \psi < 1$.

Total to total efficiency against specific speed and specific diameter is displayed in Fig. 4.45. The optimal working range of the ORC turbine prototype is for $21 < d_s < 23$ and $0.07 < n_s < 0.1$, which are achieved through the right matching of mass flow rate and rotational speed.

Finally, Fig. 4.46 presents the reduced mass flow rate – expansion ratio curves at various reduced speeds. Expansion ratios up to 4 are achieved when reduced mass flow rate are close to $8{\cdot}E^{-6}$.

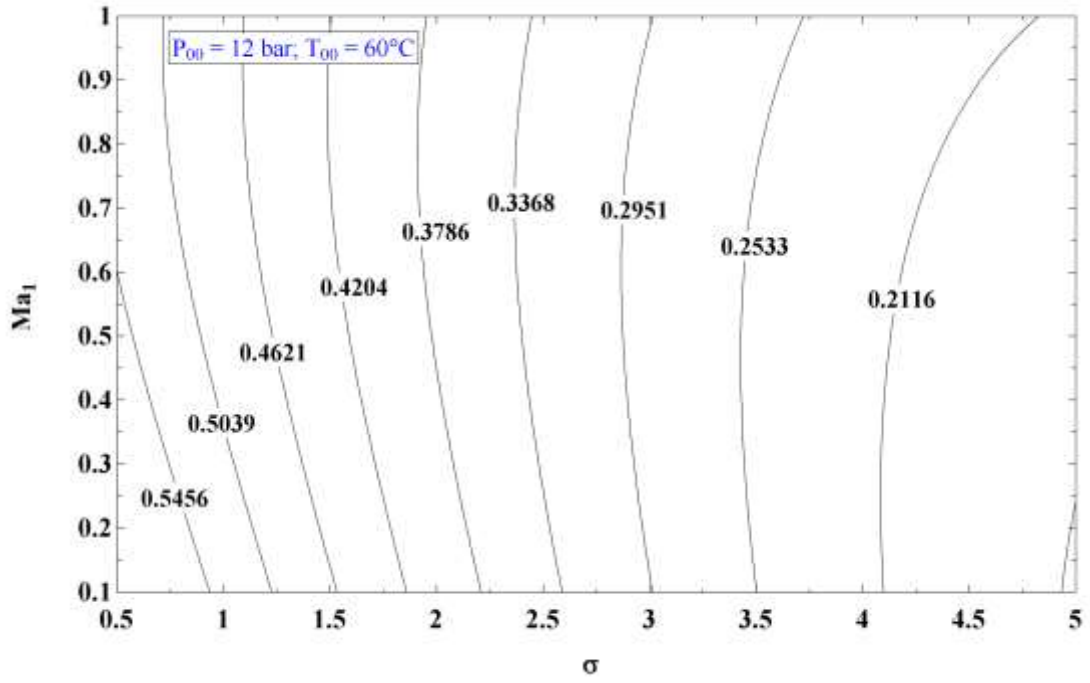

Fig. 4.43 Total to total efficiency of ORC Tesla prototype utilizing R404a as working fluid as function of **σ** and Ma_1

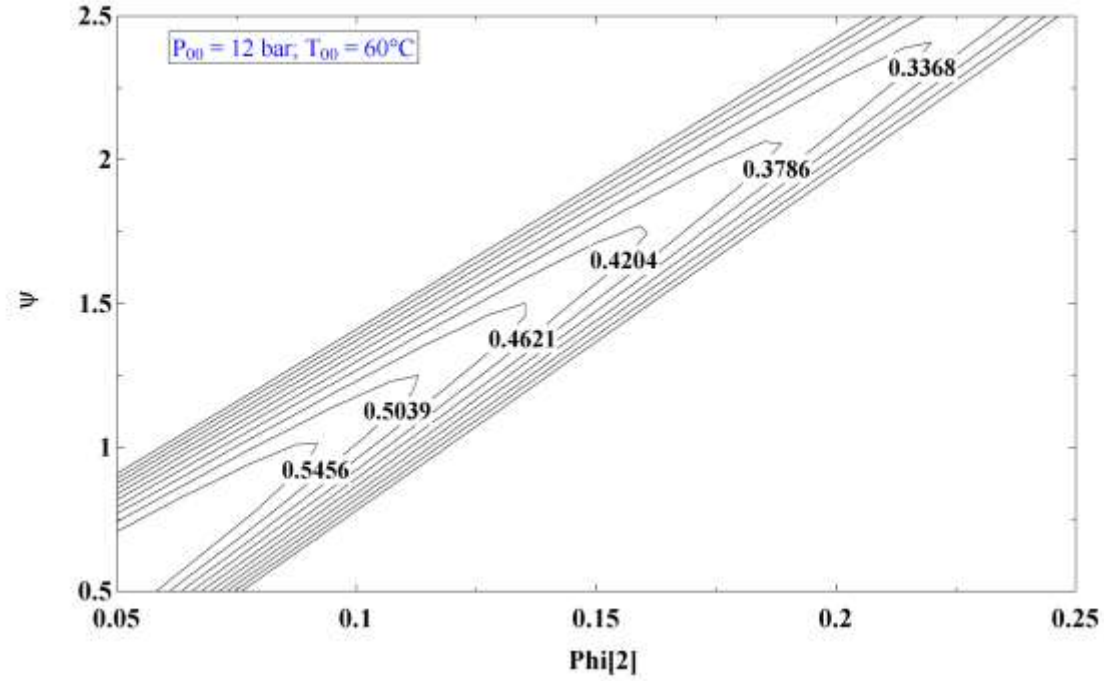

Fig. 4.44 ϕ − ψ diagram of ORC Tesla prototype utilizing R404a as working fluid

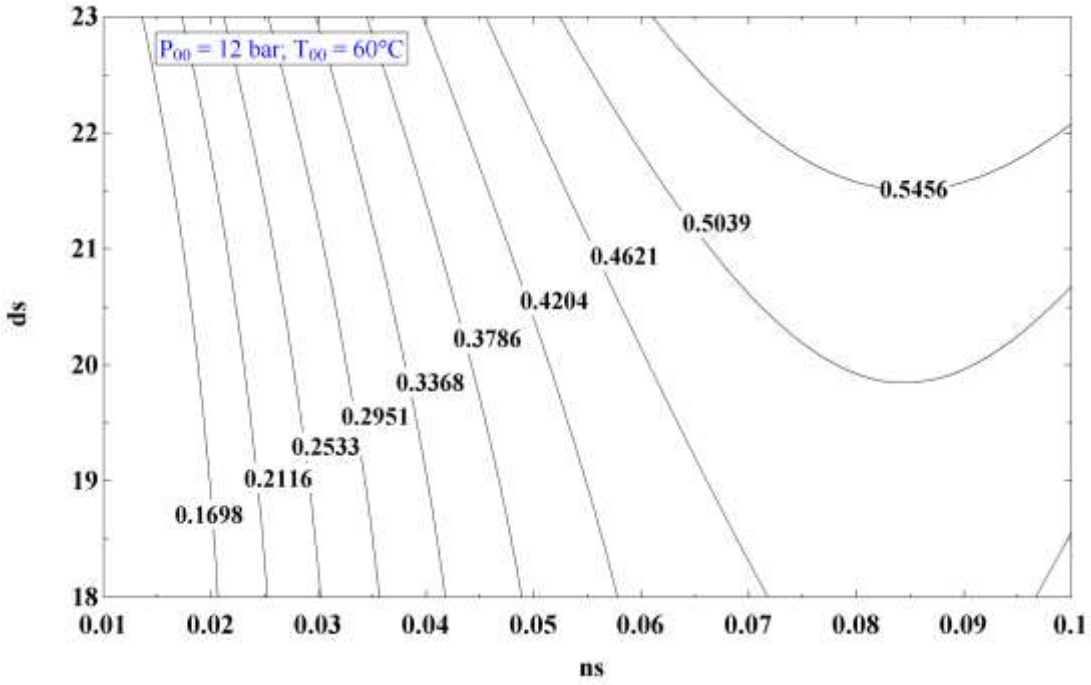

Fig. 4.45 $n_s - d_s$ diagram of ORC Tesla prototype utilizing R404a as working fluid

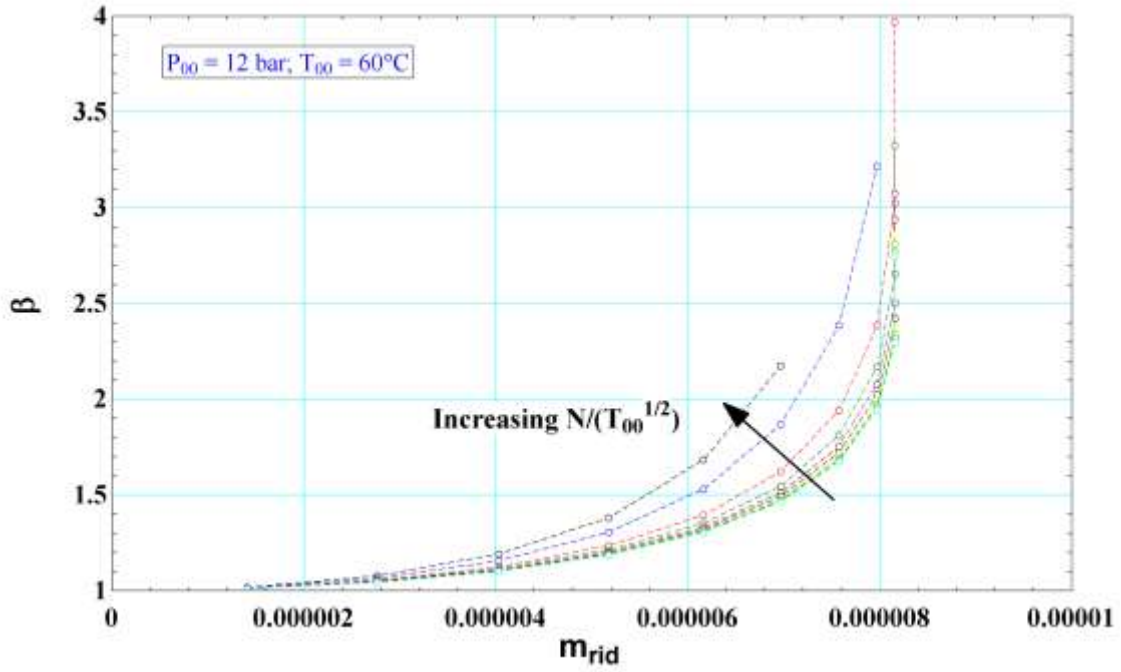

Fig. 4.46 $m_{rid} - \beta$ diagram of ORC Tesla prototype utilizing R404a as working fluid

The thermodynamic analysis assessment results are displayed in Fig. 4.47 (a–d). It is important to note the still contrasting behaviour between efficiency (Fig. 4.47a) and power (Fig. 4.47c). Indeed, Tesla turbine optimal efficiency is obtained when very low mass flow rates are considered (Fig. 4.47d). Low mass flow rates are reached for low pressures and high temperature, if the Mach number at stator outlet and the rotational velocity ratio are fixed. The developed prototype, provided the right conditions, could therefore reach a power as high as 2,132 W, with a rotational speed of about 5,500 rpm.

The ORC Tesla prototype is not a compact expander, as can be noted from Fig. 4.47b, which displays the compactness factor. The compactness factor values for this specific prototype are very small. This was due to the initial design constraint of working with a limited rotational speed.

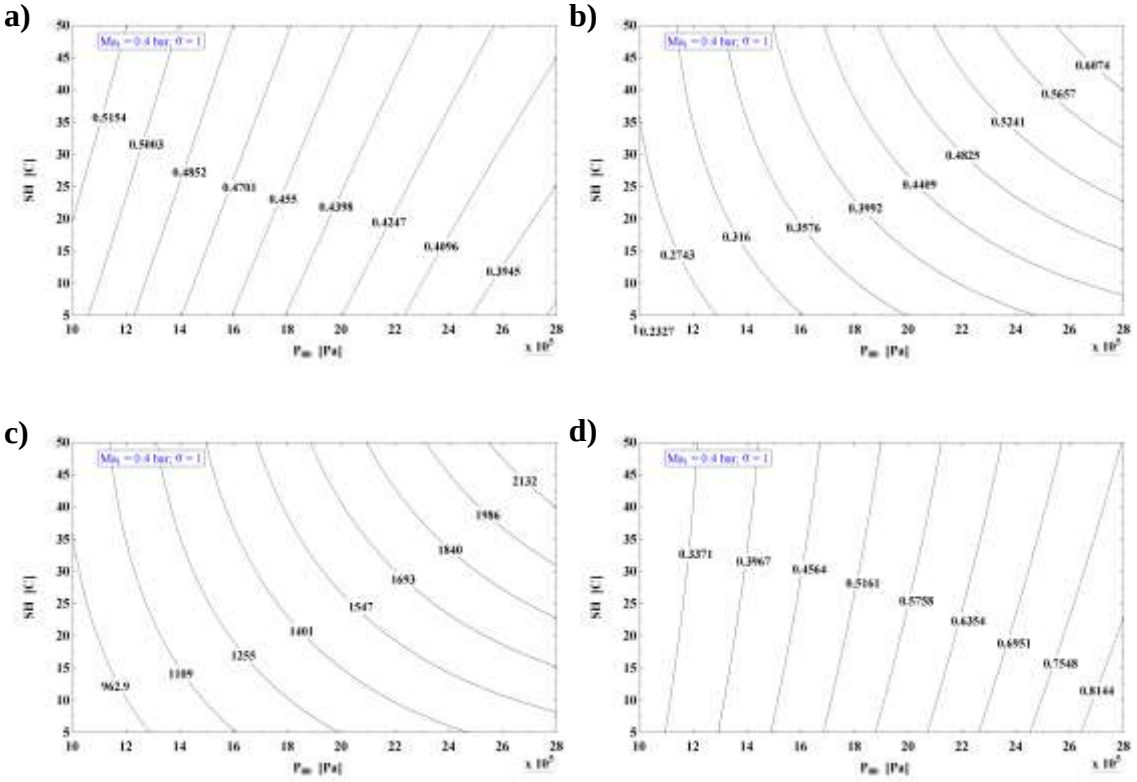

Fig. 4.47 a) η_{TT} b) Compactness factor c) Power d) Mass flow rate of ORC Tesla turbine prototype utilizing R404a as working fluid, as function of total inlet pressure and temperature

R1233d(E)

The same trends that were obtained for the ORC Tesla prototype working with R404a are found when R1233zd(E) is used instead. The $\sigma - Ma_1$ diagram (Fig. 4.48) provides the same information, stressing even more that a proper value of σ is fundamental, as high value of this coefficient will bring to a drastic drop in efficiency.

Even the $\phi - \psi$ diagram (Fig. 4.49) indicates that the optimal range of operation would similar, just admitting slightly higher load coefficients: $0.05 < \phi < 0.08$ and $0.6 < \psi < 1.2$.

The n_s–d_s diagram displayed in Fig. 4.50 suggests that the optimal operation range for the ORC turbine prototype when working with R1233zd(E) would be with $23 < d_s < 25$ and $0.08 < n_s < 0.12$.

To conclude, Fig. 4.51 assesses the reduced mass flow rate – expansion ratio curve at various reduced speeds. It is important to note that a little higher expansion ratio can be reached with this working fluid for a reduced mass flow rate of about $9 \cdot E^{-6}$.

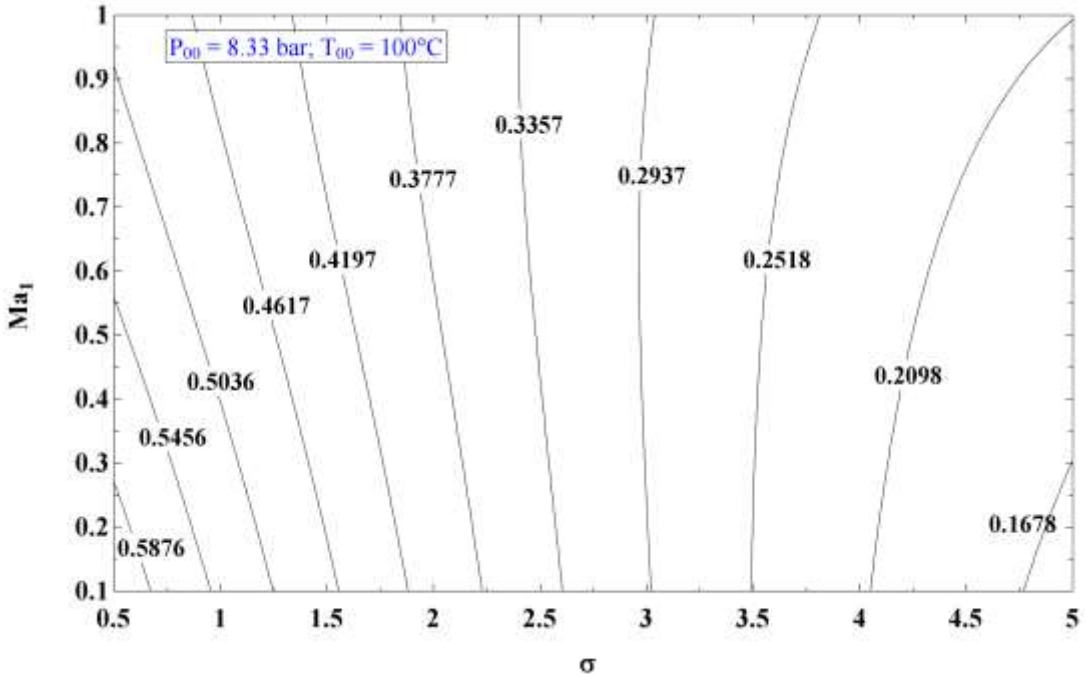

Fig. 4.48 Total to total efficiency of ORC Tesla prototype utilizing R1233zd(E) as working fluid as function of $\boldsymbol{\sigma}$ and Ma_1

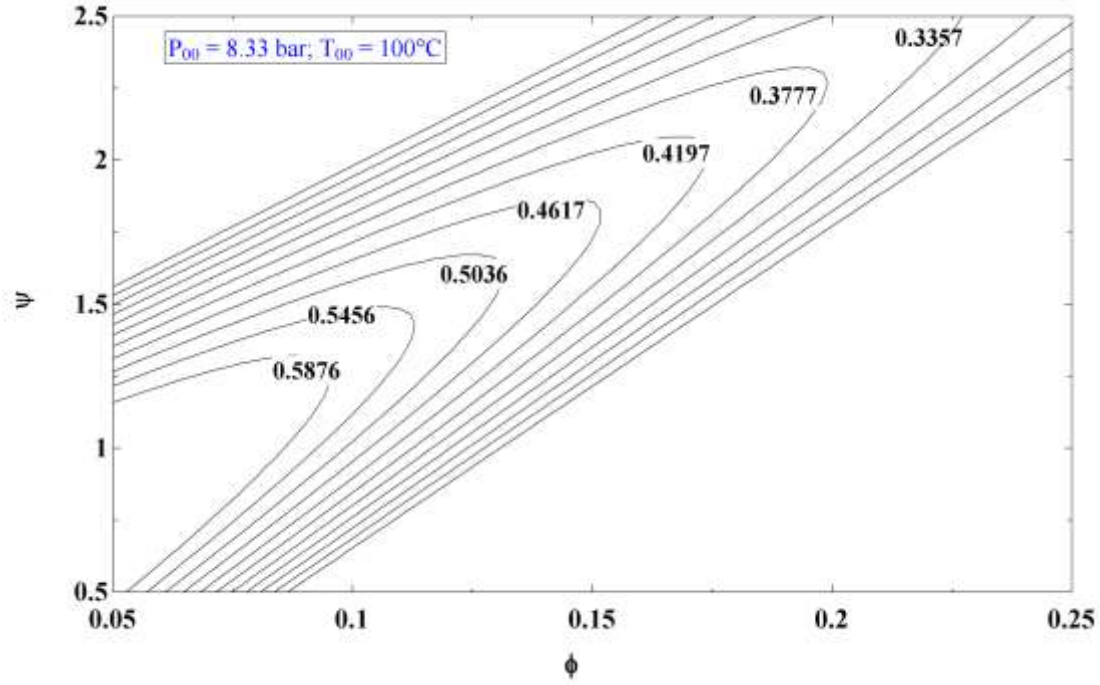

Fig. 4.49 $\phi - \psi$ diagram of ORC Tesla prototype utilizing R1233zd(E) as working fluid

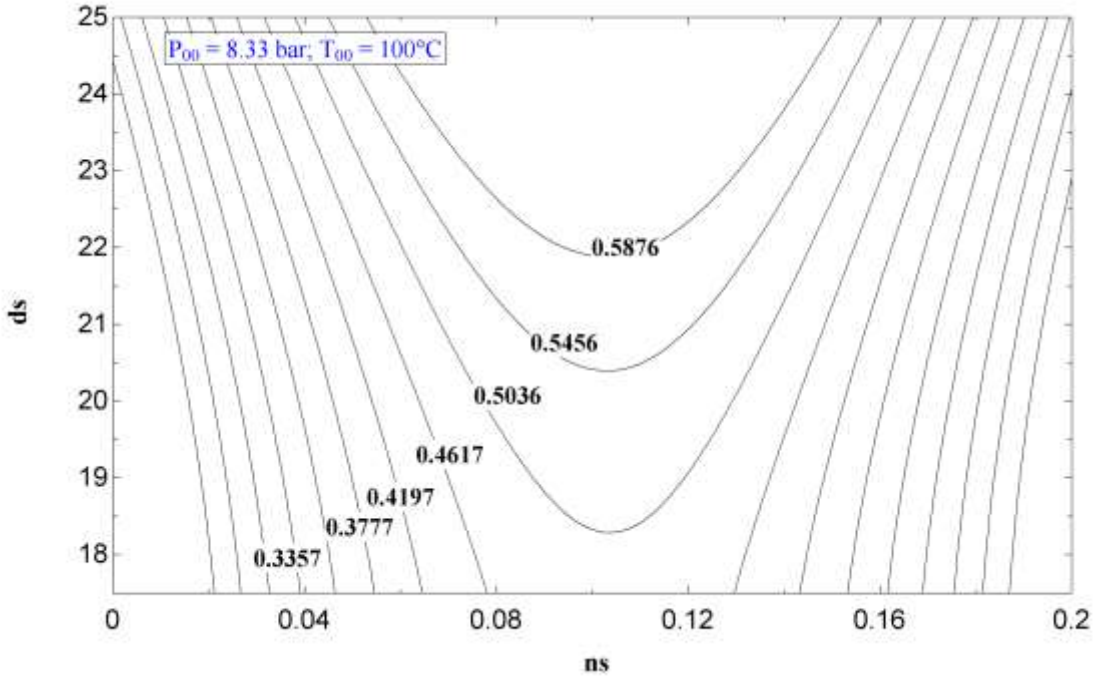

Fig. 4.50 $n_s - d_s$ diagram of ORC Tesla prototype utilizing R1233zd(E) as working fluid

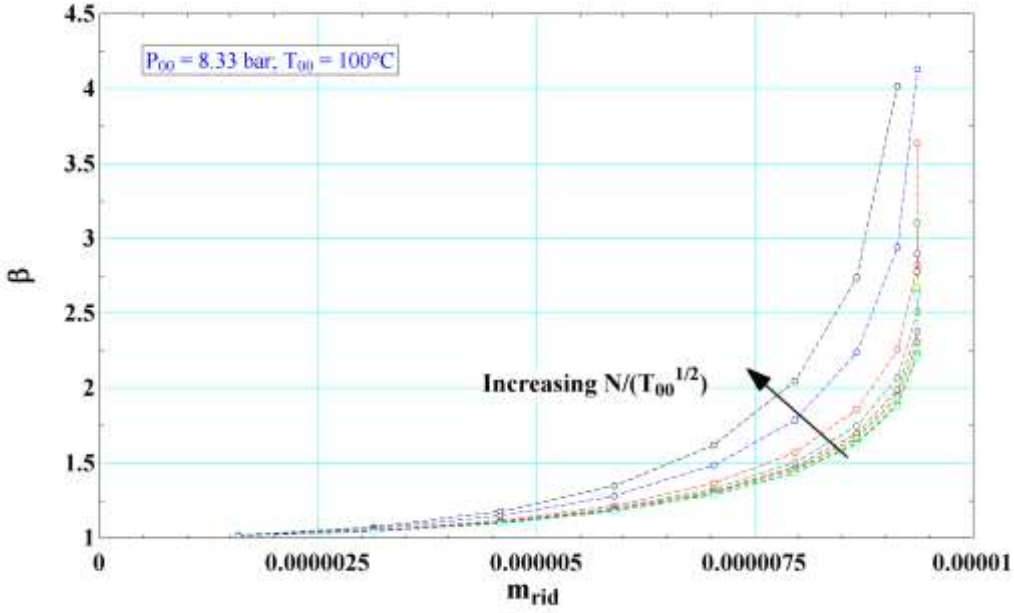

Fig. 4.51 $\mathbf{m_{rid} - \beta}$ diagram of ORC Tesla prototype utilizing R1233zd(E) as working fluid

The thermodynamic analysis assessment results are displayed in Fig. 4.52 (a–d). As for all the other cases, the opposing behaviour between efficiency (Fig. 4.52a) and power (Fig. 4.52c) is still present; directly linked to low mass flow rates trend (Fig. 4.52d). The developed ORC prototype, provided the right conditions, could therefore reach a power production as high as 1,800 W, with a rotational speed of about 5,150 rpm. As analysed for the R404a, the compactness factor (Fig. 4.52b) is definitely low.

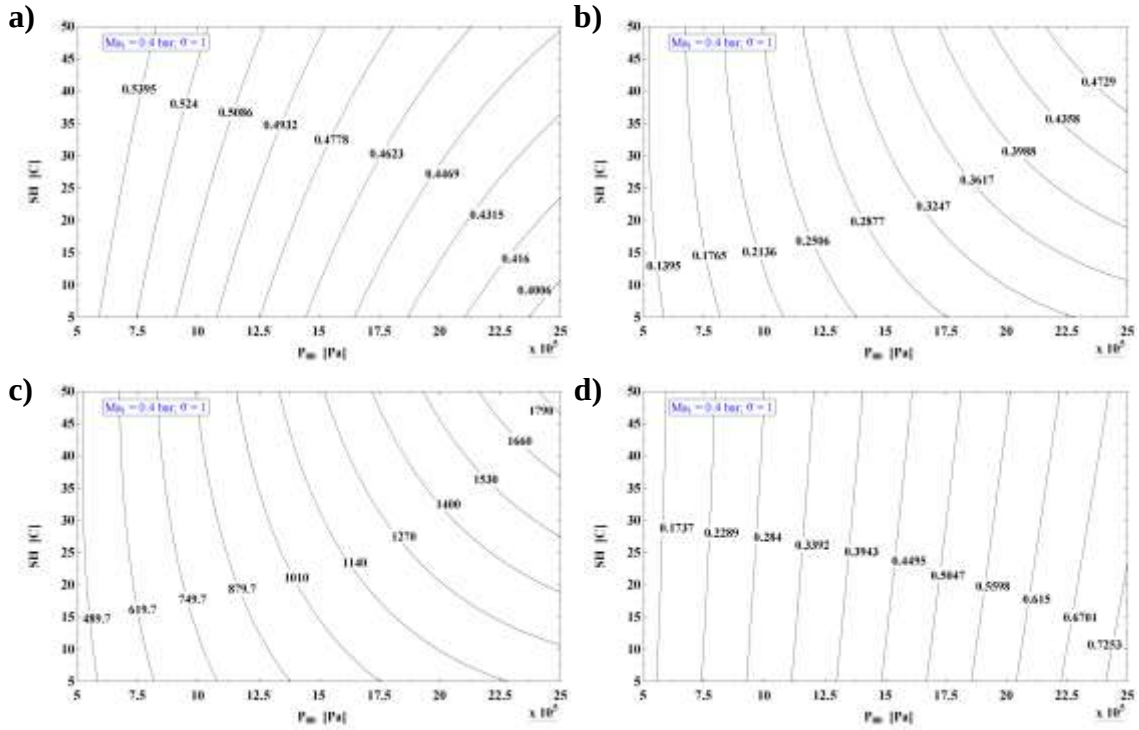

Fig. 4.52 a) η_{TT} b) Compactness factor c) Power d) Mass flow rate of ORC Tesla turbine prototype utilizing R1233zd(E) as working fluid, as function of total inlet pressure and temperature

4.2 CFD analyses

4.2.1 Air Tesla turbine

The aim of the computational assessment developed for the air Tesla prototype was to provide a benchmark on the fluid behaviour inside a Tesla turbine, in order to strengthen the results obtained with the in–house EES code.

Particularly, in Fig. 4.53 (a–d) the results of static pressure, absoulte radial velocity, absolute tangential velocity and static temperature calculated with the EES model are compared with those computed with the CFD analyses carried out with a mesh made up of 3125000 nodes. The results obtained with the k–kl–omega model are very close to the ones achieved with the 2D home–built model.

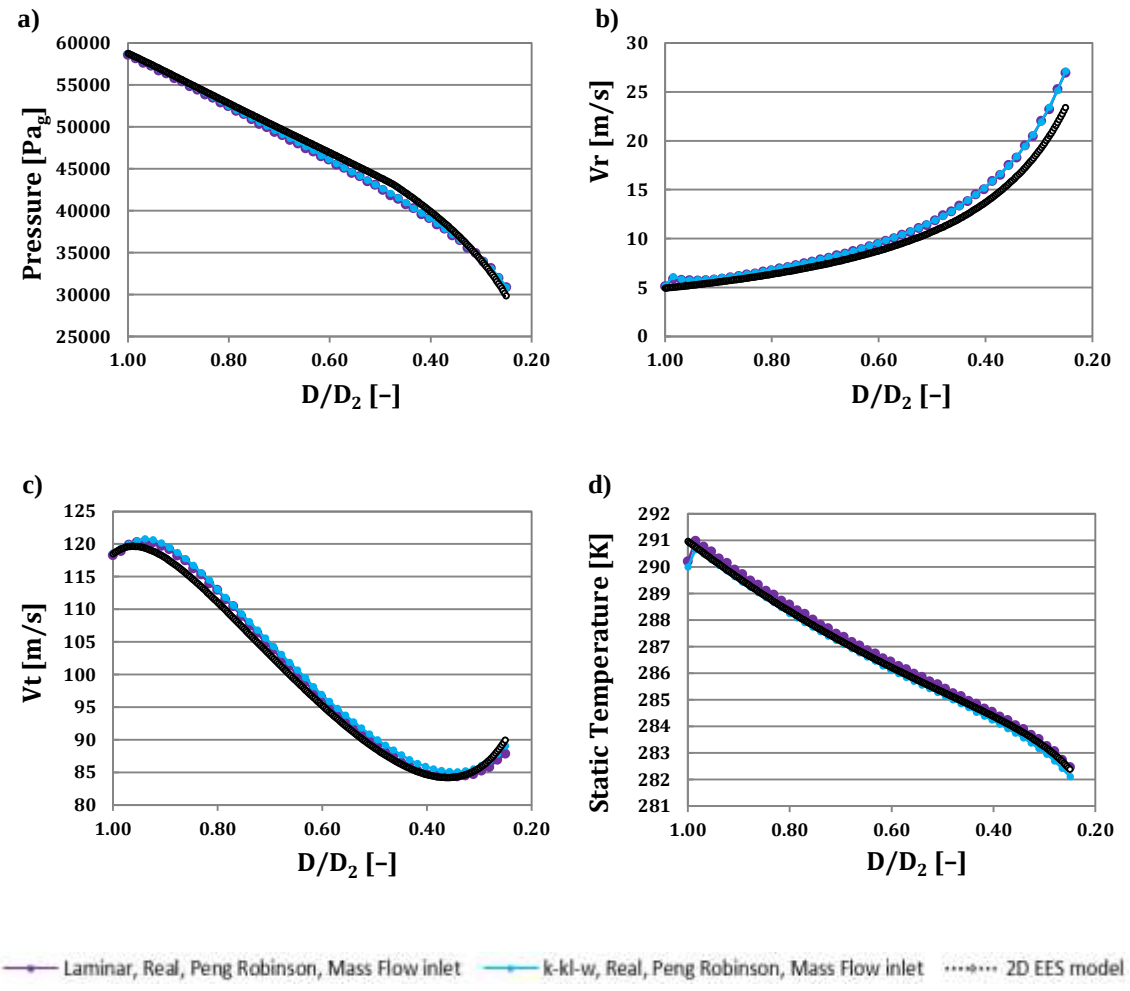

Fig. 4.53 Comparison between the results obtained with the EES and CFD analyses; a) static pressure, b) radial velocity, c) tangential velocity, d) static temperature, along the radial direction

4.2.2 ORC Tesla turbine

Rotor

Analysis with R404a working fluid

Fig. 4.54 resumes the main computational results (mass weighted average values) achieved when R404a was taken into account as working fluid. The conditions, which were fixed at rotor inlet for all the analysed cases, are resumed as follows:

- Static pressure = 1.16 MPa;
- Static temperature = 60°C;
- Mass flow rate = 0.004 kg/s;
- Inlet angle = 88°.

Three different rotational speeds (1500, 3000 and 4500 rpm) were analysed in order to assess its influence on the expander efficiency and power output, as well as to understand the changes in the velocity profiles, pressure and temperature inside the rotor channels.

The results obtained at 1500 rpm are the ones, which present highest discrepancy between the numerical models. Nonetheless, both the 2D EES in–house code and ANSYS Fluent predict clearly a very drastic reduction of tangential velocity at rotor inlet, which is the main responsible for power production. As expected, the radial velocity increases monotonically from periphery to centrum, as the wetted–wall area decreases and the mass flow rate is fixed by the continuity equation.

A very close match between the results of the 2D EES model and those of the 3D CFD model were found. Specifically, a better match in the entrance region is reached when the EES model is compared to the 4–equation SST Langtry–Menter model, in respect of the laminar simulations. This is mainly due to the underestimation of the velocity drop by the laminar model, as it does not correctly predict the velocity profile in the entry region. Basically, the two different results (which anyway are really close to each other) differ due to the axial velocity distribution.

The discrepancy of the results with rotational speeds of 3000 and 4500 rpm is almost non–existent in these cases. The reason for this is the lower difference between absolute tangential inlet velocity and peripheral speed.

When comparing the behaviour of the flow at various rotational speeds, it is necessary to assess each parameter separately. For radial velocity only the curves at 3000 rpm are presented, as the trend (i.e. increasing towards the centrum) is almost entirely coincident not depending on rotational speed, as it is determined by continuity equation. As a consequence, the static pressure decreases monotonically from periphery to centrum. It must be remarked that higher rotational speeds imply higher pressure drops. The

temperature drop is larger when pressure drop is larger, which is directly connected to the increment of rotational speed. It is interesting to notice the temperature behaviour at low revolution per minute (Fig. 4.54d). In the first part (i.e. at rotor inlet), the fluid is partially heated, due to the abrupt reduction of tangential velocity in a very short distance. The turbine fails to convert all the available work, which is dissipatedly converted into heat. Nevertheless, the related temperature variation of the fluid is quite modest.

Finally, the tangential velocity is the most interesting parameter to analyse. According to Euler Equation, its change is responsible for work transfer to the rotor. The variation of the peripheral velocity of the expander deeply affects the tangential velocity behaviour. At low speed of revolution (1500 rpm) and fixed flow velocity at rotor inlet, the flow suddenly decelerates, not being able to transfer all the work to the turbine. At intermediate speed (3000 rpm), the decrease of tangential velocity is smoother and enables a more efficient work transfer to the rotor. Finally, at high speed of revolution (4500 rpm), there is a first part of the rotor where the tangential velocity increases, so that the turbine locally transfers work to the fluid as a compressor. Therefore, from the analysed behaviour at different speeds of revolution, it is clear that, when the nozzle conditions are fixed, an optimised speed allowing the maximum power extraction at the highest efficiency exists.

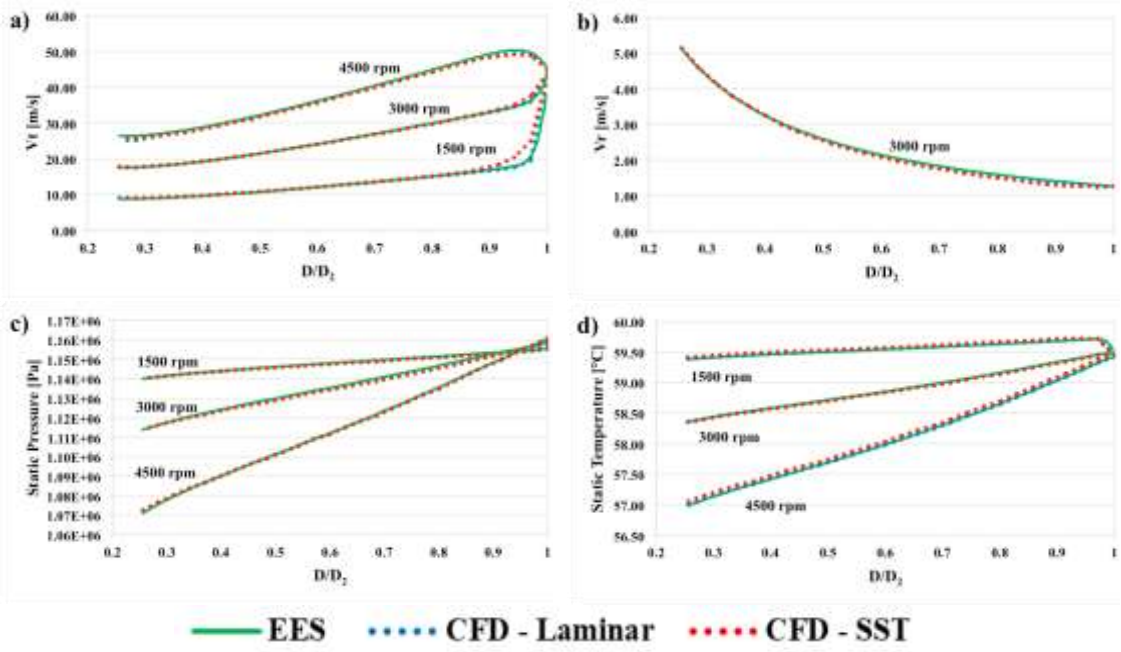

Fig. 4.54 Radial behaviour at various rpm with R404a of: a) Tangential velocity; b) Radial velocity; c) Static pressure; d) Static temperature

Tab. 4.7 summarises the results obtained both from 2D EES and 3D Fluent simulations. Specifically, it should be noticed that the efficiency is maximised in the condition where the relative tangential velocity at rotor inlet is close to zero, as can be noted in Fig. 4.54. Particularly, in Fig. 4.54a it can be noted that the for the 4500 rpm case absolute tangential velocity increases at inlet, corresponding to a negative relative tangential velocity and therefore to a reduction of the expander efficiency.

Table 4.7 Results of the 2D EES model compared to the 3D Fluent results

rpm	Rotor efficiency	Power per channel [W]	Rotor mass flow rate [kg/s]	Static pressure at rotor inlet [Pa]	Static temperature at rotor inlet [°C]
2D EES model					
1500	0.55	2.80	0.004	1155344	59.42
3000	0.69	5.45	0.004	1158488	59.47
4500	0.65	7.91	0.004	1160474	59.42
3D Fluent model					
1500	0.55	2.80	0.004	1155344	59.42
3000	0.69	5.45	0.004	1158488	59.47
4500	0.66	7.97	0.004	1160474	59.42

Analysis with R134a, r245fa and R1233zd(E) working fluids

Three further fluids were simulated in order to compare the in–house 2D code and the 3D CFD results. As shown in Figs. 4.55, 4.56 and 4.57, the results achieved with EES are in close agreement with those from Fluent, for both laminar and SST cases. The same flow behaviour of R404a was found for R134a, R245fa and R1233zd(E). Tab. 4.8 summarizes the data of the simulations run for the three fluids at various rotational speeds flowing with the mass flow rate of 0.004 kg/s. As for the R404a for radial velocity, only the curves at 3000 rpm are presented. The three fluids present the same efficiency tendency when total inlet conditions are fixed. Particularly, the performance of R245fa slightly undergoes at high rotational speed (4500 rpm) compared to R134a due to the lower critical pressure that determines higher values of density at throat, thus lower velocity which results in a lower power output. Indeed, the lower values of velocity at stator outlet determine a more pronounced flow reverse at inlet for the highest analysed rotational speed (Figs. 4.56a and 4.57a), responsible for lower values of power and efficiency.

As it is usual in ORC applications, the fixed variable is usually the high temperature of the cycle (due to the heat source). Therefore, when a Tesla turbine is considered as an expander for ORC, it seems that the optimal fluid is the one, which guarantees lower densities at fixed temperature. Lower densities at fixed temperature are reached for lower pressure of the fluid; consequently, a suitable fluid for a Tesla turbine for an ORC application is the one, which hold high critical temperature and low critical pressure.

Table 4.8 Comparison of results for different fluids at various rotational speeds (from 1500 to 4500 rpm), at the mass flow rate of 0.004 kg/s, total inlet pressure (1.2 MPa) and super heating level (37 °C)

Fluid	Rotor efficiency	Power per channel [W]	Static pressure at rotor inlet [Pa]	Static temperature at rotor inlet [°C]	Rotational speed [rpm]
R404a	0.55	2.80	1155344	59.42	1500
R134a	0.52	2.97	1159129	82.50	1500
R245fa	0.56	2.78	1158426	133.50	1500
R1233zd(E)	0.55	2.81	1160346	142.00	1500
R404a	0.69	5.45	1158488	59.47	3000
R134a	0.69	5.64	1160386	82.5	3000
R245fa	0.69	5.25	1161838	133.50	3000
R1233zd(E)	0.71	5.28	1156274	142.00	3000
R404a	0.66	7.97	1160474	59.42	4500
R134a	0.67	8.08	1154641	82.5	4500
R245fa	0.64	7.44	1160462	133.5	4500
R1233zd(E)	0.69	7.26	1114178	142	4500

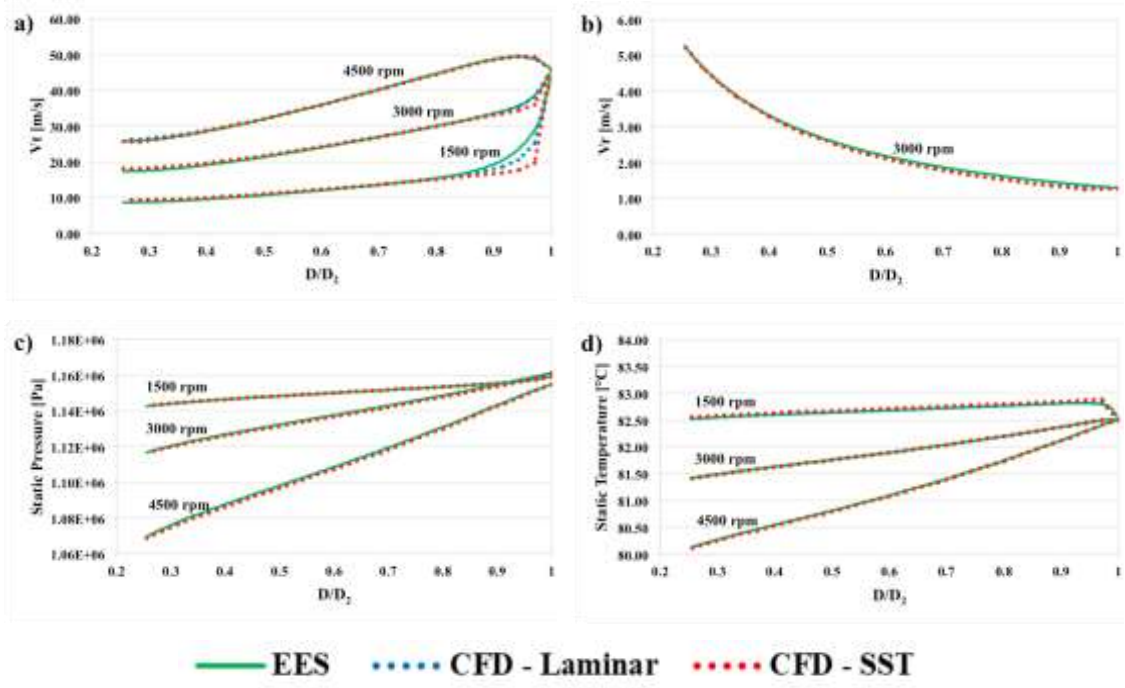

Fig. 4.55 Radial behaviour at various rpm with R134a of: a) Tangential velocity; b) Radial velocity; c) Static pressure; d) Static temperature

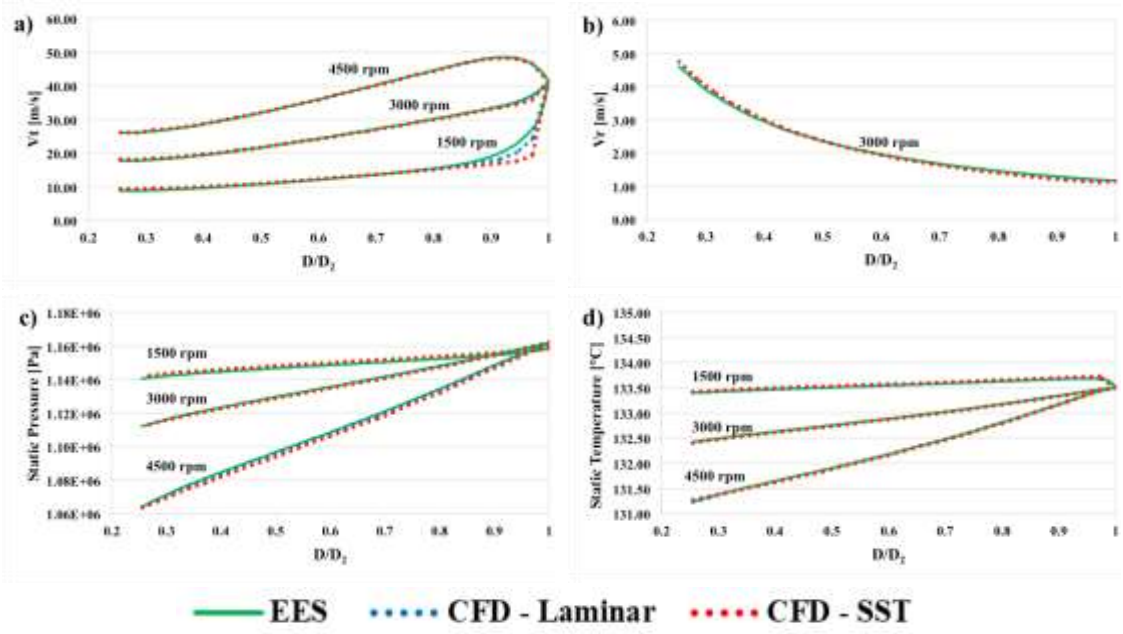

Fig. 4.56 Radial behaviour at various rpm with R245fa of: a) Tangential velocity; b) Radial velocity; c) Static pressure; d) Static temperature

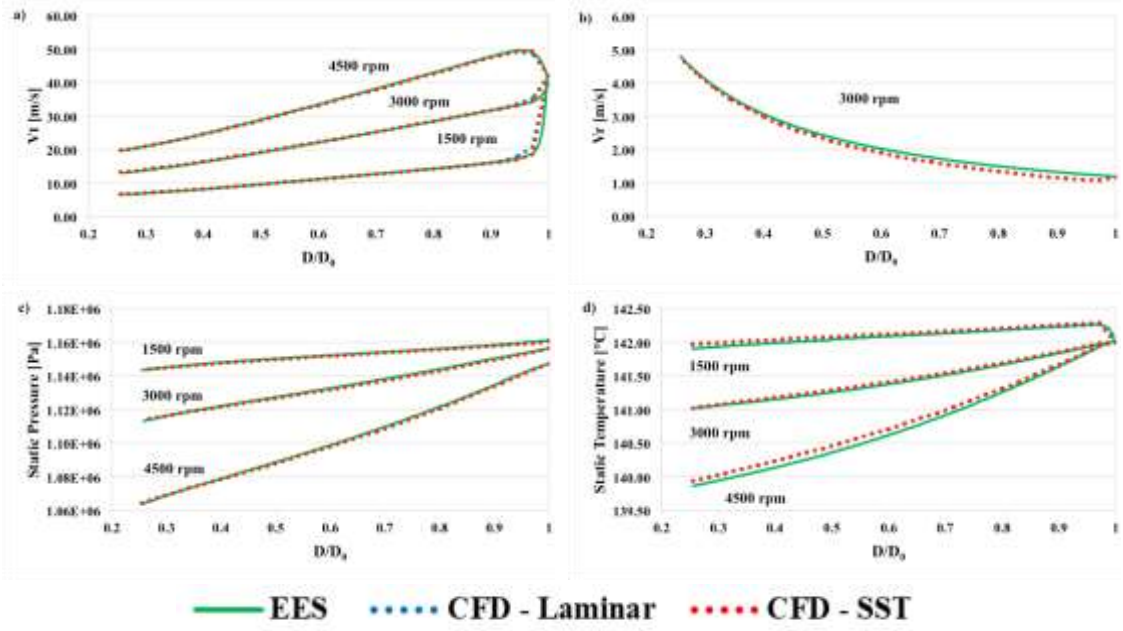

Fig. 4.57 Radial behaviour at various rpm with R1233zd(E) of: a) Tangential velocity; b) Radial velocity; c) Static pressure; d) Static temperature

Coupled Stator–Rotor simulations

The numerical analyses of the Tesla turbine with coupling of stator and rotor were performed with R1233zd(E) as working fluid. The boundary conditions values were imposed from the available data of the experimental campaign carried out at *Universitè de Liège*. Several thermodynamic points (resumed in Tab. 4.9) were simulated and the power and efficiency of the turbine computed and compared to the 2D in house code.

Table 4.9 Boundary condition for coupled stator–rotor analyses

rpm	Total inlet pressure [Pa]	Total inlet temperature [°C]	Static outlet pressure [Pa]	Static outlet temperature [°C]
1500	473535	73.42	310895	68.39
1750	476446	73.14	311083	67.82
2000	479870	73.25	312114	67.67
2250	482052	73.04	310820	67.53
2500	486119	72.98	311721	67.35
2750	489369	72.74	311641	67.01
3000	493133	72.66	311778	66.72

As it will be discussed deeply in Section 4.3.2, the simulation models do not take into account some fundamental sources of inefficiency, due to the real geometry of the turbine. Therefore, the obtained power from computational analyses cannot be compared with those from the experimental campaign, but the results are still of fundamental value as they are representing the “ideal” maximum obtainable power if the fluid does not incur in windage, partialization and pumping losses. Indeed, the simulated geometry does not take into account manufacturing issues, not correct alignment of stator and rotor channels, as well as secondary losses at the axial edges of the rotor.

Fig. 4.58 displays the contours of static pressure, static temperature, tangential velocity and radial velocity for the 3000 rpm case. Comparing the coupled model results with the rotor model results, it is very interesting to remark that partial admission effects are not negligible. Its effects can be easily highlighted when analysing the temperature trend in Fig. 4.58b. The temperature distribution inside the rotor is not uniform anymore, but it displays clearly four different temperature regions, which are due to the spiral trajectories of the fluid from the 4 nozzle admissions. Nonetheless, the difference in temperature between one stream and another is almost negligible, especially if power calculation is taken into account. The highest temperature drop occurs, as expected, at nozzle exit and the temperature drop in the rotor is very small, as is the pressure drop. Indeed, the pressure drop in the rotor is of about 30 kPa, which is a very small part of the total pressure drop of about 180 kPa (Fig. 4.58a). In this case, the Tesla turbine works essentially as an action turbine, where the pressure drop is almost entirely converted in velocity in the nozzles. Radial velocity maintains the same trend as the one assessed for the rotor model (i.e. increasing towards the centrum); as it is determined by the continuity equation. Although, close to nozzle exit, a peak of radial velocity is present. This peak does not globally

influence the results of the simulations; nonetheless, it has to be taken into account that the number of nozzles affects the flow field of the turbine.

The tangential velocity behaviour is close to the one analysed for the rotor only case. At first, the viscous forces effect allows a considerable reduction of tangential velocity, while as the flow approaches the inner radii, the angular momentum effect prevails, therefore increasing the velocity of the fluid. Furthermore, in this case the partial admission effect is not influencing the performance of the turbine in terms of power and efficiency when mass weighted average values are taken into account.

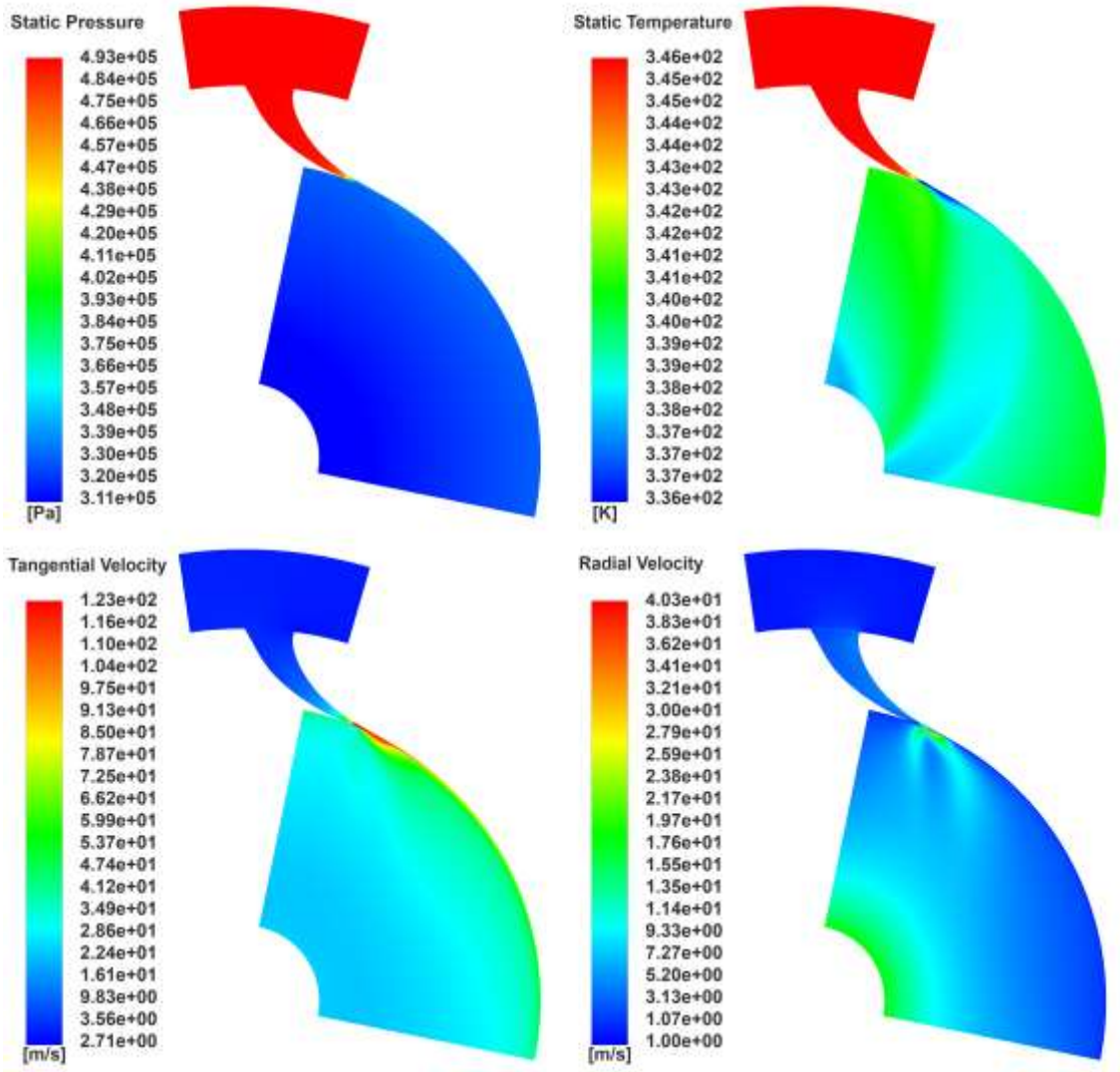

Fig. 4.58 Contours of a) static pressure b) static temperature c) tangential velocity d) radial velocity at 3000 rpm

Finally, a comparison in terms of power and efficiency is presented in Tab. 4.10 between the computed numerical results and the 2D in house code results. It has to be remarked that the 2D code is now neglecting windage, pumping and partialization losses, which conversely will be taken into account when assessing experimental data. As can be noted from Tab. 4.10, the power prediction between 2D EES code and 3D computational fluid dynamics is really close, both in terms of power and efficiency.

Table 4.10 Results of the 2D EES model compared to the 3D Fluent results

rpm	Total mass flow rate [kg/s]	Rotor efficiency	Turbine efficiency	Power per channel [W]	Total power [W]
2D EES model					
1500	0.232	0.32	0.14	4.57	274
1750	0.234	0.36	0.17	5.38	322.7
2000	0.235	0.40	0.19	6.18	371
2250	0.237	0.43	0.22	7.03	421.8
2500	0.239	0.46	0.24	7.87	472.2
2750	0.241	0.49	0.27	8.71	522.8
3000	0.242	0.51	0.29	9.57	574.3
3D Fluent model					
1500	0.232	0.30	0.15	4.55	273.2
1750	0.234	0.34	0.17	5.36	321.6
2000	0.235	0.38	0.19	6.16	369.6
2250	0.237	0.41	0.22	7.00	420.1
2500	0.239	0.44	0.24	7.84	470.1
2750	0.241	0.47	0.26	8.67	520.2
3000	0.242	0.50	0.28	9.52	571.3

4.3 Experimental Campaigns

4.3.1 Air Tesla Turbine

The experimental campaign was conducted exploring two different air mass flow rates, varying the rotational speed of the expander. The maximum rotational speed was limited by the brushless generator; the maximum achievable value was 3000 rpm. The thermodynamic conditions at turbine inlet for all tested points have been resumed in Tab. 4.11.

The comparison between experimental data and numerical prediction are displayed in Fig. 4.59 (shaft power) and 4.60 (total to total efficiency). The numerical predictions match very well the experimental test results for the investigated mass flow rate tested (0.028 and 0.030 kg/s). The limiting factor of the test bench was the admissible revolution per minute, as showed in Figs. 4.59 and 4.60, as this specific prototype could not be run at optimal speed. Indeed, Tesla turbine compactness is mainly dependent on rotational speed. If the turbine diameter requirements are strict (both for the application and mechanical issues), the expander needs to hold higher velocities in order to obtain high efficiency. On the other hand, a high radius design allows reaching high efficiency at relatively small rotational speed. The assessed prototype holds a relatively small radius, which means that optimal rotational speed would be in the order of some ten thousands rpm. At 3000 rpm, the maximum obtained net power was of 94 W. The thermodynamic power was assessed at 107 W, with a power loss due to bearings, generator and torque meter of about 13 W.

Table 4.11 Thermodynamic conditions at turbine inlet

rpm	m = 0.030 [kg/s]		m = 0.028 [kg/s]	
	T_{00} [°C]	P_{00} [bar]	T_{00} [°C]	P_{00} [bar]
300	37.81	1.49	42.78	1.39
600	40.59	1.48	43.82	1.39
900	43.27	1.48	44.87	1.39
1200	45.67	1.48	45.99	1.39
1500	47.93	1.48	47.27	1.39
1800	50.10	1.48	48.65	1.39
2100	52.11	1.48	50.06	1.39
2400	53.81	1.48	51.36	1.39
2700	55.39	1.48	52.69	1.39
3000	56.87	1.49	53.92	1.39

The maximum assessed total to total efficiency of the turbine (at 3000 rpm) was 11.3% when the lower mass flow rate tests were run. Indeed, as previously discussed, it was confirmed that efficiency is high at low mass flow rate. The mechanical efficiency of the turbine (comprehensive of torque meter and generator) was assessed as over 85%.

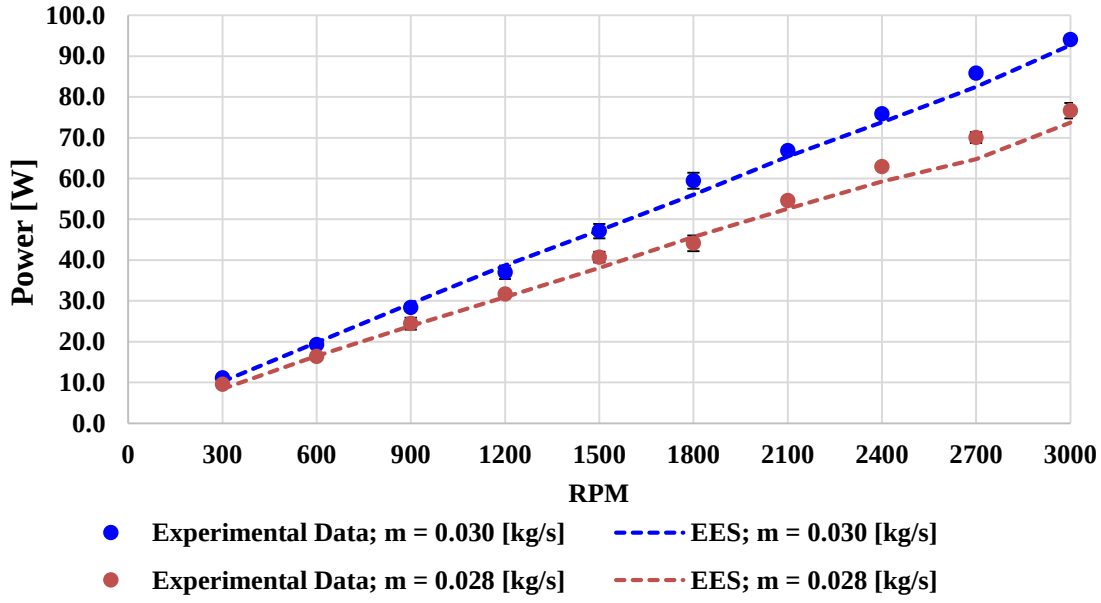

Fig. 4.59 Experimental Data vs. numerical prediction, shaft power

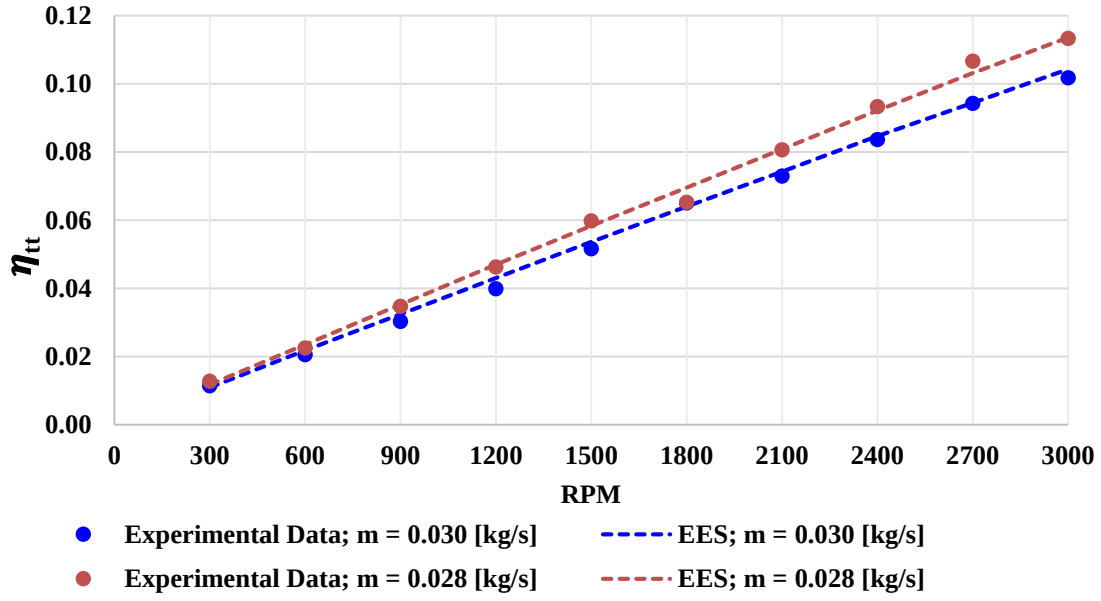

Fig. 4.60 Experimental data vs. numerical prediction, total to total efficiency

4.3.2 ORC Tesla turbine

R404a tests

The ORC Tesla turbine was firstly arranged on the test bench of University of Florence described in Section 3.3.2. The electric motor, the torque meter as well as the servo drive were the same as the one described for the air Tesla turbine tests in the Section 3.5.1. The test bench was developed within the project *Exp–HEAT*, which was funded by the EU (grant no. 605923) under the 7th Framework Program (FP7 Capacities). In Exp–HEAT project, a piston expander was experimentally tested; this expander required a very high quantitative of oil in order to achieve high efficiencies, therefore an auxiliary lubrication system was employed. This resulted in a lot of oil remaining in the test bench circuit, which unfortunately hindered the test on the Tesla expander. Indeed, as can be seen in Fig. 4.61, the turbine worked as a "honey dipper", where the oil was trapped in the gap between stator and rotor, giving rise to very high pumping losses. Various pressures and mass flow rates were tested, but none was able to achieve a stable condition, as the hindering of the oil was high. Furthermore, at first it was questioned if the turbine was correctly working, therefore it was arranged on the same test bench of the air Tesla turbine and tested with the same inlet condition P_{00} = 1.5 bar, m = 0.030 kg/s and various rotational speeds (from 300 to 3500 rpm). The experimental power produced by the turbine well matched the 2D EES model prediction, as shown in Fig. 4.62.

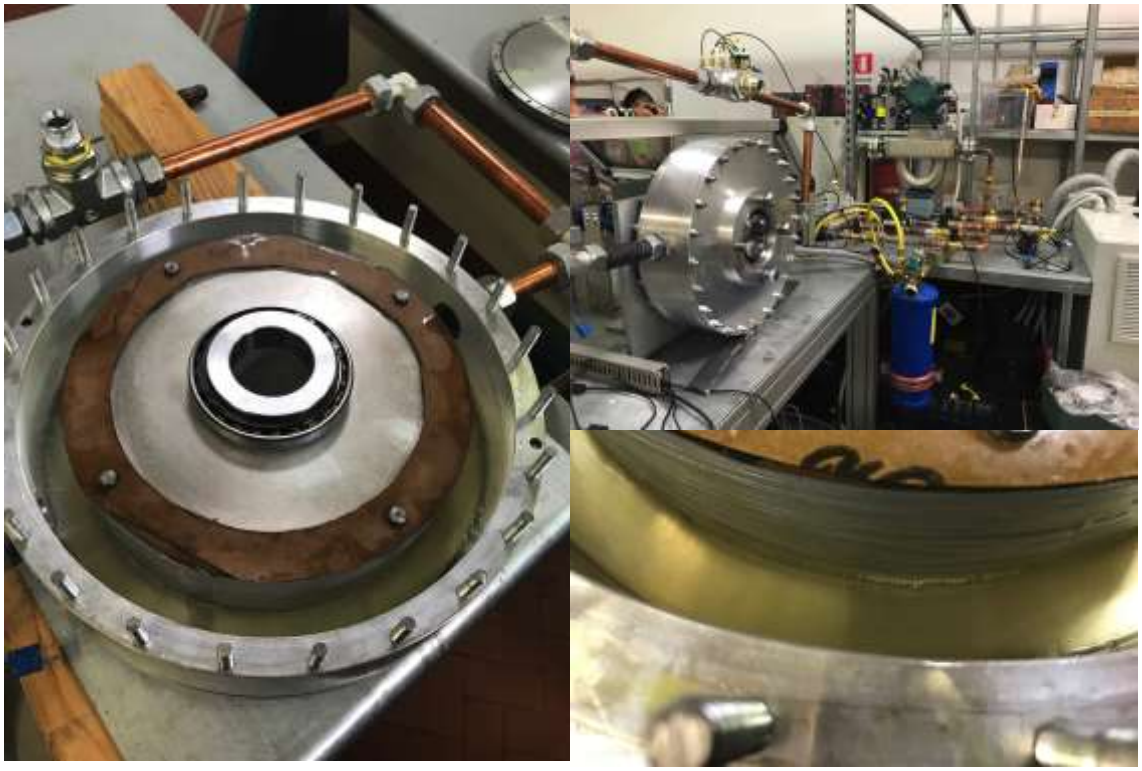

Fig. 4.61 ORC tesla turbine jammed with oil

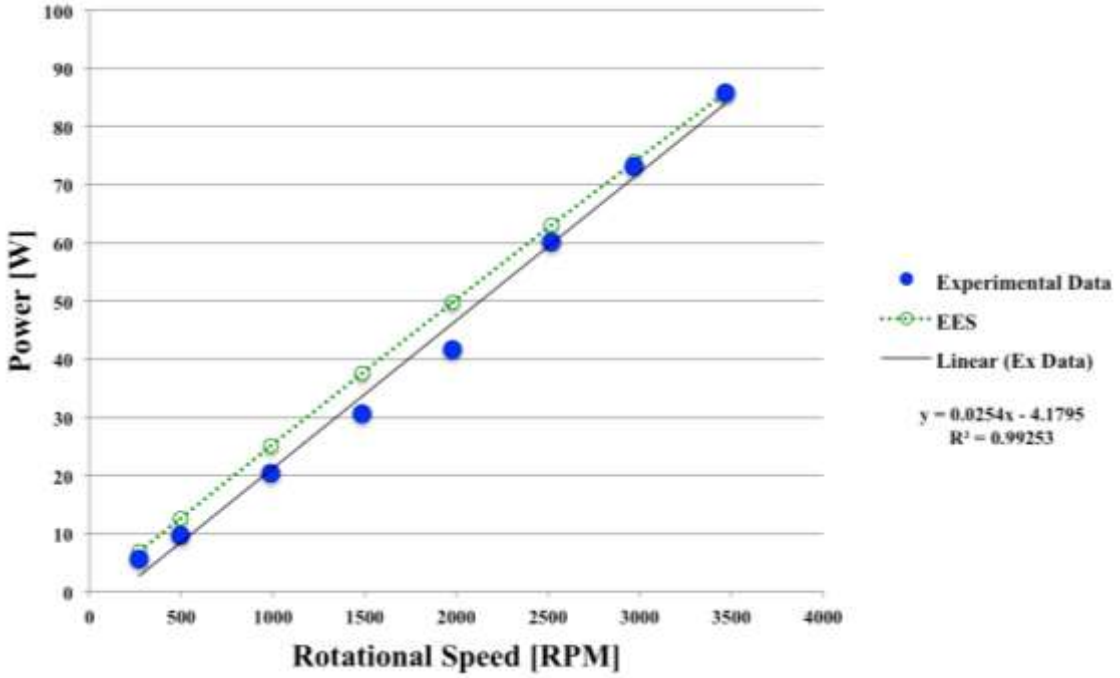

Fig. 4.62 ORC Tesla turbine utilizing air as working fluid

R1233zd(E) tests

The test bench of Université de Liège allowed for the adjustment of:

- The pump mass flow rate (through a frequency inverter), which therefore permitted the imposition of the mass flow rate of the test bench;
- The heat input (changing the heater settings of temperature and air mass flow rate), which allowed the regulation of super heating level;
- The heat output (changing condenser water mass flow rate), which provided a control on the lower pressure of the test bench;
- The rotational speed of the turbine (through a frequency inverter), which allowed to change the pressure drop in the turbine.

Therefore, the experimental campaign was conducted exploring different refrigerant mass flow rates (0.25 – 0.36 kg/s), varying the rotational speed of the expander (1000 – 5000 rpm), as well as total inlet pressure (4.7 – 6.7 bar) and super heating levels (3.2 – 46 °C). In order to have confident temperature measurements, the turbine and the inlet and outlet pipes were insulated. The explored thermodynamic conditions at turbine inlet for all tested points are resumed in Tab. 4.12.

Table 4.12 Thermodynamic conditions at turbine inlet

Nomenclature	Points	Rotational Speed [rpm]	Mass flow rate [kg/s]	T_{00} [°C]	SH [°C]	P_{00} [Pa]
D1	1	2000	0.3568	86.84	8.23	635633
	2	2500	0.3566	87.13	7.94	644701
	3	3000	0.3564	87.08	7.36	653135
	4	3500	0.3565	87.19	6.79	664151
	5	4000	0.3567	87.11	6.11	673920
D2	6	1500	0.2541	73.42	6.34	473535
	7	1750	0.2541	73.14	5.83	476446
	8	2000	0.2541	73.25	5.67	479870
	9	2250	0.2540	73.04	5.29	482052
	10	2500	0.2538	72.98	4.91	486119
	11	2750	0.2539	72.74	4.42	489369
	12	3000	0.2539	72.66	4.04	493133
D3	13	3500	0.2532	108.10	37.52	518962
	14	3250	0.2531	108.56	38.26	515830
	15	3000	0.2530	108.39	38.32	512314
	16	2750	0.2530	108.32	38.48	508854
	17	2500	0.2529	107.60	38.00	505954
	18	2250	0.2530	107.01	37.76	501261
D4	19	1500	0.3009	76.38	11.33	518794
	20	1750	0.3009	76.32	11.21	521596
	21	2000	0.3009	74.98	9.73	523252
	22	2250	0.3009	75.31	10.00	527202
	23	2500	0.3008	74.84	9.55	530978
	24	2750	0.3007	75.44	10.06	536251
	25	3000	0.3008	75.00	9.19	539307
	26	3250	0.3007	74.96	9.28	543242
	27	3500	0.3006	75.42	9.43	547545
	28	3750	0.3008	74.59	8.22	550591
D5	29	5000	0.2993	120.26	44.09	598959
	30	4500	0.2994	120.13	44.60	588417
	31	4000	0.2993	120.20	45.45	577387
	32	3500	0.2992	119.92	45.73	569026
	33	3000	0.2992	119.76	46.14	561617
D6	34	1000	0.3651	78.59	3.73	578933
	35	1500	0.3646	79.28	4.06	584299
	36	2000	0.3642	79.88	4.32	589228
	37	2500	0.3640	79.93	3.90	596259
	38	3000	0.3641	79.81	3.13	605988
	39	3500	0.3635	82.04	4.65	616757
	40	4000	0.3640	81.26	3.35	624814

Fig. 4.63 resumes the thermodynamic conditions tested as function of turbine expansion ratio. The explored range of expansion ratio is not very wide, but it still allows a very significant data analysis.

As can be depicted from Fig. 4.63 (a) and (d), higher mass flow rates are linked to higher total inlet pressure, as well as at higher expansion ratio. Nonetheless, higher expansion ratios are also obtained increasing the super heating (Fig. 4.63 (c)). The expansion ratio is indeed directly linked to the thermodynamic condition at nozzle throat. High inlet pressure implies higher mass flow rate, and therefore higher pressure drop. Moreover, higher super heating level, at same mass flow rate (data D1 and D3 or D4 and D5) is connected to a higher velocity at throat section and therefore to a higher pressure drop. High temperature implies lower densities if all other conditions are fixed. Therefore, due to mass balance, higher velocity is reached at throat and consequently at rotor inlet.

As expected, increasing rotational speed results in an increase of expansion ratio, as displayed in Fig. 4.63 (d). The slope of the curves is almost the same for all investigated conditions. The highest obtained expansion ratio (1.87) was obtained with a mass flow rate of 0.36 kg/s with a super heating level of 3.35 °C at 4000 rpm.

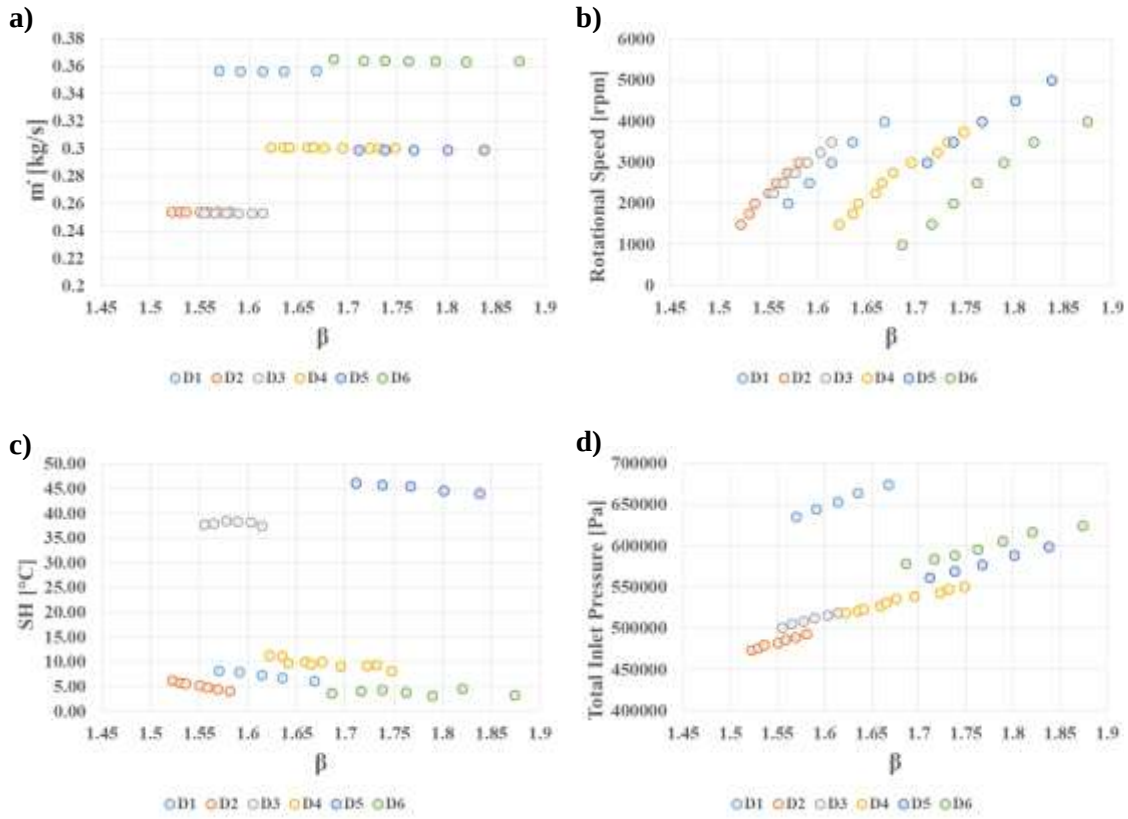

Fig. 4.63 Experimental data: mass flow rate a), rotational speed b), super heating level c) and total turbine inlet pressure d) as function of expansion ratio

The maximum achieved experimental thermodynamic power was 906 W, with a mass flow rate of 0.299 kg/s, 44 °C super heating level and 5000 rpm rotational speed. The highest power conditions were indeed obtained for high super heating levels (data D3 and D5), followed by high mass flow rate conditions (data D1 and D6). Furthermore, as expected, thermodynamic power increases as the expansion ratio augments. Fig. 4.64 displays the behaviour of thermodynamic power as function of the expansion ratio.

It is very interesting to notice that the same expansion ratio can be reached either with a high super heating level or with a higher mass flow rate, but the power production is higher in the former case. Indeed, if we take as an example, an expansion ratio of about 1.8, it can be seen from Fig. 4.64 that the turbine produces nearly 18% more power with a mass flow rate of 0.299 kg/s and a super heating level of 44.6 °C compared to the case with 0.364 kg/s of mass flow rate and a 3.2 °C super heating level. This is due to the better match between rotational speed and tangential velocity, allowing therefore a better power conversion.

Fig. 4.65 displays the thermodynamic power as function of expansion ratio and rotational speed. High expansion ratios and rotational speeds favour power production, while low rotational speeds and expansion ratios hinder the power production.

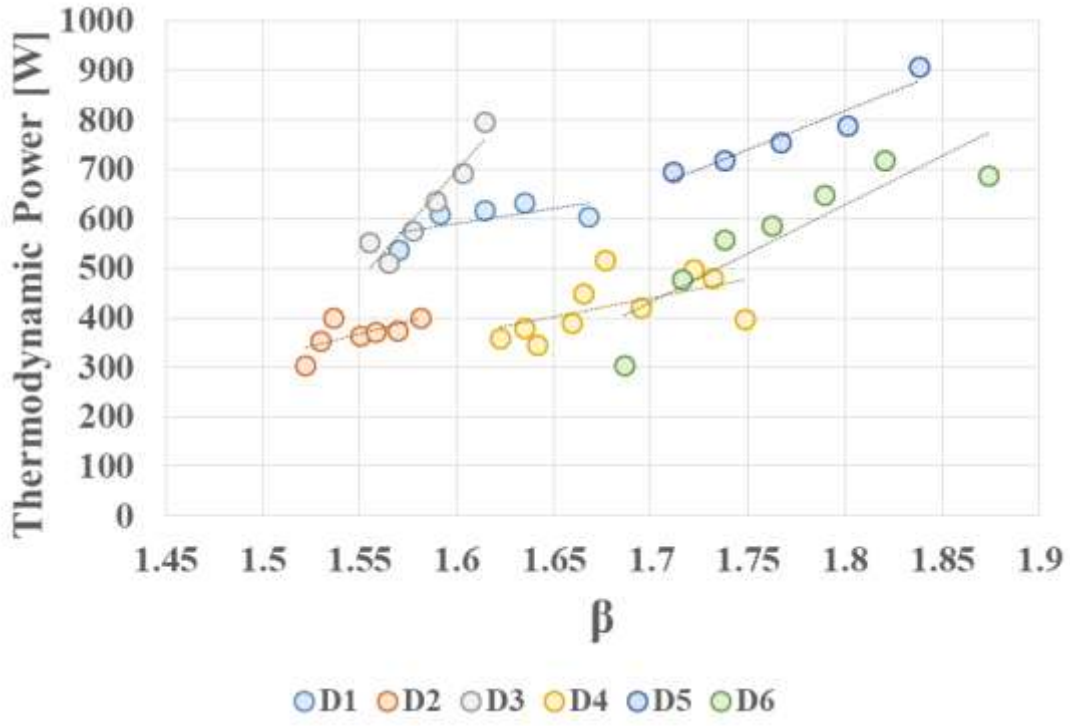

Fig. 4.64 Experimental thermodynamic power output vs. expansion ratio

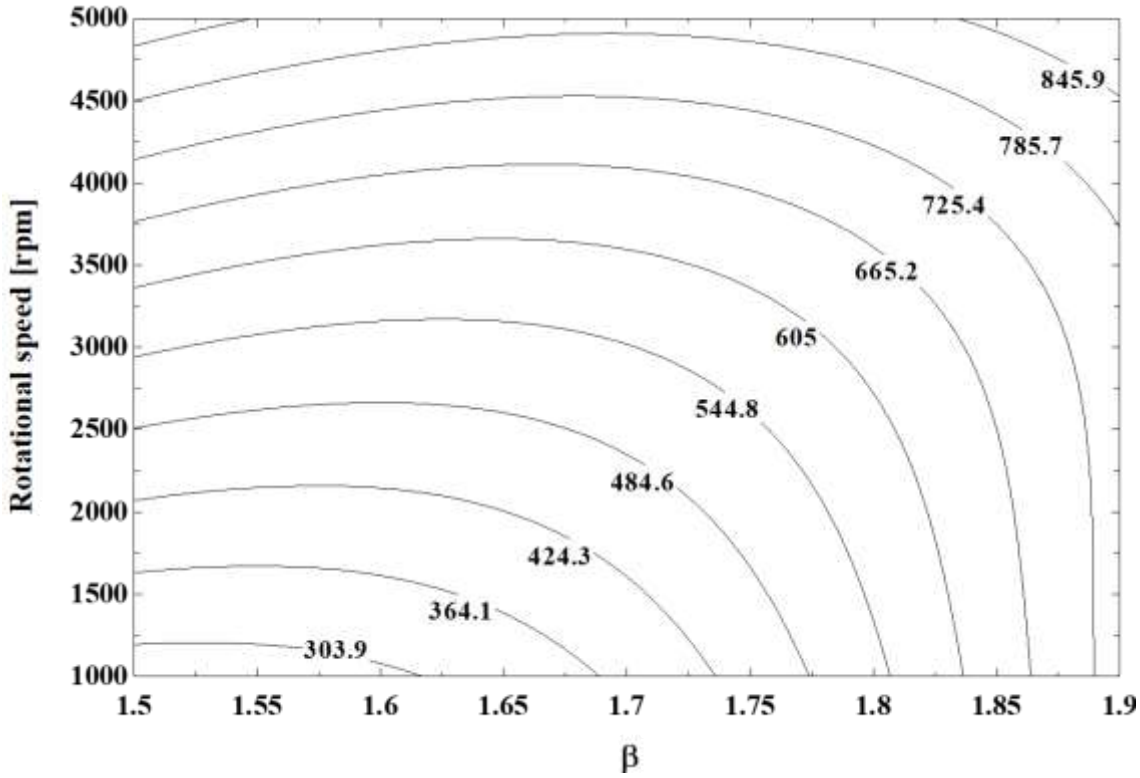

Fig. 4.65 Experimental interpolated thermodynamic power as function of expansion ratio and rotational speed

Differently from experimental thermodynamic power, the maximum achieved shaft power output was 371 W for two thermodynamic states. In the first case, it was reached with a mass flow rate of 0.299 kg/s, a super heating level of 45.5 °C and a rotational speed of 4000 rpm; the same power output was also achieved for a mass flow rate of 0.365 kg/s, a super heating level of 4.65 °C and a rotational speed of 3500 rpm.

As can be easily noticed comparing Figs. 4.64 and 4.66, the shaft power output shows a different behaviour compared to the thermodynamic one. Particularly, the behaviour of the thermodynamic power output is monotonically increasing with expansion ratio (and rotational speed), while the shaft power output presents a maximization point.

The trend of shaft power can be better understood when analysing Fig. 4.67. Indeed, in Fig. 4.67 the shaft power is displayed as a function of expansion ratio and rotational speed. Expansion ratio increases when augmenting the rotational speed of the turbine, but it also directly raises the mechanical losses due to the bearings, as well as the friction losses due to the electromagnetic coupling.

On average, a 50% organic efficiency was achieved that is a really low value, mostly attributable to the improper alignment of the magnetic coupling, which is responsible for a really high increase of the mechanical losses, due to the friction.

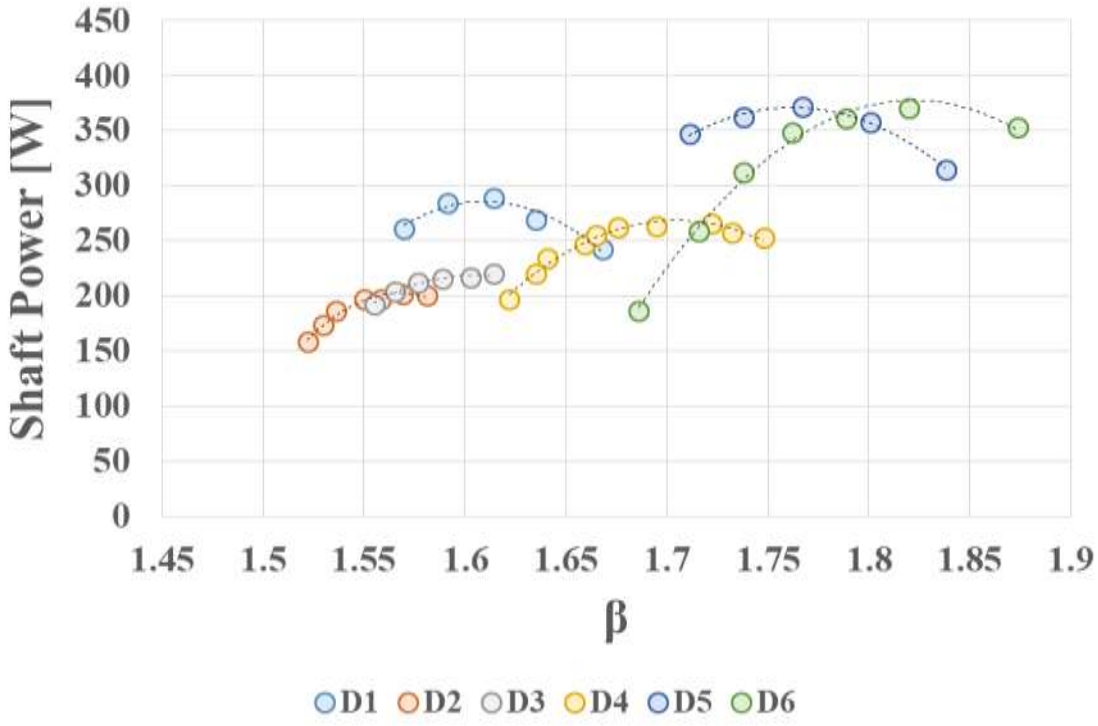

Fig. 4.66 Experimental shaft power as function of expansion ratio

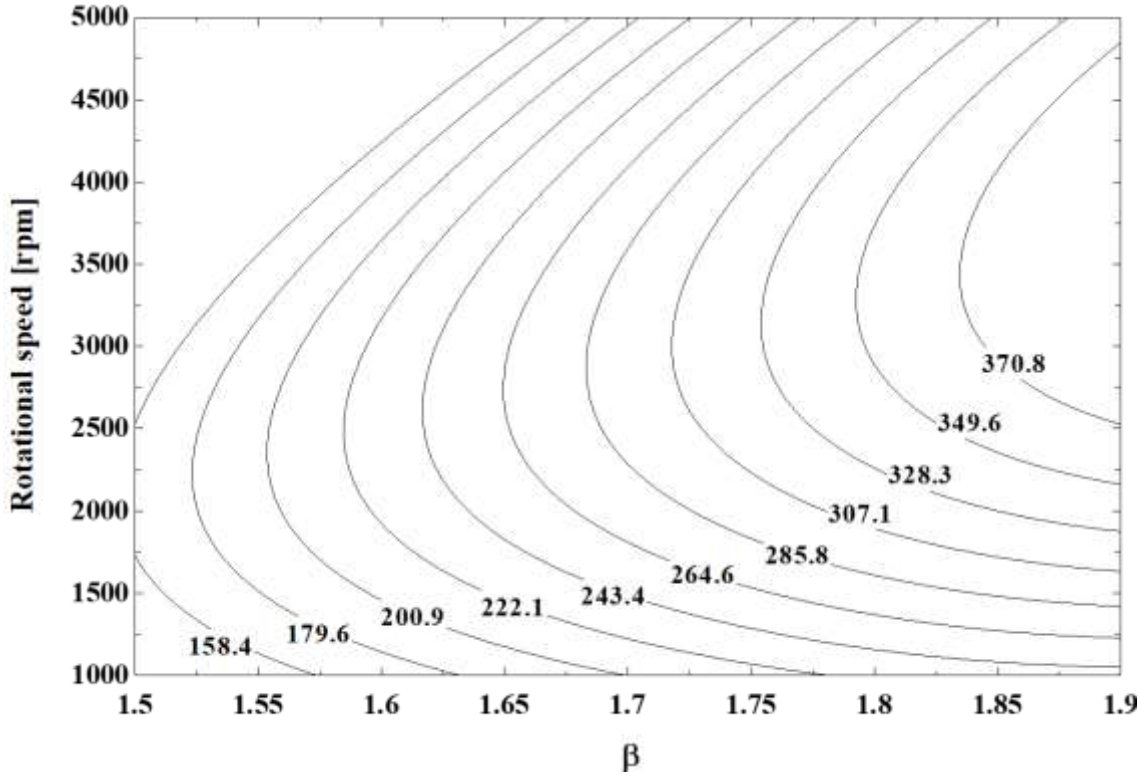

Fig. 4.67 Experimental interpolated shaft power as function of expansion ratio and rotational speed

The maximum achieved experimental thermodynamic total to total efficiency was 30% with a mass flow rate of 0.253 kg/s, a super heating level of 37.5 °C and a rotational speed of 3500 rpm.

Highest efficiency values are directly related to the thermodynamic power production; nonetheless, as expected for a Tesla turbine, higher efficiencies are achieved at low mass flow rates. Indeed, Figs. 4.64 and 4.68 are examined together. It clearly appears that there is a direct relationship between power production and efficiency. However, the low mass flow rates conditions (data groups D2 and D3) achieve higher efficiencies compared to the high mass flow rates (data groups D1 and D6). On the whole, an average 17% thermodynamic efficiency was obtained for this expander, with higher values for low mass flow rate conditions.

The shaft efficiency (Fig. 4.69), on the other hand, is directly related to the obtained shaft power. Therefore, the highest efficiency condition is achieved at the maximum power output condition, which is at a mass flow rate of 0.299 kg/s, a super heating level of 45.5 °C and a rotational speed of 4000 rpm; and the achieved value of efficiency is of 9.62%. Nonetheless, there is still an influence of the mass flow rate; at low mass flow rates, the efficiency still is still relatively high, even at lower power production.

On the whole, an average shaft efficiency of 8.2% was obtained for this expander, with higher values at low mass flow rate conditions and higher power production conditions.

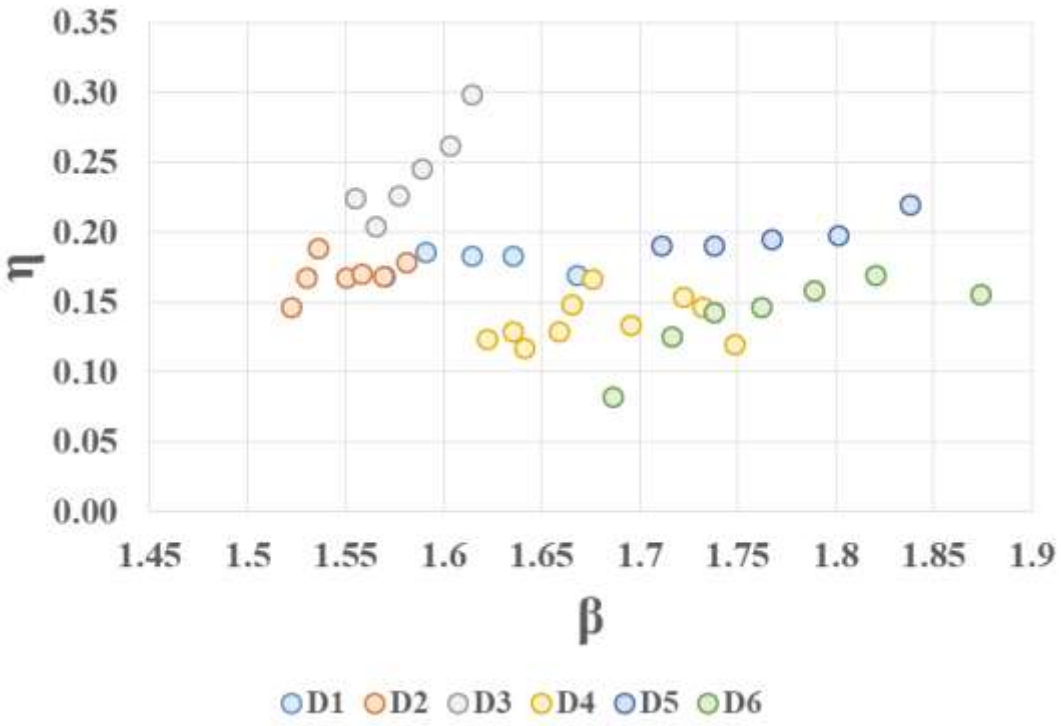

Fig. 4.68 Experimental thermodynamic efficiency of the Tesla turbine prototype vs. expansion ratio

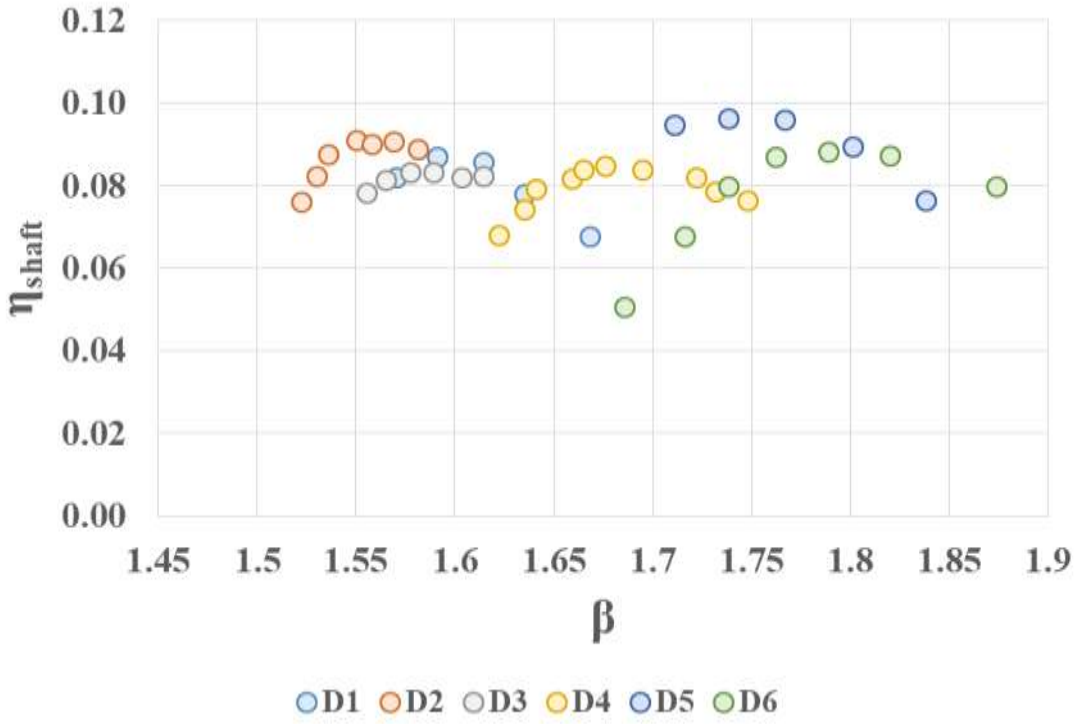

Fig. 4.69 Experimental shaft efficiency as function of expansion ratio

As can be noted from the very big difference between thermodynamic and shaft efficiency, as well as from the values of organic efficiency, the mechanical power losses of the turbine are quite high. Fig. 4.70 resumes the experimental power losses of the turbine, compared to the predicted bearing losses and the sum of bearings losses and friction losses due to the contact of the electromagnetic coupling. For the estimation of the bearings mechanical losses, the model provided by the manufacturer was applied [211]. The estimated bearing losses are expressed by Eq. (4.8).

$$P_{loss} = \omega \cdot M_{loss} \tag{4.8}$$

Where M_{loss} is the bearing frictional torque, which takes into account the rolling and sliding contributions

For the estimation of the losses derived by the contact of the electromagnetic coupling, the model of friction losses on a carrier pin was applied. The estimated pin friction losses are expressed by Eq. (4.9).

$$P_{loss,pin} = \omega \cdot M_r \tag{4.9}$$

Where M_r is the frictional torque, which is the friction force time the radius of electromagnetic coupling, with a coefficient $f = 0.15$ for steel over steel materials.

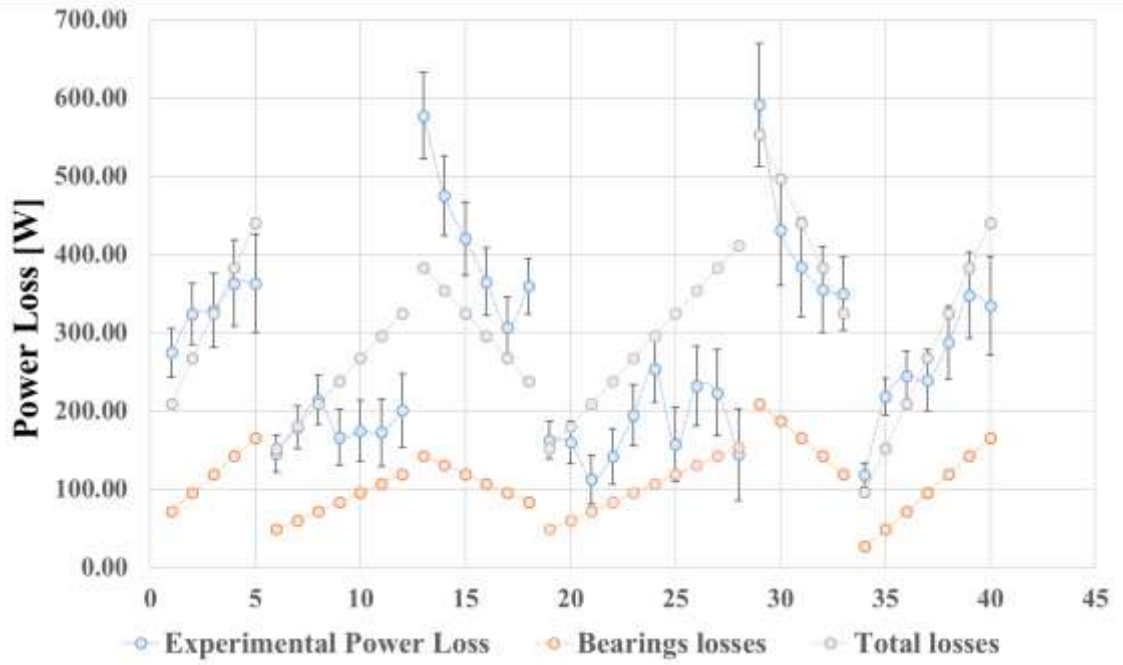

Fig. 4.70 Mechanical losses of ORC Tesla turbine

Comparison with 2D EES code

As anticipated in Section 4.2.2, the 2D in–house EES code did not initially consider partialization, windage and pumping losses. However, if these are not taken into account, the power predicted by the model is much higher, than the experimental value. Therefore, in order to improve the reliability of the Tesla turbine calculation code, a model including the effects of partial admission, windage and pumping losses was added [212].

The estimated windage losses are expressed by Eq. (4.10)

$$P_w = 0.1 \cdot \frac{\pi \cdot d_2 \cdot H \cdot \varepsilon}{2} \cdot \rho \cdot u^3 \tag{4.10}$$

Where H is the total thickness of the rotor disks (0.0008*30) and ε is the partialization degree defined as $\varepsilon = 1 - \frac{4 \cdot A_{out_{nozzle}}}{A_{in_{rotor}}}$

The estimated partialization losses are expressed by Eq. (4.11)

$$P_{pt} = 0.15 \cdot \frac{v_{1s}}{u} \cdot \dot{m} \cdot \frac{(r_2 - r_3)}{d_2} \cdot \frac{u^2}{\varepsilon} \tag{4.11}$$

Where v_{1s} is the isentropic absolute velocity at stator outlet.

The estimated pumping losses are expressed by Eq. (4.12)

$$P_{pp} = 4 \cdot C_M \cdot \rho \cdot d_2^2 \cdot u^3 \tag{4.12}$$

Where C_M is a coefficient function of Reynolds number, $C_M = 0.003 \cdot Re^{-2}$ [212].

This model was developed for partial admission steam turbine, and therefore it takes into account experimental coefficients (0.1 for windage losses and 0.15 for partialization losses), which do not proper match for an organic fluid.

Fig. 4.71 displays the effect of partial admission, windage and pumping losses in the thermodynamic diagram. Particularly, these losses increase the temperature at rotor inlet, besides increasing the entropy, which results in a reduction of the available work.

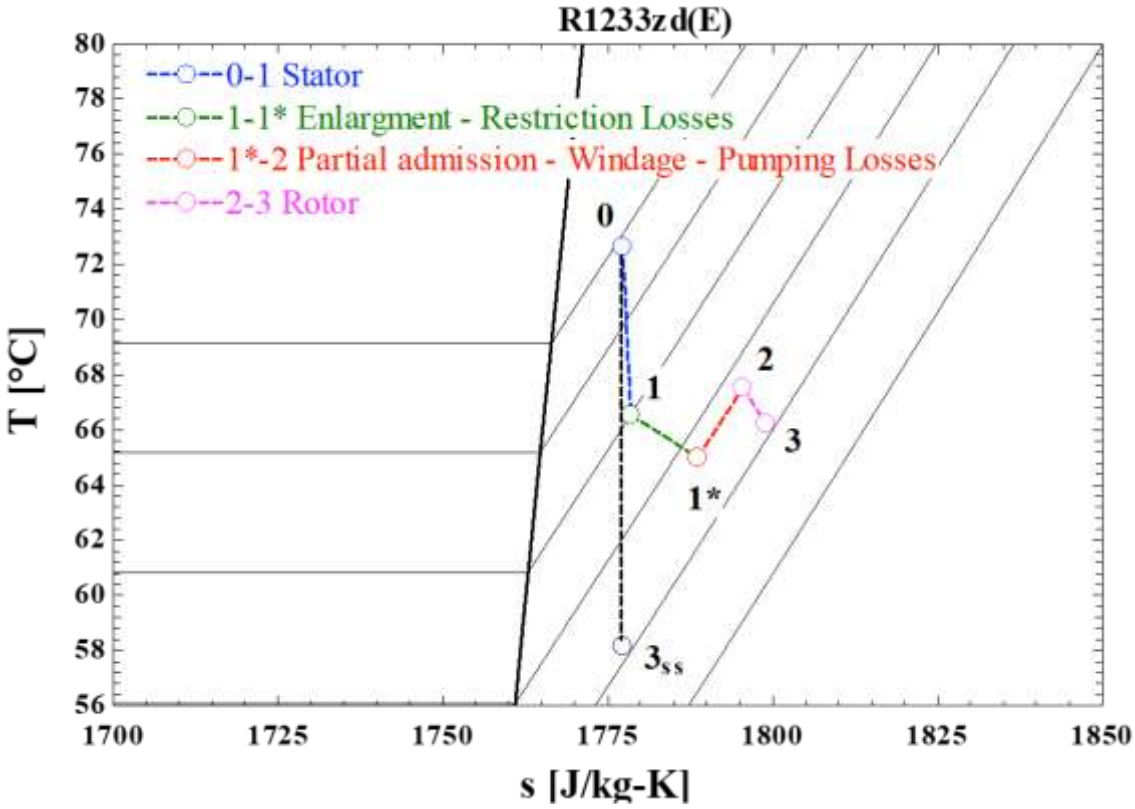

Fig. 4.71 Thermodynamic representation of losses incurring in stator–rotor gap

It was then decided to try interpolating the ratio between actual experimental power and the power calculated by the EES 2D model, including partial admission, windage and pumping losses. The experimental fit coefficient was interpolated as a function of Mach number and temperature at the stator outlet, after having included the enlargement losses.

The interpolated equation is expressed by Eq. (4.13). In spite of the not very high amount of available experimental data, which do not allow an accurate experimental fitting of the whole dataset, the procedure and the interpolated coefficient still produces a reliable

prediction. Fig. 4.72 shows the expression of the experimental interpolation surface, as a function of Mach number and temperature.

$$C_{exp} = -31.08 - 0.023 - 31.08 \cdot T + 100.8 * Ma + 0.0199 \cdot T \cdot Ma - 77.04 \cdot Ma^2 \quad (4.13)$$

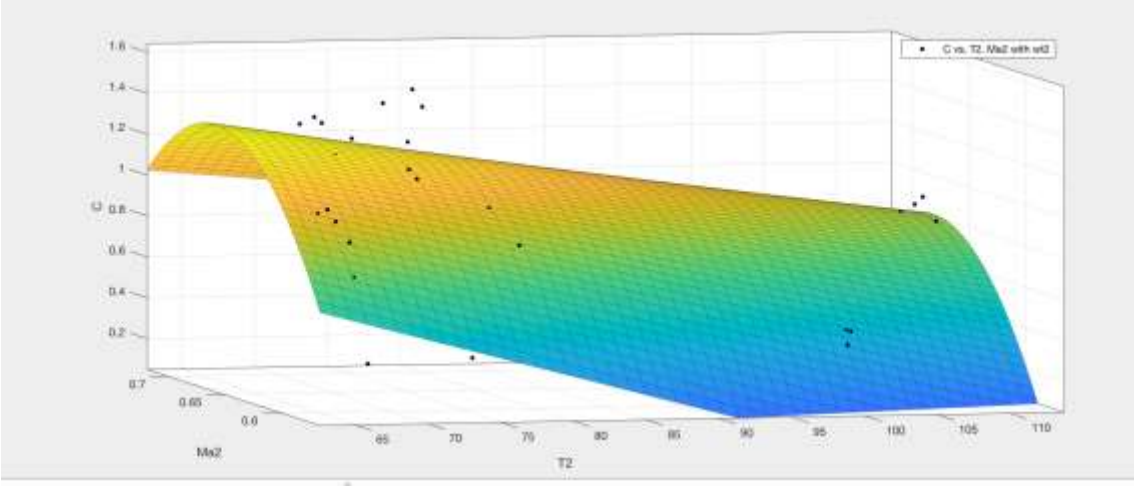

Fig. 4.72 Interpolation surface of experimental constant

Finally, the modified 2D EES in–house code, including the above models to account for the partial admission, windage and pumping losses, with the tuned experimental coefficient was applied and the results are displayed in Figs. 4.73 and 4.74.

In this way, the 2D EES code, properly describes the behaviour of both thermodynamic power output and efficiency, with a satisfactory agreement level between calculated and measured data.

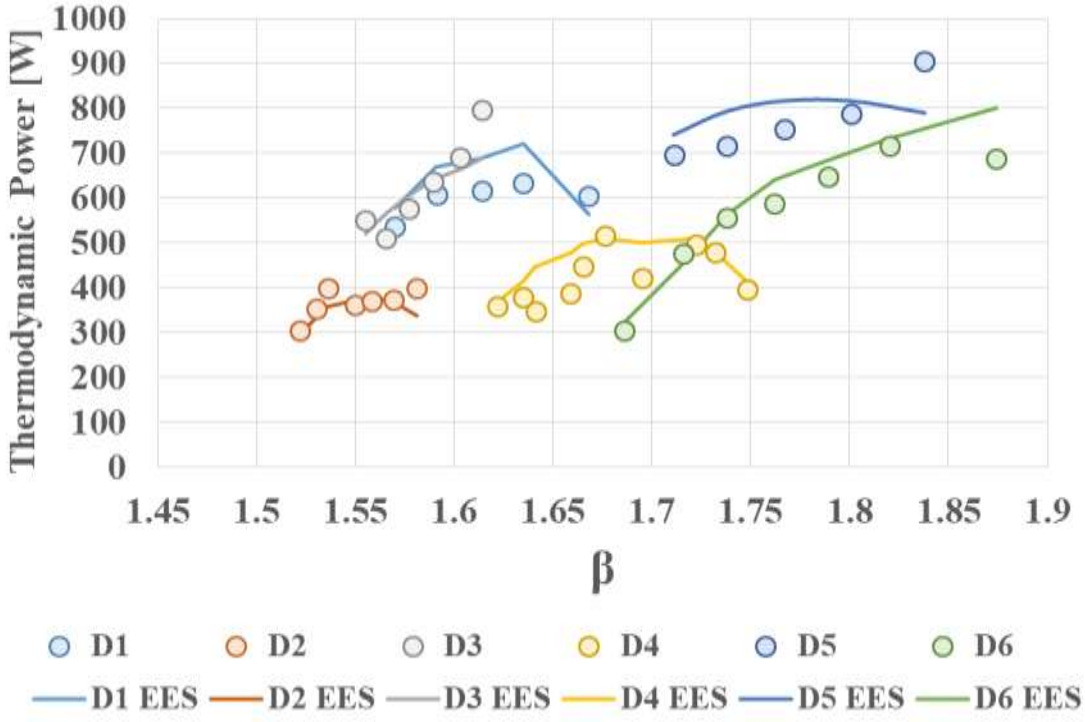

Fig. 4.73 Experimental data and numerical prediction of thermodynamic power vs. expansion ratio

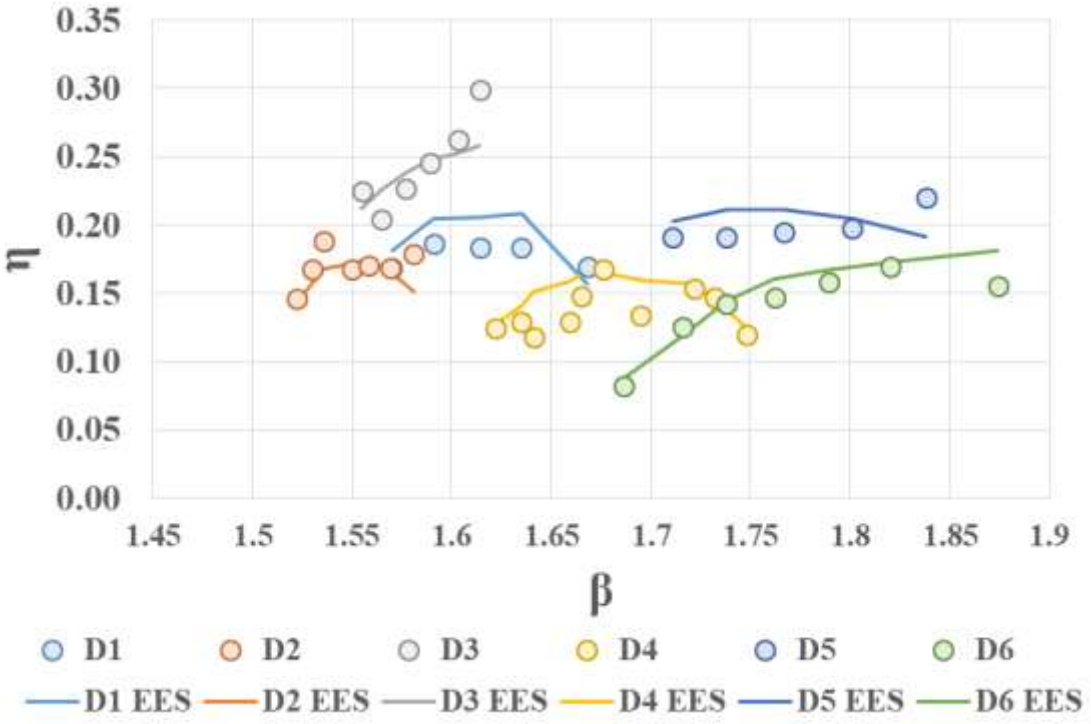

Fig. 4.74 Experimental data and numerical prediction of thermodynamic efficiency vs. expansion ratio

Comparison with 2D EES code and CFD

To conclude, 2D model (both including and neglecting partialization, windage and pumping losses), 3D CFD and experimental data (D2) are compared and displayed in Tab. 4.13. The 2D model results not including losses are close to the one obtained from 3D CFD simulations, but they are not well matching the experimental data. As discussed in the previous Section, this is due to the ideal conditions of the simulations, which assume that all the mass flow rate which exits from the stator enters the rotor. Unfortunately, it was found experimentally that part of the mass flow rate does not enter the rotor, therefore, partialization, windage and pumping losses cannot be neglected.

Finally, Tab. 4.14 shows the relative deviations between the results predicted by the EES 2D code, the SST-CFD code and the experimental data (D2). The relative error is defined as the ratio between the absolute value of the local difference between the experimental data and the numerical results, and the value of the experimental data (the relative error is referred to the experimental data). It is interesting to notice that the introduction of partialization, windage and pumping losses, allows to strongly decrease the relative deviation between numerical and experimental data.

Table 4.13 Results of 2D EES model (with and without partialization, windage and pumping losses) compared to 3D Fluent and experimental data (Dataset D2)

	Efficiency				Total power [W]			
rpm	2D EES model	2D EES model with losses	3D CFD	Experimental	2D EES model	2D EES model with losses	3D CFD	Experimental
1500	0.14	0.14	0.15	0.15	274	298	273	304
1750	0.17	0.16	0.17	0.17	323	331	322	353
2000	0.19	0.17	0.19	0.19	371	357	370	400
2250	0.22	0.17	0.22	0.17	422	371	420	363
2500	0.24	0.17	0.24	0.17	472	382	470	372
2750	0.27	0.17	0.26	0.17	523	368	520	374
3000	0.29	0.15	0.28	0.18	574	339	571	401

Table 4.14 Relative deviation between experimental data and numerical models

	Efficiency			Total power [W]		
rpm	2D EES model	2D EES model with losses	3D CFD	2D EES model	2D EES model with losses	3D CFD
1500	4.2%	2.1%	2.7%	9.9%	2.0%	10.1%
1750	1.4%	6.1%	1.4%	8.6%	6.2%	8.9%
2000	0.7%	10.7%	0.7%	7.3%	10.8%	7.6%
2250	31.0%	2.2%	31.0%	16.2%	2.2%	15.7%
2500	40.9%	2.6%	40.9%	26.9%	2.7%	26.4%
2750	60.0%	1.4%	54.0%	39.8%	1.6%	39.1%
3000	62.6%	15.5%	57.0%	43.2%	15.5%	42.5%

5 Conclusions and Recommendations

The present work collects a wide part of research activities performed during the Ph.D. course, dealing with the design of a "new–old" expander technology, for small–scale organic Rankine cycle applications. Conclusions of the developed research are now drawn, as well as recommendations for future works, which could be a spark for researchers to move forward in a field, which still presents very engaging topics to be unveiled.

5.1 Conclusions

Over the last years, energy systems research grown a strong attention towards the study and development of proper solutions for small and micro distributed systems for heat and power generation, to be applied in domestic buildings or industrial facilities. The utilization of ORCs is a sound solution in this field, especially when the cycle is made of efficient, reliable and low cost components. A critical part of micro ORCs is the expander, as it often does not combine low cost and reliability requirements. In this domain, Tesla turbine seems to be a valuable candidate to tackle these issues, as its simple structure guarantees a low cost, reliable and quite efficient expander.

Open literature review showed that Tesla turbine has gained a renewed interest in the last few years, mainly due to the higher attention that micro power generation gained on the energy market. Four principal lines of research stirred up the interest on the assessment of Tesla turbine. The first is the one carried forward by W. Rice, which developed a throughout assessment from analytical to experimental campaigns on air Tesla turbines. The second is the one conducted by A. Guha and S. Sengupta, which realized both analytical and computational assessment of the Tesla turbine, deeply assessing the role of each force inside the rotor, as well as conducting several interesting analyses to make clear the causes of inefficiency of a Tesla turbine. The third line of research is the one proposed by VP. Carey and his team, which, improved the model firstly realized by W. Rice and applied it to Watt and sub–Watt applications. The last line of research is the one brought forward by C. Schosser and M. Pfizner, which numerically and experimentally investigated the flow path behaviour inside an air Tesla turbine. Outside these four main lines of research, very interesting spot work were developed, such as those of P. Lampart or J. Song, which started to analytically and numerically analyse the Tesla turbine for ORC applications.

As highlighted by the state of the art, several analytical and numerical models were realized, and many experimental campaigns were carried out, nevertheless, the majority of these investigations were developed on Tesla turbines utilizing air as working fluid, while, in the present study, the analysis is carried out from a slightly different perspective, which is setting the focus on Tesla turbine for ORC applications. For this reason, a clear and complete design and optimization procedure for ORC Tesla turbines with a model

including real gas equations and concentrated pressure losses was developed. Furthermore, a straightforward methodology for geometry assessment as well as computational analyses on the flow behaviour inside the disks of a ORC Tesla turbine, and experimental investigations utilizing air and R1233zd(E) as working fluids, were realized.

In the first part of the work a 2D in–house code was developed in Engineering Equation Software ambient. Initially, it was tested and validated against available literature data utilizing air as working fluid. After the validation, the model was extended to organic working fluids and a full design and optimization procedure for ORC Tesla turbines was realized. A pivotal point of this first part of research was the innovative design procedure of the expander compared to the previous literature: it did not only take into account the rotor or the stator separately, but it also included all the assembled components together, from the plenum chamber to the diffuser, passing through the losses in the gap between the stator and the rotor. Furthermore, a revised conceptual modular design of the turbine was proposed and the performance of several working fluids with specific prototype size assessed. Finally, a scheme for geometry assessment was also featured in order to perform a qualitative comparison with small–size expanders, which are the direct competitor of the Tesla turbine.

The key outcomes of this part of the work may be summarised as follows:

- A novel methodology for the complete design of a Tesla turbine working both with air and organic fluids was proposed and assessed. Each component was designed taking into account the mutual relationships between the different parts of the expander.

- An innovative model for the solution of the rotor flow field was developed. Starting from an existing literature approach, the new one was generalized, considering real fluid behaviour and influence of Reynolds number on the velocity profile inside the rotor channels.

- A sensitivity analysis to each geometric and thermo–fluid dynamic parameter was carried out. It was found that performance, mass flow rate and expansion ratio are strictly connected: low mass flow rates allow better efficiency and lower power output. Low mass flow rates, for a fixed geometry of the nozzle and fixed velocity at the throat, are obtained for low density at nozzle exit (from continuity equation); therefore, high temperatures and low pressures are necessary for a proper design of the Tesla turbine rotor. The right choice of channel height and in/out rotor diameter ratio are of primary importance in optimization of the expander efficiency.

- An improved design concept was introduced simplifying the shaft/rotor assembly with a modular, robust construction principle and possibility of sealed operation.

- Due to its intrinsic working principle – work transmitted by friction – the Tesla turbine results to be competitive with conventional expanders only for low–power application, but it is not a good candidate for medium to high power as the several losses involved, such as the high kinetic energy at exhaust, the rotor efficiency drop due to the increase of mass flow rate, and the higher pressure drop into the stator/rotor gap.

- The numerical assessment indicated that the Tesla turbine appears potentially competitive with other expanders for low n_s (0.001–0.005) and high d_s (20–50) (typical range for volumetric expanders or drag turbines) with special reference to efficiency. The rotational speed has a strong influence on the expander power and efficiency, but generally, the turbine can be sized to work properly within 4000–8000 rpm.

- The most critical parameters for achieving good turbine performance were found to be the rotor inlet tangential velocity ratio, the stator throat Mach number, the rotor channel width and the rotor outlet/inlet diameter ratio. From the analyses of several computations on different working fluids, it was found that, for all fluids the throat Mach number and the rotor inlet tangential velocity ratio should be close to 1, in order to achieve high efficiencies. Furthermore, the proper value for rotor channel width was found to be a linear function of rotor inlet diameter and optimal values for rotor outlet/inlet diameter ratio were found to be between 0.3 and 0.4.

- Suitable design expansion ratios for the Tesla turbine were determined between 3.5 and 5.5. This range of expansion ratios is quite common in low temperature applications, which may be considered, therefore, to be the optimal field of application of this turbine.

- Two prototypes (one utilizing air as working fluid, the other organic fluids) were finally designed, taking into account thermodynamic considerations, mechanical restriction, as well as test bench operating ranges.

Once the fundamental principles of the turbine were unveiled, and the design of two prototypes was carried out, a computational assessment on the performance of the Tesla turbine rotor, as well as on the stator rotor interaction, was performed. The analysis was conducted through the evaluation of the flow behaviour and the consequent performance parameters of the turbine, whose size was referred to the actual built prototype. A pivotal point of this part of the work was the comparison of the results achieved by the 3D CFD model realized with the commercial code ANSYS Fluent and the 2D home built EES model. The realization of the stator rotor interaction simulations allowed understanding

that partial admission plays a fundamental role in the behaviour of the fluid inside a Tesla turbine rotor.

The key achieved results of this part of research may be summarized in the following:

- The results of the rotor simulations in ANSYS Fluent model and 2D EES in–house code were compared showing an excellent matching.

- The only rotor simulations were performed both with laminar and SST computational models. The employment of Langtry–Menter turbulence model allowed to determine the presence of transitional effects in the entrance region, which were not identified with the laminar model.

- High rotor efficiencies were predicted through the rotor only simulations for the small–scale prototype, as high as 69% at 3000 rpm for all assessed fluids.

- Stator–rotor interaction simulations allowed the understanding of the flow behaviour due to partial admission. Especially temperature is influenced by the streamlines, developing different independent bands of temperature.

- Globally the rotor only and stator–rotor simulations do not affect the prediction of work and efficiency, nonetheless, the latter simulations allow to investigate the critical points of the expander, such as the nozzle outlet operation and the influence of the gap.

- The results of the stator–rotor simulations in ANSYS Fluent model and 2D EES in–house code were compared showing a good matching of the performance prediction.

Finally, in order to increase the Technology Readiness Level (TRL) of the research, experimental activities were necessary. The TRLs are a type of estimation system defined in order to evaluate the maturity level of a specific technology, firstly developed by NASA in 1974. There are nine technology readiness levels. TRL 1 is the lowest and TRL 9 is the highest [213]. At the beginning of this research the TRL of air Tesla turbine was around 3, while ORC Tesla turbine TRL was between 1 and 2. At the end of this research work, it can estimated that the TRL for ORC Tesla turbine is increased at TRL at least 3, or between 3 and 4. Indeed, as clearly displayed in Fig. 5.1, a TRL 3 is considered when active research and technology design are performed and when there is the combination between analytical and laboratory studies, which means that first preliminary experimental results are required in order to for the technology to be considered at “proof of concept” level.

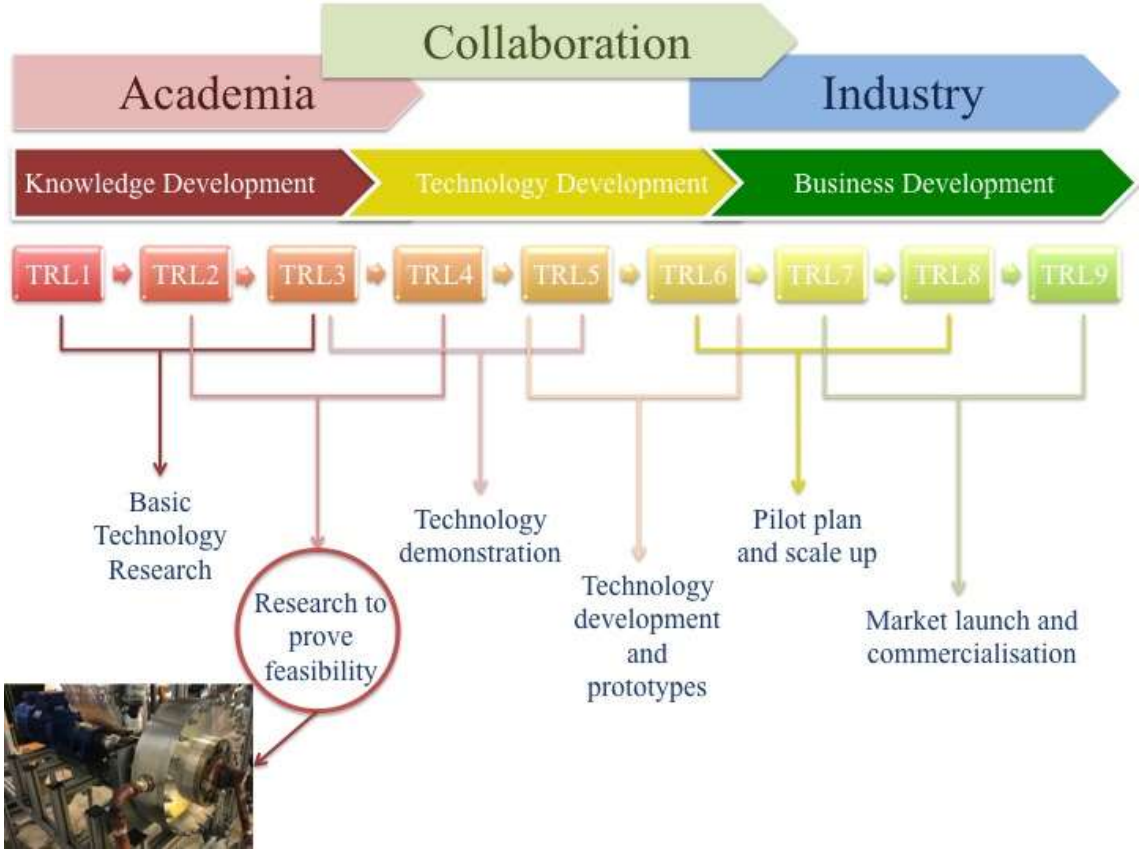

Fig. 5.1 Technology readiness level estimation system

Experimental investigations on both air Tesla turbine and ORC Tesla turbine were carried out. The experimental assessment of the air Tesla turbine allowed confirming the validity of the 2D in–house code, while the experimental campaign on the ORC Tesla turbine was the first documented with organic fluids, and therefore allowed a proof of concept of the technology. A pivotal point of this last part of research was the comparison between experimental and numerical results, which resulted in fair agreement.

The key achievements of this part of research are summarised in the following:

- An experimental test campaign was conducted with air Tesla turbine, with two different air mass flow rates at various rotational speeds. The maximum achieved efficiency was of 11.2% at 3000 rpm with a total mass flow rate of 0.028 kg/s; the maximum power output (again at 3000 rpm, but with 0.030 kg/s mass flow rate) was 94 W;

- The experimental results of the air Tesla campaign revealed a very good agreement between numerical and experimental results, thus demonstrating the soundness of the developed numerical model of the expander;

- The shaft efficiency of the air Tesla prototype (including generator and torque meter losses) was estimated over 85%;

- The maximum achievable thermodynamic efficiency of the air Tesla prototype was about 58%, with power output of 500 W.

- An experimental test campaign was conducted with ORC Tesla turbine, with several mass flow rates of R1233zd(E) at various rotational speeds and total inlet conditions. The maximum achieved thermodynamic efficiency was of 30% with a mass flow rate of 0.253 kg/s, a super heating level of 37.5 °C and a rotational speed of 3500 rpm; while the maximum experimental thermodynamic power obtained was of 906 W, with a mass flow rate of 0.299 kg/s, a super heating level of 44 °C and a rotational speed of 5000 rpm;

- The maximum achieved shaft efficiency of the ORC Tesla turbine was of 9.62 % with a mass flow rate of 0.299 kg/s, a super heating level of 45.5 °C and a rotational speed of 4000 rpm; while the maximum experimental shaft power obtained was of 371 W for two thermodynamic states: for a mass flow rate of 0.299 kg/s, a super heating level of 45.5 °C and a rotational speed of 4000 rpm; and for a mass flow rate of 0.365 kg/s, a super heating level of 4.65 °C and a rotational speed of 3500 rpm;

- The shaft efficiency of the ORC Tesla prototype (including generator and torque meter losses) was estimated at 50%, which is a really low value, but which was mostly due to the not right alignment of the magnetic coupling, which brought a really high increase of mechanical losses, due to contact friction losses;

- The modified 2D EES in–house code, taking into account the partial admission, windage and pumping losses, as well as the experimental constant coefficient properly described the trend of both thermodynamic power and efficiency, as the numerical prediction was always within the uncertainty of the measured data.

As a final remark, it can be affirmed that the here proposed analysis showed how the Tesla turbine might be a competitive solution when applied to micro and small power applications, from recovery of low pressure waste air flows to micro ORC applications. The research on this expander technology is worth of further developments, given the encouraging experimental results which demonstrated the reliability of the numerical simulations and that predicted very interesting power output and efficiency potential for a very wide range of possible micro power applications in the kW scale.

5.2 Recommendations

The most difficult task of a project is to decide its boundaries and to properly select and assess only the fundamental parts, while leaving some interesting aspects to be developed in proper future works. Hereafter a list of possible lines of research is presented, which could rise from the leveraging of the acquired know–how from this research.

- Perform further experimental tests on air Tesla turbine with different mass flow rates, rotational speeds and total inlet conditions, in order to validate the model for a wide range of conditions;
- Re–design the ORC Tesla turbine, leveraging the experimental data obtained, improving the stator–rotor coupling and substituting the electromagnetic coupling;
- Test the ORC Tesla turbine in a wider range of conditions, with higher expansion ratios;
- Test the ORC Tesla turbine with different working fluids, in order to further prove the suitability of this technology for ORC applications;
- Design a Tesla turbine for CO_2 applications, as CO_2 expansion ratios could properly match the optimal range of Tesla turbine expansion ratios;
- Develop a two–phase flow model for the Tesla turbine, combining two–phase flow and Tesla turbine theories;
- Compute numerical analyses on two–phase flow in a Tesla turbine rotor;
- Design a Tesla turbine for two–phase flows;
- Perform an experimental campaign on two–phase Tesla turbines.

References

[1] IEA, *Key Electricity trends 2017 based on monthly data*, available at: https://www.iea.org/media/statistics/KeyElectricityTrends2017.pdf, last accessed on 23rd May 2018.

[2] IEA, *CO_2 Emissions overview*, available at: http://www.iea.org/publications/freepublications/publication/CO2EmissionsfromFuelCombustionHighlights2017.pdf, last accessed on 23rd May 2018.

[3] European commission, *H2020 Work Programme 2018–2020, Secure, clean and efficient energy*, available at: http://ec.europa.eu/research/participants/data/ref/h2020/wp/2018–2020/main/h2020–wp1820–energy_en.pdf, last accessed on 23rd May 2018.

[4] Macchi E., *Theoretical basis of the Organic Rankine Cycle*, in: Macchi M. and Astolfi M., *Organic Rankine Cycle (ORC) Power Systems, Technologies and Applications*, 1st Edition, Woodhead Publishing, Elsevier.

[5] Knowledge Center for Organic Rankine Cycle, *History of ORC*, available at: http://www.kcorc.org/en/science–technology/history/, last accessed on 25th May 2018.

[6] Tartière T., Astolfi M., "A Word Overview of the Organic Rankine Cycle Market", in: *Energy Procedia*, 129, 2–9, 2017.

[7] Bronicki L.Y., *History of Organic Rankine Cycle systmes*, in: Macchi M. and Astolfi M., *Organic Rankine Cycle (ORC) Power Systems, Technologies and Applications*, 1st Edition, Woodhead Publishing, Elsevier.

[8] Invernizzi C., Iora P., Silva P., "Bottoming micro–Rankine cycles for micro–gas turbines", in: *Appl. Therm. Eng.*, 27, 100–110, 2007.

[9] Chacartegui R., Sánchez D., Muñoz J.M., Sánchez T., "Alternative ORC bottoming cycles for combined cycle power plants", in: *Appl. Energy*, 86, 2162–2170, 2009.

[10] Al–Sulaiman F.A., Dincer I., Hamdullahpur F., "Exergy analysis of an integrated solid oxide fuel cell and organic Rankine cycle for cooling, heating and power production", in: *J. Power Sources*, 195, 2346–2354, 2010.

[11] Vaja I., Gambarotta A., *"Internal Combustion Engine (ICE) bottoming with Organic Rankine Cycles (ORCs)*", in: *Energy*, 35, 1084–1093, 2010.

[12] Bonilla J.J., Blanco J.M., Lopez L., Sala J.M., “Technological recovery potential of waste heat in the industry of the Basque country”, in: *Appl. Therm. Eng.,* 17, 283–288, 1997.

[13] Desideri A., Gusev S., Van Den Broek M., Lemort V., Quoilin S., “Experimental comparison of organic fluids for low temperature ORC (organic Rankine cycle) systems for waste heat recovery applications”, in: *Energy*, 97, 460–469, 2016.

[14] Schuster A., Karellas S., Kakaras E., Spliethoff H., “Energetic and economic investigation of Organic Rankine Cycle applications”, in: *Appl. Therm. Eng.*, 29, 1809–1817, 2009.

[15] Zhai H., Dai Y.J., Wu J.Y., Wang R.Z., “Energy and exergy analyses on a novel hybrid solar heating, cooling and power generation system for remote areas”, in: *Appl. Energy*, 86, 1395–1404, 2009.

[16] Lentz A., Almanza R., “Solar–geothermal hybrid system”, in: *Appl. Therm. Eng.*, 26, 1537–1544, 2006.

[17] Heberle F., Brüggemann D., “Exergy based fluid selection for a geothermal Organic Rankine Cycle for combined heat and power generation”, in: *Appl. Therm. Eng.*, 30, 1326–1332, 2006.

[18] Fiaschi D., Manfrida G., Rogai E., Talluri L., “Exergoeconomic analysis and comparison between ORC and Kalina cycles to exploit low and medium–temperature heat from two geothermal sites”, in: *Energy Conversion and Management*, 154, 503–516, 2017.

[19] Dong L.L., Liu H., Riffat S.B., “Development of small–scale and micro–scale biomass–fuelled CHP systems – a literature review”, in: *Appl. Therm. Eng.*, 29, 2119–2126, 2009.

[20] Qiu G., Liu H., Riffat S., “Expanders for micro–CHP systems with organic Rankine cycle”, in: *Appl. Therm. Eng.*, 31, 3301–3307, 2011.

[21] Tchanche B.F., Lambrinos G.R., Frangoudakis A., Papadakis G., “Low–grade heat conversion into power using organic Rankine cycles – a review of various applications” in: *Renew. Sust. Energy Rev.*, 5, 3963–3979, 2011.

[22] Tempesti D., Manfrida G., Fiaschi D., “Thermodynamic analysis of two micro CHP systems operating with geothermal and solar energy”, in: *Appl. Energy*, 97, 609–617, 2012.

[23] Bombarda P., Invernizzi C, Gaia M., “Performance analysis of OTEC plants with multilevel Organic Rankine Cycle and solar hybridization”, in: *ASME J. Eng. Gas Turbines Power*, 135, 2013.

[24] Braimakis K., Karellas S., “Integrated thermoeconomic optimization of standard and regenerative ORC for different heat source types and capacities”, in: *Energy*, 121, 570–598, 2017.

[25] Manente G., Lazzaretto A., Bonamico E., “Design guidelines for the choice between single and dual pressure layouts in organic Rankine cycle (ORC) systems”, in: *Energy*, 123, 413–431, 2017.

[26] Shokati N., Ranjbar F., Mortaza Y., “Exergoeconomic analysis and optimization of basic, dual–pressure and dual–fluid ORCs and Kalina geothermal power plants: A comparative study”, in: *Renewable Energy*, 83, 527–542, 2015.

[27] Lee H.Y., Park S.L., Kim K.H., “Comparative analysis of thermodynamic performance and optimization of organic flash cycle (OFC) and organic Rankine cycle (ORC)”, in: *Appl. Therm. Eng.*, 100, 680–690, 2016.

[28] Li X., Zhao C., Hu X., “Thermodynamic analysis of Organic Rankine Cycle with Ejector”, in: *Energy*, 42, 342–349, 2012.

[29] Chen J., Huang Y., Niu Z., Chen Y., Luo X., “Performance analysis of a novel organic Rankine cycle with a vapor–liquid ejector”, in: *Energy Conversion and Management*, 157, 382–395, 2018.

[30] Palacz M., Haida M., Smolka J., Plis M., Nowak A.J., Banasiak K., “A gas ejector for CO_2 supercritical cycles”, in: *Energy*, 163, 1207–1216, 2018.

[31] Zhang K., Chen X., Markides N., Yang Y., Shen S., “Evaluation of ejector performance for an organic Rankine cycle combined power and cooling system”, in: *Appl. Energy*, 184, 404–412, 2016.

[32] Yari M., Mehr A.S., Zare V., Mahmoudi S.M.S., Rosen M.A., “Exergoeconomic comparison of TLC (trilateral Rankine cycle), ORC (organic Rankine cycle) and Kalina cycle using a low grade heat source”, in: *Energy*, 83, 712–722, 2015.

[33] Astolfi M., Alfani D., Lasala S., Macchi E., “Comparison between ORC and CO2 power systems for the exploitation of low–medium temperature heat sources”, in: *Energy*, 161, 1250–1261, 2018.

[34] Lecompte S., Huisseune H., Van Den Broek M., Vanslambrouck B., De Paepe M., “Review of Organic Rankine Cycle (ORC) architectures for waste heat recovery”, in: *Renewable and Sustainable Energy Reviews*, 47, 448–461, 2015.

[35] Colonna P., Casati E., Trapp C., Mathijssen T., Larjola J., Turunen–Saareti T., Uusitalo A., "Organic Rankine Cycle Power Systems: From the Concept to Current Technology, Applications, and an Outlook to the Future", in: *J. of Engineering for Gas Turbines and Power*, 137, 1–19, 2015.

[36] Bao J., Zhao L., "A review of working fluid and expander selections for Organic Rankine Cycle", in: *Renewable and Sustainable Energy Reviews*, 24, 325–342, 2013.

[37] Qiu G., "Selection of working fluids for micro–CHP systems with ORC", in: *Renewable Energy*, 48, 565–570, 2012.

[38] Quoilin S., Van Den Broek M., Declaye S., Dewallef P., Lemort V., "Techno–economic survey of Organic Rankine Cycle (ORC) systems" in: *Renewable and Sustainable Energy Reviews*, 22, 168–186, 2013.

[39] Wang D., Ling, X., Peng H., Liu L., Tao L., "Efficiency and optimal performance evaluation of organic Rankine cycle for low grade heat power generation", in: *Energy*, 50, 343–352, 2013.

[40] Talluri L., Lombardi G., "Simulation and Design Tool for ORC Axial Turbine stage", in: *Energy Procedia*, 129, 277–284, 2017.

[41] Fiaschi D., Manfrida G., Maraschiello F., "Thermo–fluid dynamics preliminary design of turbo–expanders for ORC cycles", in: *Appl. Energy*, 97, 601–608, 2012.

[42] Fiaschi D., Manfrida G., Maraschiello F., "Design and performance prediction of radial ORC turboexpanders", in: *Appl. Energy*, 138, 517–532, 2014.

[43] Fiaschi D., Innocenti G., Manfrida G., Maraschiello F., "Design of micro radial turboexpanders for ORC power cycles: From 0D to 3D", in: *Appl. Therm. Eng.*, 99, 402–410, 2016.

[44] Garg P., Karthik G.M., Kumar P., Kumar P., "Development of a generic tool to design scroll expanders for ORC applications", in: *Appl. Therm. Eng.*, 109, 878–888, 2016.

[45] Lemort V., Quoilin S., Cuevas C., Lebrun J., "Testing and modeling a scroll expander integrated into and Organic Rankine Cycle", in: *Appl. Therm. Eng.*, 29, 3094–3102, 2009.

[46] Ziviani D., Van Den Broek M., De Paepe M., "Geometry–Based Modeling of Single–Screw Expander for Organic Rankine Cycle Systems in Low–Grade Heat Recovery", in: *Energy Procedia*, 61, 100–103, 2014.

[47] Branchini L., De Pascale A., Peretto A., "Systematic comparison of ORC configurations by means of comprehensive performance indexes", in: *Appl. Therm. Eng.*, 61, 129–140, 2013.

[48] Quoilin S., Declaye S., Legros A., Guillaume L., Lemort V., "Working fluid selection and operating maps for Organic Rankine Cycle expansion machines", in: *International Compressor Engineering Conference proceedings*, 1546, 1–10, 2012.

[49] Lemort V., Legros A., *Positive displacement expanders for Organic Rankine Cycle systems*, in: Macchi M. and Astolfi M., *Organic Rankine Cycle (ORC) Power Systems, Technologies and Applications*, 1st Edition, Woodhead Publishing, Elsevier.

[50] Lemort V., Guillaume L., Legros A., Declaye A., Quoilin S., "A comparison of piston, screw and scroll expanders for small–scale Rankine cycle systems", in: *Proceedings of the 3rd International Conference on Microgeneration and Related Technologies*, 2013.

[51] Lemort V., Declaye S., Quoilin S., "Experimental characterization of a hermetic scroll expander for use in a micro–scale Rankine cycle", in: *Proceedings of the Institution of Mechanical Engineers, Part A: Journal of Power and Energy*, 226, 126–136, 2012.

[52] Zhang Y.Q., Wu Y.T., Xia G.D., Ma C.F., Ji W.N., Liu S.W., Yang K., Yang F.B., "Development and experimental study on organic Rankine cycle system with single–screw expander for waste heat recovery from exhaust of diesel engine", in: *Energy*, 77, 499–508, 2014.

[53] Zywica G., Kaczmarczyk T.Z., Inhatowicz E., "A review of expanders for power generation in small–scale organic Rankine cycle systems: Performance and operational aspects", in: *Proc. IMechE Part A: J. Power and Energy*, 230, 669–684, 2016.

[54] Preetham B.S. Weiss, L., "Investigations of a new free piston expander engine cycle", in: *Energy*, 106, 535–545, 2016.

[55] Haiqing G., Yitai M., Minxia L., "Some design features of CO_2 swing piston expander", *Appl. Therm. Eng.*, 26, 237–243, 2006.

[56] Tesla N., Turbine, U.S. Patent No. 1 061 206, 1913.

[57] Leaman A.B., *The design, construction and investigation of a Tesla turbine*, M.Sc. Thesis, University of Maryland, 1950.

[58] Armstrong J.H., *An Investigation of the Performance of a Modified Tesla Turbine*, M.Sc. Thesis, Georgia Institute of Technology, 1952.

[59] Beans E.W., *Performance characteristics of a Friction Disc Turbine*, Ph.D. Thesis, Pennsylvania State University, 1961.

[60] Rice W., "An analytical and experimental investigation of multiple–disk turbines", in: *ASME Journal of Engineering for Power*, 87, 29–36, 1965.

[61] Beans E.W., "Investigation into the performance characteristics of a friction turbine", in: *J. Spacecraft*, 3, 131–134, 1966.

[62] Matsch L., Rice W., "Potential flow between two parallel circular disks with partial admission", in: *Transactions of the ASME, Journal of Applied Mechanics*, 1967.

[63] Matsch L., Rice W., "Flow at low Reynolds number with partial admission between rotating disks", in: *Transactions of the ASME, Journal of Applied Mechanics*, 1967.

[64] Boyd K.E., Rice W., "Laminar inward flow of an incompressible fluid between rotating disks, with full peripheral admission", in: *Journal of Applied Mechanics*, 229–237, 1968.

[65] Matsch L., Rice W., "An asymptotic solution for laminar flow of an incompressible fluid between rotating disks", in: *Transactions of the ASME, Journal of Applied Mechanics*, 1968.

[66] Adams R., Rice W., "Experimental investigation of the flow between corotating disks", in: *Transactions of the ASME, Journal of Applied Mechanics*, 844–849, 1970.

[67] Boyak B.E., Rice W., "Integral method for flow between corotating disks", in: *ASME Journal of Basic Engineering*, 93, 350–354, 1971.

[68] Lawn M.J., *An investigation of multiple–disk turbine performance parameters*, M.Sc. Thesis, Arizona State University, 1972.

[69] Lawn M.J., Rice W., "Calculated design data for multiple–disk turbine using incompressible fluid", in: *Transactions of the ASME, Journal of Fluid Engineering*, 252–258, 1974.

[70] Pater L.L., Crowther E., Rice W., "Flow regime definition for flow between corotating disks"in: *Transactions of the ASME, Journal of Fluid Engineering*, 29–34, 1974.

[71] Bassett C.E., "An integral solution for compressible flow through disc turbines", in: *Proceedings of the 10th Intersociety Energy Conversion Engineering Conference*, Newark, Delaware, 1975.

[72] Garrison P.W., Harvey D.W., Catton I., "Laminar compressible flow between rotating disks", in: *Transactions of the ASME, Journal of Fluid Engineering*, 382–388, 1976.

[73] Steidel R., Weiss H., "Performance test of a bladeless turbine for geothermal applications". *Technical Report Report No. UCID–17068*, California Univ., Livermore (USA), Lawrence Livermore Lab., 1976.

[74] Truman C.R., Rice W., Jankowski D.F., "Laminar throughflow of varying–quality steam between corotating disks", in: *Transactions of the ASME, Journal of Fluid Engineering*, 194–200, 1978.

[75] Truman C.R., Rice W., Jankowski D.F., "Laminar throughflow of a fluid containing particles between corotating disks", in: *Transactions of the ASME, Journal of Fluid Engineering*, 87–92, 1979.

[76] Allen J.S., *A model for fluid between parallel, co–rotating annular disks*, M.Sc. Thesis, University of Dayton, Ohio, 1990.

[77] Rice W., "Tesla Turbomachinery", in: *Proceedings of IV International Nikola Tesla Symposium*, 1991.

[78] Sandilya P., Biswas G., Rao D.P., Sharma A., "Numerical simulation of the gas flow and mass transfer between two coaxially rotating disks", in: *Numerical Heat Transfer*, 39, 285–305, 2001.

[79] Patel N., Schmidt D.D., "Biomass boundary layer turbine power system", in: *Proceedings of International Joint Power Generation Conference*, Phoenix, 2002.

[80] Lezsovits F., "Decentralized energy supply possibilities based on biomass", in: *PERIODICA POLYTECHNICA SER. MECH. ENG.*, 47, 151–168, 2003.

[81] Ladino A.F.R., "Numerical simulation of the flow field in a friction–type turbine (Tesla turbine)", Technical Report, Vienna University of Technology, 2004.

[82] Ladino A.F.R, *Numerical simulation of the flow field in a friction–type turbine (Tesla turbine)*, M.Sc. Thesis, Vienna University of Technology, 2004.

[83] Couto H.S., Duarte J.B.F., Bastos–Neto D., "The Tesla turbine revisited", in: *8th Asia–Pacific International symposium on Combustion and Energy Utilization*, Sochi, 2006.

[84] Batista M., "A note on steady flow of incompressible fluid between two co–rotating disks", in: *Physics*, Cornell University Library, 2007.

[85] Bloudicek P., Palousek D., “Design of Tesla turbine”, in: *Proceedings of Konference diplomovych praci*, Brno, 2007.

[86] Deam R.T., Lemma E., Mace B., Collins R., “On scaling down turbines to millimeter size”, in: *Transaction of ASME, Journal of Engineering for Gas Turbines and Power*, 130, 1–9, 2008.

[87] Lemma E., Deam R.T., Toncich D., Collins R., “Characterisation of a small viscous flow turbine”, in: *Experimental Thermal and Fluid Science*, 33, 96–105, 2008.

[88] Valente A., “Installation for pressure reduction of hydrocarbon gases in a near isothermal manner”, in: *Proceedings of Abu Dhabi International Petroleum Exhibition and Conference*, 2008.

[89] Crowell R., “Generation of electricity utilizing solar hot water collectors and a Tesla turbine”, in: *Proceedings of the ASME 3rd International Conference of Energy Sustainability*, California, 2009.

[90] Hoya G.P., Guha A., “The design of a test rig and study of the performance and efficiency of a Tesla disc turbine”, in: *Proc. IMechE, Part A: J. Power and Energy*, 223, 451–465, 2009.

[91] Guha A., Smiley B., “Experiment and analysis for an improved design of the inlet and nozzle in Tesla disc turbines”, in: *Proc. IMechE, Part A: J. Power and Energy*, 224, 261–277, 2009.

[92] Lampart P., Kosowski K., Piwowarski M., Jedrzejewski L., “Design analysis of Tesla micro–turbine operating on a low–boiling medium”, in: *Polish Maritime Research*, 28–33, 2009.

[93] Carey V.P., “Assessment of Tesla Turbine Performance for Small Scale Rankine Combined Heat and Power Systems”, in: *J. Eng. Gas Turbines Power*, 132, 1–8; 2010.

[94] Carey V.P., “Computational/Theoretical Modelling of Flow Physics and Transport in Disk Rotor Drag Turbine Expanders for Green Energy Conversion Technologies”, in: *Proc. of the ASME 2010 International Mechanical Engineering Congress & Exposition*, Vancouver, Canada; 2010.

[95] Emran T.A., Alexander R.C., Stallings C.R., DeMay M.A., Traum M.J., “Method to accurately estimate Tesla turbine stall torque for dynamometer or generator load selection”, in: *ASME Early Career Technical Journal*, Atlanta, 2010.

[96] Puzyrewski R., Tesch K., “1D model calibration based on 3D calculations for Tesla turbine”, in: *Task quarterly, scientific bulletin of academic computer centre in Gdansk*, 14, 237–248, 2010.

[97] Romanin V., Carey, V.P., Norwood, Z., “Strategies for performance enhancement of Tesla turbines for combined heat and power applications”, in: *Proceedings of the ASME 4th International Conference on Energy Sustainability*, Phoenix, 2010.

[98] Batista M., “Steady flow of incompressible fluid between two co–rotating disks”, in: *Appl. Mathematical Modelling*, 35, 5225–5233, 2011.

[99] Choon T.W., Rahman A.A., Jer F.S., Aik L.E., “Optimization of Tesla turbine using Computational Fluid Dynamics approach”, in: *IEEE Symposium on Industrial Electronics and Applications (ISIEA2011)*, 2011.

[100] Cirincione N, *Design, construction and commissioning of an organic Rankine cycle waste heat recovery system with a Tesla hybrid turbine expander*, M.Sc. Thesis, Colorado State University, 2011.

[101] Emran T.A., *Tesla turbine torque modelling for construction of a dynamometer and turbine*, M.Sc. Thesis, University of North Texas, 2011.

[102] Ho–Yan B.P., “Tesla turbine for Pico Hydro applications”, in: *Guelph Engineering Journal*, 4, 1–8, 2011.

[103] Krishnan V.G., Iqbal Z., Maharbiz M.M., “A micro Tesla turbine for power generation from low pressure heads and evaporation driven flows”, in: *Proceedings of Transducers ’11*, Beijing, 2011.

[104] Lampart P., Jedrzejewski L., “Investigations of aerodynamics of Tesla bladeless microturbines”, in: *Journal of Theoretical and Applied Mechanic*, 49, 2, 477–499, 2011.

[105] Podergajs M., *The Tesla Turbine*, Seminar notes, University of Ljubiana, 2011.

[106] Romanin V.D., Carey V.P., “An integral perturbation model of flow and momentum transport in rotating microchannels with smooth or microstructured wall surfaces”, in: *Physics of Fluids*, 23, 1–11, 2011.

[107] Borate H.P., Misal N.D., “An effect of surface finish and spacing between discs on the performance of disc turbine”, in: *International Journal of Applied Research in Mechanical Engineering*, 2, 25–30, 2012.

[108] Peshlakay A., *Challenging the versatility of the Tesla turbine: Working fluid variations and turbine performance*, M.Sc. Thesis, Arizona State University, 2012.

[109] Romanin V.D., Krishnan V.G., Carey V.P., Maharbiz M.M., "Experimental and analytical study of a sub–watt scale Tesla turbine performance", in: *Proceedings of the ASME 2012 International Mechanical Engineering Congress & Exposition*, Houston, 2012.

[110] Romanin V.D., *Theory and Performance of Tesla turbines*, Ph.D. Thesis, Berkeley University, California, 2012.

[111] Sengupta S., Guha A., "A theory of Tesla disc turbines", in: *Proc. of the Institution of Mechanical Engineers, Part A: Journal of Power and Energy*, 226, 651–663, 2012.

[112] Van Wageningen T., Design analysis for a small scale hydrogen peroxide powered engine for a flapping wing mechanism micro air vehicle, M.Sc. Thesis, Delft University of Technology, 2012.

[113] Bao G., Shi Y., Cai N., "Numerical modelling research on the boundary layer turbine using organic working fluid", in: *Proceeding of International Conference on Power Engineering (ICOPE–13),* Wuhan, China, 2013.

[114] Deng Q., Qi W., Feng Z., "Improvement of a theoretical analysis method for Tesla turbines", in: *Proceedings of ASME Turbo Expo 2013: Turbine Technical Conference and Exposition*, San Antonio, 2013.

[115] Guha A, Sengupta S, "The fluid dynamics of the rotating flow in a Tesla disc turbine", in: *European Journal of Mechanics B/Fluids*, 37, 112–123, 2013.

[116] Guimaraes L.N.F., Marcelino N.B., Placco G.M., Nascimento J.A., Borges E.M., Barrios A.G., "Heat–electricity conversion systems for a Brazilian space micro nuclear reactor", in: *International Nuclear Atlantic Conference*, Recife, 2013.

[117] Gupta H.E., Kodali S., "Design and Operation of Tesla turbo machine – A state of the art review", in: *International Journal of Advanced Transport Phenomena*, 2, 7–14, 2013.

[118] Khan M.U.S., Ali E., Maqsood M.I., Nawaz H., "Modern improved and effective design of boundary layer turbine for robust control and efficient production of green energy", in: *6th Vacuum and surface conference of Asia and Australia, Journal of Physics conference series 349*, 2013.

[119] Khan M.U.S, Maqsood M.I., Ali E., Jamal S., Javed M., "Proposed applications with implementation techniques of the upcoming renewable energy resource, the Tesla turbine", in: *6th Vacuum and surface conference of Asia and Australia, Journal of Physics conference series 349*, 2013.

[120] Krishnan V.G., Romanin V.D., Carey V.P., Maharbiz M.M., “Design and scaling of microscale Tesla turbines”, in: *Journal of Micromechanics and Microengineering*, 23, 2013.

[121] Placco G.M., Guimaraes N.F., Dos Santos R.S., “Passive residual energy utilization system in thermal cycles on water–cooled power reactors”, in: *International Nuclear Atlantic Conference*, Recife, 2013.

[122] Sengupta S., Guha A., “Analytical and computational solutions for three–dimensional flow–field and relative pathlines for the rotating flow in a Tesla disc turbine”, in: *Computers & Fluids*, 88, 344–353, 2013.

[123] Yang Z., Weiss H.P., Traum M.J. “Dynamic dynamometry to characterize disk turbines for space–based power”, in: *Proceedings of the Wisconsin Space conference*, 2013.

[124] Zhao D., Khoo J., “Rainwater and air driven 40 mm bladeless electromagnetic energy harvester”, in: *Appl. Physics Letters*, 103, 1–4, 2013.

[125] Guha, A., Sengupta S., “Similitude and scaling laws for the rotating flow between concentric discs”, in: *Proceedings of the Institution of Mechanical Engineers, Part A, Journal of Power and Energy*, 28, 429–439, 2014.

[126] Guha, A., Sengupta S., “The fluid dynamics of work transfer in the non–uniform viscous rotating flow within a Tesla disc turbomachine”, *Physics of Fluids*, 26, 1–27, 2014.

[127] Hasan A., Benzamia A., “Investigating the impact of air temperature on the performance of a Tesla turbine – using CFD modelling”, in: *International Journal of engineering Innovation & Research*, 3, 794–802, 2014.

[128] Pandey R.J., Pudasaini S., Dhakal S., Uprety R.B., Neopane H.P., “Design and Computational Analysis of 1 kW Tesla turbine”, in: *International Journal of Scientific and Research Publications*, 4, 1–5, 2014.

[129] Schosser C., Lecheler S., Pfizner M., “A test rig for the investigation of the performance and flow field of Tesla friction turbines”, in: *Proceedings of ASME Turbo Expo 2014: Turbine Technical Conference and Exposition*, Dusseldorf, 2014.

[130] Shimeles S., *Design, simulation of fluid flow and optimization of operational parameters in Tesla multiple–disk turbine*, M.Sc. Thesis, Addis Ababa University Institute of Technology, 2014.

[131] Siddiqui M.S., Ahmed H., Ahmed S., “Numerical simulation of a compressed air driven Tesla turbine”, in: *Proceedings of the ASME 2014 Power Conference, Baltimore,* 2014.

[132] Singh A., “Inward flow between stationary and rotating disks”, in: *Journal of Fluids Engineering,* 136, 1–5, 2014.

[133] Thawichsri K., Nilnont W., “A study on performance comparison of two–size Tesla turbines application in Organic Rankine Cycle machine”, in: *International Symposium on the Fusion Technologies,* Jeonju, 2014.

[134] Zhao D., Ji C., Teo C., Li S., “Performance of small–scale bladeless electromagnetic energy harvesters driven by water or air”, in: *Energy,* 74, 99–108, 2014.

[135] Baginski P., Jedrzejewski L., “The strength and dynamic analysis of the prototype of the Tesla turbine”, in: *Diagnostyka,* 16, 17–24, 2015.

[136] Guimaraes L.N.F., Ribeiro G.B., Braz Filho F.A., Nascimento J.A., Placco G.M., De Faria S.M., “Technology development for nuclear power generation for space application”, in: *International Nuclear Atlantic Conference,* Sao Paulo, 2015.

[137] Holland K., *Design, construction and testing of a Tesla Turbine,* M.Sc. Thesis, Laurentian University, Sudbury, 2015.

[138] Kölling A., Lisker R., Hellwig U., Wildenauer F., “Friction expander for the generation of electricity (fege)”. In: *International Conference on Renewable Energies and Power Quality (ICREPQ’15),* La Coruna, 2015.

[139] Krishnan V., *Design and Fabrication of cm–scale Tesla Turbines,* Ph.D. Thesis, Berkeley University, California, 2015.

[140] Neckel A.L., Godinho M., “Influence of geometry on the efficiency of convergent–divergent nozzles applied to Tesla turbines”, in: *Experimental Thermal and Fluid Science,* 62, 131–140, 2015.

[141] Nedelcu, D., Guran P., Cantaragiu A., “Theoretical and experimental research performed on the Tesla turbine”, in: *Analele Universitatii Eftimie Murgu resita,* 22, 255–263, 2015.

[142] Raje A., Singh B., Churai R., Borwankar P., “A review of Tesla turbine”, in: *International Journal of Mechanical Engineering and Technology,* 6, 28–31, 2015.

[143] Ruiz M., *Characterization of single phase and two–phase heat and momentum transport in a spiralling radial inflow micro channel heat sink,* Ph.D. thesis, Berkeley University, California, 2015.

[144] Ruiz M., Carey V.P., "Experimental study of single phase heat transfer and pressure loss in a spiralling inflow micro channel heat sink", in: *ASME Journal of Heat Transfer*, 137, 1–8, 2015.

[145] Schosser C., Pfitzner M., "A numerical study of the three–dimensional incompressible rotor airflow within a Tesla turbine", in: *Conference on Modelling Fluid Flow (CMFF'15)*, Budapest, 2015.

[146] Thawichsri K., Nilnont W., "A comparing on the use of centrifugal turbine and Tesla turbine in an application of organic Rankine cycle", in: *International Journal of Advanced Culture Technology*, 3, 58–66, 2015.

[147] Bankar N., Chavan A., Dhole S., Patunkar P., "Development of hybrid Tesla turbine and current trends in application of Tesla turbine", in: *International Journal for Technological Research in Engineering*, 3, 1504–1507, 2016.

[148] Herrmann–Priesnitz B., Calderon–Munoz W.R., Salas E.A., Vargas–Uscategui A., Duarte–Mermoud M.A., Torres D.A., "Hydrodynamic structure of the boundary layers in a rotating cylindrical cavity with radial inflow", in: *Physics of fluids*, 28,1–16, 2016.

[149] Jose R., Jose A., Benny A., Salus A., Benny B., "An experimental study on the various parameters of Tesla turbine using CFD", in: *International Advanced Research Journal in Science, Engineering and Technology*, Thiruvananthapuram, 2016.

[150] Jose R., Jose A., Benny A., Salus A., Benny B., "A theoretical study on surface finish, spacing between discs and performance of Tesla turbine", in: *International Advanced Research Journal in Science, Engineering and Technology*, Thiruvananthapuram, 2016.

[151] Joshi K.N., Sanghvi M.N., Dave T.D., "Hybrid Tesla Pelton wheel turbine", in: *International Journal of Scientific & Engineering Research*, 7, 1702–1707, 2016.

[152] Qi W., Deng Q., Feng Z., Yuan Q., "Influence of disc spacing distance on the aerodynamic performance and flow field of Tesla turbines", in: *Proceedings of ASME Turbo Expo 2016: Turbomachinery Technical Conference and Exposition*, Seoul, 2016.

[153] Schosser C., Fuchs T., Hain R., Lecheler S., Kahler C., "Three–dimensional particle tracking velocimetry in a Tesla turbine rotor using a non–intrusive calibration method", in: *18th International Symposium on the Application of Laser and Imaging Techniques to Fluid Mechanics*, Lisbon, 2016.

[154] Schosser C., *Experimental and numerical investigations and optimisation of Tesla–radial turbines*, Ph.D. Thesis, Bundeswehr University, Munich, 2016.

[155] Sengupta, S., Guha A., "Flow of a nanofluid in the microspacing within co–rotating discs of a Tesla turbine", in: *Appl. Mathematical Modelling*, 40, 485–499, 2016.

[156] Zahid I., Qadir A., Farooq M., Zaheer M.A., Qamar A., Zeeshan H.M.A., "Design and analysis of prototype Tesla turbine for power generation applications", in: *Technical Journal, University of Engineering and Technology*, Taxila, 2016.

[157] Alrabie M.S., Altamimi F.N., Atlarrgemy M.H., Hadi F., Akbar M.K., Traum M.J., "Method to design a hydro tesla turbine for sensitivity to varying laminar Reynolds number modulated by changing working fluid viscosity", in: *Proceedings of the ASME Power and Energy Conference*, Charlotte, 2017.

[158] Damodhar R., Mruthyunjava K.N., Naveen K., Prabhakar P., Rakhesh H.S., "Design and fabrication of portable water turbine", in: *International Research Journal of Engineering and Technology*, 4, 2584–2590, 2017.

[159] Guha A., Sengupta S., "A non–dimensional study of the flow through co–rotating discs and performance optimization of a Tesla disc turbine", in: *Proc. IMechE Part A: Journal of Power and Energy*, 1–18, 2017.

[160] Li R., Wang H., Yao E., Li M., Nan W., "Experimental study on bladeless turbine using incompressible working medium", in: *Advances in Mechanical Engineering*, 9, 1–12, 2017.

[161] Lisker R., Hellwig U., Wildenauer FX., "Thin film condensation in a Tesla Turbine", in: *Wiss Beitr TH Wildau*, 21, 71–76, 2017.

[162] Mandal A., Saha S., "Performance analysis of a centimetre scale Tesla turbine for micro–air vehicles", in: *International Conference on Electronics, Communication and Aerospace Technology*, 2017.

[163] Polisetti S., Charan S.V., Miryala M., "Fabrication and study of the performance affecting the efficiency of a bladeless turbine", in: *International Journal of Scientific Research in Science and Technology*, 3, 78–82, 2017.

[164] Schosser C., Lecheler S., Pfitzner M., "Analytical and numerical solutions of the rotor flow in Tesla turbines", in: *Periodica Polytechnica Mechanical Engineering*, 61, 12–22, 2017.

[165] Shah V., Dhokai S., "Tesla turbine experiment", in: *International Journal of Science and Research*, 6, 113–116, 2017.

[166] Shah V., Dhokai S., Patel P., “Bladeless turbine – a review”, in: *International Journal of Mechanical Engineering and Technology*, 8, 232–236, 2017.

[167] Song J., Gu C.W., “1D model analysis of Tesla turbine for small scale organic Rankine cycle (ORC) system”, in: *Proceedings of ASME turbo Expo: Turbomachinery Technical Conference and Exposition*, Charlotte, 2017.

[168] Song J., Gu C.W., Li X.S., “Performance estimation of Tesla turbine applied in small scale Organic Rankine Cycle (ORC) system”, in: *Appl. Therm. Eng.*, 110, 318–326, 2017.

[169] Thiyagarajan V., GokulKumar V., Karthickeyan B., Kumar NE., Nikilaesh A., “Tesla turbine powered solar refrigerator”, in: *International Journal of Recent Trends in Electrical & Electronics*, 4, 50–55, 2017.

[170] Umashankar M., Anirudh V., Pishey K., “Investigation of Tesla turbine”, in: *International Journal of Latest Technology in Engineering, Management & Applied Science*, 6, 23–27, 2017.

[171] Variava J.M., Bhavsar A.S., “Evaluation of Tesla turbo machine as turbine”, in: *International Journal of Advance Research and Innovative Ideas in Education*, 3, 3670–3682, 2017.

[172] Sengupta S., Guha A., “Inflow–rotor interaction in Tesla disc turbines: Effects of discrete inflows, finite disc thickness, and radial clearance on the fluid dynamics and performance of the turbine”, in: *Proc. IMechE Part A: Journal of Power and Energy*, 1–21, 2018.

[173] Song J., Ren X.D., Li X.S., Gu C.W., Zhang M.M., “One–dimensional model analysis and performance assessment of Tesla turbine”, in: *Appl. Therm. Eng.*, 134, 546–554, 2018.

[174] Traum M.J., Hadi F., Akbar M.K., “Extending ‘assessment of Tesla turbine performance’ Model for sensitivity–focused experimental design”, in: *ASME Journal of Energy Resources Technology*, 140, 1–7, 2018.

[175] Manfrida G., Pacini L., Talluri L., “A revised Tesla turbine concept for ORC applications”, in: *Energy Procedia*, 129, 1055–1062, 2017.

[176] Manfrida G., Talluri L., “Fluid dynamics assessment of the Tesla turbine rotor”, in: *Thermal Science*, 2018.

[177] Manfrida G., Pacini L., Talluri L., “An upgrade Tesla turbine concept for ORC applications”, in: *Energy*, 158, 33–40, 2018.

[178] Talluri L., Fiaschi D., Neri G., Ciappi L., "Design and optimization of a Tesla turbine for ORC applications", in: *Appl. Energy*, 226, 300–319, 2018.

[179] Klein S.A., Nellis G.F., *Mastering EES*, f–Chart software, 2012.

[180] Glassman A.J., *Computer Program for Design Analysis of Radial–inflow Turbines*, National Aeronautics and Space Administration, Technical report, 1976.

[181] Ventura C.A.M., Jacobs P.A., Rowlands A.S., Petrie–Repar P., Sauret E., "Preliminary Design and Performance Estimation of Radial Inflow Turbines: An Automated Approach", in: *Journal of Fluids Engineering*, 134, 1–13, 2012.

[182] Anderson J.D., *Fundamentals of aerodynamics*, 3rd ed., McGraw Hill, NewYork, 2001.

[183] Shepherd D.G., *Principles of turbomachinery*, The Macmillan Company, New York, 1956.

[184] Shames I.H., *Mechanics of fluids*, 4th ed., McGraw–Hill Professional, NewYork, 2002.

[185] Butenko V.A., Rylov Y.P., Chikov V.P., "Experimental investigation of the characteristics of small–sized nozzles", in: *Fluid Dyn*, 11, 936–939, 1976.

[186] Rohlik H.E., *Radial Inflow Turbines*, NASA SP 290, 3, 10, 1975.

[187] Whitfield A., Baines N.C., *Design of Radial Turbomachines*, Longman Scientific and Technical, 1990.

[188] Dixon S.L., *Fluid Mechanics and Thermodynamics of Turbomachinery*, 5th ed., Pergamon Press, 2005.

[189] Idel'chik I.E., *Handbook of Hydraulic Resistance, Coefficients of Local Resistance and of Friction*, first edition; 1960.

[190] Munson R.B., Okiishi T.H., Huebsch W.W., Rothmayer A.P., *Fundamentals of Fluid Mechanics*, 7th ed., John Wiley and Sons, Inc., 2013.

[191] Cengel Y., *Heat and mass transfer*, 3rd ed., McGraw Hill, NewYork, 2006.

[192] McDonald A.T., Fox R.W., "Effects of swirling Inlet Flow on Pressure Recovery in conical diffusers", in *AIAA Journal*, 9, 1971.

[193] Bhandari V.B., *Machine Design Data Book*, 2nd ed., McGraw Hill, New Delhi, 2014.

[194] Dyrobes, *Rolling Element Bearings*, available at: https://dyrobes.com/help1800/Rotor/html/dyro17qs.htm, last accessed on 2nd July 2018.

[195] Gargiulo E.P., Jr., "A Simple Way to Estimate Bearing Stiffness", in*: Machine Design*, 107–110, 1980.

[196] Hertz H., "Über die Berührung fester elastischer Körper und über die Härte", in: *Verhandlungen des Vereins zur Beförderung des Gewerbefleisses*, 449–463, 1882.

[197] Hamrock B.J., Anderson, W.J., "Analysis of an arched outer–race ball bearing considering centrifugal forces", in: *ASME Journal of Lubrication technology*, 95, 265–276, 1973.

[198] Hamrock B.J. Anderson, W.J., "Rolling–element bearings", in: *NASA Reference publication*, 1105, 57, 1983.

[199] SKF, *Requisite minimum load*, available at: http://www.skf.com/it/products/bearings–units–housings/roller–bearings/principles/selection–of–bearing–size/dynamic–bearing–loads/requisite–minimum–load/index.html, last accessed on 2nd July 2018.

[200] SKF, "Angular contact ball bearings, double row, 3207 A–2ZTN9/MT33", available at: http://www.skf.com/group/products/bearings–units–housings/ball–bearings/angular–contact–ball–bearings/double–row–angular–contact–ball–bearings/double–row/index.html?designation=3207%20A–2ZTN9/MT33, last accessed on 2nd July 2018.

[201] SKF, *Deep groove ball bearings, 61817–2RZ*, available at: http://www.skf.com/group/products/bearings–units–housings/ball–bearings/deep–groove–ball–bearings/single–row–deep–groove–ball–bearings/deep–groove–ball–bearings/index.html?designation=61817–2RZ&unit=imperialUnit, last accessed on 2nd July 2018.

[202] Tillner–Roth R., Baehr H.D., "An international standard formulation for the thermodynamic properties of 1,1,1,2–Tetrafluoroethane (HFC–134a) for temperatures from 170 K to 455 K and pressures up to 70 MPa", in: *Journal of Physical and Chemical Reference Data*, 23, 657–729, 1994.

[203] Lemmon E.W., Jacobsen R.T., "An international standard formulation for the thermodynamic properties of 1, 1, 1–trifluoroethane (HFC–143a) for temperatures from 161 to 450 K and pressures to 50 MPa", in: *Journal of Physical and Chemical Reference Data*, 29, 521–552, 2000.

[204] Lemmon E.W., Jacobsen R.T., "A new functional form and new fitting techniques for equations of state with application to pentafluoroethane (HFC–125)", in*: Journal of physical and chemical reference data*, 34, 69–108, 2005.

[205] Lemmon E.W., Span R., "Short fundamental equations of state for 20 industrial fluids", in*: Journal of Chemical & Engineering Data*, 51, 785–850, 2006.

[206] Mondéjar M.E., McLinden M.O., Lemmon E., "Thermodynamic properties of trans–1Chloro–3.3.3–trifluoropropene (R1233zd(E): Vapor Pressure, (p, ρ, T) Behavior, and Speed of Sound Measurements, and Equation of State", in: *Journal of Chemical & Engineering Data*, 60, 2477–2489, 2015.

[207] Aljundi I.H., "Effect of dry hydrocarbons and critical point temperature on the efficiencies of organic Rankine cycle", in: *Renewable Energy*, 36, 1196–1202, 2011.

[208] Dumont O., Parthoens A., Dickes R., Lemort V., "Experimental investigation and optimal performance assessment of four volumetric expanders (scroll, screw, piston and roots) tested in a small–scale organic Rankine cycle system", in *Energy*, 165, 1119–1127, 2018.

[209] Cohen H., Rogers G.F.C., Saravanamuttoo H.I.H, *Gas Turbine Theory*, Longman Group Limited, England, 1996.

[210] Balje O.E., *Turbomachines, a guide to design, selection and theory*, John Wiley and sons, New York, 1981.

[211] SKF, The SKF model for calculating the frictional moment, available at: http://www.skf.com/binary/86–299767/The%20SKF%20model%20for%20calculating%20the%20frictional%20moment_tcm_12–299767.pdf, last accessed on July 2018.

[212] Traupel W., *Thermische Turbomaschinen Zweiter Band Geländerte Betriebsbedingungen, Regelung, Mechanische Probleme, Temperaturprobleme*, Springer–Verlag, New York, 1977.

[213] NASA, Technology Readiness Level, available at: http://www.nasa.gov/content/technology–readiness–level/#.U5Vnl_ldVKY, accessed on October 2018.